Surface Interactions for Atomic Layer Deposition and Etching of Wide Band Gap Materials Based on Fluorine Chemistry

by

Daniel C. Messina

A Dissertation Presented in Partial Fulfillment
of the Requirements for the Degree
Doctor of Philosophy

Approved October 2021 by the
Graduate Supervisory Committee:

Robert J. Nemanich, Chair
Stephen Goodnick
Fernando A. Ponce
David Smith

ARIZONA STATE UNIVERSITY

December 2021

ABSTRACT

In this dissertation, the surface interactions of fluorine were studied during atomic layer deposition (ALD) and atomic layer etching (ALE) of wide band gap materials. To enable this research two high vacuum reactors were designed and constructed for thermal and plasma enhanced ALD and ALE, and they were equipped for *in-situ* process monitoring.

Fluorine surface interactions were first studied in a comparison of thermal and plasma enhanced ALD (TALD and PEALD) of AlF_3 thin films prepared using hydrogen fluoride (HF), trimethylaluminum (TMA), and H_2-plasma. The ALD AlF_3 films were compared *in-situ* using ellipsometry and X-ray photoelectron spectroscopy (XPS). Ellipsometry showed a growth rate of 1.1 Å/ cycle and 0.7 Å/ cycle, at 100°C, for the TALD and PEALD AlF_3 processes, respectively. XPS indicated the presence of Al-rich clusters within the PEALD film. The formation of the Al-rich clusters is thought to originate during the H_2-plasma step of the PEALD process. The Al-rich clusters were not detected in the TALD AlF_3 films. This study provided valuable insight on the role of fluorine in an ALD process.

Reactive ion etching is a common dry chemical etch process for fabricating GaN devices. However, the use of ions can induce various defects, which can degrade device performance. The development of low-damage post etch processes are essential for mitigating plasma induced damage. As such, two multistep ALE methods were implemented for GaN based on oxidation, fluorination, and ligand exchange. First, GaN

surfaces were oxidized using either water vapor or O_2-plasma exposures to produce a thin oxide layer. The oxide layer was addressed using alternating exposures of HF and TMG, which etch Ga_2O_3 films. Each ALE process was characterized using *in-situ* using ellipsometry and XPS and *ex-situ* transmission electron microscopy (TEM). XPS indicated F and O impurities remained on the etched surfaces. Ellipsometry and TEM showed a slight reduction in thickness. The very low ALE rate was interpreted as the inability of the Ga_2O_3 ALE process to fluorinate the ordered surface oxide on GaN (0001).

Overall, these results indicate HF is effective for the ALD of metal fluorides and the ALE of metal oxides.

DEDICATION

To my family and the pursuit of knowledge.

ACKNOWLEDGMENTS

I would like to express my sincere gratitude towards my advisor, Dr. Robert J. Nemanich, for the opportunity to work in his research group and for the advice and encouragement he provided throughout my graduate studies. Dr. Nemanich's knowledge and support was invaluable. His diligent efforts and enthusiasm will inspire me throughout my entire life.

I would also like to extend thanks to my committee members, Dr. Stephen Goodnick, Dr. Fernando A. Ponce, and Dr. David Smith for their helpful suggestions towards the development of this work.

Additionally, I would like to thank all past and present the members of the Nanoscience Laboratory (NSL), especially to Dr. Brianna Eller, Dr. Xingye Wang, and Franz Koeck who gave me guidance on research and constructing equipment. I would like to thank Dr. Mei Hao, Yichen Yao, Dr. Anna Zaniewski, and Dr. Yu Yang for familiarizing me with the equipment. I thank Robert Mecham and Avani Patel for the helpful discussions.

To Dr. Zhiyu Huang, Kevin Hatch, Jesse Brown, and Kari Slotten I give special thanks. Zhiyu and I worked long nights on our NASA project and on the middle ultraviolet reflective coating paper. I learned many principles of optical coatings and ellipsometry from him. Kevin Hatch and I worked tirelessly to develop ALE processes for the PNDIODES project. I appreciate all the help Kevin gave me. Jesse Brown and I joined the NSL at the same time and went through our graduate classes together. The time him and I

spent completing assignments, discussing physics, and maintaining the NSL vacuum equipment was invaluable. Finally, I thank Kari Slotten for patterning my GaN samples.

I thank Dr. Paul Scowen and Dr. Hongbin Yu for this aid during the NASA project. I thank Jaime Quintero at the ASU NanoFab for the deposition of ALD Al_2O_3 used for the AlF_3 growths. Without those samples, I could not have completed this work. At the Goldwater Materials Science Facility, I would also like to thank David Wright for his oversight in filling the HF-pyridine cylinders. The use of his inert purge glove box was integral to the ALD of metal fluorides and ALE of oxides and nitrides.

For their help with TEM measurements, I would like to thank Saurabh Vishwakarma, Dr. David Smith, and Dr. Martha McCartney for their detailed work.

To the Department of Physics business office, I thank Deborah Denson, Sheryl Quenzer, Karin Moen, Ixchell Paape, and Lisa Andreotti for their aid in purchasing the equipment for the ALD/ALE reactors.

This research was supported by National Aeronautics and Space Administration under Grant No. NNH14ZDA001N-SAT, the Advanced Research Projects Agency-Energy, as part of PNDIODES, under Grant No. DE-AR0000868, and the U.S. Department of Energy (DOE), Office of Science, as part of ULTRA, an energy Frontier Research Center funded by Basic Energy Sciences (BES), under Award No. DE-SC0021230. I also acknowledge the use of facilities within the John. M. Cowley Center for High Resolution Electron Microscopy and the NanoFab, at Arizona State University, supported in part by the NSF program NNCI-ECCS-1542160.

TABLE OF CONTENTS

Page

LIST OF TABLES xii

LIST OF FIGURES xiii

CHAPTER

1 INTRODUCTION 1

1.1 Background 1

1.2 Atomic Layer Processes 4

1.2.1 Atomic Layer Deposition 4

1.2.2 Atomic Layer Etching 8

2.1 Dissertation Approach 12

References 15

2 EXPERIMETNAL TECHNIQUES 23

2.1 Introduction 23

2.2 Photoelectron Spectroscopy 25

2.2.1 Pricicples of Photoelectron Spectrscopy 25

2.2.2 X-ray Photoelectron Spectrscopy 30

2.2.3 Characterizaton 31

2.2.3.1 Peak Fitting 31

2.2.3.2 Film Composition 32

2.2.3.3 Film Thickness 34

2.2.3.4 Example: Aluminum Fluoride Thin Films 37

CHAPTER Page

2.2.3.4.1 Peak Fitting 37

2.2.3.4.2 Film Composition 40

2.2.3.4.3 Film Thickness 42

2.3 Ellipsometry 44

2.3.1 Principles of Ellipsometry 44

2.3.2 Optical Modeling 45

2.3.2.1 Cauchy Model 45

2.3.2.2 Pseudo-Substrate Model 46

2.3.2.3 Drude Model 46

2.3.2.4 Effective Medium Approximation 47

2.3.2 Example: In Situ Ellipsometry of Aluminum Fluoride Thin Films 48

2.4 Atomic Layer Deposition 50

2.4.1 Principles of Atomic Layer Deposition 50

2.4.2 Plasma Enhanced Atomic Layer Deposition 52

2.4.2.1 Plasma Basics 53

2.4.2.2 Plasma Configurations 55

2.4 Atomic Layer Etching 57

2.4.1 Principles of Atomic Layer Etching 57

References 61

3 DEVELOPING ATOMIC LAYER PROCESSING RECTORS ENABLED BY FLUORINE CHEMISTRY 65

CHAPTER Page

3.1 Reactor Requirements 65

3.2 Reactor Subsystems 67

3.2.1 Pressure 67

3.2.1.1 Vacuum Generation and Measurement 68

3.2.1.1.1 Sample Transfer and Idling 68

3.2.1.1.2 Processing 69

3.2.1.2 Gas Delivery 70

3.2.2 Temperature 73

3.2.2.1 Reactor Walls and Delivery Tubing 73

3.2.2.2 Sample Stage 74

3.2.2.3 Precursor Vessels 78

3.2.3 Remote Inductively Coupled Plasma 79

3.2.3.1 The Helical Resonator 79

3.2.3.2 Plasma Generation 81

3.2.4 Exhaust Abatement 83

3.2.5 Sample Transfer 89

3.2.6 Programmatic Control 90

3.3 Process Monitoring 96

3.3.1 Pressure 96

3.3.2 Ellipsometry 98

3.3.3 Quadrupole Mass Spectroscopy 98

CHAPTER Page

References....100

4 COMPARISON OF ALUMINUM FLUORIDE THIN FILMS GROWN BY THERMAL AND PLASMA ENHANCED ATOMIC LAYER DEPOSITION....101

4.1 Abstract....101

4.2 Introduction....102

4.3 Experimental....107

4.3.1 Sample Preperation....107

4.3.2 Film Deposition....108

4.3.3 In Situ Characterizaton....110

4.3.3.1 Ellipsometry....110

4.3.3.1 X-ray Photoelectron Spectrscopy....111

4.4 Results....111

4.4.1 X-ray Photoelectron Spectrscopy....112

4.4.2 Ellipsometry....117

4.5 Discussion....121

4.4 Summary and Conclusions....122

Acknowledgements....123

References....124

5 ATOMIC LAYER ETCHING OF GALLIUM NITRIDE ENABLED BY WATER VAPOR AND O2-PLASMA OXIDATION....132

CHAPTER Page

5.1 Abstract 132

5.2 Introduction 133

5.3 Experimental 137

5.3.1 Sample Preperation 138

5.3.2 Equipment 138

5.4 Results 141

5.4.1 X-ray Photoelectron Spectrscopy 142

5.4.2 Ellipsometry 146

5.4.3 Transmission Electron Microsopy 147

5.5 Discussion 150

5.4 Conclusions 151

Acknowledgements 152

References 153

6 Summary and Future Work 159

6.1 Summary and Current Work 159

6.2 Outline of Future Work 161

6.2.1 Atomic Layer Deposition of Gallium Fluoride 161

6.2.2 Plasma Enhanced Atomic Layer Etching of Gallium Oxide Polymorphs Grown by Plasma Enhanced Atomic Layer Deposition 162

References 165

REFERENCES 171

CHAPTER Page

APPENDIX

A COPYRIGHT PRERMISSION 201

LIST OF TABLES

Table Page

1.1 Electronic Properties of Single Crystal Semiconductor Materials. 2

2.1 Peak Center, FWHM (Round Bracket), and Area [Square Brackets] for Core Level Scans Observed for The TALD AlF_3 Films on TALD Al_2O_3. 40

2.2 Slater Subshell Photoionization Cross Sections at 1487 eV for F, O, and Al. 41

2.3 Relevant Quantities for Calculating the Surface Stoichiometry for Each Step in the TALD AlF_3 Deposition Shown in FIG 2.9. 41

2.4 Film Thickness for the PEALD AlF_3 *In Situ* Ellipsometry Depending on the Applied Optical Model. 50

4.1 Reactants used for the ALD of AlF_3 along with the Growth Temperatures (T_g), Growth Rate per Cycle (GPC), and F/Al Ratios (3 Is Stoichiometric).....105

4.2 Peak Centers And FWHM (Brackets) For All Peak Fitted Core Levels Observed for the TALD and PEALD AlF_3 Films on TALD Al_2O_3. 116

LIST OF FIGURES

Figure Page

1.1 Schematic of a Two-reactant ALD Process Based on Sequential Self-limited Surface Reactions. 5

1.2 Design Parameters and Results of a Middle Ultraviolet Reflective Coating Based on Alternating Layer of ALD AlF_3 and Al_2O_3 on Sapphire. 7

1.3 Schematic of a Thermal and Plasma Enhanced Atomic Layer Etching Processes. 9

1.4 Schematic of the Front and Side Views of (a) a Planar Field Effect Transistor (FET), (B) a FinFET, and (C) a Gate-all-around FET (GAAFET). 10

1.5 Illustration of Implementing an ALE Process to Remove RIE Induced Damage to Improve Device Performance. 11

1.6 A schematic illustration of the GaN ALE processes. 12

2.1 Image of the Nano Science Laboratory (NSL) Ultrahigh Vacuum Transfer Line Integrated with a Number of Growth and Characterization Chambers. 24

2.2 Schematic of a Photoemission Spectroscopy System. 25

2.3 Electron Inelastic Mean Free Path (Escape Depth) Dependence on Electron Kinetic Energy. 27

2.4 Probability an Electron, from Depth X with Mean Free Path Λ, Will Reach the Surface. 27

2.5 Illustration of the Electron Excitations in XPS and UPS. 29

2.6 Illustration of the Single Line Approach for Measuring a Thin Film's Thickness T by XPS. 35

Figure Page

2.7 Illustration of the Multiline Approach for Thin Film Thickness Calculations by XPS. 37

2.8 Survey Scan of an AlF_3 Film Deposited by Thermal Atomic Layer Deposition (TALD) with All Major Features Identified. 38

2.9 XPS Core Levels for the F 1s, O 1s, C 1s, and Al 2p for Thermal Atomic Layer Deposited AlF_3. 39

2.10 XPS Band Gap Estimation from the F 1s and Loss Peak for the TALD AlF_3 Film. 43

2.11 Illustration of the Reflection of Polarized Light off a Sample Surface. 44

2.12 Film Thickness from in Situ Ellipsometry During the PEALD AlF_3 Growth over 40 Cycles. 49

2.13 Illustration of a Thermal ALD Process for Aluminum Oxide Using Alternating Exposures of Trimethylaluminum and Water Vapor. 51

2.14 Growth Rate per Cycle Dependence on Temperature for an Ideal ALD Process. 51

2.15 Illustration of an PEALD Al_2O_3 Deposition Using Trimethylaluminum and Atomic Oxygen from a Remote Inductively Coupled Plasma. 52

2.16 Unitless Potential Difference Between the Plasma Sheath and the Substrate Surface as a Function of Atomic Mass or Ion Mass. 54

Figure Page

2.17 Various Plasma Configurations for ALD Reactors. (A) Radical-enhanced, (B) Direct Plasma-assisted, (C) Remote Plasma, and (D) Direct Plasma Reactor with Mesh. 55

2.18 Schematic of an ALE Cycle. 57

2.19 Illustration of the Process Window for Thermal ALE. 58

2.20 A Schematic Illustration of the GaN TALE and PEALE Process. 60

3.1 Schematic of (a) the Fluoride Plasma Enhanced Atomic Layer Processing (F-PEALP) and (b) the Oxide PEALP (O-PEALP) Reactors. 66

3.2 Precursor Vapor and Process Gas Delivery Lines for the ALP Systems with the Pneumatic Valves Labeled. 71

3.3 Front (A), Bottom (B), and Top (C) Views of the Initial ALP Sample Stage Mounted onto a Rotary Flange. 74

3.4 Schematic of the Temperature Control Box Circuit for Sample and Precursor Vessel Heating. 76

3.5 Circuit Diagram of the RF Generator, Impedance Matching Network, Helical Resonator, and Inductively Coupled Plasma. 81

3.6 Block Diagram of the MWH-5-01 Impedance Matching Network. 82

3.7 Schematic of the ALP Reactors Exhaust Abatement. 84

3.8 Illustration of a Possible Configuration of the Multi-trap Filter. 85

3.9 Schematic of the Ebara A70W Two-stage Dry Pump. 86

3.10 Schematic of the CS Clean Systems Acid Dry Bed. 87

Figure Page

3.11 Exploded View of the Bionics Electrochemical Gas Analyzer. 88

3.12 Schematic of the Sample Transfer System for the ALP Reactors. 90

3.13 Control Interfaces for (A) the Fluoride ALP Reactor and (B) the Oxide ALP Reactor. 91

3.14 Block Diagram of (A) a Simple ALP Structure and (B) of the Structure Programmed for the Fluoride ALP. 92

3.15 Process Structure for the Oxide ALP Program. 93

3.16 Screen Shot of the Pressure Recording Program. 97

3.17 Reactor Pressure During the Plasma Enhanced Atomic Layer Deposition of AlF_3. 98

4.1 XPS Spectra of the F 1s, O 1s, C 1s, and Al 2p Core Levels for TALD AlF_3. ...113

4.2 XPS Spectra of the F 1s, O 1s, C 1s, and Al 2p Core Levels for PEALD AlF_3. 115

4.3 Film Thickness from In Situ Ellipsometry and Process Pressure of the TALD AlF_3 growth. 118

4.4 Film Thickness from In Situ Ellipsometry and Process Pressure of the PEALD AlF_3 growth. 120

5.1 A Schematic Illustration of the GaN ALE Processes. 137

5.2 F 1s, O 1s, C 1s, N 1s, and Ga 3d Core Levels of the GaN (0001) Surfaces at Various Process Steps. 143

5.3 Surface Stoichiometry for Each Process Step. 145

5.4 In Situ Ellipsometry Scans During the GaN PEALE and TALE Processes. 147

Figure Page

5.5 Transmission Electron Microscopy of the (A - B) Control Sample, (C - D) the Plasma Oxidized, and (E - F) Thermally Oxidized GaN Samples. 149

CHAPTER 1

INTRODUCTION

1.1 Background

Wide and ultrawide band gap (WBG and UWBG) semiconductor materials have enhanced electrical characteristics in comparison to conventional semiconductor materials such as Si, Ge, or GaAs. WBG and UWBG materials are classified as those with a band gap between 2 – 4 eV and greater than 4 eV, respectively.[1-3] The electronic properties of selected conventional and WBG semiconductors are shown in Table 1.1. In general, larger band gaps correlate to larger breakdown electric fields and electron saturation velocities, which are beneficial for power and high frequency electronics, respectively.[1, 2] WBG and UWBG semiconductors have been used for a variety of applications including diodes,[4-7] transistors,[8] power devices,[9-11] electron emitters,[12] ultraviolet optoelectronics,[13-15] particles detectors,[16-18] among many others. The development of GaN-based radiofrequency (RF) and microwave high-electron mobility transistors (HEMTs) have been implemented in many commercial applications including 5th and 6th generation (5G and 6G) mobile cellular networks.[19, 20] The fabrication of these high impact technologies requires nanoscale precision for both material growth and removal.

Table 1.1. Electronic properties of single crystal semiconductor materials. In some cases, electron and hole properties are denoted by "*e*" and "*h,*" respectively. Table adapted from Tsao *et al*.[2]

		Si	4H-SiC	GaN	β-Ga_2O_3	Diamond
Bandgap	E_g (eV)	1.1	3.3	3.4	4.8	5.5
e (*h*) Mobility	μ ($cm^2/V/s$)	1450 (450)	950 (115)	2000 (350)	300 (<100?)	4000 (3800)
Breakdown Electric Field	E_B (MV/cm)	0.3	3	5	8	10
Thermal Conductivity	κ (W/cm/K)	1.3	5	1.3	~0.2	20
e (*h*) Saturation Velocity	v_{sat} (10^7 cm/s)	1.0 (0.4)	2.0 (1.0)	2.0 (1.7)		1.5 (1.1)
Dielectric Constant	ε	11.7	10	8.9	10	5.7

Fabrication of semiconductor devices often relies of wet chemical or dry chemical etch process for patterning. At times, wet chemical etching is not suitable due to the inert nature of some materials (e.g. GaN).[21] A subset of dry chemical etching is reactive ion etching (RIE) which utilizes plasma species to remove material. In RIE, material is typically removed through the formation of halides then desorbed by ion bombard.[22-24] However, the use of a plasma can induce various defects, which can degrade device

performance by increasing leakage current or lowering breakdown voltage.[25, 26] Previously, this issue has been addressed by depositing high dielectric constant (high-*k*) materials to suppress leakage currents.[27] Alternative methods have focused on developing multi-step RIE processes or post etch treatments to mitigate plasma induced damage. [28, 29] Atomic layer etching (ALE) is one such method.

As mentioned, high-*k* dielectrics are often used as an interfacial layer between semiconductor and metal contacts; such a configuration is referred to as a metal-insulator-semiconductor structure (MIS).[27, 30-34] The use of metal oxides and nitrides grew in popularity because of their ability to suppress quantum mechanical tunneling more effectively than SiO_2 layers.[27, 32, 35, 36] However, with the advent of WBG and UWBG semiconductors, a new class of gate dielectrics is required. Selection of a material as a gate dielectric requires consideration of the band alignment with the semiconductor material.[27] In particular, the confinement of electrons at an interface requires the conduction band offset where the dielectric's conduction band minimum (CBM) is above that of the semiconductor's CBM. For WBG and some UWBG semiconductors, oxides such as HfO_2, Al_2O_3, or Ga_2O_3 have been sufficient. However, for UWBG semiconductors such as diamond a novel class of dielectrics is required and metal fluorides appear to be a class of material that can meet the needs. The incorporation of metal fluorides as a dielectric in UWBG MIS devices would require high purity, uniform and conformal, layers to meet the demands of electric devices.

1.2 Atomic Layer Processes

The development of thin film deposition and etching techniques is an essential process for the miniaturization of electronic devices in the semiconductor industry. The trend for smaller devices has led to the requirement of atomic scale control over thin film deposition and etching. Additionally, for smaller devices with a high aspect ratio, the deposition and etching of thin films is required to be uniform and conformal. Relative to other thin film deposition and etching techniques, only atomic layer deposition and atomic layer etching (ALD and ALE) meet these requirements. These advantages have positioned ALD as a mainstream technology in the fabrication of nanoelectronics. However, ALE is an emerging technique that is not as matured, nor has it been integrated into fabrication processing.

1.2.1 Atomic Layer Deposition

Atomic layer deposition (ALD) is a chemical vapor deposition (CVD) technique. Both CVD and ALD employ vapor transport to enable gas solid interactions. Unlike CVD, ALD achieves film growth using sequential exposures of reactants separated by inert gas purges schematically shown in FIG 1.1. A key characteristic of ALD is the self-limiting nature of the growth process. Self-limiting growth is achieved for a surface that has a limiting number of reactive sites for reactant adsorption. In general, there is a temperature window where excess precursor desorbs from the surface. Moreover, the self-limiting surface reactions must occur in all reactant steps at the same substrate temperature. Thus, in an ideal ALD reaction, there is a temperature range (or growth window) where the growth proceeds in a layer-by-layer mode, and the layer thickness per ALD cycle is

essentially constant. The growth per cycle (GPC) for an ALD process can increase or decrease at temperatures above or below the growth window due to a variety of reasons related to the adsorption-desorption kinetics.[37-39] The substrate temperature is typically chosen within the growth window to prevent precursor self-interaction and decomposition, while also facilitating self-limiting surface reactions. The self-limiting nature of ALD enables precise thickness control along with high purity, uniform, and conformal layers.

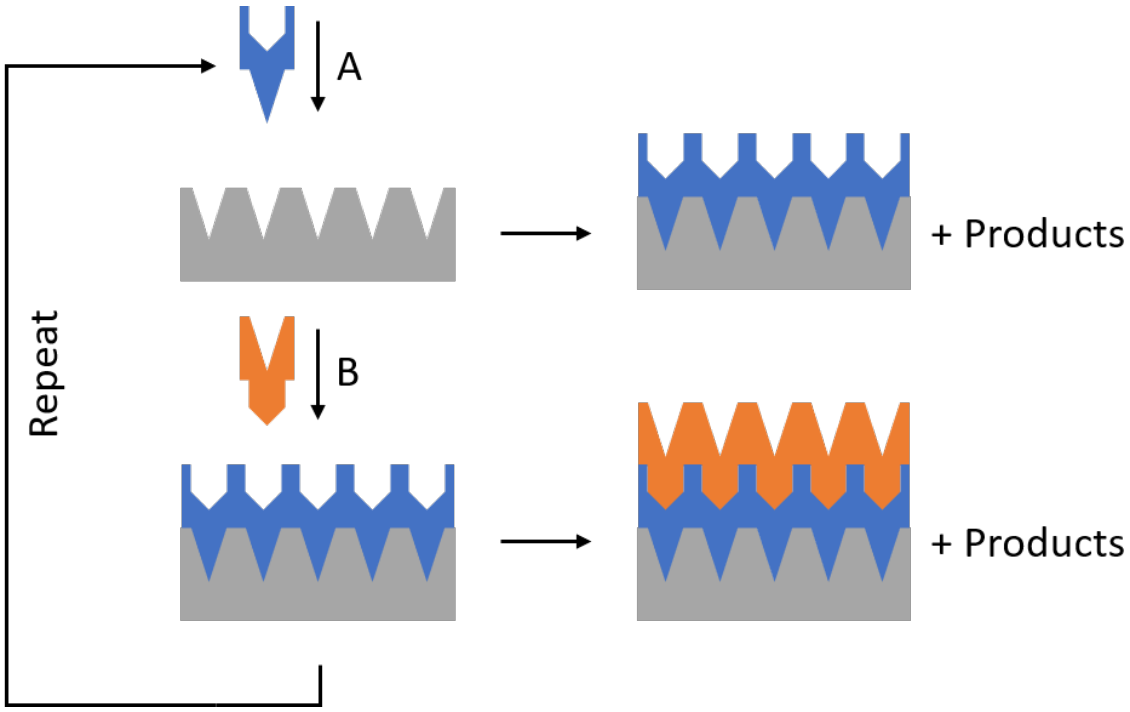

FIG 1.1. Schematic of a two-reactant ALD process based on sequential self-limited surface reactions. Image adapted from George et al.[40] Copyright © 1996, American Chemical Society.

ALD of oxides and nitrides has matured over the past ten to twenty years due to their use as high dielectric (high-*k*) constant gate dielectrics for metal-oxide/insulator-semiconductor devices (MOS/MIS).[27, 30-34] The ALD of metal fluorides is not as well developed though a number of chemical routes have been demonstrated. However, the

selection of reactants is more difficult due to the lack of safe, easy-to-handle, fluoride precursors. Initial fluoride ALD used NH_4F and volatile metal halides (TiF_4 and TaF_5) as fluorine sources.[41-46] More recently, metal fluorides have been deposited using anhydrous HF (AHF), HF-pyridine (HF-P) mixtures, and SF_6-plasma.[47-55] Selection of reactants for ALD processes is of utmost importance to minimize potential impurities. Reactant selection often requires consideration of the intended application. For example, when ALD AlF_3 is used for far ultraviolet optics, formation of oxides and nitrides can degrade optical performance, due to adsorption at lower wavelengths. Additionally, the vacancies or metal impurities can induce Fermi level pinning, which is detrimental to electrical device performance.

In this work, a method for plasma enhanced ALD of AlF_3 is presented and compared to a thermal ALD AlF_3 process. The ALD AlF_3 processes were enabled by the construction of a custom metal fluoride ALD reactor designed for minimal impurity incorporation. The AlF_3 processes utilized alternating exposures of hydrogen fluoride (HF) and trimethylaluminum (TMA) to achieve self-limiting growth. In the plasma enhanced variant, a remote H_2-plasma step was implemented after each HF exposure to prepare the surface prior to start of the next cycle.

These AlF_3 processes were developed to meet the requirements for the construction of an ultraviolet (UV) reflective coating. AlF_3 and Al_2O_3 were ideal materials as they have a low and high reflectivity, respectively, and large band gaps.[56] It was demonstrated that ALD could be used to fabricate an all-dielectric high reflectivity middle UV coating (FIG 1.2).[56] This was an original use of ALD to fabricate a middle UV reflective coating based on AlF_3 and Al_2O_3. The AlF_3 processes developed in this dissertation have also been

implemented to characterize the band alignment of AlF_3 on diamond surfaces with various surface terminations. Analysis of these experiments will provide valuable insight on the surface interactions of HF for the deposition of AlF_3.

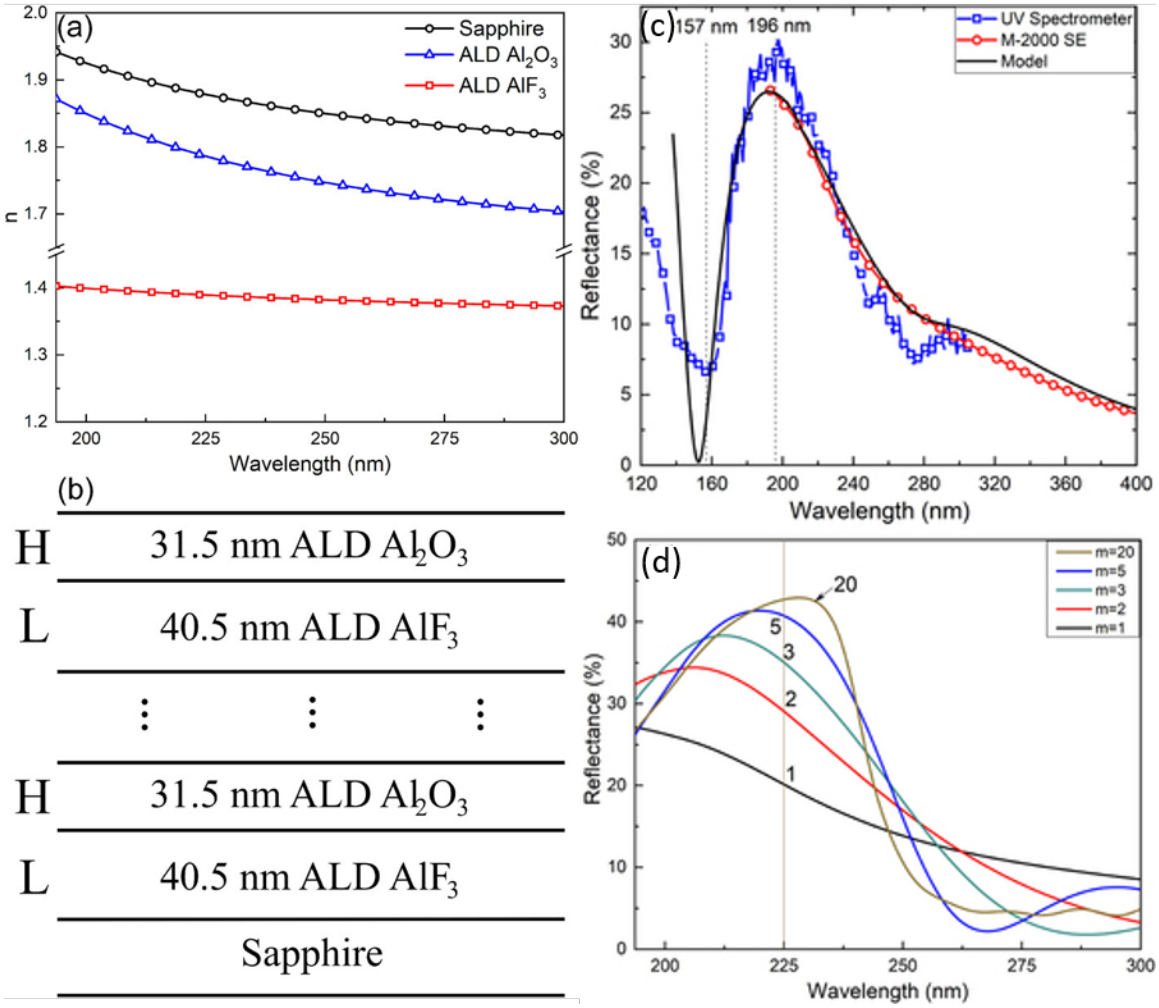

FIG 1.2. Design parameters and results of a middle ultraviolet reflective coating based on alternating layer of ALD AlF_3 and Al_2O_3 on sapphire. In (a) the refractive index of each dielectric is shown in the middle ultraviolet. In (b), the multilayer coating stack design where "H" and "L" indicate high and low index layers, respectively. The final result for a single bilayer is shown in (c) with the theoretical and experimental measurements

indicated. Finally, (d) shows a model of the coating extended past a single bilayer. Image adapted from Huang et al.[56] Copyright © 2021, American Vacuum Society.

1.2.2 Atomic Layer Etching

Atomic layer etching (ALE) is a thin film removal technique with atomic scale precision. Similar to ALD, ALE is a self-limiting or pseudo self-limiting thin film removal technique.[57, 58] ALE achieves self-limiting material removal using sequential exposures of precursors, or reactants, separated by inert gas purges. A model ALE process (FIG 1.3) would consist of a surface modification step and a removal step separated by purging steps. Self-limiting etching is achieved, as there are a limited number of reactive surface sites for precursor adsorption. The self-limiting aspect does not have to occur during the second reactant exposures. Instead, the second reactant must be inert towards the unmodified surface. A thermal ALE process can be classified in a variety of ways based on the precursor used; the number of steps required or the reaction mechanisms. To date, a number of different mechanisms have been identified for thermal ALE.[59] These mechanisms commonly revolve around surface conversion, oxidation, fluorination, and ligand exchange. Additionally, plasma ALE processes tend to be anisotropic (or directional) while thermal ALE processes are generally isotopic.[58, 59]

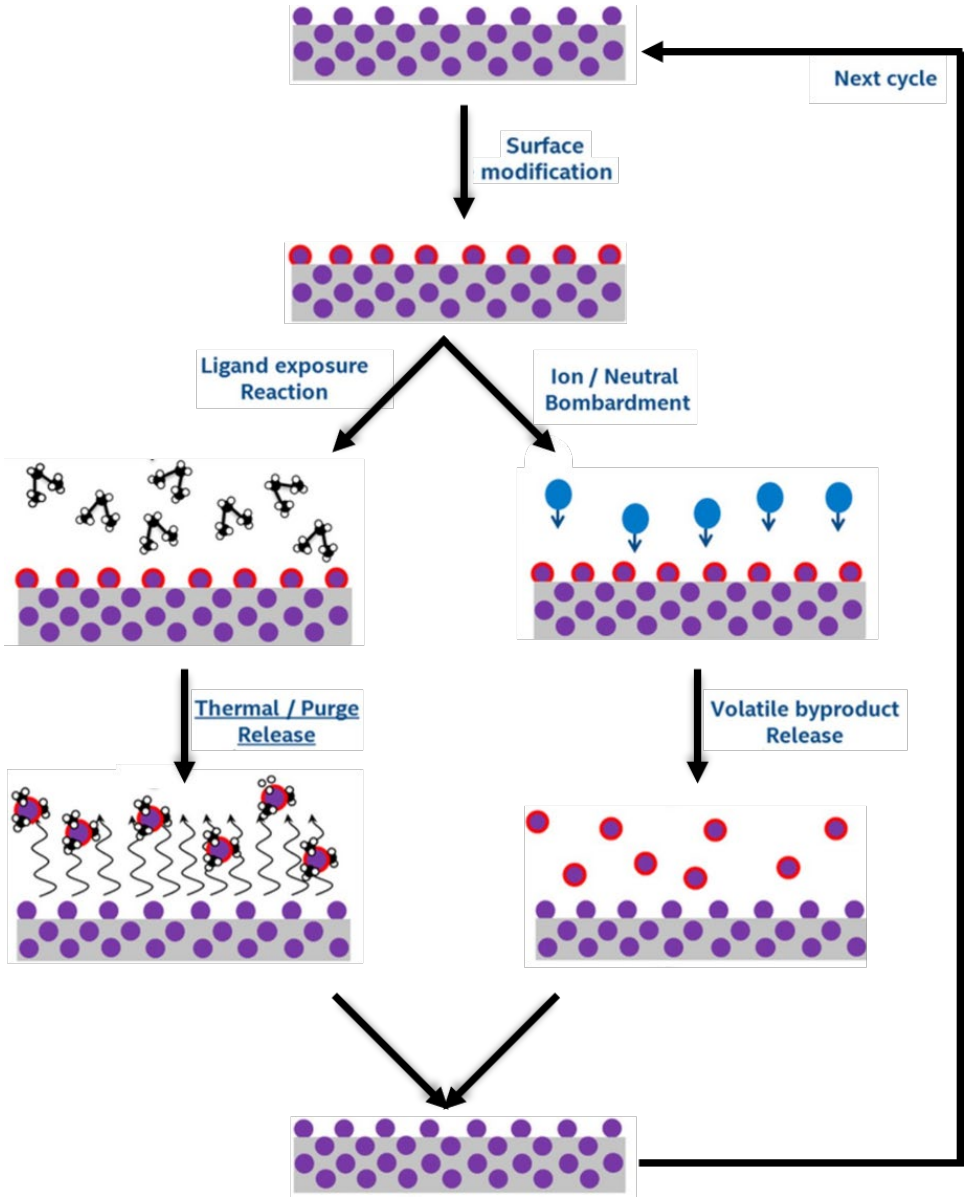

FIG 1.3. Schematic of a thermal and plasma enhanced atomic layer etching processes. Image adapted from Carver *et al.*[36] Copyright © CC BY-NC-ND 4.0.

Most ALE process do not exhibit a well-defined temperature window in which the etch rate is constant. The etch window, or process window, is chosen to optimize the reaction rates of each step as well as the byproduct desorption rate. Outside of this process window, etching may not occur which in some cases deposition may occur. Within the

process window, the etch per cycle (EPC) can vary depending on the temperature dependence of the reaction and desorption rates of each precursor. The etch rates can be less than or greater than one atomic layer per cycle but are typically less than 1 nm.

ALE processes have been implemented for a variety of novel processes including 3-D field effect transistors (FET) (FIG 1.4), such as the FinFET and gate-all-around FET (GAAFET), and creating UV reflective surfaces.[60-64] The development of FinFETs and GAAFETs have led to lower power consumptions and higher performance at a marginal increase in cost.[65] To fabricate a 3-D structure such as the FinFET of GAAFET, dry anisotropic etch processes such as reaction ion etching (RIE) are used. Typically, RIE implements halogen based plasmas, which are used to form nonvolatile metal halides that are then removed via ion-bombardment.[22-24] However, the use of ion bombardment can induce various defects, which can degrade device performance by increasing leakage current or lowering breakdown voltage.[25, 26]

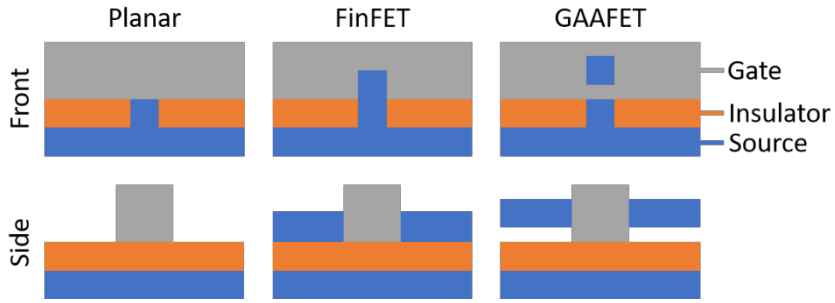

FIG 1.4. Schematic of the front and side views of (a) a planar field effect transistor (FET), (b) a FinFET, and (c) a gate-all-around FET (GAAFET).

Recently, multi-step etch processes and post etch treatments have been developed to mitigate plasma induced damage, including ALE.[28, 29] The ion induced damage of an RIE surface is thought to extend tens of nanometers into the material with the bulk of the

damage concentrated at the surface. Thus, ALE is an ideal material removal technique that could be implemented to remove the surface RIE damage as indicated in FIG 1.5.

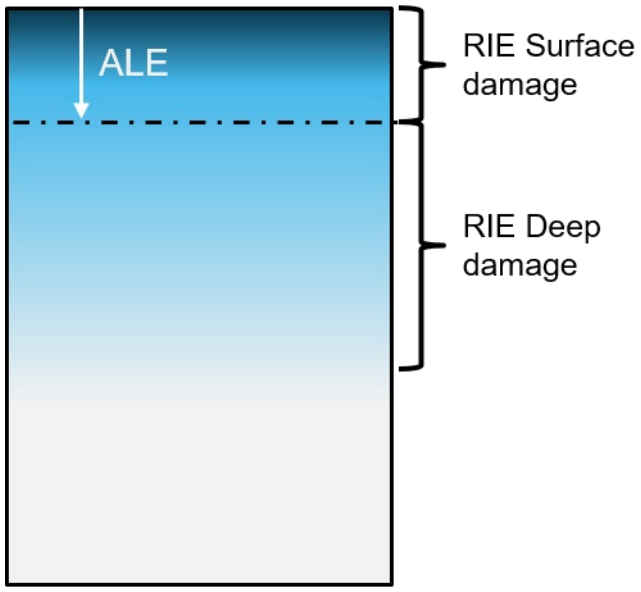

FIG 1.5. Illustration of implementing an ALE process to remove RIE induced damage to improve device performance.

In this work, two multi-step processes were developed for ALE of GaN (0001), and are schematically shown in FIG 1.6. To enable this research, a custom fluoride atomic layer deposition and etching chamber was designed and constructed. Initial research focused on developing a plasma enhanced ALD method for Ga_2O_3 prior to development of GaN ALE. The Ga_2O_3 etch process relied on alternating exposures of hydrogen fluoride and trimethylgallium to achieve self-limiting etching. The two GaN ALE processes differed by the oxidation method and the number of Ga_2O_3 etch cycles required to remove the surface oxide. Development of such processes could be implemented on GaN surfaces to removed RIE induced damage and to reduce surface defects thus improving device performance. These ALE processes relied on the HF surface interactions to effectively create a fluoride

layer, which could be removed via ligand exchange. Without the strong oxidation potential of the fluoride, these ALE methods would not be possible.

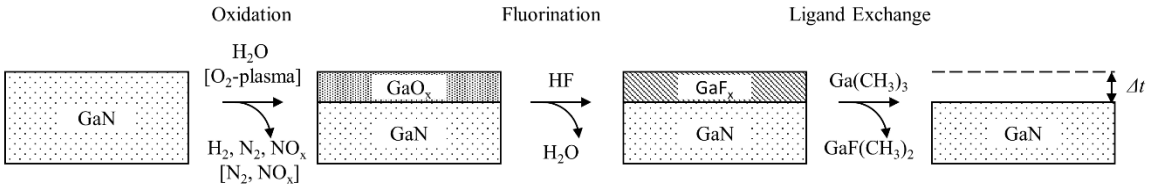

FIG 1.6. A schematic illustration of the GaN ALE processes. The GaN was oxidized either using a water vapor or remote O_2-plasma exposure to create a thin surface oxide. The surface oxide was removed using a Ga_2O_3 ALE process.

2.1 Dissertation Approach

The experimental techniques employed in these studies are detailed in Chapter 2. The characterization techniques include X-ray photoemission spectroscopy (XPS) and ellipsometry. Examples are provided for the analysis of XPS and ellipsometry measurements. Finally, the basic principles of atomic layer deposition and etching are presented.

Chapter 3 presents the design constraints and construction of the fluoride atomic layer deposition and etching systems used in this work. This chapter is split into four main sections consisting of process requirements, equipment and subsystems, programmatic control, and process monitoring. The process requirements and system design are discussed for pressure, temperature, plasma, and precursor abatement. Additionally, an overview of the equipment used is given along with methods in which the equipment could be remotely controlled. The control program for the atomic layer deposition and etching systems is then

described including a basic description of the program architecture. Finally, the process monitoring capabilities and limitations are described.

In Chapter 4, a detailed comparison of ALD of AlF_3 thin films is presented using trimethylaluminum (TMA), hydrogen fluoride (HF), and H_2. Two sets of films were grown using a thermal ALD (TALD) and plasma enhanced ALD (PEALD) processes. In TALD of AlF_3 using HF and TMG, excess HF adsorbed onto the AlF_3 surface after each cycle.[48] As such, a remote H_2-plasma was implemented with the intention to remove the excess adsorbed HF possibly leading to a denser film with improved electrical characteristics. The ALD processes were studied using *in situ* ellipsometry to determine film thickness and growth rates. XPS was implemented before and after each deposition allowing for determination of chemical states and film stoichiometry. XPS of the PEALD AlF_3 layers showed the presence of Al-Al impurities interpreted as Al-rich clusters attributed to the use of a H_2-plasma.

In Chapter 5, a comparison is made for different atomic layer etching (ALE) methods for GaN based on oxidation, fluorination, and ligand exchange. The GaN ALE processes differ by the oxidation method in which either water vapor or remote O_2-plasma exposures were implemented. The surface oxide was then removed via a novel Ga_2O_3 thermal ALE process utilizing a number of alternating exposures of HF and trimethylgallium. Each ALE process was monitored by *in situ* ellipsometry. XPS as employed to characterize the surface composition and impurity states at each process step. Additionally, the thermal and plasma enhance methods were performed on patterned wafers allowing the use of transmission electron microscopy (TEM). XPS indicated F, O, and C impurities remained on the etched surfaces for both ALE processes. TEM indicated

the etch rates were much less than expected with the etched surface roughness comparable to the unetched surface.

In Chapter 6, the significance of the Chapter 4 and 5 results is discussed and summarized. Past and ongoing applications of the ALD AlF_3 thin films are presented. Additionally, two topics for future work are outlined: ALD of GaF_3 and ALE of Ga_2O_3 polymorphs.

The studies presented in this dissertation provide a more complete understanding of the surface interactions for atomic layer deposition and etching due to fluorine chemistry.

References

[1] S. Fujita, Wide-bandgap semiconductor materials: For their full bloom, Japanese Journal of Applied Physics **54**, 030101 (2015).

[2] J. Y. Tsao, S. Chowdhury, M. A. Hollis, D. Jena, N. M. Johnson, K. A. Jones, R. J. Kaplar, S. Rajan, C. G. Van de Walle, E. Bellotti, C. L. Chua, R. Collazo, M. E. Coltrin, J. A. Cooper, K. R. Evans, S. Graham, T. A. Grotjohn, E. R. Heller, M. Higashiwaki, M. S. Islam, P. W. Juodawlkis, M. A. Khan, A. D. Koehler, J. H. Leach, U. K. Mishra, R. J. Nemanich, R. C. N. Pilawa-Podgurski, J. B. Shealy, Z. Sitar, M. J. Tadjer, A. F. Witulski, M. Wraback and J. A. Simmons, Ultrawide-Bandgap Semiconductors: Research Opportunities and Challenges, Advanced Electronic Materials **4**, 1600501 (2018).

[3] M. Higashiwaki, R. Kaplar, J. Pernot and H. Zhao, Ultrawide bandgap semiconductors, Applied Physics Letters **118**, 200401 (2021).

[4] S. Guha and N. A. Bojarczuk, Ultraviolet and violet GaN light emitting diodes on silicon, Applied Physics Letters **72**, 415-417 (1998).

[5] S. Han, S. Yang and K. Sheng, Fluorine-Implanted Termination for Vertical GaN Schottky Rectifier With High Blocking Voltage and Low Forward Voltage Drop, IEEE Electron Device Letters **40**, 1040-1043 (2019).

[6] H. Umezawa, M. Nagase, Y. Kato and S.-i. Shikata, High temperature application of diamond power device, Diamond and Related Materials **24**, 201-205 (2012).

[7] I. C. Kizilyalli, T. Prunty and O. Aktas, 4-kV and 2.8-mΩ -cm^{-2} Vertical GaN p-n Diodes With Low Leakage Currents, IEEE Electron Device Letters **36**, 1073-1075 (2015).

[8] A. Alzahrani, A. Alruqi, B. Karki, M. Kalutarakoralalage, J. Jasinski and G. U. Sumanasekera, Direct fabrication and characterization of vertically stacked Graphene/h-BN/Graphene tunnel junctions, Nano Express (2021).

[9] H. Fu, K. Fu, C. Yang, H. Liu, K. A. Hatch, P. Peri, D. Herath Mudiyanselage, B. Li, T.-H. Kim, S. R. Alugubelli, P.-Y. Su, D. C. Messina, X. Deng, C.-Y. Cheng, R. Vatan Meidanshahi, X. Huang, H. Chen, T.-H. Yang, J. Zhou, A. M. Armstrong,

A. A. Allerman, E. T. Yu, J. Han, S. M. Goodnick, D. J. Smith, R. J. Nemanich, F. A. Ponce and Y. Zhao, Selective area regrowth and doping for vertical gallium nitride power devices: Materials challenges and recent progress, Materials Today (2021).

[10] Y. Zhang, Z. Liu, M. J. Tadjer, M. Sun, D. Piedra, C. Hatem, T. J. Anderson, L. E. Luna, A. Nath, A. D. Koehler, H. Okumura, J. Hu, X. Zhang, X. Gao, B. N. Feigelson, K. D. Hobart and T. Palacios, Vertical GaN Junction Barrier Schottky Rectifiers by Selective Ion Implantation, IEEE Electron Device Letters **38**, 1097-1100 (2017).

[11] Y. Zhang, M. Sun, Z. Liu, D. Piedra, M. Pan, X. Gao, Y. Lin, A. Zubair, L. Yu and T. Palacios, presented at the 2016 IEEE International Electron Devices Meeting (IEDM), 2016 (unpublished).

[12] F. A. Koeck, M. Benipal, H. Surdi and R. J. Nemanich, presented at the 2020 IEEE 21st International Conference on Vacuum Electronics (IVEC), 2020 (unpublished).

[13] S. Zhao, S. Y. Woo, S. M. Sadaf, Y. Wu, A. Pofelski, D. A. Laleyan, R. T. Rashid, Y. Wang, G. A. Botton and Z. Mi, Molecular beam epitaxy growth of Al-rich AlGaN nanowires for deep ultraviolet optoelectronics, APL Materials **4**, 086115 (2016).

[14] V. Jmerik, A. Toropov, V. Davydov and S. Ivanov, Monolayer-Thick GaN/AlN Multilayer Heterostructures for Deep-Ultraviolet Optoelectronics, physica status solidi (RRL) – Rapid Research Letters **15**, 2100242 (2021).

[15] W. Sun, C.-K. Tan and N. Tansu, AlN/GaN Digital Alloy for Mid- and Deep-Ultraviolet Optoelectronics, Scientific Reports **7**, 11826 (2017).

[16] J. Holmes, M. Dutta, F. A. Koeck, M. Benipal, J. Brown, B. Fox, R. Hathwar, H. Johnson, M. Malakoutian, M. Saremi, A. Zaniewski, R. Alarcon, S. Chowdhury, S. M. Goodnick and R. J. Nemanich, A 4.5 μm PIN diamond diode for detecting slow neutrons, Nuclear Instruments and Methods in Physics Research Section A: Accelerators, Spectrometers, Detectors and Associated Equipment **903**, 297-301 (2018).

[17] J. M. Holmes, M. Dutta, F. A. Koeck, M. K. Benipal, R. Hathwar, J. Brown, B. Fox, H. Johnson, A. Zaniewski, R. Alarcon, S. Chowdhury, S. M. Goodnick and R.

J. Nemanich, Neutralizing the polarization effect of diamond diode detectors using periodic forward bias pulses, Diamond and Related Materials **94**, 162-165 (2019).

[18] J. Holmes, J. Brown, F. A. Koeck, H. Johnson, M. K. Benipal, P. Kandlakunta, A. Zaniewski, R. Alarcon, R. Cao, S. M. Goodnick and R. J. Nemanich, Performance of 5-μm PIN diamond diodes as thermal neutron detectors, Nuclear Instruments and Methods in Physics Research Section A: Accelerators, Spectrometers, Detectors and Associated Equipment **961**, 163601 (2020).

[19] R. Hall, 5G and GaN: Future innovations (Published, 2021)

[20] N. Flaherty, (eenewseurope.com, 2021).

[21] D. Zhuang and J. H. Edgar, Wet etching of GaN, AlN, and SiC: a review, Materials Science and Engineering: R: Reports **48**, 1-46 (2005).

[22] S. J. Pearton, J. C. Zolper, R. J. Shul and F. Ren, GaN: Processing, defects, and devices, Journal of Applied Physics **86**, 1-78 (1999).

[23] M. E. Lin, Z. F. Fan, Z. Ma, L. H. Allen and H. Morkoç, Reactive ion etching of GaN using BCl_3, Applied Physics Letters **64**, 887-888 (1994).

[24] R. J. Shul, G. B. McClellan, S. A. Casalnuovo, D. J. Rieger, S. J. Pearton, C. Constantine, C. Barratt, R. F. K. Jr., C. Tran and M. Schurman, Inductively coupled plasma etching of GaN, Applied Physics Letters **69**, 1119-1121 (1996).

[25] S. Huang, Q. Jiang, K. Wei, G. Liu, J. Zhang, X. Wang, Y. Zheng, B. Sun, C. Zhao, H. Liu, Z. Jin, X. Liu, H. Wang, S. Liu, Y. Lu, C. Liu, S. Yang, Z. Tang, J. Zhang, Y. Hao and K. J. Chen, presented at the 2014 IEEE International Electron Devices Meeting, 2014 (unpublished).

[26] H. S. Lee, D. Y. Jung, Y. Park, J. Na, H. G. Jang, H. S. Lee, C. H. Jun, J. Park, S. O. Ryu, S. C. Ko and E. S. Nam, 0.34 V_T AlGaN/GaN-on-Si Large Schottky Barrier Diode With Recessed Dual Anode Metal, IEEE Electron Device Letters **36**, 1132-1134 (2015).

[27] J. H. Choi, Y. Mao and J. P. Chang, Development of hafnium based high-k materials—A review, Materials Science and Engineering: R: Reports **72**, 97-136 (2011).

[28] N. R. Johnson, J. K. Hite, M. A. Mastro, C. R. EddyJr. and S. M. George, Thermal atomic layer etching of crystalline GaN using sequential exposures of XeF_2 and BCl_3, Applied Physics Letters **114**, 243103 (2019).

[29] P. Peri, K. Fu, H. Fu, Y. Zhao and D. J. Smith, Characterization of As-Grown and Regrown GaN-on-GaN Structures for Vertical p-n Power Devices, Journal of Electronic Materials **50**, 2637-2642 (2021).

[30] M. R. Esmaeili-Rad, F. Li, A. Sazonov and A. Nathan, Stability of nanocrystalline silicon bottom-gate thin film transistors with silicon nitride gate dielectric, Journal of Applied Physics **102**, 064512 (2007).

[31] S. Takagi, T. Maeda, N. Taoka, M. Nishizawa, Y. Morita, K. Ikeda, Y. Yamashita, M. Nishikawa, H. Kumagai, R. Nakane, S. Sugahara and N. Sugiyama, Gate dielectric formation and MIS interface characterization on Ge, Microelectronic Engineering **84**, 2314-2319 (2007).

[32] C. G. Parker, G. Lucovsky and J. R. Hauser, Ultrathin oxide-nitride gate dielectric MOSFET's, IEEE Electron Device Letters **19**, 106-108 (1998).

[33] S. K. Jang, J. Youn, Y. J. Song and S. Lee, Synthesis and Characterization of Hexagonal Boron Nitride as a Gate Dielectric, Scientific Reports **6**, 30449 (2016).

[34] T. P. Ma, Making silicon nitride film a viable gate dielectric, IEEE Transactions on Electron Devices **45**, 680-690 (1998).

[35] M. Coll, J. Fontcuberta, M. Althammer, M. Bibes, H. Boschker, A. Calleja, G. Cheng, M. Cuoco, R. Dittmann, B. Dkhil, I. El Baggari, M. Fanciulli, I. Fina, E. Fortunato, C. Frontera, S. Fujita, V. Garcia, S. T. B. Goennenwein, C. G. Granqvist, J. Grollier, R. Gross, A. Hagfeldt, G. Herranz, K. Hono, E. Houwman, M. Huijben, A. Kalaboukhov, D. J. Keeble, G. Koster, L. F. Kourkoutis, J. Levy, M. Lira-Cantu, J. L. MacManus-Driscoll, J. Mannhart, R. Martins, S. Menzel, T. Mikolajick, M. Napari, M. D. Nguyen, G. Niklasson, C. Paillard, S. Panigrahi, G. Rijnders, F. Sánchez, P. Sanchis, S. Sanna, D. G. Schlom, U. Schroeder, K. M. Shen, A. Siemon, M. Spreitzer, H. Sukegawa, R. Tamayo, J. van den Brink, N. Pryds and F.

M. Granozio, Towards Oxide Electronics: a Roadmap, Applied Surface Science **482**, 1-93 (2019).

[36] C. T. Carver, J. J. Plombon, P. E. Romero, S. Suri, T. A. Tronic and R. B. Turkot, Atomic Layer Etching: An Industry Perspective, ECS Journal of Solid State Science and Technology **4**, N5005-N5009 (2015).

[37] R. L. Puurunen, Surface chemistry of atomic layer deposition: A case study for the trimethylaluminum/water process, Journal of Applied Physics **97**, 121301 (2005).

[38] V. Miikkulainen, M. Leskelä, M. Ritala and R. L. Puurunen, Crystallinity of inorganic films grown by atomic layer deposition: Overview and general trends, Journal of Applied Physics **113**, 021301 (2013).

[39] N. E. Richey, C. de Paula and S. F. Bent, Understanding chemical and physical mechanisms in atomic layer deposition, The Journal of Chemical Physics **152**, 040902 (2020).

[40] S. M. George, A. W. Ott and J. W. Klaus, Surface Chemistry for Atomic Layer Growth, The Journal of Physical Chemistry **100**, 13121-13131 (1996).

[41] M. Mäntymäki, J. Hämäläinen, E. Puukilainen, F. Munnik, M. Ritala and M. Leskelä, Atomic Layer Deposition of LiF Thin Films from Lithd and TiF_4 Precursors, Chemical Vapor Deposition **19**, 111-116 (2013).

[42] T. Pilvi, E. Puukilainen, U. Kreissig, M. Leskelä and M. Ritala, Atomic Layer Deposition of MgF_2 Thin Films Using TaF_5 as a Novel Fluorine Source, Chemistry of Materials **20**, 5023-5028 (2008).

[43] T. Pilvi, M. Ritala, M. Leskelä, M. Bischoff, U. Kaiser and N. Kaiser, Atomic layer deposition process with TiF_4 as a precursor for depositing metal fluoride thin films, Appl. Opt. **47**, C271-C274 (2008).

[44] M. Mäntymäki, M. J. Heikkilä, E. Puukilainen, K. Mizohata, B. Marchand, J. Räisänen, M. Ritala and M. Leskelä, Atomic Layer Deposition of AlF_3 Thin Films Using Halide Precursors, Chemistry of Materials **27**, 604-611 (2015).

[45] T. Pilvi, K. Arstila, M. Leskelä and M. Ritala, Novel ALD Process for Depositing CaF_2 Thin Films, Chemistry of Materials **19**, 3387-3392 (2007).

[46] T. Pilvi, E. Puukilainen, F. Munnik, M. Leskelä and M. Ritala, ALD of YF_3 Thin Films from TiF_4 and $Y(thd)_3$ Precursors, Chemical Vapor Deposition **15**, 27-32 (2009).

[47] Y. Lee, H. Sun, M. J. Young and S. M. George, Atomic Layer Deposition of Metal Fluorides Using HF–Pyridine as the Fluorine Precursor, Chemistry of Materials **28**, 2022-2032 (2016).

[48] Y. Lee, J. W. DuMont, A. S. Cavanagh and S. M. George, Atomic Layer Deposition of AlF_3 Using Trimethylaluminum and Hydrogen Fluoride, Journal of Physical Chemistry C **119**, 14185-14194 (2015).

[49] M. Ylilammi and T. Ranta-aho, Metal Fluoride Thin Films Prepared by Atomic Layer Deposition, Journal of The Electrochemical Society **141**, 1278-1284 (1994).

[50] J. Hennessy and S. Nikzad, Atomic Layer Deposition of Lithium Fluoride Optical Coatings for the Ultraviolet, Inorganics **6**, 46 (2018).

[51] J.-P. Jones, J. Hennessy, K. J. Billings, F. C. Krause, J. Pasalic and R. V. Bugga, Communication—Atomic Layer Deposition of Aluminum Fluoride for Lithium Metal Anodes, Journal of The Electrochemical Society **167**, 060502 (2020).

[52] J. Hennessy, A. D. Jewell, K. Balasubramanian and S. Nikzad, Ultraviolet optical properties of aluminum fluoride thin films deposited by atomic layer deposition, Journal of Vacuum Science & Technology A **34**, 01A120 (2015).

[53] J. Hennessy, A. D. Jewell, F. Greer, M. C. Lee and S. Nikzad, Atomic layer deposition of magnesium fluoride via bis(ethylcyclopentadienyl)magnesium and anhydrous hydrogen fluoride, Journal of Vacuum Science & Technology A **33**, 01A125 (2014).

[54] M. F. J. Vos, H. C. M. Knoops, R. A. Synowicki, W. M. M. Kessels and A. J. M. Mackus, Atomic layer deposition of aluminum fluoride using $Al(CH_3)_3$ and SF_6 plasma, Applied Physics Letters **111**, 113105 (2017).

[55] M. F. J. Vos, H. C. M. Knoops, W. M. M. Kessels and A. J. M. Mackus, Reaction Mechanisms during Atomic Layer Deposition of AlF_3 Using $Al(CH_3)_3$ and SF_6 Plasma, The Journal of Physical Chemistry C (2021).

[56] Z. Huang, D. C. Messina, B. Eller, F. A. Koeck, P. Scowen and R. J. Nemanich, Multilayer ultraviolet reflective coating based on atomic layer deposited aluminum oxide and fluoride Journal of Vacuum Science & Technology A **39**, 042402 (2021).

[57] K. J. Kanarik, T. Lill, E. A. Hudson, S. Sriraman, S. Tan, J. Marks, V. Vahedi and R. A. Gottscho, Overview of atomic layer etching in the semiconductor industry, Journal of Vacuum Science & Technology A **33**, 020802 (2015).

[58] A. Fischer, A. Routzahn, S. M. George and T. Lill, Thermal atomic layer etching: A review, Journal of Vacuum Science & Technology A **39**, 030801 (2021).

[59] S. M. George, Mechanisms of Thermal Atomic Layer Etching, Accounts of Chemical Research **53**, 1151-1160 (2020).

[60] W. Lu, Y. Lee, J. Murdzek, J. Gertsch, A. Vardi, L. Kong, S. M. George and J. A. d. Alamo, presented at the 2018 IEEE International Electron Devices Meeting (IEDM), 2018 (unpublished).

[61] W. Lu, Y. Lee, J. C. Gertsch, J. A. Murdzek, A. S. Cavanagh, L. Kong, J. A. del Alamo and S. M. George, In Situ Thermal Atomic Layer Etching for Sub-5 nm InGaAs Multigate MOSFETs, Nano Letters **19**, 5159-5166 (2019).

[62] M.-L. Chen, X. Sun, H. Liu, H. Wang, Q. Zhu, S. Wang, H. Du, B. Dong, J. Zhang, Y. Sun, S. Qiu, T. Alava, S. Liu, D.-M. Sun and Z. Han, A FinFET with one atomic layer channel, Nature Communications **11**, 1205 (2020).

[63] F. K. Hsueh, C. Y. Lee, C. X. Xue, C. H. Shen, J. M. Shieh, B. Y. Chen, Y. C. Chiu, H. C. Chen, M. H. Kao, W. H. Huang, K. S. Li, C. T. Wu, K. L. Lin, K. M. Chen, G. W. Huang, M. F. Chang, C. Hu and W. K. Yeh, presented at the 2019 IEEE International Electron Devices Meeting (IEDM), 2019 (unpublished).

[64] J. Hennessy, C. S. Moore, K. Balasubramanian, A. D. Jewell, K. France and S. Nikzad, Enhanced atomic layer etching of native aluminum oxide for ultraviolet optical applications, Journal of Vacuum Science & Technology A **35**, 041512 (2017).

[65] C. Auth, C. Allen, A. Blattner, D. Bergstrom, M. Brazier, M. Bost, M. Buehler, V. Chikarmane, T. Ghani, T. Glassman, R. Grover, W. Han, D. Hanken, M. Hattendorf, P. Hentges, R. Heussner, J. Hicks, D. Ingerly, P. Jain, S. Jaloviar, R. James, D. Jones, J. Jopling, S. Joshi, C. Kenyon, H. Liu, R. McFadden, B. McIntyre, J. Neirynck, C. Parker, L. Pipes, I. Post, S. Pradhan, M. Prince, S. Ramey, T. Reynolds, J. Roesler, J. Sandford, J. Seiple, P. Smith, C. Thomas, D. Towner, T. Troeger, C. Weber, P. Yashar, K. Zawadzki and K. Mistry, presented at the 2012 Symposium on VLSI Technology (VLSIT), 2012 (unpublished).

[66] N. Draeger, FinFETs Give Way to Gate-All-Around (Lam Research, Published, 2020)

CHAPTER 2

EXPERIMENTAL TECHNIQUES

2.1 Introduction

This dissertation presents a variety of material growth and removal experiments accomplished using instruments in the Arizona State University (ASU) Nano Science Laboratory (NSL). The NSL houses a unique multi-chambered ultra-high vacuum (UHV) system allowing for transfer between characterization and sample processing chambers without exposure to atmosphere. The UHV system, FIG 2.1, consists of a ~21 m transfer line, five characterization chambers, a storage box, two load-locked chambers, and eight processing chambers. Each chamber is separated from the transfer line using a gate valve. The transfer line and storage box are maintained at ~2E-9 Torr using five cryogenic pumps located at various positions. Samples are inserted into the transfer line using load-locked chambers. Transport of samples between chambers is accomplished using a cart, with three sample slots, attached to a pulley system driven by a manual crank. Samples are transferred between chambers and the cart using magnetically coupled transfer rods. The *in situ* instruments employed in this research are the X-ray and ultraviolet photoelectron spectroscopy (XPS/UPS) system for electronic surface characterization, the fluoride plasma enhanced atomic layer processing (F-PEALP) system for the growth of metal fluorides and etching of metal oxides, and the oxide plasma enhanced atomic layer processing (O-PEALP) system for growth of metal fluorides and etching of oxides and nitrides. The F-PEALP including the use of a multi-wavelength ellipsometer (MWE) for monitoring deposition and etching of thin films. The O-PEALP also used an MWE is was

also equipped with a quadrupole mass spectrometer (QMS) for monitoring gas-phase products from surface reactions. Both the F-PEALP and O-PEALP will be described in detail in Chapter 3.

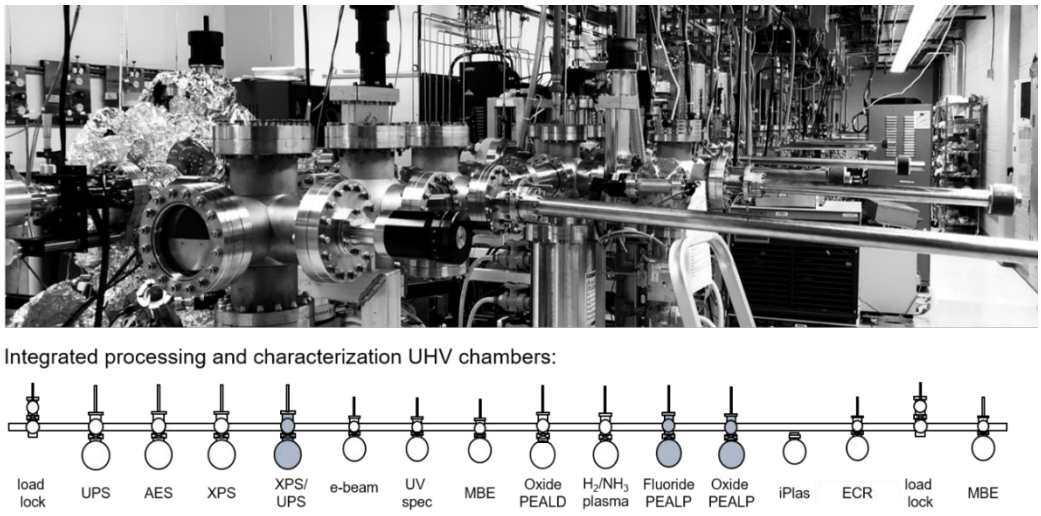

FIG 2.1. Image of the Nano Science Laboratory (NSL) ultrahigh-vacuum transfer line integrated with a number of growth and characterization chambers. The shaded chambers indicate the ones used in this research. (UPS – Ultraviolet photoelectron spectroscopy, AES – Auger electron spectroscopy, XPS – X-ray photoelectron spectrometer, e-beam – Electron Beam Physical Vapor Deposition system, UV Spec – Ultraviolet spectroscopy, MBE – Molecular Beam Epitaxy System, PEALD – Plasma Enhanced Atomic Layer Deposition system, PEALP – Plasma Enhanced Atomic Layer Processing system, iPlas – Microwave Plasma Chemical Vapor Deposition system, ECR – Electron Cyclotron Resonance Plasma Enhanced Chemical Vapor Deposition system).

Other instruments and facilities, within the NSL, utilized in this research includes a wet chemical room for sample preparation and cleaning and an atomic force microscopy for surface morphology. Outside of the NSL, facilities within the ASU Eyring Materials

Center and the ASU NanoFab were used including a thermal atomic layer deposition system, an electron beam deposition system, and a spectroscopic ellipsometer for various optical measurements.

2.2 Photoelectron Spectroscopy

2.2.1 Principles of Photoelectron Spectroscopy

Photoemission spectroscopy (PES) stems from the photoelectric effect which was analyzed by Albert Einstein in 1905.[1] The photoelectric effect occurs that when a photon strikes a surface and electrons are excited and emitted from the surface. As such, a PES system, shown in FIG 2.2, requires a photon source, electron optics, an electron hemispherical analyzer, and an electron detector all held at high to ultrahigh vacuum (<10E-7 Torr).

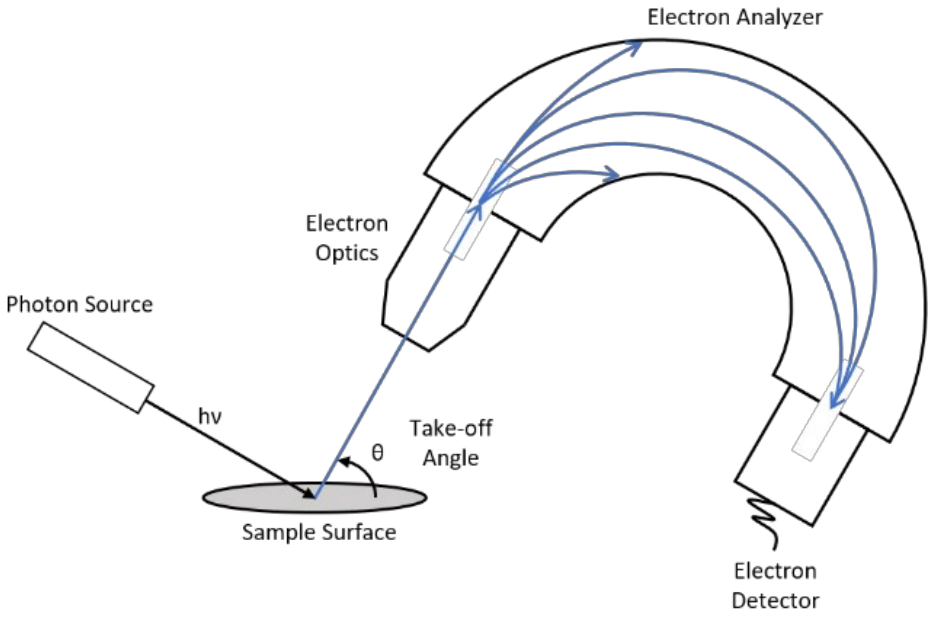

FIG 2.2. Schematic of a photoemission spectroscopy system. Here, *hv* is the photon energy and θ is the electron take-off angle.

In PES, the majority of the excited electrons do not escape from the sample surface due to scattering and/or recombination events. The depth in which electrons can escape, called the "escape depth", can be expressed in terms of the inelastic mean free path, λ_{in}, of the photoelectrons which is dependent on electronic and physical properties of the probed material, shown in FIG 2.3 and discussed later in Section 2.3.2. In general, ~95% of the photoelectron signal comes from the first $3\lambda_{in}$ as shown in FIG 2.4. Meanwhile, scattered electrons with sufficient energies can escape the surface as secondary electrons which contribute to the background of the measured spectrum. The electron optics typically consists of a series of electrostatic lenses that collect emitted electrons and focus them into a hemispherical analyzer slit entrance. In the hemispherical analyzer, a bias is applied to the concentric hemispherical sections allowing for selectivity of electrons with certain energies, called the pass energy, E_p. Electrons with energy E_p travel through the analyzer after which they strike the electron detector. The detector typically consists of an electron multiplier which accelerates electrons towards a surface to produce secondary electron emission. This process is repeated to create electron avalanche and by extension, a measurable current.

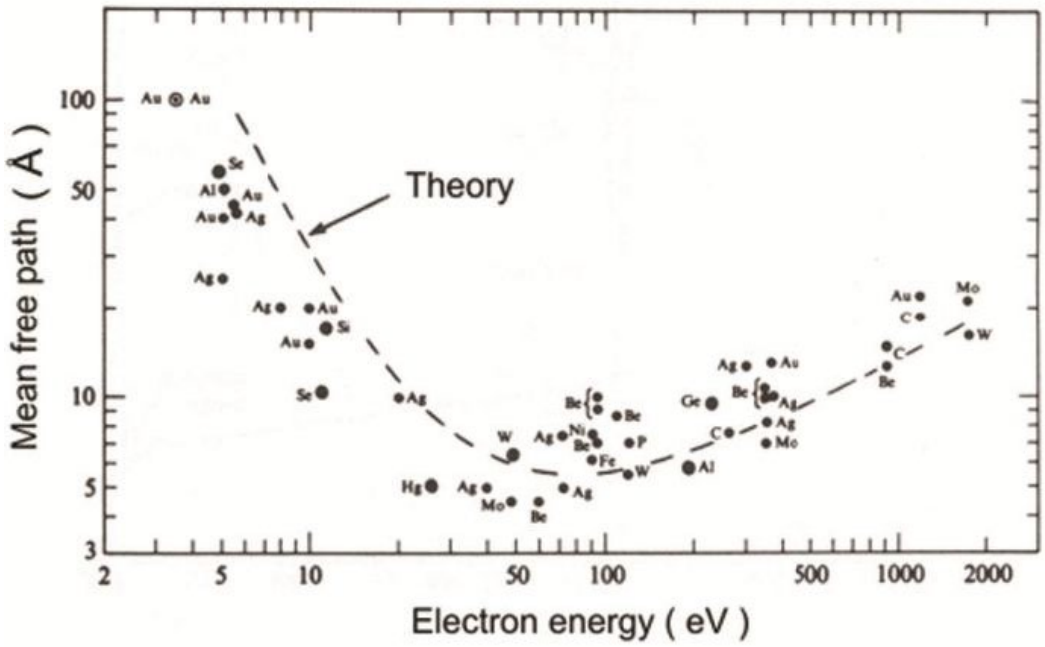

FIG 2.3. Electron inelastic mean free path (escape depth) dependence on electron kinetic energy.[2] Copyright © 1979, Heyden & Son Ltd.

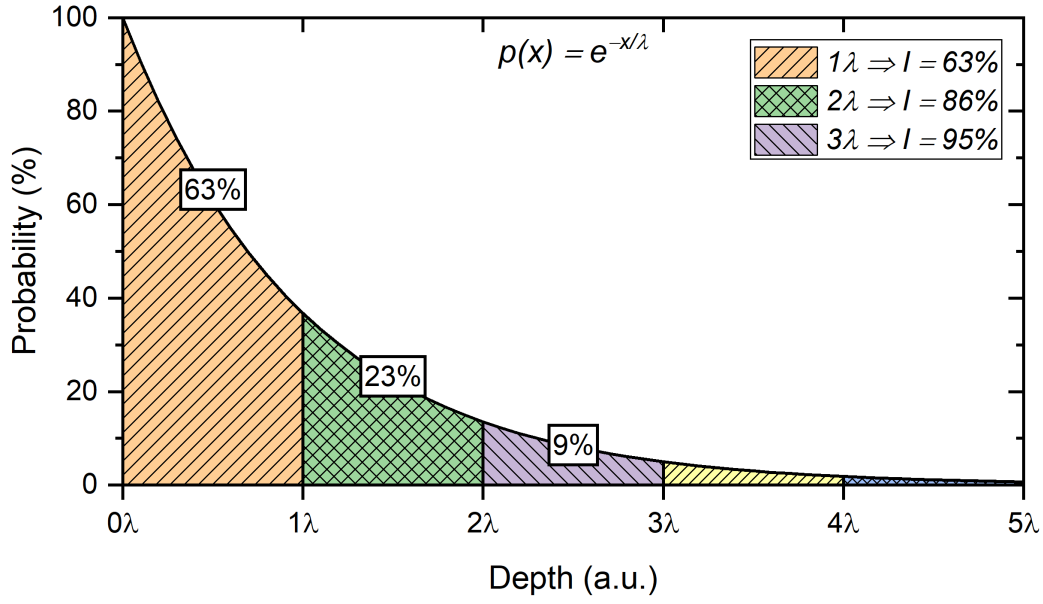

FIG 2.4. Probability an electron, from depth x with mean free path λ, will reach the surface. Note that 95 % of the electrons originate from the first 3λ. In this figure, λ is set to one.

PES systems often have two operating modes for the electron lenses and the hemispherical analyzer: fixed retard ratio (FRR) and fixed analyzer transmission (FAT). In FRR mode, electrons are retarded to the pass energy E_p of the analyzer such that the $E_k/E_p = const.$, where E_k is the electron kinetic energy. In this mode the energy resolution, $\Delta E/E$, is a constant value which can be increased by increasing the E_k/E_p ratio, where ΔE is the energy transmission window. In this case, the absolute value of ΔE and the analyzer transmission T is proportional to E_p and hence E_k. In FAT mode, the electrons are deceleration to a fixed pass energy and the electron lenses are adjusted to retard the selected E_k to the accepted range by the analyzer. This results in a constant energy resolution. The resulting measured intensity is then proportional to $N(E_k) \cdot E_k$ and $N(E_k)/E_k$ in FRR and FAT mode, respectively. Here, $N(E_k)$ is the electron density of states at the electron kinetic energy. Typically, FRR is used in Auger electron spectroscopy while FAT mode is used for PES. The energy resolution in PES is given by Eq. (2.1).

$$E_r = {}^{E_p s}/_{2r} \tag{2.1}$$

Where E_p is the pass energy, s is the entrance slit size, and r is the radius of the hemispherical analyzer.

Generally, PES can be divided into X-ray photoelectron spectroscopy (XPS) and ultraviolet electron spectroscopy (UPS) depending on the photon energy used. Due to the difference in photon energy, XPS is typically implemented for analysis of core level states and can probe ~10 nm. UPS focuses on electronic structure in the valence band range, FIG 2.5, and has a sampling depth of ~1 nm.

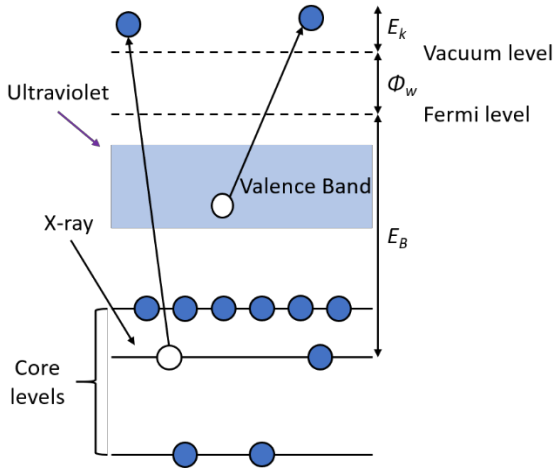

FIG 2.5. Illustration of the electron excitations in XPS and UPS. Here, E_k is the electron kinetic energy, and Φ_w is the sample work function, and E_B is the photoelectron binding energy.

When a surface is exposed to photons with a sufficient energy resulting in the emission of photoelectrons, the electron binding energy can be expressed in terms of the kinetic energy by Eq. (2.2).

$$E_B = h\nu - E_k - \Phi_w \tag{2.2}$$

Where E_B is the electron binding energy of the electron in the material, $h\nu$ is the photon energy, E_k is the photoelectron's kinetic energy, Φ_w is the spectrometer work function. Here, the binding energy of the electron is expressed relative to the Fermi energy of the highest occupied state. In UPS, a negative bias is applied between the analyzer and sample to allow the low kinetic energy photoelectrons to overcome the spectrometer work function, Eq. (2.3).

$$E_B = h\nu - E_k - \Phi_w - eV \tag{2.3}$$

Here e is the electron charge and V is the applied voltage. As UPS measurement were not used in this research, it will not be discussed in depth.

2.2.2 X-ray Photoelectron Spectroscopy

In this study, an integrated PES system (VG Scientia, R3000 XPS/UPS) was employed to characterize chemical states and impurity states arising from the growth and etching of thin films. This XPS/UPS system has a base pressure of 4E-10 Torr. The XPS portion consists of a monochromated Al K_α source (Scientia, MX 650) with a photon energy of 1486.7 eV and a narrow bandwidth of 0.2 eV. For UPS, a high intensity UV source (Prevac, UVS 40A2) optimized for He I and He II radiation, at 21.22 eV and 40.82 eV, respectively, is used. The spectrometer uses a 135 mm mean radius hemispherical analyzer (Scientia, R3000) which has a high-resolution of 0.03 eV full width half maximum (FWHM) for both XPS and UPS measurements. The X-ray monochromator and main chamber as separated by a 0.75 μm thick aluminum foil.

This system generates X-rays by bombarding a water-cooled aluminum anode with a finely focused electron beam from a tungsten cathode. The electron beam size on the band is ~ 1 mm by 3 mm which is equal to the X-ray spot size on the sample. The monochromator consists of seven α-SiO_2 toroidal crystals. Six of the quartz crystals are arranged along a circle around a central crystal. The crystals are heated to 55 °C to avoid photon energy shifts due to thermal fluctuations. These quartz crystals are arranged on a 650 mm diameter Rowland circle. The monochromator operates based on Bragg's law given by Eq. (2.4)

$$2d \sin\theta = n\lambda \tag{2.4}$$

Where d is the distance between two crystal planes, θ is the refractive angle, and λ is the wavelength of the incident photon. The geometry of the Rowland circle ensures that only

a narrow band of X-rays will be diffracted onto the surface. This results in monochromatic X-rays with a narrow bandwidth of 0.2 eV.

The electron hemispherical analyzer (Scientia, R3000) is used for XPS and UPS measurements. The mean radius of the analyzer is 135 mm. Prior to entering the analyzer, electrons emitted from the sample must pass through a series of electrostatic lens configured to collect and transfer electrons to a 0.2 mm by 20 mm curved slit. The slit can be adjusted to be straight or curve. Additionally, the slit size can be increase to 0.4 mm wide for increased intensity but decreased energy resolution. As electrons enter the analyzer, the inner sphere is positively biased while the outer is negatively biased to only allow electrons with a chosen pass energy. On the exit of the analyzer sits a field termination mesh, two multi-channel plates (electron multipliers), a phosphorus screen, and a charge-coupled detector (CCD) camera. The CCD camera is configured to present measurements in 2D: energy versus spatial/angular coordinates. This translates to electronic states versus kinetic or binding energy. The R3000 analyzer has an energy resolution less than 0.1 eV for XPS measurements at 100 eV pass energy.

2.2.3 Characterization

2.2.3.1 Peak Fitting

Identification and analysis of core levels and chemical states is an important aspect of XPS. There are several characteristics related to core level spectra which indicate the nature of the chemical bonding: background, intensity, position, and full width half-maximum (FWHM). The first step of analyzing core level spectra is fitting the background due to secondary electrons. Generally, backgrounds are fitted using step-down functions,

linear fits, Shirley, or Tougaard backgrounds.[3] Once a proper background is chosen, spectra can be fit using Voigt functions, a convolution of Gaussian and Lorentzian functions, or other line shapes. The intensity of a core level is most reliably determined by integrating the area of the corresponding Voigt function. Typically, intensity measurements are reliable within 10 %. The peak position is determined by deconvoluting the core level spectra into Voigt functions. The uncertainty on the peak center depends on the energy increments during data acquisition. The peak width is determined at the half maximum, hence FWHM, and varies with chemical state, thermal motion, spectrometer, and X-ray source. In most cases, core level spectra feature overlapping peak which must be deconvolved for accurate determination of all chemical states. Such a task is typically not straight forward as many chemical states have similar energy ranges. Understanding the surface chemistry allows for introduction of constraints for reliable fitting in terms of expected core level positions, energy separations, and FHWMs.

2.2.3.2 Film Composition

A core feature of XPS is the ability to determine surface stoichiometry or composition. For a homogenous sample, the intensity of the core-level peak, in counts per second, is dependent on system parameters and material properties, Eq. (2.5).[4]

$$I = nf\sigma y\lambda_{in}AT \tag{2.5}$$

Here, n is the atomic number density (atoms per cm^3), f is the X-ray flux (photons per $cm^2 \cdot s$), σ is the photoelectric cross-section for the probed core level, y is the efficiency in of the photoelectric process for formation of the normal photoelectron energy, λ_{in} is the inelastic mean free path of photoelectrons in the sample, A is the sample area where

photoelectrons are detected, and T is the detector efficiency. Note that only n, σ, and λ_{in} are material dependent. Eq. (5) can be rearranged for the atomic number density, Eq. (2.6).

$$n = I/\sigma\lambda_{in}FyAT \tag{2.6}$$

The denominator can be simplified to $n = I/(S\Phi)$ by defining the atomic sensitivity factor (ASF), S, as $S = \sigma\lambda_{in}$, and the spectrometer transmission function (STF), Φ, as $\Phi = FyAT$. The STF can be determine by measuring an atomically clean standard such as single crystal. If one considers a strong line, for each element, in a heterogenous material, then the ratio of the two elements given by Eq. (2.7).

$$\frac{n_1}{n_2} = \frac{I_1/S_1}{I_2/S_2} \tag{2.7}$$

To determine the stoichiometry of a surface, or atomic fraction, C_x, one takes the atomic number density of a constituent and divides it by the sum of all the atomic number densities of the constituent elements, Eq. (2.8). Fortunately, the STF cancels out leaving only S.

$$C_x = \frac{n_x}{\sum n_i} = \frac{I_x/S_x}{I_i/S_i} \tag{2.8}$$

To calculate S, one requires knowledge of the material properties. As stated, S is dependent on the photoelectric cross-section (PECS) and the inelastic mean free path of the photoelectron transition. The PECS can be obtained from Scofield et al[5] where relativistic single potential calculations were performed for most elements using the Hartee-Slater atomic model. The PECS were calculations were performed at photon energies of 1254 and 1487 eV corresponding to the Mg and Al K_α X-ray transitions, respectively. It should be noted that use of the PECSs requires accounting for spin-orbit (SO) splitting of the chosen core level. When the SO splitting energy difference is greater

than the energy resolution of the spectrometer, single states can be selected. Otherwise, the sum of the SO states PECSs needs to be considered.

The second material dependent parameter is the inelastic mean free path (IMFP), λ_{in}, of the core level electrons in the sample material. The IMFP can be measured directly using electron energy loss spectroscopy or it can be estimated using various predictive models. The two most common models for calculating the IMFP are the Tanuma, Powell, and Penn algorithm (TPP-2M) and Seah's model.[2, 6, 7] The TPP-2M model requires knowledge of the electron kinetic energy, number of valence electrons per atom or molecule, the material density, molecular mass, and electronic band gap. Alternatively, Seah's model requires the average atomic number, the molecular mass, material density, and the electronic band gap or the heat of formation. IMFPS calculated using both methods were found to have a relative error of 7.9 – 8.8 % for their respective elements or compounds.[8] Thus calculation of stoichiometry by XPS requires assumptions of physical and electronic properties of the sample materials. These assumptions can lead to uncertainties of 10 – 20 %.[4]

2.2.3.3 Film Thickness

XPS allows for the determination of a film thickness using either a single or multi-line core level approach.[9, 10] The single line approach relies on measuring a core-level transitions before and after the addition of an overlayer material, shown in FIG 2.6. This method is the simplest and only requires analysis of a chosen core-level peak. The thickness can then be calculated using Eq. (2.9) and Eq. (2.10).[9, 10]

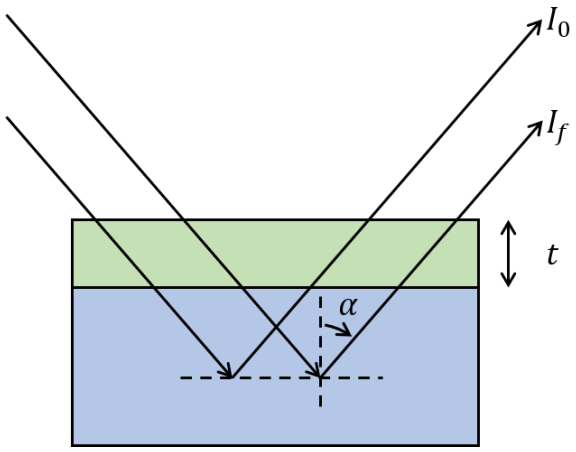

FIG 2.6. Illustration of the single line approach for measuring a thin film's thickness *t* by XPS. Image adapted from Jablonski.[10] Copyright © 2019, Elsevier B.V.

$$t = -L_{TH}^{f}(E_s)\cos(\alpha)\ln(\frac{I_f}{I_0}) \tag{2.9}$$

$$L_{TH}^{f}(E_s) = \lambda_{in}(1 - 0.738\omega) \tag{2.10}$$

Here, t is the film thickness, $L_{TH}^{f}(E_s)$ is the effective attenuation length of the substrate photoelectrons with energy E_s in the overlayer f, α is the photoelectron emission angle relative to the sample normal, I_f is the integrated intensity of the final substrate peak and I_0 is the integrated intensity of the initial substrate peak. The EAL is dependent on the inelastic mean free path, λ_{in}, and a parameter known as the scattering albedo, ω. The albedo is directly related to the IMFP and the electron transport mean free path (TRMFP), λ_{tr}, by Eq. (2.11).

$$\omega = \frac{\lambda_{in}}{\lambda_{in} + \lambda_{tr}} \tag{2.11}$$

The electron transport mean free path (TRMFP) can be calculated using Eq. (2.12) and Eq. (2.13).

$$\lambda_{tr} = (N\sigma_{tr})^{-1} \tag{2.12}$$

$$\sigma_{tr} = \int_{4\pi} (1 - \cos\theta) \frac{d\sigma_{el}}{d\Omega} d\Omega \tag{2.13}$$

Where N is the atomic number density (atoms per unit volume) and σ_{tr} is the transport cross section (TCS). θ is the polar elastic-scattering angle and $d\sigma_{el}/d\Omega$ is the differential elastic scattering cross section. To determine the TRMFP for molecules or alloys, a weight average of the TCS, for each constituent element, can be taken. Thankfully, the TCS for most elements has been measured at electron energies up to 30 keV.[11, 12] This allows for quick determination of the TRMFP, scattering albedo, and thus EAL enabling thin film thickness calculations. Alternatively, the Simulation of Electron Spectra for Surface Analysis (SESSA) program can be used for easy calculation of the EAL and simulation of XPS spectra.[13]

The multiline approach, illustrated in FIG 2.7, for the thin film thickness calculation requires three measurements: the uncovered substrate, the thin film, and the bulk film.[9] Using these measurements for the strongest core level lines of the substrate and the film material, the thickness is then given by Eq. (14).

$$t = -L_{TH}^{f}(E_s)\cos(\alpha)\ln\left(1 + \frac{I_s^{\infty}}{I_s}\frac{I_f}{I_f^{\infty}}\right) \tag{2.14}$$

Here, I_s^{∞} is the integrated intensity of the uncovered substrate, I_s is the integrated intensity from the covered substrate core level, I_f^{∞} is the integrated intensity of the infinitely thick film, and I_f is the integrated intensity of the thin film.

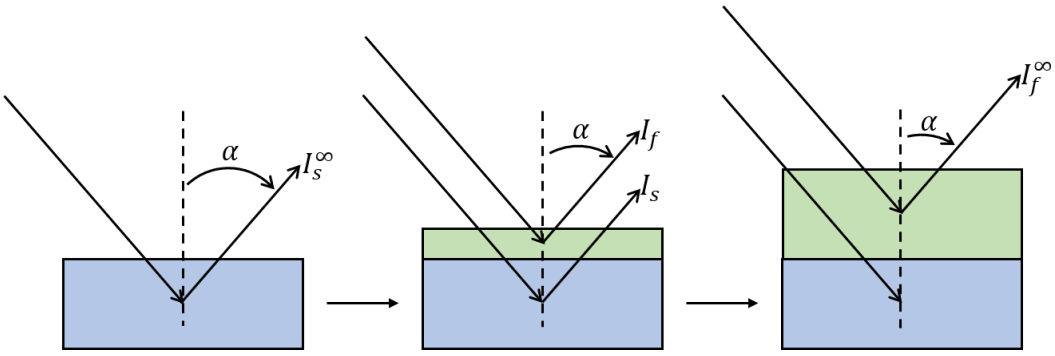

FIG 2.7. Illustration of the multiline approach for thin film thickness calculations by XPS. Image adapted from Jablonski.[10] Copyright © 2019, Elsevier B.V.

2.2.3.4 Example: Aluminum Fluoride Thin Films

2.2.3.4.1 Peak Fitting

XPS surface spectra is a useful tool for identification of chemical states. A typical XPS experiment includes a low-resolution survey scan over a large energy range and then a number of higher resolution narrow scans for all identified core levels and impurity states. An example of a survey scan is given in FIG 2.8 for a thermal atomic layer deposited (TALD) aluminum fluoride (AlF_3) thin film (~17 nm). The survey scan allows for quick identification of core levels. Survey scans tend to use a large step size and a higher pass energy. For the example shown, a step size and pass energies were 0.25 eV and 200 eV, respectively. The corresponding uncertainly on peak position and width was 0.39 eV and 0.30 eV, respectively.

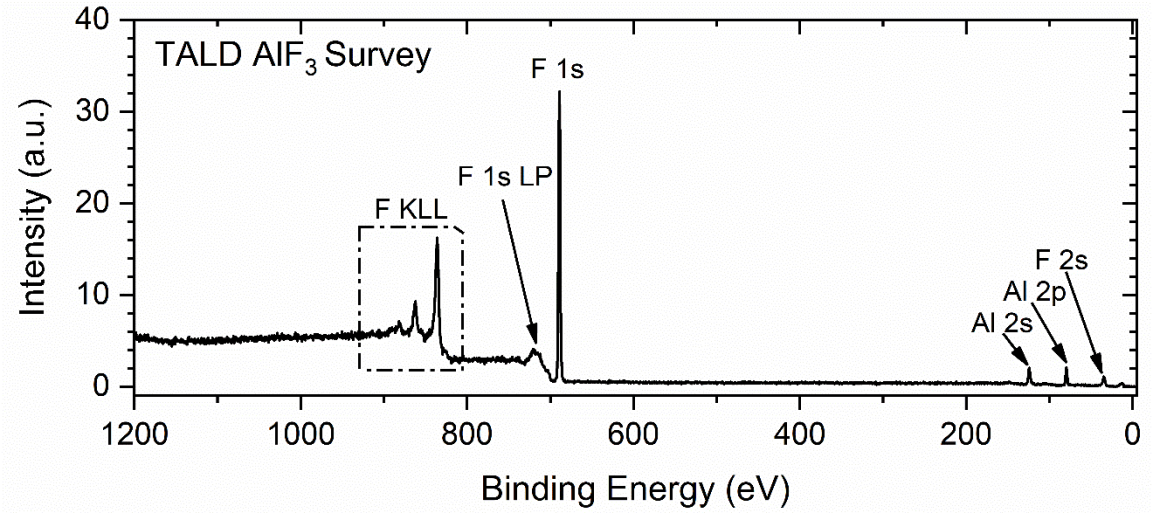

FIG 2.8. Survey scan of an AlF_3 film deposited by thermal atomic layer deposition (TALD) with all major features identified. F KLL corresponds to Auger electrons. F LP is the electron energy loss peak from F 1s electrons scattering off phonons. The slight bump between the F 2s and 0 eV is the valence band structure.

Survey scans are not well suited for chemical state identification. As such, higher resolution narrow scans are often acquired for each identified core level. For the AlF_3 film shown in FIG 2.8, spectra were acquired for the F 1s, O 1s, and Al 2p core levels, shown in FIG 2.9. The C 1s core level was not shown as carbon impurities were below the detection limit ($10^{20} – 10^{19}$ atoms·cm^{-3}). The backgrounds of the F 1s, O 1s, and Al 2p core level spectra were fit using a Shirley background with Gaussian-Lorentzian line shapes, or Voigt functions. Spectra was acquire using a step size of 0.05 eV and a pass energy of 100 eV. The corresponding uncertainty on the peak centers and widths where 0.15 eV and 0.16 eV, respectively. The fitted peak parameters (peak center, FWHM, and area) are provided in Table 2.1 and will be used later in §2.2.3.4.2 and §2.2.3.4.3 for film composition and thickness calculations, respectively.

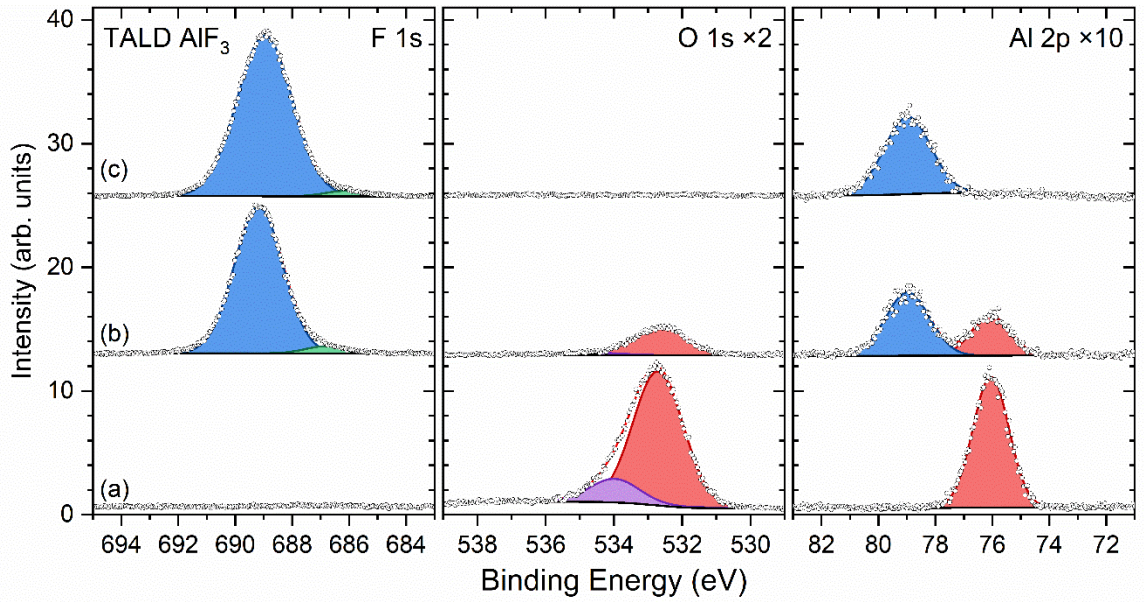

FIG 2.9. XPS core levels for the F 1s, O 1s, C 1s, and Al 2p for thermal atomic layer deposited AlF_3. (a) shows the core levels of the initial UV-O_3 cleaned surface; (b) is after 40 TALD AlF_3 cycle and (c) is after an additional 120 cycles. The components of each region are noted in Table 2.1 according to their binding energy. Image adapted from Messina *et al*.[14]

Table 2.1. Peak center, FWHM (round bracket), and area [square brackets] for core level scans observed for the TALD AlF_3 films on TALD Al_2O_3. In the Al 2p region, a single peak was used for each core level as the 0.4 eV spin-orbit splitting could not be resolved. Peak centers were aligned to the Al_2O_3 substrate core levels. Peak centers and FWHMs are in eV while areas are in eV-counts/s. Table adapted from Messina *et al*.[14]

AlF_3 Thin Films	F 1s		O 1s		Al 2p	
	1st	2nd	1st	2nd	1st	2nd
(a) UV-O_3 Exposure	-	-	532.7	534.0	76.1	-
	-	-	(1.7)	(1.7)	(1.5)	-
	-	-	[9.9]	[1.7]	[1.7]	-
(b) 40 cycles	686.8	689.2	532.6	534.6	76.1	79.0
	(1.7)	(2.0)	(1.8)	(1.9)	(1.6)	(1.8)
	[1.0]	[25.3]	[2.1]	[0.2]	[0.6]	[1.0]
(c) 120 cycles	686.1	689.0	-	-	-	79.0
	(1.6)	(2.3)	-	-	-	(1.9)
	[0.8]	[31.5]	-	-	-	[1.3]

2.2.3.4.2 Surface Composition

Analyzed XPS spectra of thermal atomic layer deposited (TALD) aluminum fluoride (AlF_3) thin films is presented in FIG 2.8 and FIG 2.9 with the fitted peak parameters listed in Table 2.1. Using the fitted peak parameters, the film composition can be determined for each deposition step shown in FIG 2.9. To do so, Scofield photoionization cross sections for the F 1s, O 1s, and Al 2p core levels, Table 2.2, are

required.[5] Using these subshell PCS's with Eq. (2.8) allows for calculation of the surface stoichiometry, shown in Table 2.3.

Table 2.2. Hartee-Slater subshell photoionization cross sections at 1487 eV for F, O, and Al.[5]

Element	$1s_{1/2}$	$2s_{1/2}$	$2p_{1/2}$	$2p_{3/2}$	$3s_{1/2}$	$3p_{1/2}$	$3p_{3/2}$
F	2.9300	0.1405	0.0065	0.0128	-	-	-
O	4.4300	0.2100	0.0161	0.0317	-	-	-
Al	-	0.753	0.1811	0.3560	0.0535	0.0011	0.0022

Table 2.3. Relevant quantities for calculating the surface stoichiometry for each step in the TALD AlF_3 deposition shown in FIG 2.9. Since the spin-orbit splitting of the Al 2p states could not be measured, the sum of the Al 2p PCS's is taken. Values are calculated from the relevant values listed in Table 2.1 and Table 2.2.

AlF_3 Thin Films	$I_{F\ 1s}/S_{F\ 1s}$	$I_{O\ 1s}/S_{O\ 1s}$	$I_{Al\ 2p}/S_{Al\ 2p}$	$\sum_i I_i/S_i$	Stoichiometry
(a) UV-O_3 Exposure	0.0	4.0	3.1	7.1	$Al_{1.0}F_{0.0}O_{1.3}$
(b) 40 cycles	5.9	0.8	2.9	9.6	$Al_{1.0}F_{2.1}O_{0.3}$
(c) 120 cycles	7.3	0.0	2.4	9.7	$Al_{1.0}F_{3.1}O_{0.0}$

After the final AlF_3 deposition, the Al:F ratio is calculated to be 1:3.1 implying a fluorine rich film. As noted previously the uncertainty of this method is 10 – 20 % due to the use of theoretical cross-sections and inelastic mean free paths.[4]

2.2.3.4.3 Film Thickness

The XPS spectra acquired for the TALD AlF_3 thin film, shown in FIG 2.8 and FIG 2.9, allow for calculation of the thin film thickness using the single and multi-line approaches. The calculations were performed using the fitted peak parameters in Table 2.1. In the single line approach, the AlF_3 film thickness is calculated based on the attenuation of the Al 2p core level from FIG 2.9(a)-(b) using Eq. (2.9). For the multiline approach, Eq. (2.14), all three steps of FIG 2.9 are used to determine the measured intensities. Both approaches require the film density and band gap be known in order to estimate the IMFP and thus the EAL. The film density can be estimate from the stoichiometry. In §2.2.3.4.2, the TALD AlF_3 film as found to have an F/Al ratio of 3.1.

The electronic band gap can be estimated from the F 1s loss peak shown in FIG 2.10 using a method described by Yang *et al*.[15]

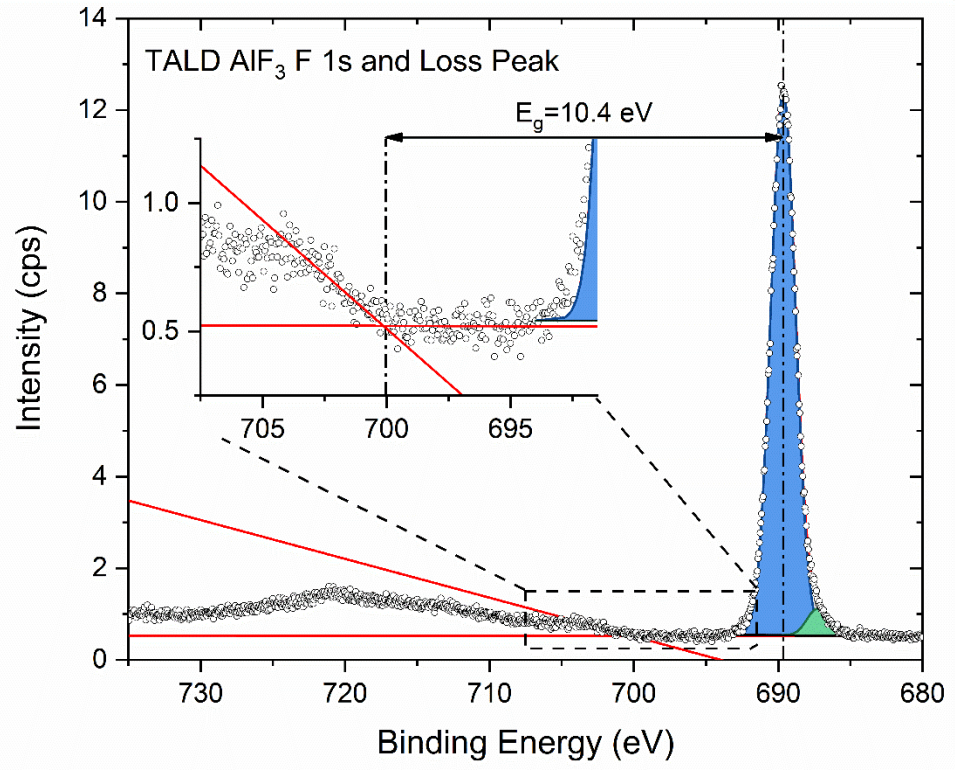

FIG 2.10. XPS band gap estimation from the F 1s and loss peak for the TALD AlF_3 film.

Based on the estimated band gap of the AlF_3 film, the effective attenuation length for the Al 2p Al-O core level can be estimated using the SESSA software.[13] Using the above values, an IMFP and TRMFP of 4.7 nm and 46.8 nm, respectively, was found. Applying Eq. (2.10) and Eq. (2.11), we find the EAL to be 4.3 nm. The resulting thicknesses from the single line and multi-line approach are 4.8 nm and 5.3 nm, respectively. The difference in thickness likely originates from the broadening of the Al-F core level after the deposition shown in FIG 2.9(c).

2.3 Ellipsometry

2.3.1 Principles of Ellipsometry

Ellipsometry is an optical technique which measure dielectric properties of thin films based on changes in polarization. The operating principle of ellipsometry is that s-polarized and p-polarized light are reflected differently at a sample surface or interface as shown in FIG 2.11. Ellipsometry measures the ratio of the *s*- and *p*- polarized reflected light as the complex reflectance ratio ρ defined as $\rho = r_p/r_s = \tan(\Psi)\, e^{-i\Delta}$. Here, ρ is defined in terms of the amplitude ratio, Ψ, and the phase difference, Δ, of the *s* and *p* polarized light. In general, an incident beam of linearly polarized light reflected off a surface produces an elliptically polarized reflected beam.

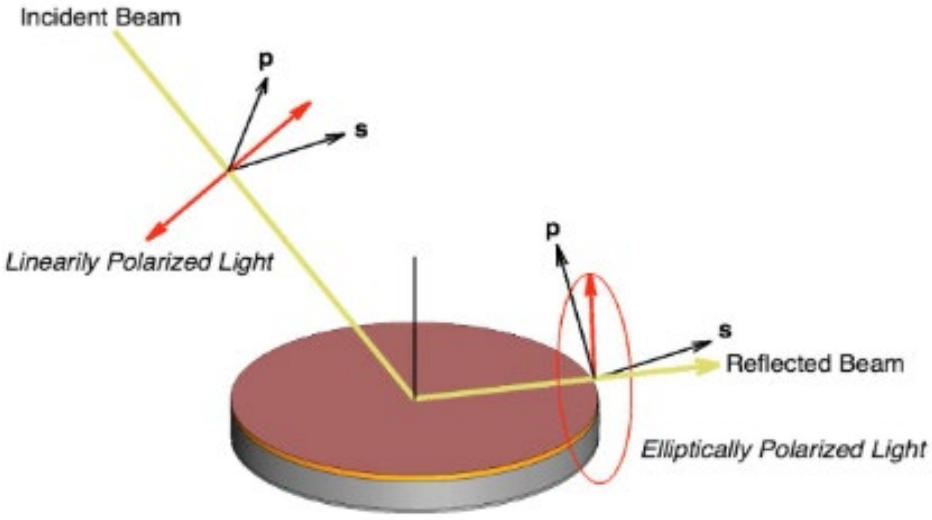

FIG 2.11. Illustration of the reflection of polarized light off a sample surface.[16] Copyright © 2017, Film Sense LLC.

In this work, multiwavelength ellipsometry (MWE) was used *in situ* to observe the growth of thin films in real time. In MWE, only a few wavelengths are used in comparison to a spectroscopic ellipsometer (SE) which typically features a 100's of wavelengths. The

MWE (Film Sense, FS-1) uses four light emitting diodes centered at 465 nm, 525 nm, 580 nm, and 635 nm. The ellipsometer was mounted at a fixed angle of ~45°. The ellipsometer determines the polarization state of the reflected beams by the Division-of-Amplitude-Polarimeter (DOAP) method where all four Stokes parameters are measured simultaneously.[17] An ellipsometer software package (Film Sense, Desktop v1.15) was used to analyze the ellipsometric parameters Ψ and Δ. To effectively determine film thickness via ellipsometry, optical models must be applied to the ellipsometric data.

2.3.2 Optical Modeling

Optical modeling is an essential part of ellipsometric data analysis. Without the application of such models, a film's thickness cannot be measured. The accuracy of an optical model is indicated by the fit difference (Fit Diff.) which is similar to the mean square error (MSE). The fit difference, in the Film Sense software, is minimized via the Marquardt-Levenberg method to determine the most likely fit. A fit diff. of 0.0001 corresponds to an uncertainty of 0.1 %.[16] Modeling typically requires changing fit parameters, such as thickness, to minimize the fit difference.

2.3.2.1 Cauchy Model

The Cauchy dispersion model, Eq. (2.15), is a three-parameter model which works best for materials with minimal optical adsorption in visible wavelengths. As a result, the Cauchy model shows a monotonous decreasing refractive index with increasing wavelength.

$$n = A + \frac{B}{\lambda^2} + \frac{C}{\lambda^4}, k = 0 \quad (2.15)$$

Here, λ is the wavelength, n is the refractive index, k is the extinction coefficient, and A, B, and C are empirical parameters.

2.3.2.2 Pseudo-Substrate Model

Pseudo substrate analysis is a method which can simplify the analysis of real time data. The pseudo model is an approximation in which a stack of distinct layers is assumed to be a single entity. As such the effective optical constants at each wavelength are determined for the underlying materials. This approximation leads to improved accuracy as measurement errors and errors in the optical models of the underlying films are canceled out.[16]

2.3.2.3 Drude Model

The dielectric constant of simple conductors can be accounted for using the Drude model. The Drude model explains the transport properties of electrons in materials by application of Ohm's Law and kinetic theory; effectively treating electrons as a gas. The resulting frequency dependent dielectric function can be written in terms of a resonance frequency, called the plasma frequency, ω_p, as shown in Eq. (2.16) .[18]

$$\epsilon(\omega) = 1 - {\omega_p^2}/{\omega^2} \quad (2.16)$$

$$\omega_p = \sqrt{{ne^2}/{\epsilon_0 m}} \quad (2.17)$$

Where ω is the frequency, n is the number density of the electron gas, ϵ_0 is the permittivity of free space, and m is the electron mass.

2.3.2.4 Bruggeman Effective Medium Approximation

In this work, analysis of plasma enhanced atomic layer deposited AlF_3 thin films were found to have Al impurities with a volume fraction of ~0.14. As such, applying a Cauchy model to the AlF_3 film with Al impurities resulted in an inaccurate model; thus, an effective medium approximation had to be applied. For mixed materials, the effective optical constants can be estimated using an effective medium approximation (EMA). For a multicomponent mixture system, the effective dielectric constant, $\tilde{\epsilon}$, can be expressed using Eq. (2.18).[19]

$$\frac{\tilde{\epsilon} - \epsilon_h}{\epsilon_h + (\tilde{\epsilon} - \epsilon_h)L} = \sum_i f_i \frac{\epsilon_i - \epsilon_h}{\epsilon_h + (\epsilon_i - \epsilon_h)L} \tag{2.18}$$

Where ϵ_h is the host material, L is the depolarization factor dependent on the mixture morphology, f_i and ϵ_i are the volume fractions and dielectric constants of the i-th inclusion, respectively. It is important to note that the sum of all volume fractions is one. If the mixture is assumed to be homogenous, one arrives at the Bruggeman effective medium approximation, Eq. (2.19).[20]

$$0 = \sum_i f_i \frac{\epsilon_i - \tilde{\epsilon}}{\tilde{\epsilon} + (\epsilon_i - \tilde{\epsilon})L} \tag{2.19}$$

2.3.3 Example: In Situ Ellipsometry of Aluminum Fluoride Thin Films

The growth of aluminum fluoride (AlF_3) thin films by plasma enhanced atomic layer deposition (PEALD) were found to have Al-rich clusters. The concentration of Al impurities was first investigated by XPS in which a volume concentration of ~14 % was found. During the PEALD AlF_3 growth, MWE was utilized allowing for determination of film thickness. Due to the incorporation of Al impurities, the transparent Cauchy model was inadequate for modeling the PEALD AlF_3 layer. As such, the AlF_3 layer was assumed to be a homogenous mixture of AlF_3 and Al-rich clusters allowing for application of the Bruggeman effective medium approximation, Eq, (2.19). The substrate was accounted for using a pseudo substrate model. In FIG 2.12, the *in situ* ellipsometry for the PEALD AlF_3 growth is shown for 40 cycles. The plot contains three models each with a different concentration of Al-rich clusters.

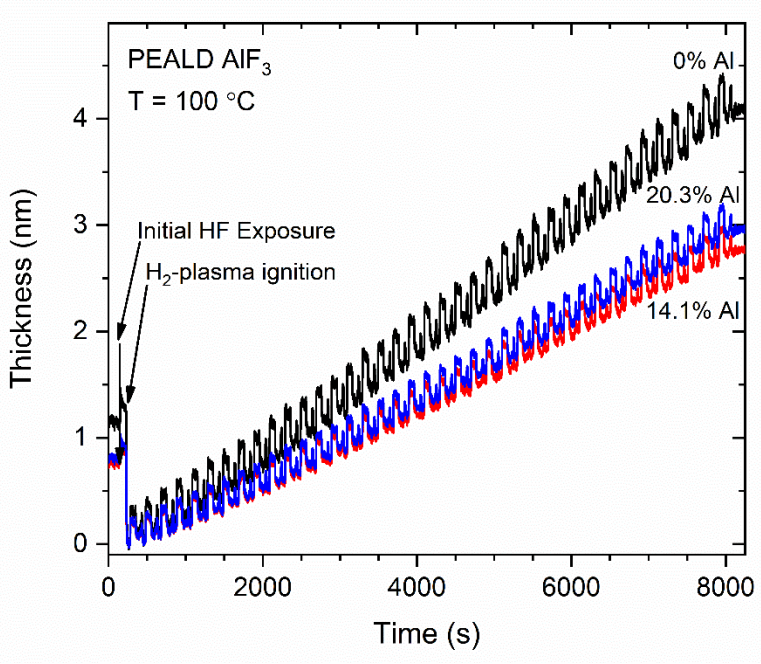

FIG 2.12. Film thickness from *in situ* ellipsometry during the PEALD AlF_3 growth over 40 cycles. Three optical models are shown with varying concentration of Al-rich clusters.

In all models, the film thickness was allowed to vary over a period of five minutes after the deposition had finished. The first model assumed no Al impurities while the second model employed the impurity concentration determined by XPS. Finally, the third model allowed the Al impurity incorporation to vary along with film thickness. The results of these three models are applied in FIG 2.12 and summarized in Table 2.4.

Table 2.4. Film thickness for the PEALD AlF_3 *in situ* ellipsometry depending on the applied optical model. The AlF_3 was modeled using a transparent Cauchy model while the Al used the Drude model. The aforementioned models were mixed using the Bruggeman effective medium approximation.

Model	% Al	Film Thickness (nm)	Uncertainty (nm)
1	0	4.1	0.05
2	14.1	2.8	0.01
3	20.3	3.0	0.02

2.4 Atomic Layer Deposition

2.4.1 Principles of Atomic Layer Deposition

Atomic layer deposition (ALD) is a thin film deposition technique stemming from chemical vapor deposition (CVD). Both CVD and ALD employ vapor transport to enable gas solid interactions. Unlike CVD, ALD achieves film growth using sequential exposures of precursors, or reactants, separated by inert gas purges, illustrated in FIG 2.13. A key characteristic of ALD is the self-limiting nature of the growth process. Self-limiting growth is achieved for a surface that has a limited number of reactive sites for precursor adsorption, and there is a temperature window where the excess precursor desorbs from the surface. Moreover, the self-limiting surface reactions must occur in both half cycles at the same substrate temperature. Thus, in an ideal ALD reaction, there is a temperature range (or growth window) where growth proceeds in a layer-by-layer mode, and the layer thickness per ALD cycle is essentially constant. The growth per cycle (GPC) of an ALD process can increase or decrease at temperatures above or below the growth window due to a variety

of reasons related to adsorption-desorption kinetics, FIG 2.14.[21-23] The substrate temperature is typically chosen within the growth window to prevent precursor self-interaction, and decomposition, while also facilitating self-terminating surface reactions. The self-limiting nature of ALD enables precise thickness control along with high purity, uniform, and conformal layers.

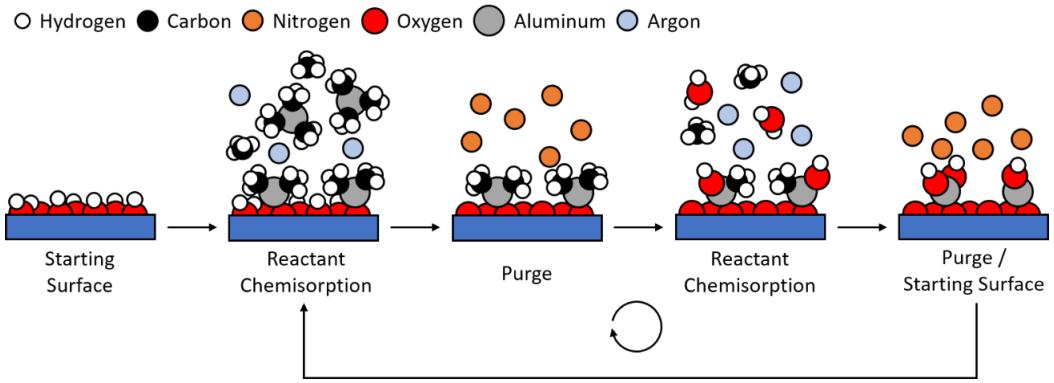

FIG 2.13. Illustration of a thermal ALD process for aluminum oxide using alternating exposures of trimethylaluminum and water vapor. In this process, argon is used as a carrier gas and each step is separated by a nitrogen. Both reactants react via ligand exchange.

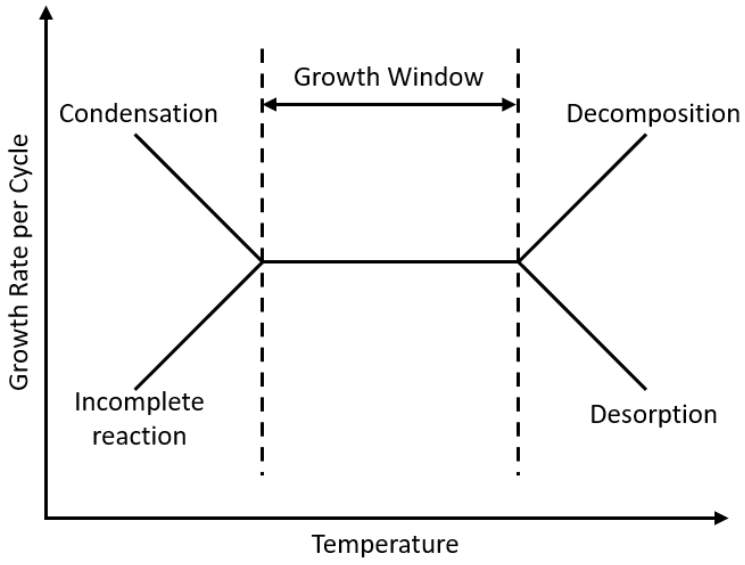

FIG 2.14. Growth rate per cycle dependence on temperature for an ideal ALD process.

2.4.2 Plasma Enhanced Atomic Layer Deposition

Plasma enhanced ALD (PEALD) is an energy-enhanced variant of ALD in which plasma species are used as a reactant, as shown in FIG 2.15. In general, the high reactivity of plasma generated radicals and the kinetic energy of ions can drive surface reactions allowing for lower deposition temperatures.[24, 25] The free radicals can enable surface reactions at temperatures appropriate for the process (e.g. using O instead of H_2O or O_2 for oxide ALD). In this case the free radicals participate in the ligand exchange and the surface reaction. The result is often higher purity and higher density films. The self-limiting reaction conditions must still be met in PEALD, and typically the plasma is only applied for one reactant.

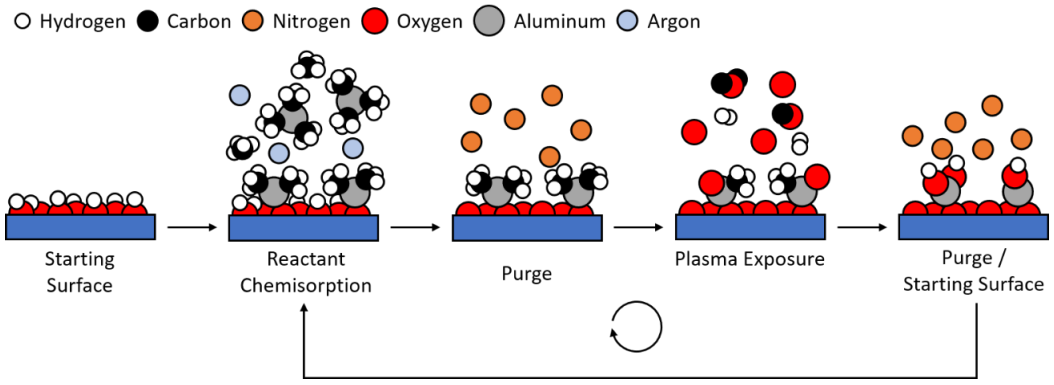

FIG 2.15. Illustration of an PEALD Al_2O_3 deposition using trimethylaluminum and atomic oxygen from a remote inductively coupled plasma. In this process, argon is used as a carrier gas and each step is separated by a nitrogen.

Despite the benefits of PEALD, there are some drawbacks in comparison to thermal ALD (TALD). During PEALD, exposure to some reactive plasma species may lead to undesirable reactions. Occasionally, a plasma may cause oxidation, or nitridation of a substrate at a faster rate than the film deposition. The result is a thick oxidized or nitridized

layer underneath the film, which would impact device behavior.[26-29] Additionally, ion bombardment can induce defects by bond breaking or atom displacement. Ion bombardment can be mitigated by use of a remote plasma configuration, as employed in this research, where ion densities are orders of magnitude less than plasma radical densities.[30] Finally, PEALD processes may show decreased conformality on high aspect ratio structures due to loss of radicals to recombination.[25]

2.4.2.1 Plasma Basics

Plasma is one of the four fundamental states of matter consisting of a gas of ions and free electrons. On average, a plasma is electrostatically neutral meaning the electric potential of the positive ions is balanced by that of the negative ions and electrons. The most common method of generating a plasma is using an electric field to ionize a gaseous specie. This is accomplished by accelerating and heating the electrons of the gas. One such set up, involves a copper coil wrapped around a dielectric tube, such as quartz or sapphire. If a high frequency alternating current is applied to the coil, with a sufficient power, an electric filed can be created that ionizes the gases flowing through the tube. A plasma generated in this manner creates low energy electrons (<10 eV) with a corresponding temperature of $10^4 – 10^5$ K. These electrons can further excite the reactant gas forming ions and radicals.

While charged particles play a critical role in a plasma, their density can be orders of magnitude less than that of the plasma radicals, i.e. neutrals, depending on the ionization cross section. In general, the flux of electrons and ions at a sample surface is much lower than the flux of plasma radicals. As such, the radicals dominate surface reactions. However

the ion energy at the sample surface can be much higher than electrons and ions in the plasma due to the formation of a positive space-charge layer, called the “plasma sheath”, between the plasma and substrate surface. The formation of the plasma sheath can accelerate ions into the surface. The potential difference of the substrate surface and the plasma can be expressed using Eq. (2.20) which is plotted in FIG 2.16.[25]

$$V_p - V_s = \frac{T_e}{2e}\left(1 + \ln\left(\frac{m_i}{2\pi m_e}\right)\right) \tag{2.20}$$

Here, V_p and V_s are the potentials in the plasma and at the substrate surface, respectively, T_e is the electron temperature, e is the electron charge, m_i is the ion mass, and m_e is the electron mass. For He, N, O, and F plasmas, the potential difference can be upwards to ~4.5 T_e. Often the actual value differs based on plasma conditions and reactor configuration.

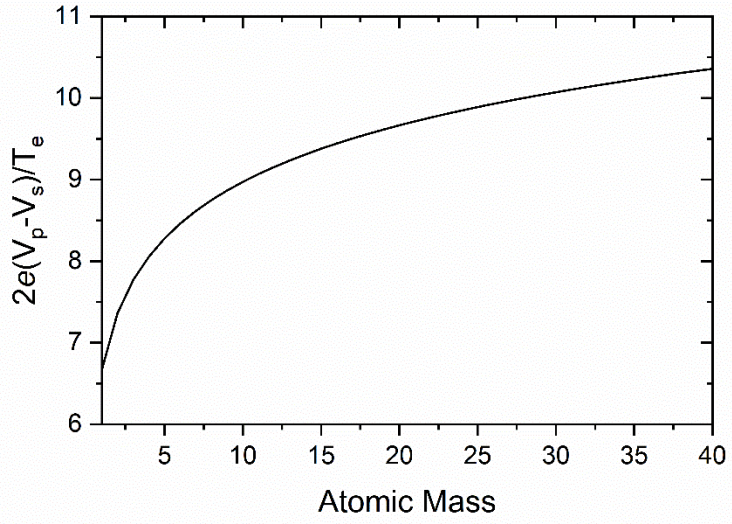

FIG 2.16. Unitless Potential difference between the plasma sheath and the substrate surface as a function of atomic mass or ion mass.

In PEALD two main mechanism enhance surface reactions. First, high energy plasma species supplement the substrate thermal energy often enabling lower growth

temperatures. The concentration of plasma species can be control by varying gas parameters (e.g. flow rate, composition, and pressure) or plasma parameters (e.g. applied power and bias). Thus, the energy delivered to the surface can be tuned. Second, ions can be used to increase reaction rates and rearrange adsorbed molecules. Similar to high energy plasma species, varying gas and plasma parameters can tune the ion energy and density. In general, the plasma sheath thickness and plasma pressure control the ion flux, or ion bombardment, at the sample surface which can cause undesirable damage. The degree of ion bombardment can be negated depending on reactor configuration. Typically, ion bombardment occurs at voltages $\gtrsim$100 V.[31]

2.4.2.2 Plasma Configurations

Many reactor configurations exist allowing for the application of plasma in ALD. These configurations typically differ by the how the plasma is generated and how far the plasma generation, or source, region is from the sample surface. Three types of plasma generation, shown in FIG 2.17, are most common: radical enhanced, direct plasma-assisted, and remote plasma.

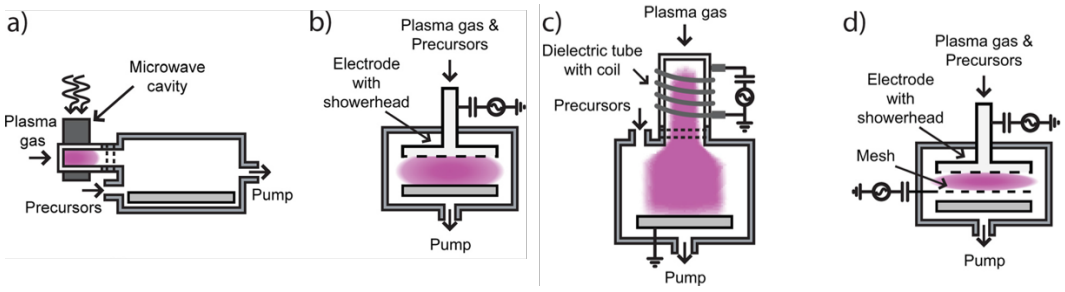

FIG 2.17. Various plasma configurations for ALD reactors. (a) radical-enhanced, (b) direct plasma-assisted, (c) remote plasma, and (d) direct plasma reactor with mesh. Image adapted from Profijt et al.[25] Copyright © 2011, American Vacuum Society.

Radical enhanced plasma processing, FIG 2.17(a), generates plasma species far away from the sample surface. The plasma species flow from the source to the substrate through a tube. This configuration allows the plasma species to lose energy while undergoing collision and recombination. Radical enhanced plasmas are typically implemented in PEALD reactors and also for surface cleaning. Direct plasmas, FIG 2.17(b), are generated by flow a gas between two parallel electrodes. The substrates can either be placed on an electrode or is used as an electrode. As the sample is directly in the plasma source region, the substrate is exposed to high concentrations of plasma species. A variation of this method is shown in FIG 2.17(d); here a biased mesh is placed between the electrodes. This configuration enables confinement of the plasma such that the sample is no longer in the plasma source region. The third configuration, FIG 2.17(c), is a remote plasma. Here, the plasma is generated remotely such that substrate is not in the source region. Unlike the radial enhanced configuration, the plasma is directly above the sample surface. In comparison to the direct plasma, the remote configuration has independent substrate and plasma conditions. In general, this leads to greater freedom and control of plasma properties. A strong advantage of remote plasma configurations is the distance between source and substrate surface which often allows for use of ellipsometry for *in situ* measurements. As such, this work implements the use of a remote plasma for all plasma enhanced atomic layer deposition and etching processes.

2.5 Atomic Layer Etching

2.5.1 Principles of Atomic Layer Etching

Atomic layer etching (ALE) is a self-limiting or pseudo self-limiting thin film removal technique with sub-nanometer precision.[32, 33] Like ALD, ALE achieves self-limiting material removal using sequential exposures of precursors, or reactants, separated by inert gas purges. A model ALE process, shown in FIG 2.18, consists of a surface modification step and a removal step separated by purging steps. A key characteristic of ALE is the self-limiting or pseudo self-limiting nature of the etch process. Self-limiting etching is achieved as there is a limited number of reactive surface sites for precursor adsorption. Unlike ALD, the self-limiting aspect does not have to occur during the second reactant exposures. Instead, the second reactant must be inert towards the unmodified surface.

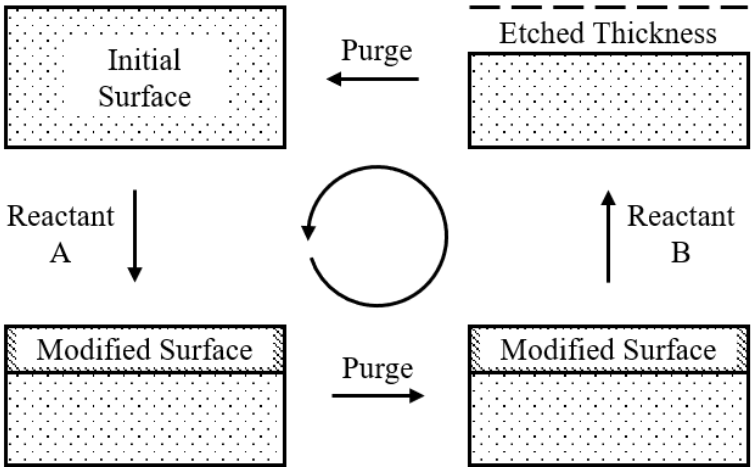

FIG 2.18. Schematic of an ALE cycle. In the first step, the surface is exposed to reactant A which modifies the surface composition. The modified surface is then exposed to reactant B which etches the modified surface leaving the sample thinner. Both reactant exposures are separated by purge steps to remove excess reactant and reaction byproducts.

This process is repeated until the desired thickness is removed. Image adapted from George.[34] Copyright © 2020, American Chemical Society.

ALE differs from ALD in that there is not a well-defined temperature window in which the etch rate is constant. Instead, the etch window, or process window, shown in FIG 2.19, is chosen such that the reaction rates of reactant A and B as well as the desorption rate of reactant B's byproducts are greater than zero. Outside of this process window, the substrate is not etched. Within the process window, the etch rate per cycle (EPC) can vary depending on the temperature dependence of the reaction and desorption rates. It should be noted that like ALD, etch rates can be less than or greater than one atomic layer per cycle but are within one order of magnitude.

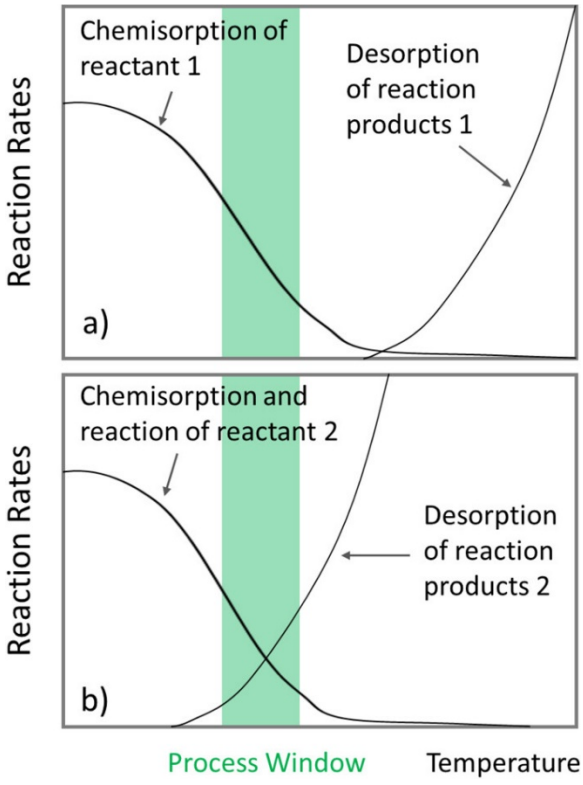

FIG 2.19. Illustration of the process window for thermal ALE. (a) shows the chemisorption temperatrue dependence of reactant 1 and the desorption of reactant 1's reaction

byproducts. Here, no etching occurs and the surface is modifed. In (b), the modifed surface is exposed to reactant 2 which removes some or all of the modifed surface. Image reprinted from Fischer et al.[33]

ALE processes can be classified in a variety of ways based on precursors used, the number of steps required for etching, or on the reaction mechanisms. To date, ten reaction mechanisms have been identified for thermal ALE.[34] These methods revolve around surface conversion, oxidation, fluorination, and ligand exchange. In this work, a multi-step process was implemented for the ALE of GaN consisting oxidation, fluorination, and ligand exchange. Oxidation can occur through a variety of methods; used in this work was thermal and remote plasma oxidation using water vapor and oxygen radicals, respectively. Once an oxide was created, it was fluorinated using hydrogen fluoride. The metal fluoride was then removed via ligand exchange using trimethylgallium. This process is illustrated in FIG 2.20.

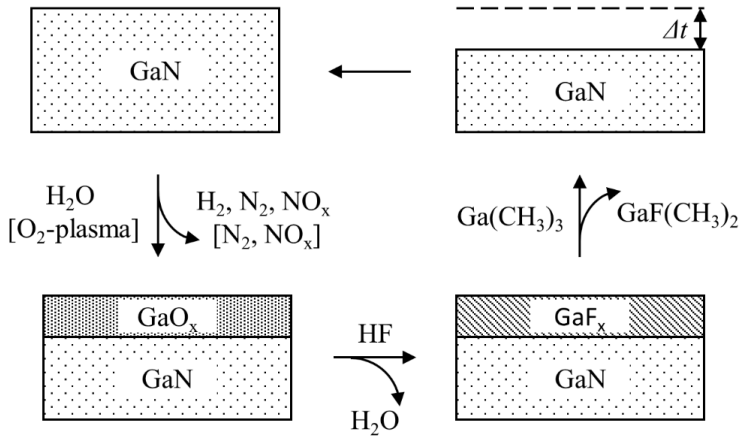

FIG 2.20. A schematic illustration of the GaN TALE and PEALE process. In the first step, the GaN surface is oxidized using either water vapor or O_2-plasma. Next, the surface is fluorinated using HF. Finally, the surface is exposed to trimethylgallium to remove the surface fluoride. Between each step is an inert gas purge.

References

[1] A. Einstein, Concerning an Heuristic Point of View Toward the Emission and Transformation of Light, American Journal of Physics **33**, 5 (1965).

[2] M. P. Seah and W. A. Dench, Quantitative electron spectroscopy of surfaces: A standard data base for electron inelastic mean free paths in solids, Surface and Interface Analysis **1**, 2-11 (1979).

[3] A. G. Shard, Practical guides for x-ray photoelectron spectroscopy: Quantitative XPS, Journal of Vacuum Science & Technology A **38**, 041201 (2020).

[4] J. F. Moulder, W. F. Stickle, P. E. Sobol and K. D. Bomben, (Perkin-Elmer Corporation, Eden Prairie, Minnesota, USA 1979), pp. 25-26.

[5] J. H. Scofield, Hartree-Slater subshell photoionization cross-sections at 1254 and 1487 eV, Journal of Electron Spectroscopy and Related Phenomena **8**, 129-137 (1976).

[6] C. J. Powell, Practical guide for inelastic mean free paths, effective attenuation lengths, mean escape depths, and information depths in x-ray photoelectron spectroscopy, Journal of Vacuum Science & Technology A **38**, 023209 (2020).

[7] H. Shinotsuka, S. Tanuma, C. J. Powell and D. R. Penn, Calculations of electron inelastic mean free paths. X. Data for 41 elemental solids over the 50 eV to 200 keV range with the relativistic full Penn algorithm, Surface and Interface Analysis **47**, 871-888 (2015).

[8] M. P. Seah, An accurate and simple universal curve for the energy-dependent electron inelastic mean free path, Surface and Interface Analysis **44**, 497-503 (2012).

[9] A. Jablonski and J. Zemek, Overlayer thickness determination by XPS using the multiline approach, Surface and Interface Analysis **41**, 193-204 (2009).

[10] A. Jablonski, Evaluation of procedures for overlayer thickness determination from XPS intensities, Surface Science **688**, 14-24 (2019).

[11] A. Jablonski and C. J. Powell, Improved algorithm for calculating transport cross sections of electrons with energies from 50 eV to 30 keV, Physical Review B **76**, 085123 (2007).

[12] A. Jablonski, Corrigendum: Photoelectron transport in the surface region of solids: universal analytical formalism for quantitative applications of electron spectroscopies (2015J. Phys. D: Appl. Phys.48075301), Journal of Physics D: Applied Physics **49**, 289501 (2016).

[13] NIST Database for the Simulation of Electron Spectra For Surface Analysis (SESSA), (National Institute of Standards and Technology, Gaithersburg, MD, 2018); https://www.nist.gov/srd/nist-standard-reference-database-100

[14] D. C. Messina, B. S. Eller, P. Scowen and R. J. Nemanich, Comparison of aluminum fluoride thin films growth by thermal and plasma enhanced atomic layer deposition, (unpublished).

[15] J. Yang, B. S. Eller, M. Kaur and R. J. Nemanich, Characterization of plasma-enhanced atomic layer deposition of Al2O3 using dimethylaluminum isopropoxide, Journal of Vacuum Science & Technology A **32**, 021514 (2014).

[16] *FS-1 Manual v1.50*. (Film Sense, LLC, Lincoln, NE, 2017).

[17] R. M. A. Azzam, Division-of-amplitude Photopolarimeter (DOAP) for the Simultaneous Measurement of All Four Stokes Parameters of Light, Optica Acta: International Journal of Optics **29**, 685-689 (1982).

[18] N. W. Ashcroft and N. D. Mermin, in *Solid State Physics*, edited by N. W. Ashcroft and N. D. Mermin (Cengage Learning, 2021).

[19] O. Stenzel, in *Optical Coatings: Material Aspects in Theory and Practive*, edited by O. Stenzel (Springer, 2014), pp. 21.

[20] D. A. G. Bruggeman, Berechnung verschiedener physikalischer Konstanten von heterogenen Substanzen. I. Dielektrizitätskonstanten und Leitfähigkeiten der Mischkörper aus isotropen Substanzen, Annalen der Physik **416**, 636-664 (1935).

[21] R. L. Puurunen, Surface chemistry of atomic layer deposition: A case study for the trimethylaluminum/water process, Journal of Applied Physics **97**, 121301 (2005).

[22] V. Miikkulainen, M. Leskelä, M. Ritala and R. L. Puurunen, Crystallinity of inorganic films grown by atomic layer deposition: Overview and general trends, Journal of Applied Physics **113**, 021301 (2013).

[23] N. E. Richey, C. de Paula and S. F. Bent, Understanding chemical and physical mechanisms in atomic layer deposition, The Journal of Chemical Physics **152**, 040902 (2020).

[24] H. Kim, Characteristics and applications of plasma enhanced-atomic layer deposition, Thin Solid Films **519**, 6639-6644 (2011).

[25] H. B. Profijt, S. E. Potts, M. C. M. van de Sanden and W. M. M. Kessels, Plasma-Assisted Atomic Layer Deposition: Basics, Opportunities , and Challenges, Journal of Vacuum Science & Technology A **29**, 050801 (2011).

[26] B. H. Kim, W. S. Jeon, S. H. Jung and B. T. Ahn, Interstitial Oxygen Incorporation into Silicon Substrate during Plasma Enhanced Atomic Layer Deposition of Al_2O_3, Electrochemical and Solid-State Letters **8**, G294 (2005).

[27] S.-W. Kim, S.-H. Kwon, S.-J. Jeong and S.-W. Kang, Improvement of Copper Diffusion Barrier Properties of Tantalum Nitride Films by Incorporating Ruthenium Using PEALD, Journal of The Electrochemical Society **155**, H885 (2008).

[28] T. O. Kääriäinen and D. C. Cameron, Plasma-Assisted Atomic Layer Deposition of Al_2O_3 at Room Temperature, Plasma Processes and Polymers **6**, S237-S241 (2009).

[29] A. Foroughi-Abari and K. C. Cadien, *In-Situ* Spectroscopic Ellipsometry Study of Plasma-Enhanced ALD of Al_2O_3 on Chromium Substrates, Journal of The Electrochemical Society **159**, D59-D64 (2011).

[30] H. Kim and I.-K. Oh, Review of plasma-enhanced atomic layer deposition: Technical enabler of nanoscale device fabrication, Japanese Journal of Applied Physics **53**, 03DA01 (2014).

[31] M. A. Lieberman and A. J. Lichtenber, (John Wiley & Sons, New York, 2005).

[32] K. J. Kanarik, T. Lill, E. A. Hudson, S. Sriraman, S. Tan, J. Marks, V. Vahedi and R. A. Gottscho, Overview of atomic layer etching in the semiconductor industry, Journal of Vacuum Science & Technology A **33**, 020802 (2015).

[33] A. Fischer, A. Routzahn, S. M. George and T. Lill, Thermal atomic layer etching: A review, Journal of Vacuum Science & Technology A **39**, 030801 (2021).

[34] S. M. George, Mechanisms of Thermal Atomic Layer Etching, Accounts of Chemical Research **53**, 1151-1160 (2020).

CHAPTER 3

DEVELOPING ATOMIC LAYER PROCESSING REACTORS ENABLED BY FLUORINE CHEMISTRY

3.1 Reactor Requirements

The development of a reactor for atomic layer deposition (ALD) of metal fluorides and atomic layer etching (ALE) of metal oxides and nitrides requires careful consideration of material properties, enabling physics, and chemistry. A reactor capable of thermal and plasma enhanced processing is even more complicated due to the additional hardware, software, and other requirements for consistent plasma generation. In this section, the requirements for fluoride atomic layer deposition and etching (ALD and ALE), or atomic layer processing (ALP), reactors will be outlined. These reactors, shown in FIG 3.1, were constructed with both thermal and plasma enhanced ALP (TALP and PEALP) in mind. The ALD of metal fluorides and ALE of metal oxides was enabled by use of hydrogen fluoride, a highly toxic and corrosive chemical compound, various pyrophorics (trimethylaluminum and trimethylgallium), and plasmas (H_2 and O_2).

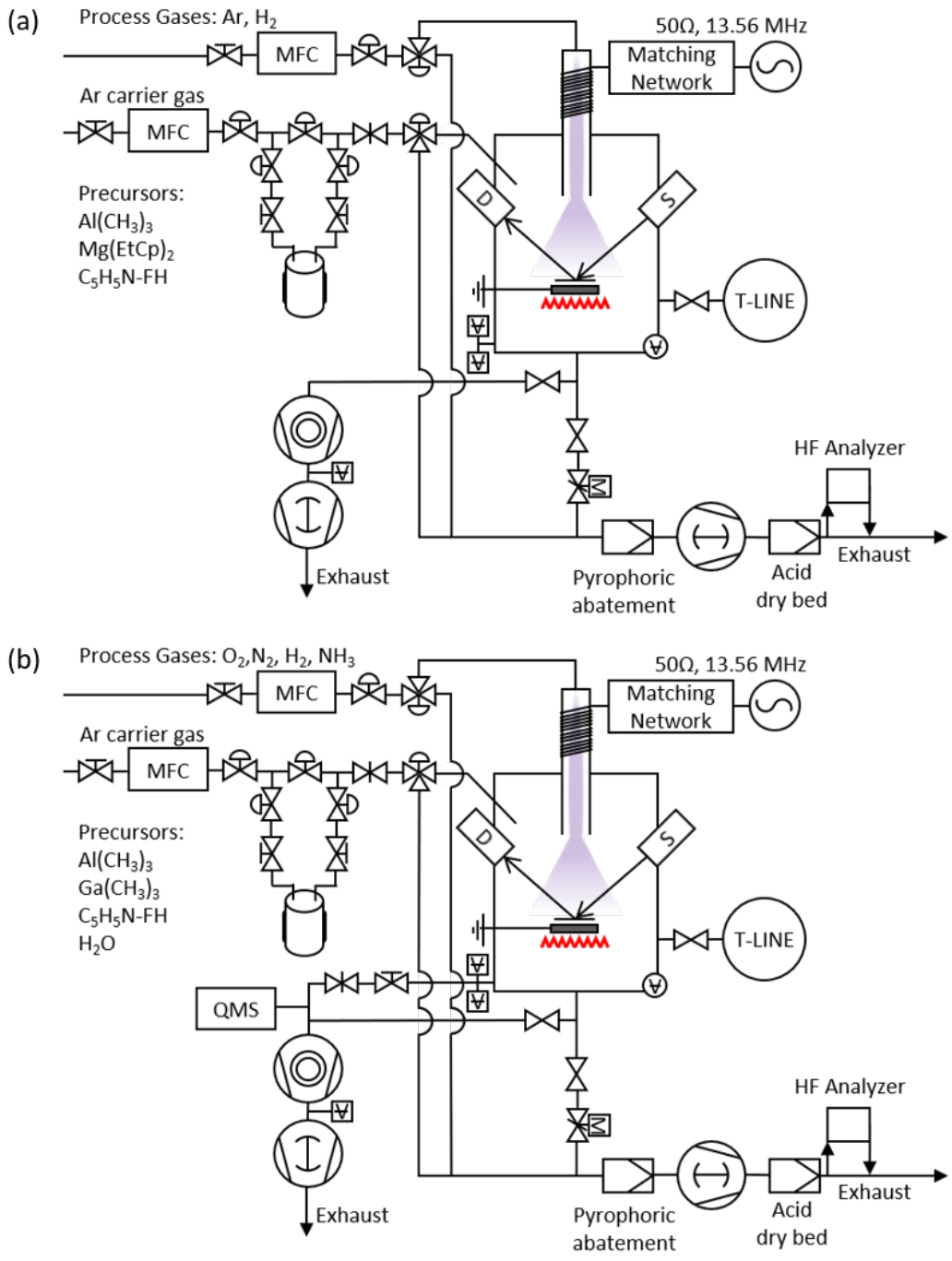

FIG 3.1. Schematic of (a) the fluoride plasma enhanced atomic layer processing (F-PEALP) and (b) the oxide PEALP (O-PEALP) reactors. Both systems are equipped for *in situ* ellipsometry measurements the O-PEALP is also equipped with a quadrupole mass spectrometer.

3.2 Reactor Subsystems

3.2.1 Pressure

As with most chemical vapor deposition (CVD techniques, ALP requires a vacuum during processing for ease of gas or vapor delivery and high purity films. The pressure requirement for ALP are much more relaxed than CVD as ALP reactors typically operate between 1E-3 – 1 Torr. A variety of methods exist for generating a rough vacuum, but the employment of rotary oil pumps or dry roots pumps is the most common. Use of oil pumps often requires oil filters to prevent oil vapor from entering the reactor and introducing impurities (hydrocarbons, fluorocarbons, etc). Additionally, use of an oil pump on an ALP reactor would require consideration of the chemical compatibility of all reactants with the pump oil. As such, dry roots pumps have become popular as oil is not directly employed in generating a vacuum, and oil mist filters are not required. The ultimate pressure of an oil or dry roots pump is about 1E-3 Torr. Since ALP tends to operate at pressures up to ~ 1 Torr, a butterfly valve, or exhaust throttling valve (ETV), is often used to control the process pressure. ETVs are often actuated using an electric motor enabling fast and remote operation. An electric ETV is used in combination with a pressure gauge allowing for a proportional-integral-derivative (PID) controller to be used. A PID controller enables dynamic control of reactor's pressure.

Other pressure consideration includes sample transfer and the use of in situ characterization techniques. In this work, the ALP reactors were integrated into a high vacuum transfer line. Doing so required that the ALP reactors have a dedicated pumping system for sample transfer; a turbomolecular pump backed by a dry roots pump. In one of the ALP systems, a quadrupole mass spectrometer (QMS) was integrated into it allowing

for determination of gas phase byproducts. A QMS requires a pressure of <5.5E-6 Torr and operate at higher pressures resulting in electrical arcing between the quadrupoles.

3.2.1.1 Vacuum Generation and Measurement

3.2.1.1.1 Sample Transfer and Idling

The ALP reactors utilized a high vacuum pumping system separated by a gate valve from the reactor. A base pressure of ~2E-8 Torr was achieved using a turbomolecular pump (Pfeiffer, HiPace 80) backed by a dry roots pump (Pfeiffer, ACP15). A variety of pressure gauges were implemented for accurate measurements from ultra-high vacuum (UHV) to atmosphere. For pressure ranging from 760 – 1E-2 Torr, a convection enhanced Pirani gauge (CP) (MKS, 317) was used on the reactors. The CP gauge was used when venting (e.g. bring to atmospheric pressure) the ALP reactors and as a secondary gauge during processing. An additional CP gauge (MKS, 275) is placed on the turbo and dry pump to measure the turbo back pressure. A cold cathode (CC) sensor (MKS, 431) allowed measurement between 5E-3 – 1E-11 Torr. The CC allows monitoring of system pressure and, and it can be used as a rudimentary leak checker at high vacuum.

Pressure measurements were logged electronically as the CP and CC gauges are connected to a vacuum system controller (VSC) (MKS, 946). The VSCs can be configured to have multiple CC, CP, or mass flow controller (MFC) slots depending on hardware configuration. Communication between the VSC and control computer is accomplished via a serial connection using the RS-232 standard. A custom LabVIEW virtual instrument (VI) was written to query, command, and log data from the VSC. The LabVIEW VI allows for

logging of system pressure enabling calculation of leak rates, partial pressures, and reactor effective volume.

3.2.1.1.2 Processing

The deposition of metal fluorides and etching of metal oxides requires the use of volatile metal precursor and corrosive halides. As such, a dedicated process pump was employed during processing. The process pump (Ebara, A70W) is a two-stage dry roots pump that uses 14.2 SLM (standard liters per minute) of N_2 to dilute incoming gases. The use of the N_2 dilution flow extends the longevity of the A70W. When no N_2 dilution flow is used, a base pressure of ~5E-4 Torr is achieved. The N_2 dilution flow has been observed to back flow into the reactor at ~5E-4 torr. Thus, during processing the minimum pressure is ~1E-4 Torr.

Process pressure is dynamically controller using an exhaust throttling valve (ETV) (MKS, 253B), a capacitance manometer (CMM) (MKS, 627F), and a proportional-integral-derivative (PID) controller (MKS, 651C). The CMM has a pressure range of 0.1 – 1000 mTorr with 0.2 % accuracy. The ETV has a slow actuation (open to close) time of 7.5 s in comparison to similar models which is undesirable for production environments. The ETV and CMM are connected directly to the PID controller using a DE-subminiature 9-pin (DE-9) connector for RS-232 communication though only three conductors are used. The PID controller takes measurements from the CMM, queries the user's desired pressure set point, and actuates the ETV accordingly. During an ALP process, the PID is queried for the reactor pressure and commanded to change the ETV to be open, closed, or to a predefined position.

Commands and queries sent to the PID controller is done so using a custom LabVIEW SubVI that allows for remote control. A SubVI in LabVIEW is akin to a hardware software driver or a subroutine. The SubVI enables remote selection of the ETV and querying of the reactor pressure. Process pressure is recorded using a custom LabVIEW program and is plotted in real time.

3.2.1.2 Gas Delivery

Fine control of process gases and precursor vapors is essential for ALP. A common method to control fluid flow is the use of a mass flow controller (MFC). An MFC consists of an inlet port, an outlet port, a mass flow sensor, and a proportional control valve. MFCs are fitted with a PID control system which is given an input signal, such as a desired fluid flow rate, that is compared to the calibrated mass flow sensor's value then adjusts the control valve accordingly. MFCs are commonly calibrated for nitrogen gas with conversion factors available for other fluids. For the ALP systems constructed for this work, 100 sccm (standard cubic centimeters per minute) MFCs (MKS, GE50A) were used for control of process and carrier gases. The GE50As are able communicate via two protocols: RS-232 and Ethernet.

MFC configuration and calibration required use of an embedded user interface accessible over Ethernet using a computer and a web browser. When calibrating, a user has to input the gas correction factor and specify the inlet pressure and temperature. For example, the gas correct factor for H_2 and Ar are 1.01 and 1.39, respectively. As such, the maximum flow rate of the H_2 and Ar MFCs becomes 99.0 sccm and 71.9 sccm, respectively. For routine use, the MFCs were connected to the aforementioned 946 VSCs

using DE-15 cables. The VSC are connected to a control computer for remote control. To enable programmatic control of the MFCs, a custom LabVIEW VI was written for interface with the 946's MFC cards. Each precursor and process gas had different flow rates and were delivered through a series of manual and pneumatic valves to the reactor, shown in FIG 3.2. The precursors used argon as a carrier gas with flow rates varying between 3 sccm to 15 sccm depending on precursor vapor pressure. Plasma source gases and purge gases were supplied at 35 sccm and 30 sccm, respectively.

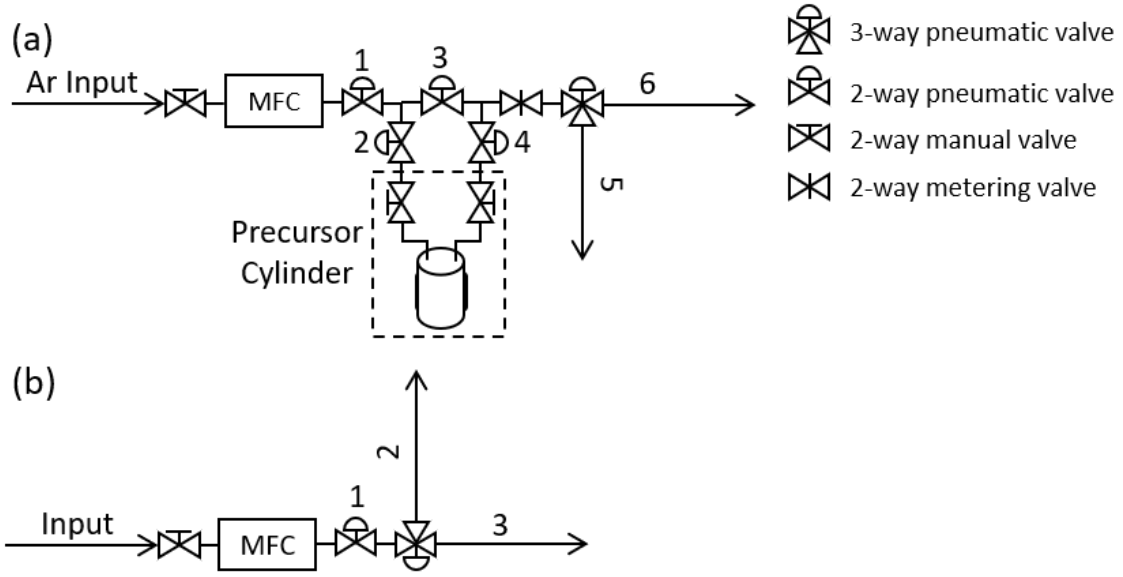

FIG 3.2. Precursor vapor and process gas delivery lines for the ALP systems with the pneumatic valves labeled. In (a) the precursor delivery line is shown. Valve 1 is the carrier gas inlet, valve 2 is the cylinder inlet (for bubbling), valve 3 is the cylinder bypass, valve 4 is the cylinder outlet, valve 5 is the exhaust inlet, and valve 6 is the chamber inlet. In (b), the process gas delivery line is shown. Valve 1 is the process gas inlet, valve 2 is the chamber inlet, and valve 3 is the exhaust inlet. The box labeled "MFC" is the mass flow controller for each line. Each process gas and precursor have a separate delivery line.

Pneumatic valves were used for the delivery of all gases and vapor. The precursor delivery lines were constructed for bubbling and/or vapor draw of precursors. Actuation of the pneumatic valves requires the use of a gas manifold with a number of solenoid valves. The gas manifolds consisted of a modular manifold (SMC, SS5Y3), a field bus controller (SMC, EX600), and up to sixteen solenoid valves (SS3100-5U1). The EX600 is a modular serial interface platform offering a full suite of diagnostic and programmable parameters. To remotely actuate a valve, a command has to be sent to the EX600 using the EtherNET/IP (Ethernet over Industrial Protocol) standard. To communicate with the EX600, DE-5C to RJ45 cable is used. In some instances, EX600s were daisy chained for convenience. While communication with the EX600s could have been accomplished using a standard computer, a LabVIEW Real-Time Operating System (RTOS) (National Instruments, Phar Lap ETS 13.1) was implemented to ensure reliability and precise process timings. The RTOS system utilizes a peripheral component interconnect express (PCIe) card (National Instruments, PCIe-8233) enabling communication with the EX600 controllers. The RTOS computer is connected via a local network to the control computer allowing for RTOS applications to be run remotely. Finally, a custom LabVIEW VI was written for precise valve actuation and error handling.

An additional feature of one precursor line is the presence of a 50 μm diameter orifice on the pneumatic valve 4, shown in FIG 3.2(a). This orifice was installed due to the high vapor pressure of the precursor (trimethylgallium) as the vapor pressure exceeds 200 Torr at room temperature. Without the orifice an excess of material was being delivered into the chamber using short pulse times. This resulted in the formation of metallic gallium on the sample backside, sample holder, and the chamber walls. The installation of a 50 μm

diameter orifice reduced amount of material delivered by a factor of ten (~200 mTorr to 20 mTorr transients over 30 s with a 0.1 s pulse). A similar set up could be applied to other high vapor pressure precursors (such as hydrogen fluoride) leading to finer control of precursor delivery and cost savings.

3.2.2 Temperature

3.2.2.1 Reactor Walls and Delivery Tubing

Heating of the reactor walls and delivery tubing is important in ALP to prevent the condensation of precursor molecules and maintain a decent vacuum quality. When a vacuum system is unheated, water vapor can condense onto the walls and act as a virtual leak. This leads to decreased pumping speeds as water vapor will constantly be desorbing/adsorbing onto chamber walls. To prevent this, the ALP reactor walls were wrapped with heating tape. The heating tape consists of a wire grid encased in a rubber polymer. The wire grid is resistivity heated with the application of a current. For these ALP systems, the heating tape temperature was controlled using a variable transformed. The transformer output was set by a manual knob until a temperature of 100 °C was achieved. Similarly, some precursor delivery lines were maintained at 100 °C to prevent condensation. For precursors with a low boiling point such as HF and trimethylgallium, heating was not necessary. Additionally, heating of the trimethylaluminum (TMA) delivery line, to 100 °C, ensures that the TMA molecules arrive in the reactor as a monomer rather than a dimer or trimer.[1]

3.2.2.2 Sample Stage

In thermal ALD or ALE, the substrate must be at a sufficient temperature for chemical reactions to occur. As such a heating stage for the substrate was required. The heating stage, shown in FIG 3.3, is fixed to a rotary flange and extends into the center of the reactor. The stage consists of a twist-lock sample holder, electric and thermal insulators (white), a coiled nichrome (~$Ni_{80}Cr_{20}$) heating element, a K-type thermocouple (nickel-chromium), and copper feed throughs. In FIG 4(a), the twist-lock receptacle is shown on top. The electric insulator (white discs) are made from pyrolytic boron nitride and the thermal insulator (white blocks) were fabricated from macor, a fluorphlogopite mica in a borosilicate glass matrix ($(SiO_2)_{46}(MgO)_{17}(Al_2O_3)_{16}(K_2O)_{10}(B_2O_3)_7F_4$). While macor is an excellent thermal insulator, it should have been avoided as its reactivity with HF is unknown and two (SiO_2 and Al_2O_3) of the five oxides are known to be etched using fluorination and ligand exchange.

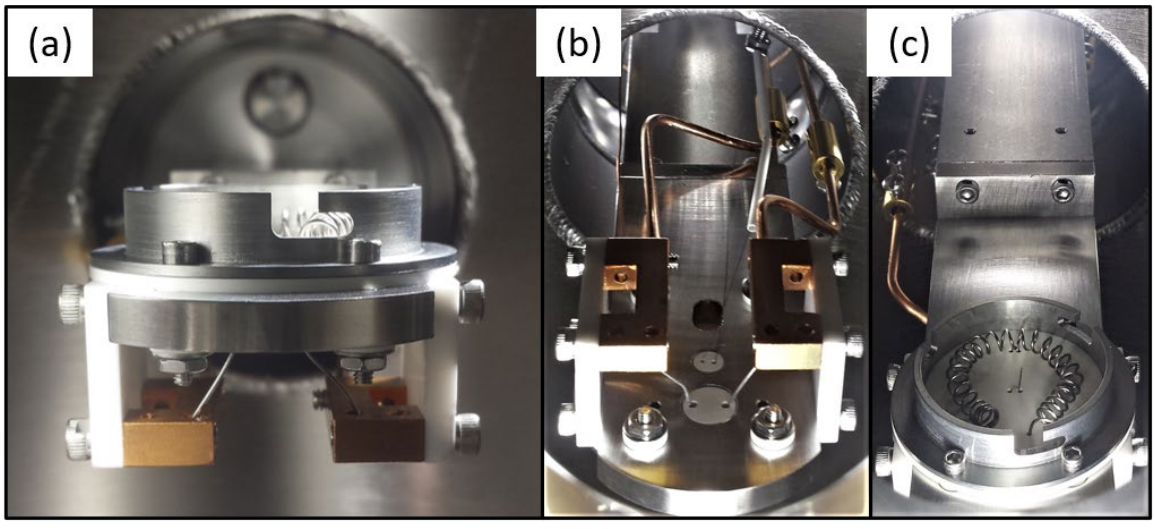

FIG 3.3. Front (a), bottom (b), and top (c) views of the initial ALP sample stage mounted onto a rotary flange. In (b), the wiring is shown. The white hollow cylinders on the

thermocouple feedthrough is boron nitride. In (c), the nichrome heating element is shown in a ~13 mm diameter circle with a K-type thermocouple in the center. Later, all exposed wiring was properly isolated using boron nitride ceramic beads.

Heating of the substrate sample is accomplished by applying a current via the thick copper rods and blocks to the heating coil, shown in FIG 3.3(b) – (c). As the current passes through the coil, the coil heats up and produces infrared photons. Additionally, it is expected that this set up would produce a small magnetic field which could provide inductive heating. It is assumed that the resistive heating is much greater than the inductive heating. The temperature can be measured using a thermocouple placed in the center of the heating coil. As the distance between the thermocouple tip and where the substrate sits is very small (<2 mm), it is assumed the substrate temperature is that of the thermocouple. This method of heating can be misleading if the sample substrate material is infrared transparent.

Temperature can be measured using a thermocouple where the voltage is temperature dependent. The operating principles relies on the Seebeck effect which states an electric potential develops across two electrical conductors when there is a temperature gradient. As such, the two ends (referred to as positive and negative) of a thermocouple have a slightly difference composition. A change in temperature induces a voltage which is fed to a PID controller. A Eurotherm 2216e PID controller was implemented for substrate temperature control. The PID controller was connected to a phase-angle fired 16 A solid-state relay (SSR) (Eurotherm, EFIT16A) allowing for fast dynamic temperature control. A schematic of the temperature control circuit is shown below in FIG 3.4.

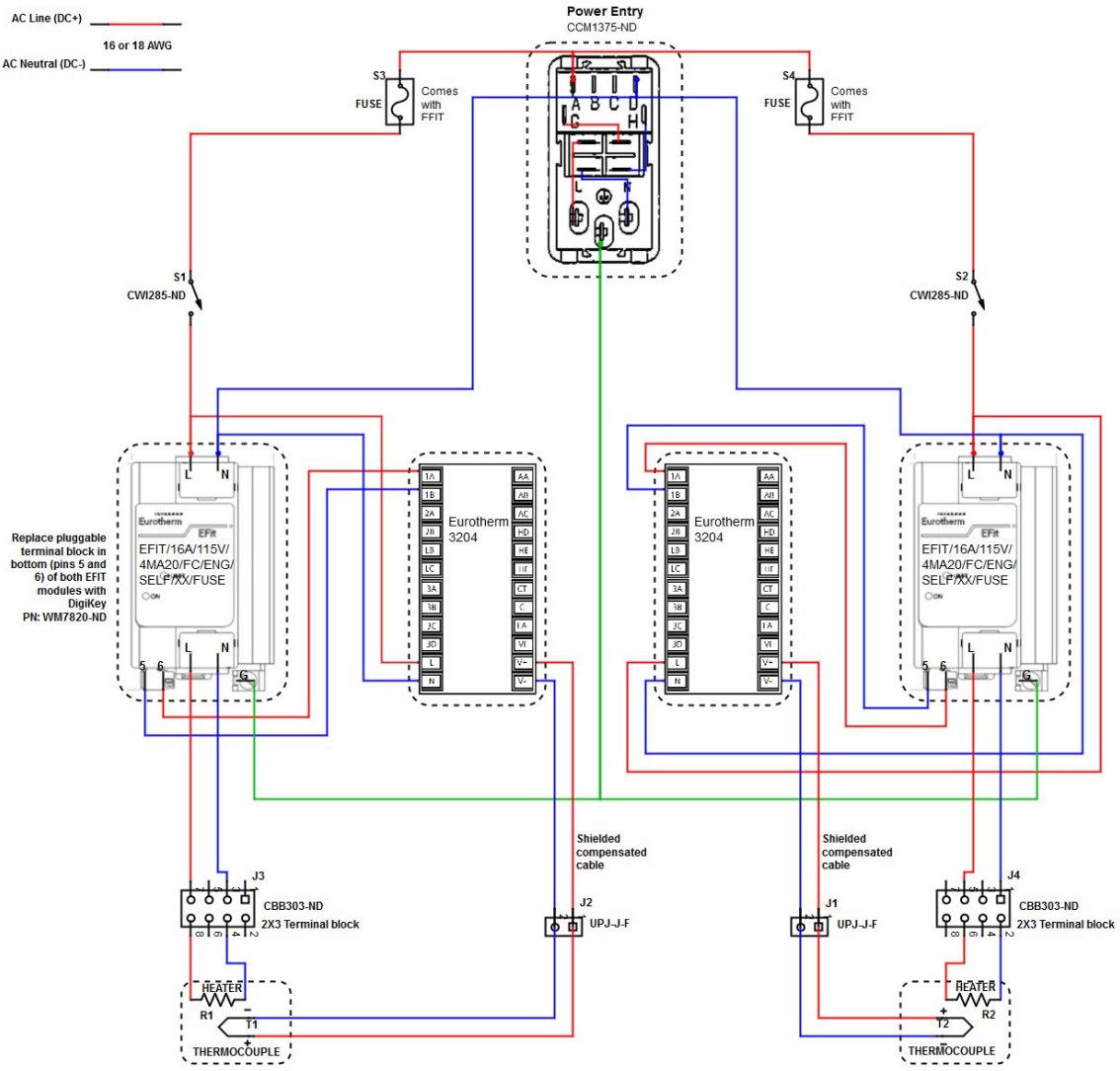

FIG 3.4. Schematic of the temperature control box circuit for sample and precursor vessel heating. Each circuit is configured for two controllers though it is easily modified for a single controller.

The PID temperature control system operates in a standard way. Initially, a small current is applied such that the heating element starts to heat up. As that happens, infrared photons are emitted which are incident on the thermocouple. The incident photons transfer energy into the thermocouple which causes a change in voltage. Due to the difference in the alloying of the positive and negative sides of the thermocouple, a potential difference

is measured. The PID controller measures this voltage and references it to a tabulated reference table to convert it to a temperature. The PID controller checks if the temperature is the user's set point. If not, a 4-20 mA signal is sent to the SSR to increase the applied current. This is repeated until the set point is reached.

The PID controller is configured specifically for the heating element used. The controller uses an autotune function which determines a variety of properties related to the response of the heating element and the application of a current. The autotune function is best applied when a coil is replaced and under operating pressures. A finely tuned controller allows for the temperature to be steadily increased until a desired set point is reached. For example, the ALP reactors are configured to increment the temperature by 1 °C every 2 seconds until the user setpoint is reached. To ensure system longevity and prevent burning out the heating element, the current output on the PID controller is limited to 20%. Additionally, the SSR is equipped with a potentiometer which further limits the applied current, up to 70 %. In total, the applied current is limited to 0.96 A to prevent melting the heating element. With this configuration, substrate temperatures can quickly reach 400 °C. The current limits can be increased if necessary.

Programmatic control of the temperature control is not currently possible as the PID controllers are not connected to the control computer. The PID controllers, specifically the Eurotherm 2216e models, are fitted with a communication card for RS-232 communication. Implementation of remote control would require two steps: (1) connection of a male to female RS-232 DE-9 cable from the PID controller to the control computer and (2) the development of a custom LabVIEW SubVI. The cable connection is easily done but requires a free serial connection to the control computer. Alternatively, if an open USB

(universal serial bus) port is found, an RS-232 to USB cable and driver could be used. Unfortunately, there are no open ports at this time (serial or UBS) so an expansion card (PCIe) or USB to USB junction would be needed. The second requirement (writing a LabVIEW VI) would require configuring the PID controller for remote communication and carefully readying the associated manual to find the relevant commands and formatting. Implementation of programmatic temperature control would allow exploration of temperature modulated atomic layer processes or temperature programmed desorption.

3.2.2.3 Precursor Vessels

Similar to the sample heater, the precursor vessels use the temperature control configuration, shown in FIG 3.4. Instead of separate thermocouples and heating elements, an all-in-one cloth heating jacket is used to wrap around the cylindrical precursor vessels. The cloth heating jackets are similar to aforementioned heating tape but have a J-type (Fe, Cu-Ni alloy) thermocouple. The PID controllers (Eurotherm, 3204) are configured for fast-cycling output and are connected to a solid-sate relay (Eurotherm, EFIT16A). The SSRs here do not have a current limiter. The PID controller is set to only output a maximum of 10 % of the possible current.

The set point, or resting temperature, of the precursor cylinders is chosen based off the precursor vapor pressure and to ensure thermal stability over ambient. For example, trimethylgallium (TMG), HF–pyridine (HF-P), trimethylaluminum (TMA), and water have vapor pressures of >200 Torr, ~100 Torr, 20 Torr, and 17 Torr at room temperature, respectively, which is more than sufficient for vapor draw. As such, the cylinders were heated to 25 °C as the ambient temperature can fluctuate between 20 – 21 °C. The vapor

pressure can be calculated based off of experimental data using the Antoine equation. The Antoine equation is semi-empirical correlation describing the vapor pressure and temperature of materials. This equation is based off the Clausius-Clapeyron relation which relates the change in pressure with respect to temperature to the specific latent heat, temperature, and specific volume of the material. The Antoine equation fitted parameters are available for some materials (H_2O, HF, pyridine, TMA, etc.) on the NIST Chemistry WebBook and in literature.[2]

3.2.3 Remote Inductively Coupled Plasma

Remote inductively coupled plasma (ICP) processing is an important aspect of the ALP reactors. The remote ICPs have been proven to be versatile and have been used for chamber cleans, sample cleaning, and material deposition. As mentioned in §2.4.2.1, a remote plasma configuration allows for the delivery of a high density of plasma radicals to the substrate surface. The density of plasma radicals is dependent on the parameters (flow rate, pressure, and composition) and plasma parameters (power, bias, frequency). In this work, a 13.56 MHz radiofrequency (RF) ICP was implemented. No bias was applied, and samples were typically grounded. Sample surfaces were ~250 mm from the plasma source region. In this section, some plasma basics, hardware requirements, and experimental setup will be described.

3.2.3.1 The Helical Resonator

ICP coils are commonly driven by a 13.56 MHz RF 50 Ohm generator through a capacitive impedance matching network. FIG 3.1, show schematics of the oxide free

PEALP and oxide PEALP reactors. Each reactor is near identical in terms of plasma configuration with minor differences in coil fabrication. This configuration is referred to as a helical resonator. When an RF current is applied through a helical coil, an electromagnetic field is produced. The applied power is transferred from the electric field to the plasma electrons within a certain thickness, called the skin depth, near the plasma surface. The power is transferred through ohmic dissipation and by collisionless heating processing. Collisionless heating processes occur when bulk plasma electrons are subjected to oscillating inductive electric fields within the skin depth. Electrons within the skin depth are accelerated and thermalized. For efficient gas ionization, the geometry of the coil must be considered.

The design of a helical resonator requires consideration of the operating frequency. The length of the coil should be a quarter of the wavelength. For a 13.56 MHz wave, one wavelength corresponds to 22.1 m thus the coil length should be 5.5 m in length for maximum efficiency. Based on previous design used within the Nanoscience Lab, a 13-turn 32 mm diameter helical coil with a pitch of ~10 mm was used. The pitch must be chosen such that the space prevents the ionization of air. The total coil length was 1.3 m which is about one sixteenth of the wavelength. For resonance to occur, Eq. (3.1) must be satisfied.

$$2\pi r N = m\frac{\lambda}{4} \tag{3.1}$$

Where λ is the wavelength, m is an integer, and r is the coil radius. Using this resonance condition for a 32 mm diameter helix, 13 turns is obtained for $m = 4$.

3.2.3.2 Plasma Generation

To generate a stable RF ICP for ALP, a RF power supply and impedance matching network is required. In this work, a 13.56 MHz 50 Ω generator (MKS, Elite 300) was used in combination with a 50 Ω impedance matching network. A circuit diagram of the described setup is shown in FIG 3.5.

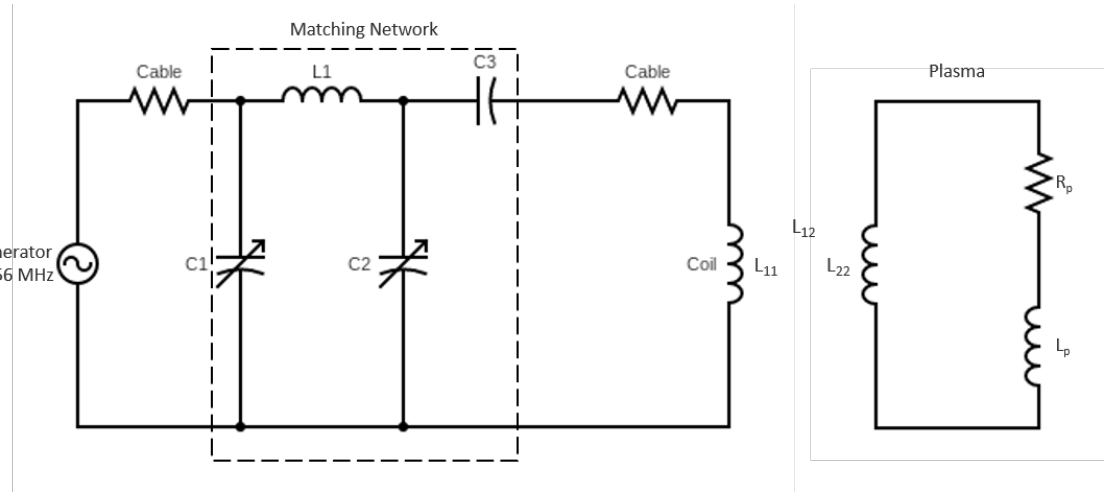

FIG 3.5. Circuit diagram of the RF generator, impedance matching network, helical resonator, and inductively coupled plasma. Image adapted from Park et al.[3] Copyright © 1997, IEEE.

Here, C1 – C3 and L1 are part of the automatic impedance matching network, shown in FIG 3.6. C1 and C2 are variable capacitors driven by stepper motors which work to minimize the impedance of the circuit. The coil is the left most inductor with the mutual inductance L_{11} shown. On the far left is the effective circuit diagram of the plasma.

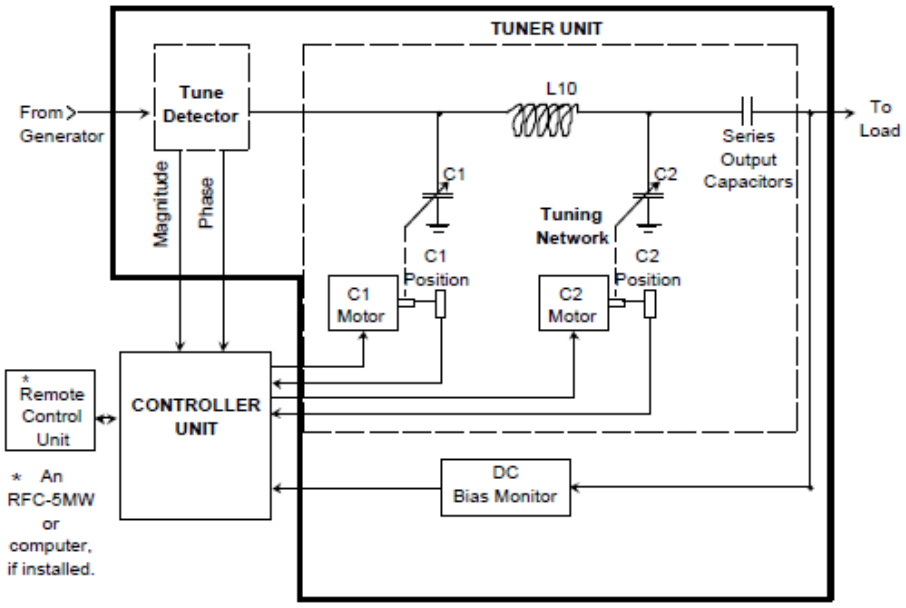

FIG 3.6. Block diagram of the MWH-5-01 impedance matching network.[4] Copyright © 1997, ENI.

The generation of an RF ICP using the MKS Elite 300 RF generator and the MWH-01-05 automatic matching network requires the reactor pressure be greater than 25 mTorr. A plasma is generated when the RF generator is either sent a command or turned on manually. The RG generator will apply a current to the helical coil through the matching network. Initially, the matching network will use the previous capacitor positions of C1 and C2. If the plasma parameters are different, then plasma ignition will not be immediate. While the impedance is being minimized, the RF generator will balance the reverse current. To facilitate remote operation of the RF generator and the impedance matching network, a custom LabVIEW SubVI was written allowing for turning on and off the plasma and changing the plasma power via the control computer. The impedance matching network was configured for automatic matching such that no communication or manual input is necessary. Unfortunately, this can lead to long ignition delays if the plasma parameters

differ from the previous ignition. For example, if the previous ignition was at 100 W and 100 mTorr of H_2 and the new plasma is 100 W and 100 mTorr of Ar, there will be an ignition delay as the matching network works to minimize the circuit impedance. The ignition delay would occur if the pressure, power, or gas composition has changed.

To prevent the time delay from minimizing the impedance, a plasma is typically ignited mirroring the same process parameters before starting a process. An alternative solution would involve reconfiguring the impedance matching network to accept commands and queries from a control computer. The matching network supports RS-232 communication with the ability to query capacitor positions. Using this query, one could build a table of capacitor positions for various pressures, gas compositions, and powers. As long as the plasma parameters were known before hand, the variable capacitor settings could be sent to the matching network prior to ignition. This would enable fast dynamic ignition of the ICP but requires the more initial work.

3.2.4 Exhaust Abatement

Reactive precursors are essential for chemical vapor deposition and dry etching techniques such as atomic layer deposition and etching. Unfortunately, volatile compounds tend to have a hazard associated with them. For example, trimethylaluminum and trimethylgallium are pyrophoric compounds that combust on exposure to air; hydrogen fluoride is an extremely toxic and corrosive chemical that can be fatal from contact of if inhaled. As such, design of a system using these chemicals requires careful consideration of the abatement of unreacted molecules. Thus, the ALP reactors feature a multistep exhaust abatement system, shown in FIG 3.7, including the dilution of unreacted

precursors, the abatement of pyrophorics and acids, and continuous measurement of acid concentration on the system exhaust.

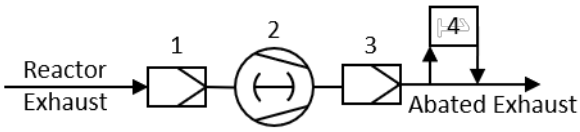

FIG 3.7. Schematic of the ALP reactors exhaust abatement. Each piece of equipment is labeled as follows: (1) multi-trap for pyrophorics, (2) process pump with a N_2 dilution flow, (3) an acid dry bed for HF abatement, and (4) an electrochemical gas analyzer to determining residual HF concentration.

After unreacted precursor vapors, process gases, or reaction byproducts exit the ALP reactors, they pass through a multi-trap system, illustrated in FIG 3.8. This multi-trap (Mass-Vac, Multi-trap) consists of a three-step process. First, the gases enter the trap where heavier molecules are knocked down and some vapors condensed. Second, the gases pass through a set of five activated charcoal filters where larger particles are removed. In the third stage, finer particles pass through a set of five stainless-steel gauze filters removing finer particles. Finally, the gases exit the multi-trap and enters two-stage dry process pump. As mentioned previously, the process pump uses a nitrogen dilution flow that has been observed to back flow into the reactor with a partial pressure of ~5E-5 Torr. It can be inferred that the exhaust in the multi-trap is slightly diluted by the N_2 dilution flow. This multi-trap is effective for the abatement of pyrophorics and highly flammable liquids or vapors (e.g. trimethylgallium, trimethylaluminum, and bis(ethylcyclopentaienyl)magnesium).

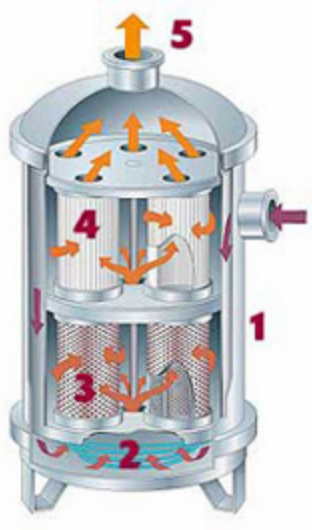

FIG 3.8. Illustration of a possible configuration of the multi-trap filter. In step 1, heavy particles are knocked down and some condensates can be formed. The remaining gas then flows through a cooling coil, step 2, where more condensable are removed and the unabated gas temperature is lowered. In step 3, the remaining gas makes its filtering pass through a set of filters. Finally, in step 4, the gas pass through a series of fine particulate filters before exiting the cylinder. For the systems discussed, the cooling coil was not implemented. Illustration taken from the operations manual.[5] Copyright © 1987, Mass-Vac Inc.

Eventually the multi-trap filters will expire. The filter lifetime depends on system use. A common symptom of expired filters is an increased base pressure and the presence of dust or particulate in one's reactor. Thus, it is important to monitor the reacts base pressure. Alternatively, pressure gauges could be placed on the inlet and outlet of the trap. Reading the pressure drop across the filter would provide insight on when the filters have been spent.

After passing though the multi-trap, the exhaust enters the process pump. At this point, the exhaust is assumed to be free of pyrophorics and flammable vapors. Though the

hydrogen fluoride or gaseous metal fluorides remain active. The two-stage dry pump, schematically shown in FIG 3.9, uses a N_2 dilution flow at 14.2 slm injected at various points in the pumping section. The dilution of the exhaust gases helps to prevent corrosion of the internal components exposed to the exhaust.

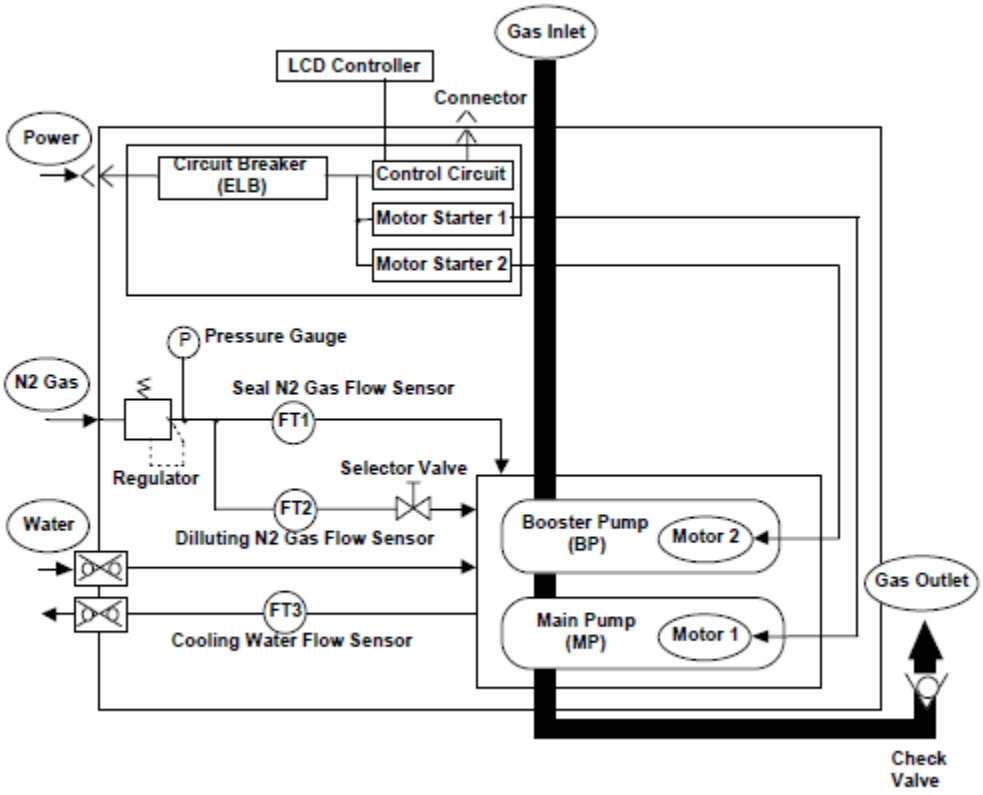

FIG 3.9. Schematic of the Ebara A70W two-stage dry pump. Of note, is the use of a N_2 dilution flow to prolong the longevity of the pump. Image taken from the Ebara A70W operating manual.[6] Copyright © 1995, Ebara Corporation.

Upon exiting the process pump, the diluted exhaust flows into an acid dry bed (CS Clean Systems, Novasafe Dry Bed Abatement System) shown in FIG 3.10. The dry bed system reduces the hazard associated with flammable, toxic, or corrosive gases and vapors. The dry bed consists of about 9.5 L of scrubbing media including two layers of resin chosen

specifically to abate hydrogen fluoride. The 9.5 L of scrubbing media is able to abate ~ 1 L of hydrogen fluoride. The dry bed uses a chemical paper detector that changes colors when exposed to unabated gases. The paper is observable from the outside of the cannister. When the paper is fresh, it is a yellow color but turns either red or green if the acid or caustic is spent, respectively. An additional toxic gas detection system is placed on the dry bed exhaust outlet. After passing through the dry bed, the exhaust goes through the building exhaust.

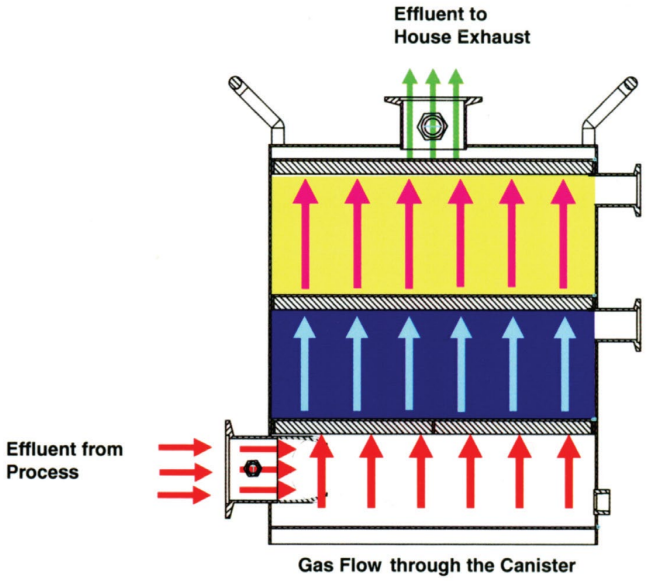

FIG 3.10. Schematic of the CS Clean Systems Acid Dry Bed. Image obtained from the acid dry bed manual.[7] Copyright © 2015, CS Clean Systems Inc.

In addition to the paper indicator, an electrochemical gas analyzer (Bionics, SH-1003-WAD) is used, shown in FIG 3.11. This gas analyzer is specifically configured for hydrogen fluoride and has a lower detection limit of 0.1 ppm. The detector is a suction type gas detector equipped with a membrane pump which draws in the exhaust. A key element is the electrochemical gas sensor. The electrochemical gas sensor operates based on the

principle of membrane electrolysis, which states that when a molecule passes through a membrane attached to an electrode, an electrochemical reaction occurs. If the electrode is in contact with an electrolyte, a redox reaction occurs at a counter electrode, which then produces a current. The current is then directly proportional to the gas concentration. The current is recorded using an onboard microprocessor. The gas analyzer has the ability to communicate through RS-232 through a proprietary software. Additionally, a 4-20 mA output can be connected to an audible/visual alarm.

FIG 3.11. Exploded view of the Bionics electrochemical gas analyzer. Image take from the gas analyzer operations manual.[8] Copyright © 2021, New Cosmos BIE B.V.

Abatement of the precursor gases and vapor is an essential part of the ALP reactors. Without proper abatement, the exhaust would pose numerous hazards to the surrounding areas. With the implementation of the multi-trap, acid dry bed, and toxic gas analyzer there is certainty that unreacted precursors are rendered inert. Of course, when the filters are spent, the entire assemblies will need to opened and refurbished. Fortunately, the disposal and refurbishment of the filters is outlined in the respective manual and is straight forward. Each portion of the exhaust abatement line requires weekly to biweekly checks to ensure proper operation. The electrochemical gas analyzer requires that the electrolyte be checked

periodically as it is subject to evaporation. Additionally, the electrolyte (Bionics, EL-3136) and membrane are recommended to be replaced every six months. After the electrolyte is replaced, the sensor will have to be recalibrated.

3.2.5 Sample Transfer

The ability to transfer samples *in situ* between processing and characterization chambers is a huge benefit for all systems in the Nanoscience Laboratory. *In situ* transfer removes the possibility of atmospheric contaminants allowing for films to be studied under near pristine conditions. Sample transfer to the ALP reactors is accomplished by using twist-lock sample holders, stages, and a magnetically coupled transfer rod, schematically shown in FIG 3.12. The sample stage is mounted on a rotatable flange allowing for easy sample transfer from the transfer line. To move sample in and out of the chamber, a magnetically coupled transfer rod is used. The transfer rod has a cup with three pin slots similar to the sample stage shown in FIG 3.3. Each sample holder has five to six pins that are able rotated to lock into the sample holder and transfer rods. Sample transfer in and out of the ALP reactors is accomplished under high vacuum and has a few requirements. First, the sample heater must be off or have a set point of 0 °C. Secondly, the sample temperature should be below 120 °C. Finally, the reactor and transfer line pressures must be below 5E-7 Torr though lower is ideal.

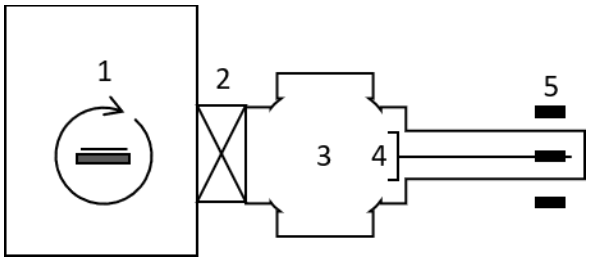

FIG 3.12. Schematic of the sample transfer system for the ALP reactors. (1) is the rotatable sample stage, (2) a gate valve, (3) the ultra-high vacuum transfer line, (4) the sample transfer rod, and (5) the magnetic coupling allowing for linear translation.

3.2.6 Programmatic Control

An ALP reactor requires the execution of multiple tasks in particular sequence at specific timings. Often times, a set of tasks is repeated tens of times depending on the desired thickness grown or material removed. As such, programmatic control of an ALP reactor is desirable. As stated previously, the majority of the equipment is configured for electronic communication using protocols such as RS-232 and EtherNET/IP. The essential functions for ALP are pneumatic valve actuation, throttling valve control, mass flow control, pressure control, and plasma generator. The ALP of this dissertation requires these five functions. For the described ALP reactors and associated equipment, a custom LabVIEW program was written comprised of 11 variable libraries, 8 custom controls, 42 SubVIs, and one top level user interface, shown in FIG 3.13. Each SubVI handles a specific function such as valve actuation, RF generator command, and MFC control among many others.

(a) Fluoride ALP Reactor

(b) Oxide ALP Reactor

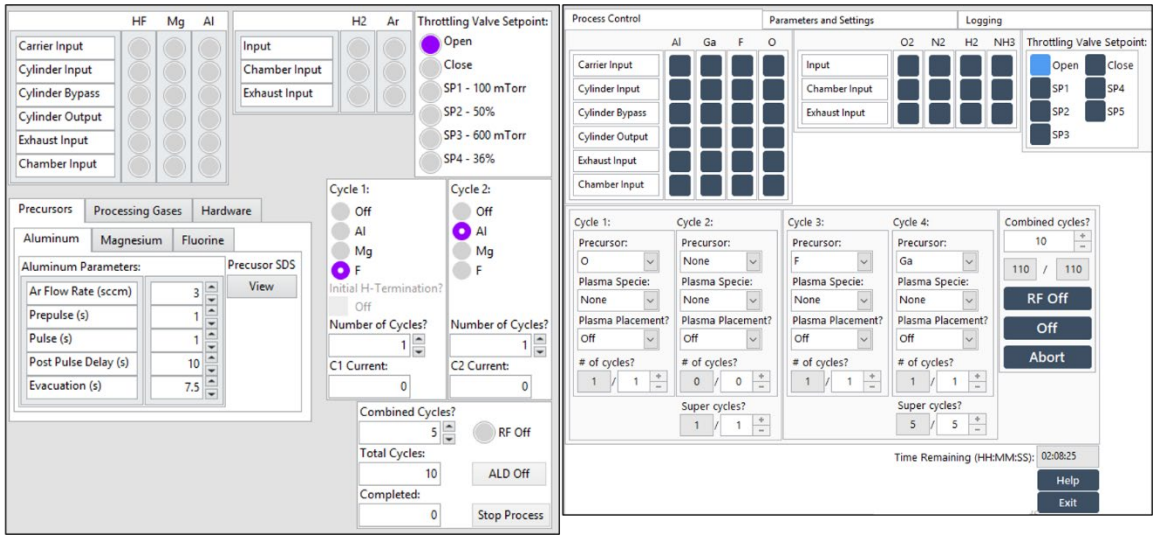

FIG 3.13. Control interfaces for (a) the fluoride ALP reactor and (b) the oxide ALP reactor. The fluoride ALP features an older version of the program.

ALP is based on sequential exposures of reactants separated by inert gas purges. a simple two reactant process would involve four separate steps: reactant 1, purge, reactant 2, purge. This sequence can be viewed as an ABCB…ABCB process were A would be reactant 1, B would be the purge, and C is the reactant 2. The sequence is a for-loop that terminates after a set number of repetitions as shown in FIG 3.14(a). In FIG 3.14(b), the structure indicated by the fluoride ALP, FIG 3.13(a), is shown. The process for the newer oxide ALP program, FIG 3.13(b), is shown in FIG 3.15. The bulk of the programs can be referred to as nested for-loops inside timed event driven case structures.

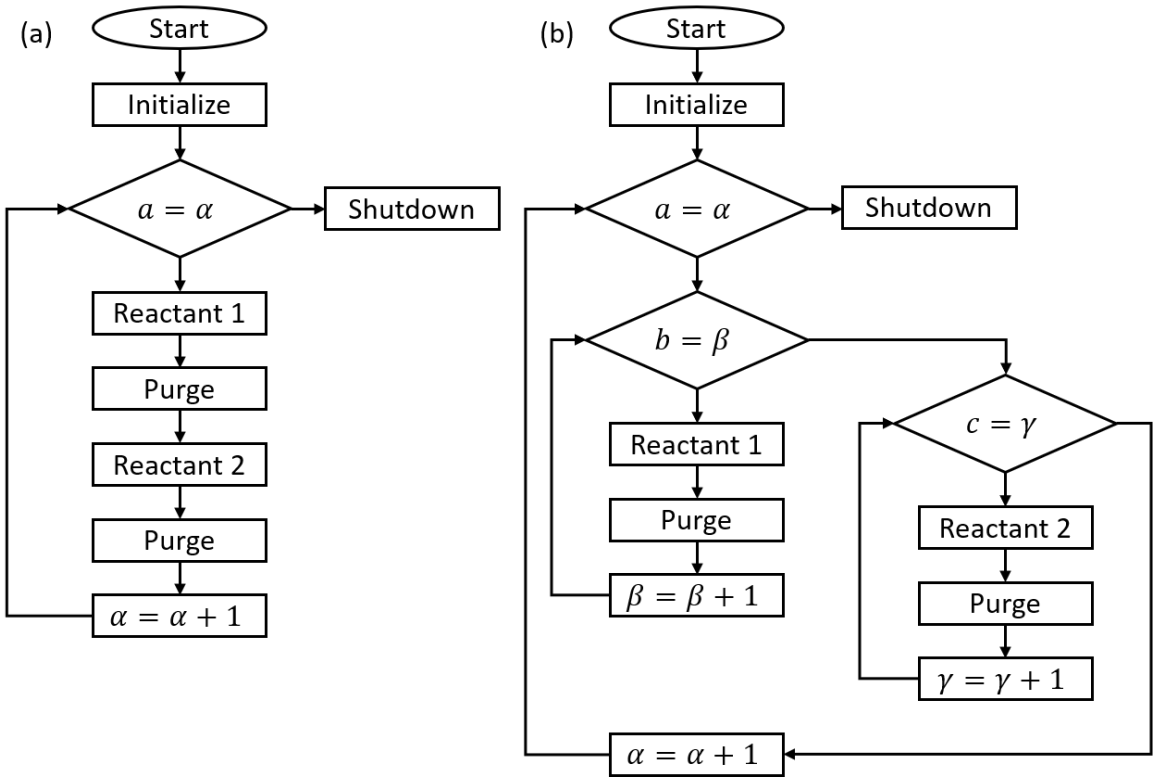

FIG 3.14. Block diagram of (a) a simple ALP structure and (b) of the structure programmed for the Fluoride ALP.

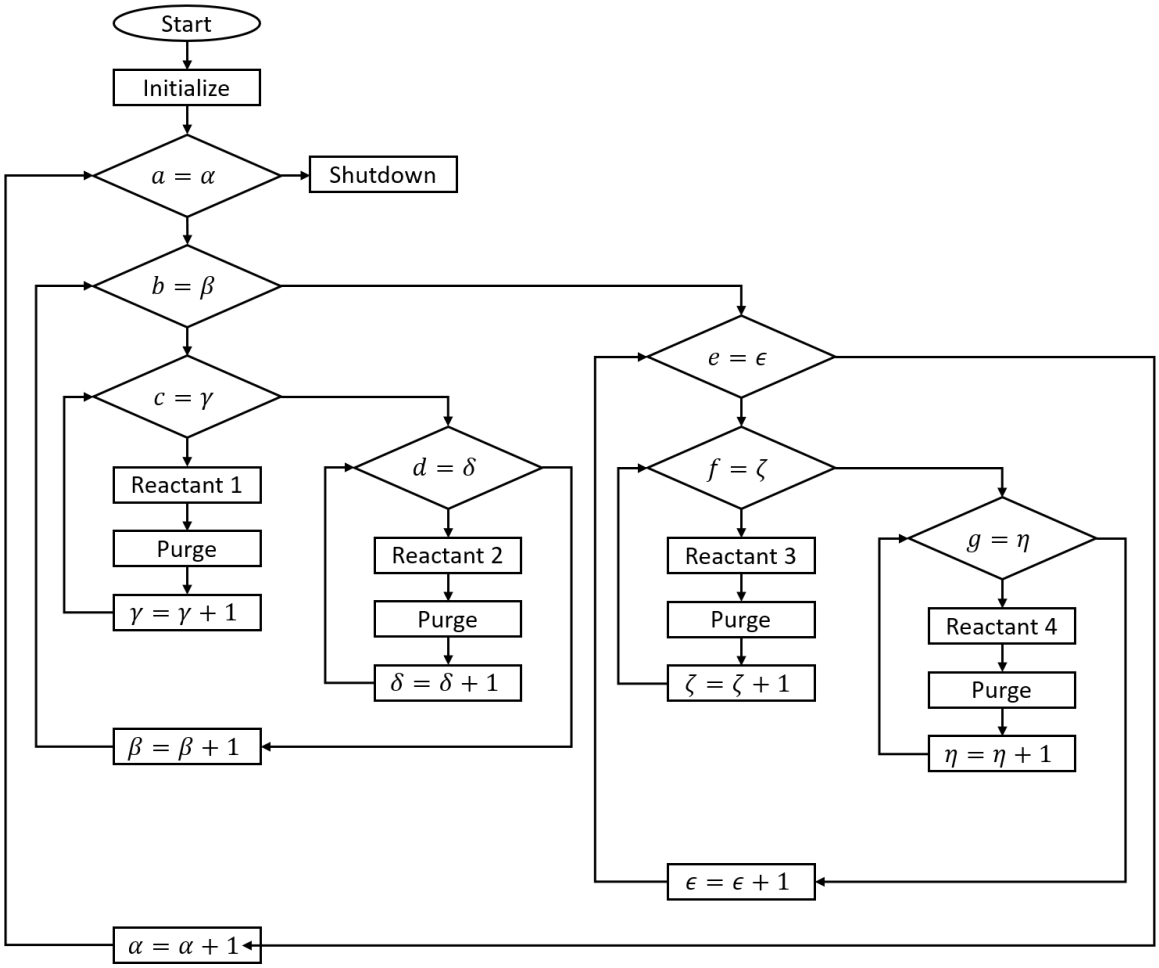

FIG 3.15. Process structure for the oxide ALP program.

The program executes as shown in FIG 3.14(b) and FIG 3.15 for the fluoride and oxide ALP reactors, respectively. The ALP programs have four distinct SubVI: system initialization, precursor step, purge step, and system shutdown. The reactant step can be split into either a precursor vapor step or a remote plasma step. In the next few paragraphs, a brief overview of each SubVI or process step will be given. In general, a process would only be initiated after the sample is at temperature, the reactor pumping has been switched to the process pump, and the RF generator has been turned on.

When a user switches the “off” boolean to “on,” in FIG 3.13, the processes in FIG 3.14 and FIG 3.15 are initiated. Flipping this switch locks the program preventing manual control. The first step is the execution of the system initialization SubVI. This SubVI contains a variety of functions. The first task the SubVI executes as a comparison of the selected process gases and precursors. If a plasma step is selected, two sets of commands are sent to the RF generator: enable remote commands (initialize) and set applied power. The first command allows remote communication with the RF generator while the second set tells the generator what power to apply. If the initialization command is not received, the RF generator will not respond to commands. If the power is not set, current will not be applied during a plasma step. Next, the SubVI looks again at the selected process gases and precursors and prepares the respective gas lines. For each selected precursor and process gas, the respective mass flow control is set to a user defined setpoint. Additionally, a series of pneumatic valves are opened. For process gases, valve 1, FIG 3.2(b), is opened. Whereas for precursors lines, FIG 3.2(a), valves 1, 3, and 5 are opened allowing for the carrier gas to flow directly into the exhaust. Finally, the exhaust throttling valve (ETV) is closed over a span of 7.5 s. At this point, the RF generator and gas lines are primed. Next, a purge step is triggered.

Each purge step starts with a pulse into the exhaust (valve 3, FIG 3.2(b)) to release built up pressure in the gas line. Without this pulse, the reactor pressure would spike to >1 Torr. After 1.5 s has elapsed, the ETV is set to open, valve 2 is opened, and valve 3 is closed. Valve 2 is held open for the duration of the purge. Afterwards, valve 3 is closed the ETV is closed over a span of 7.5 s. The program then checks which type of reactant step to execute.

The first reactant step type is a plasma step. This step starts with the source gas pulsed into the exhaust, for 1.5 s, using valve 3, FIG 3.2(b). Valve 2 opens and valve 3 is closed. A command is then sent to the ETV to go to setpoint 1 which usually corresponds to 100 mTorr. The setpoint pressure can be changed in the settings tab. The reactor pressure is allowed to stabilize to 100 mTorr over a user defined duration, usually 5 s. After this time has elapsed, a command is sent to the RF generator to apply ionize the gas. Assuming the capacitors were previously tuned, ignition occurs immediately. The RF excitation runs according to the user define plasma exposure time before terminating. Valve 2 is then closed, and a purge step is started.

The second reactant type is a precursor vapor exposure. The plumbing for the precursor lines, FIG 3.2(a), is more complicated than that for the process gases, FIG 3.2(b). At this point, valves 1, 3, and 5 have been opened, during the initialization step, flowing the carrier gas into the exhaust. The first step is opening valve 6 to the chamber then closing valve 5. After 1 s has elapsed, valve 4 is quickly open for a user defined duration before closing; this is referred to as the precursor pulse. The precursor vapor and carrier gas flow into the chamber for the duration of the exposure time before opening valve 5 and closing valve 6. A purge step is then started.

The system shutdown step is the next main SubVI. After all the cycles, super cycles, and combined cycles have finished, the program initiates the system shutdown SubVI. This SubVI starts with a purge step while closing all precursor and process gas valves, excluding the purge gas line. After the purge has finished, the purge gas line is closed, and all of the mass flow controllers are closed. The end purge time can extend to longer durations. During processing, a typical purge time is 30 s; however, the end purge time is usually 30

minutes. After the system shutdown SubVI runs, the process is finished, and the program returns to accepting manual input.

The ALP programs allow for easy setup of simple processes. Improvement of the ALP programs could include a more user-friendly interface and translation of the oxide ALP program to the fluoride ALP reactor control computer. Additionally, restructuring the program to a tree-based architecture would allow for more flexible process development and set up.[9]

3.3 Process Monitoring

3.3.1 Pressure

Pressure monitoring is a powerful tool allowing for quick viewing of process pressure or system characteristics. As mentioned previously, each pressure gauge is connected to a controller, which allows for remote communication. To enable pressure monitoring, a custom LabVIEW program was written to record pressure measurements at all times. This program, shown in FIG 3.16, queries the 651C pressure controller or a 946 vacuum system controller depending on the pressure range. Measurements can easily be exported as a text or as comma separated values allowing for external production of plots, as shown in FIG 3.17.

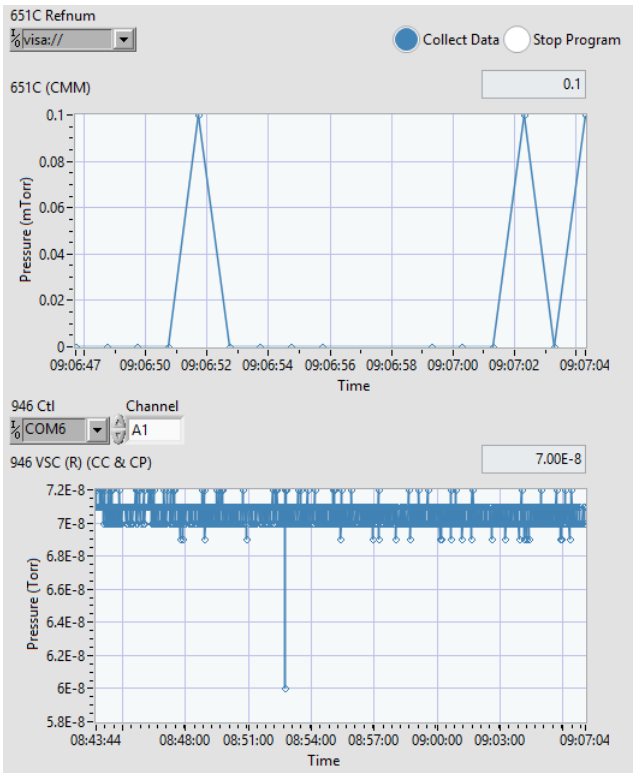

FIG 3.16. Screen shot of the pressure recording program. The top plot using the capacitance manometer (CMM) and communicates directly with the real-time operating system. The bottom plot queries a 946 vacuum system controller to obtain the pressure measured by either the cold cathode or convection enhanced Pirani gauges depending on the selected channel.

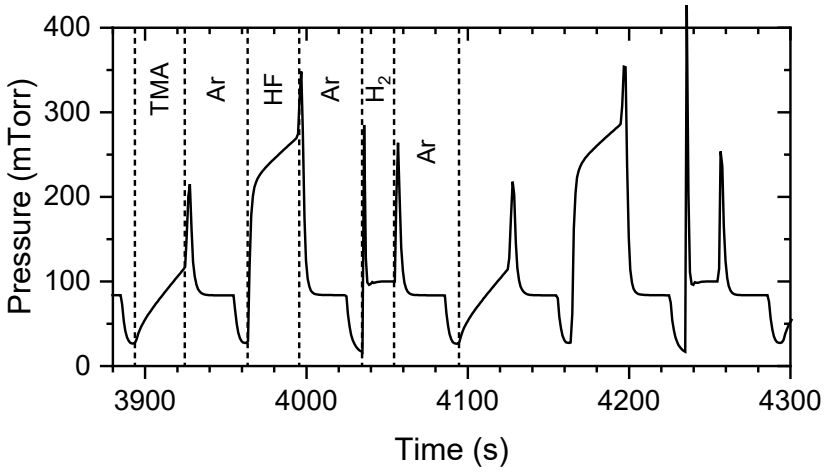

FIG 3.17. Reactor pressure during the plasma enhanced atomic layer deposition of AlF_3. The dashed lines indicate the beginning and ends of reactant and purge steps.

3.3.2 Ellipsometry

A multi-wavelength ellipsometer is mounted to the ALP reactors allowing for in situ growth or etching measurements during processing. This is a powerful tool allowing for quick verification of growth or etching, measurements of film thickness, and determination of growth or etch rates. The ellipsometer (Film Sense, FS-1) has been described in §2.3. The ellipsometer is connected to the control computer via ethernet and is accessible through a web browser. The vendor supplied software is used for calibration, measurements, and initial analysis.

3.3.3 Quadrupole Mass Spectroscopy

The Oxide ALP reactor, FIG 3.1(b), is equipped with a quadrupole mass spectrometer (QMS) (Stanford Research Systems, RGA200). The QMS has a range of 200 amus and can sample partial pressures to 10E-12 Torr in 30 ms. The QMS is configured to

sample ALP gaseous by products by implementation of a precision metering valve and a flexible metal bellow. The QMS used a vendor supplied software in either a standalone executable or a separately compiled LabVIEW program. The standalone program allows for the sampling of 10 charge-to-mass ratios at a time for a given pressure versus time plot while the LabVIEW version has no limit to the number of charge-to-mass ratios.

The initial purpose of the QMS was to enable measurement of gas phase products raising from atomic layer etching. Unfortunately, due to the large surface area of the chamber and presence of various oxides, the reaction byproducts were indistinguishable from the background. Regardless the use of a QMS is a valuable tool for leak checking and monitoring vacuum quality. Future use of the QMS for process monitoring could include using high surface area samples to attempt to increase the concentration of gaseous byproducts. Another alternative would be coating the internal chamber surfaces with a material inert to the ALD and ALE processes.

References

[1] G. Vass, G. Tarczay, G. Magyarfalvi, A. Bödi and L. Szepes, HeI Photoelectron Spectroscopy of Trialkylaluminum and Dialkylaluminum Hydride Compounds and Their Oligomers, Organometallics **21**, 2751-2757 (2002).

[2] NIST Chemistry WebBook Standard Reference Database Number 69, (National Institute of Standards and Technology, 2021);

[3] P. Jong-Chul and K. Bongkoo, Impedance model of helical resonator discharge, IEEE Transactions on Plasma Science **25**, 1398-1405 (1997).

[4] *MWH-5 Automatic Matching Impedance Network*. (MKS, 2005).

[5] *MV Multi-Trap® High Capacity, High Efficiency Vacuum Inlet or Exhaust Trap*. (Mass-Vac, North Billerica, MA, 2021).

[6] *Multi-Stage Dry Vacuum Pump*. (Ebara Corporation).

[7] *Novasafe Dry Bed Abatement System*. (CS Clean Systems, Danbury, CT, 2017).

[8] *Guide to Installation and Operation, Gas Detector SH-1003-WAD, SH-1007-WAD*. (Bionics Instruments, Tokyo, Japan, 2009).

[9] B. D. Piercy and M. D. Losego, Tree-based control software for multilevel sequencing in thin film deposition applications, Journal of Vacuum Science & Technology B **33**, 043201 (2015).

CHAPTER 4

COMPARISON OF ALUMINUM FLUORIDE THIN FILMS GROWN BY THERMAL AND PLASMA ENHANCED ATOMIC LAYER DEPOSITION

Submitted in collaboration with Daniel C. Messina, Brianna S. Eller, Paul A. Scowen, and Robert J. Nemanich to the Journal of Vacuum Science & Technology A.

4.1 Abstract

Films of AlF_3 deposited by thermal and plasma enhanced atomic layer deposition (ALD) have been compared using *in situ* multi-wavelength ellipsometry (MWE) and monochromatic X-ray photoelectron spectroscopy (XPS). The AlF_3 films were grown using cyclic exposures of trimethylaluminum (TMA), hydrogen fluoride (HF), and H radicals from a remote H_2 inductively coupled plasma. Films were characterized *in situ* using MWE and XPS for growth rate, film composition, and impurity incorporation. The MWE showed a growth rate of 1.1 Å per cycle and 0.7 Å per cycle, at 100°C, for thermal and plasma enhanced ALD AlF_3 films, respectively. Carbon incorporation was below the XPS detection limit. The plasma enhanced ALD AlF_3 film showed the presence of Al-Al chemical states, in the Al 2p scans, suggesting the presence of Al-rich clusters with a concentration of 14 %. The Al-rich clusters are thought to originate during the hydrogen plasma step of the PEALD process. The Al-rich clusters were not detected in thermal ALD AlF_3 films using the same precursors and substrate temperature.

4.2 Introduction

Aluminum fluoride (AlF_3) has an ultrawide band gap of >10 eV[1, 2] and thin AlF_3 films can be used in ultraviolet (UV) interference optics, passivation of novel battery surfaces, and gate dielectric layers in electronic devices. The ultrawide band gap and low refractive index, 1.39 at 193nm,[3] that differs from other optical materials, makes it an ideal material for UV reflective and antireflective coatings,[4-6] interference mirrors,[7] and bandpass filters.[8, 9] Films of AlF_3 have been used as acid corrosion resistant coatings for lithium ion batteries,[10] where thin AlF_3 layers (<10nm) on cathode[11] and anode surfaces[12, 13] have demonstrated improved thermal stability,[14] capacity retention,[15] and discharge capacity.[10, 16] Additionally, evaporated AlF_3 films on oxidized Si, showed a fixed negative charge near the interface that provides a drift field in solar cell structures.[1, 17-22] The use of AlF_3 in UV optics, chemical passivation, and electronic applications requires high purity, uniform and conformal, layers with precise thickness control.

Atomic layer deposition (ALD) is a thin film deposition technique stemming from chemical vapor deposition (CVD). Both CVD and ALD employ vapor transport to enable gas solid interactions. Unlike CVD, ALD achieves film growth using sequential exposures of precursors, or reactants, separated by purge or evacuation steps. A key characteristic of ALD is the self-limiting nature of the growth process. Self-limiting growth is achieved for a surface that has a limited number of reactive sites for precursor adsorption, and there is a temperature window where the excess precursor desorbs from the surface. Moreover, the self-limiting surface reactions must occur in both half cycles at the same substrate temperature. Thus, in an ideal ALD reaction, there is a temperature range (or growth window) where growth proceeds in a layer-by-layer mode, and the layer thickness per ALD

cycle is essentially constant. The growth per cycle (GPC) of an ALD process can increase or decrease at temperatures above or below the growth window due to a variety of reasons related to adsorption-desorption kinetics.[23-25] The substrate temperature is typically chosen within the growth window to prevent precursor self-interaction, and decomposition, while also facilitating self-terminating surface reactions. The self-limiting nature of ALD enables precise thickness control along with high purity, uniform, and conformal layers.

Plasma enhanced ALD (PEALD) is an energy-enhanced variant of ALD in which plasma species are used as a reactant. In general, the high reactivity of plasma generated radicals and the kinetic energy of ions can drive surface reactions allowing for lower deposition temperatures.[26, 27] The free radicals can enable surface reactions at temperatures appropriate for the process (e.g. using O instead of H_2O or O_2 for oxide ALD). In this case the free radicals participate in the ligand exchange and the surface reaction. The result is often higher purity and higher density films. The self-limiting reaction conditions must still be met in PEALD, and typically the plasma is only applied for one reactant.

Despite the benefits of PEALD, there are some drawbacks in comparison to thermal ALD (TALD). During PEALD, exposure to some reactive plasma species may lead to undesirable reactions. Occasionally, a plasma may cause oxidation, or nitridation of a substrate at a faster rate than the film deposition. The result is a thick oxidized or nitridized layer underneath the film, which would impact device behavior.[28-31] Additionally, ion bombardment can induce defects by bond breaking or atom displacement. Ion bombardment can be mitigated by use of a remote plasma configuration, as employed in this research, where ion densities are orders of magnitude less than plasma radical

densities.[32] Finally, PEALD processes may show decreased conformality on high aspect ratio structures due to loss of radicals to recombination.[27]

A number of chemical routes have been demonstrated for ALD of metal fluorides However, the selection of precursors is more difficult due to the lack of safe, easy-to-handle, fluoride precursors. Initial fluoride ALD processes used NH_4F or volatile metal halides (TiF_4 and TaF_5).[33-38] In one case, metal fluorides were deposited by oxide chemistry using hexafluoroacetylacetone (hfac), ozone, and various metalorganics.[39] More recently, metal fluorides have been deposited using anhydrous HF (AHF) or HF-pyridine (HF-P) mixtures.[12, 40-45] A comparison of ALD AlF_3 growth processes is shown in Table 1 detailing precursors, growth temperature, growth rate, and film stoichiometry. Selection of precursors for ALD processes is of utmost importance to minimize potential impurities. Precursor selection often requires consideration of the intended application. For example, when ALD AlF_3 is used for UV optics, formation of oxides and nitrides can degrade optical performance, due to adsorption at lower wavelengths. As such, Al precursors containing oxygen or nitrogen should be avoided while organometallics, such as trimethylaluminum (TMA, $Al(CH_3)_3$), may achieve the required purity. Some different reactants used for ALD of AlF_3 are shown in Table 4.1. Unlike the ALD of oxides and nitrides, use of plasma excited species as reactants has not been extensively explored for metal fluorides.

Table 4.1. Reactants used for the ALD of AlF_3 along with the growth temperatures (T_g), growth rate per cycle (GPC), and F/Al ratios (3 is stoichiometric). Trimethylaluminum ($Al(CH_3)_3$, TMA) is the most common metal precursors while tris(dimethylamino)aluminum ($Al(N(CH_3)_2)_3$, TDMAA) and dimethylaluminum hydride ($AlH(CH_3)_2$, DMAH) have also been used. Fluorine precursors include titanium tetrafluoride (TiF_4), tantalum pentafluoride (TaF_5), anhydrous HF (HF, AHF), HF-pyridine ($C_5H_5N{\cdot}(HF)_x$, HF-P), and sulfur hexafluoride (SF_6) plasma. The '*' Indicates use of a remote radiofrequency inductively coupled plasma while '**' indicates films grown at 150 °C.

Reactant			T_g (°C)	GPC (Å)	F/Al Ratio	Ref.
A	B	C				
$AlCl_3$	TiF_4	–	160 – 340	3.2 – 0.2	3.50 – 2.99	[36]
TMA	TaF_5	–	125	1.9	2.53	[46]
TMA	AHF	–	100 – 200	1.2 – 0.5	2.9 – 3.1	[44, 47]
TMA	HF-P	–	75 – 200	1.27 – 0.50	2.85**	[41]
TMA	SF_6*	–	50 – 300	1.50 -0.55	3.1 – 2.9	[48, 49]
TDMAA	AHF	–	150	0.6	–	[47]
DMAH	AHF	–	150	1.0	–	[47]
TMA	HF-P	–	100	1.1	3.1	This
TMA	HF-P	H_2*	100	0.7	2.8	Work

The mechanism for TALD of AlF_3, using trimethylaluminum ($Al(CH_3)_3$, TMA) and HF, was proposed by Lee et al. where the ALD reaction could be split into two half-reactions, Eq. (4.1) and Eq. (4.2), shown below[41]:

$$HF_{(ads)} + Al(CH_3)_{3(g)} \rightarrow AlF(CH_3)_{2(ads)} + CH_{4(g)} \quad (4.1)$$

$$AlF(CH_3)_{2(abs)} + 3HF_{(g)} \rightarrow AlF_{3(s)} + HF_{(ads)} + 2CH_{4(g)} \quad (4.2)$$

In the first half-reaction, $Al(CH_3)_3$ reacts with surface HF, from the previous half-cycle, to produce $AlF(CH_3)_2$ (e.g. DMAF) surface species and methane. Quadrupole mass spectroscopy measurements have indicated that $AlF(CH_3)_2$ are the main species adsorbed during the TMA exposure.[41] During the HF exposure, where Eq. (4.2) applies, the surface is fluorinated producing $AlF_{3(s)}$ and $CH_{4(g)}$ with excess HF adsorbing onto the surface. Quartz crystal microbalance measurements suggested that, at 100°C, one HF molecule adsorbs on the surface for each Al surface site.[41] The adsorption of HF onto AlF_3 surfaces is thought to occur through the formation of a dative bond between the HF and Al surface centers.[41, 50] ALD AlF_3 films grown using this process showed low impurity concentrations with oxygen impurities ~2 atomic %.[41]

This study examines the differences between TALD and PEALD AlF_3 thin films using TMA, HF-P, and atomic H from a remote H_2 inductively coupled plasma (ICP). Exposure to atomic H, implemented after the HF step, is used to investigate whether the process could remove excess adsorbed HF and affect the AlF_3 growth, impurity incorporation, and material properties. Removal of adsorbed HF would enable self-limiting reactions between TMA and the H-terminated AlF_3 surface, rather than with the excess adsorbed HF.

Growth of TALD and PEALD AlF_3 films was performed in the same ALD reactor, which was equipped with an *in situ* multi-wavelength ellipsometry (MWE) that was implemented to monitor growth rates. Through ultra-high vacuum (UHV) sample transfer, surfaces were characterized using *in situ* X-ray photoelectron spectroscopy (XPS), before and after deposition, to determine surface chemical states and defect configurations.

4.3 Experimental

ALD AlF_3 films were grown on Si wafers passivated with a 10 nm TALD layer of Al_2O_3. The Al_2O_3 passivated Si was cleaned, ex-situ, with a UV-ozone exposure prior to insertion into a UHV multi-chamber system. The UHV multi-chamber system includes a load-locked chamber, a UHV transfer line (base pressure 4E-9 Torr), an X-ray photoemission spectroscopy (XPS) system, a fluoride ALD reactor, and various other characterization and deposition chambers.[51-54] The AlF_3 depositions were monitored using *in situ* ellipsometry, and XPS was performed before and after each AlF_3 deposition.

4.3.1 Sample Preparation

The thermal and plasma ALD AlF_3 layers were prepared on Si substrates protected with a thin (~10 nm) Al_2O_3 layer. The Al_2O_3 layer was employed to prevent unintentional etching of SiO_2, and Si after HF adsorption and subsequent H_2-plasma exposure in the plasma ALD AlF_3 process. The protective Al_2O_3 films were grown on 25.4 mm diameter boron-doped Si (100) wafers (Virginia Semiconductor) using a commercial TALD tool (Cambridge, Savannah S100) with TMA and H_2O, as precursors. The substrate temperature was 185 °C and a growth rate of ~1.0 Å per cycle was achieved during the 10 nm deposition

as measured by ellipsometry. Substrates were stored in atmosphere until needed. Prior to the AlF_3 depositions, samples were cleaned using a 10-minute UV-O_3 exposure to remove atmospheric contaminates.

4.3.2 Film Deposition

AlF_3 films were deposited by plasma enhanced and thermal ALD using a fluoride ALD reactor equipped with an *in situ* multiwavelength ellipsometer and remote radio frequency (RF) plasma generation. The ALD reactor utilized two pumping systems for high vacuum sample transfer and the second for processing. The high vacuum pumping (base pressure 2E-9 Torr) was achieved using a turbomolecular pump (Pfeiffer, HiPace 80) backed by a dry roots pump (Pfeiffer, ACP 15). During processing, a larger two-stage dry roots pump (Ebara, A70W) was used (processing base pressure 4E-5 Torr). A multi-filter trap (Mass-Vac, Multi-Trap) between the chamber and processing pump was used to abate unreacted trimethylaluminum. On the A70W outlet, an acid dry bed filter (CS Clean, NovaSafe) was used to neutralize unreacted hydrogen fluoride. Additionally, the A70W utilized a N_2 (99.998 %) dilution flow at a flow rate of 14.2 SLM (standard liters per minute). The N_2 dilution flow was observed to backflow into the ALD reactor with a partial pressure of ~5E-5 Torr.

ALD AlF_3 reactions were performed using trimethylaluminum ($Al(CH_3)_3$, TMA) (STREM, 97 %), hydrogen fluoride-pyridine ($C_5H_5N{\cdot}(HF)_x$, HF-P) (Sigma-Aldrich, 70 % w.t. HF), and H_2 (Matherson Tri-Gas, 99.999%). The TMA and HF-P storage cylinders were held at 30 °C. TMA and HF were dosed into an Ar carrier gas, where the Ar carrier gas was supplied at 5 sccm (standard cubic centimeters per minute) through a mass flow

controller (MKS, GE50A). The TMA delivery tubing and reactor walls were held at 100 °C, to prevent precursor condensation. The HF delivery line was not heated. During the depositions, the substrates were radiatively heated, to 100 °C, using a nichrome heating element and a PID controller (Eurotherm, 2216e).

Reactor pressure was dynamically controlled using an exhaust throttling valve (MKS, 253B), a capacitance manometer (MKS, 627F), and a PID controller (MKS, 651C). Pressure was recorded using a custom LabVIEW program at 1 s intervals. Plasma excitation was achieved using a 13.56 MHz RF generator (MKS, Elite 300), a 50 Ω impedance matching network (MKS, MWH-05), and a 13-turn diameter copper coil wound around a 32 mm fused quartz tube. The quartz tube extended into the ALD reactor to ~10 cm above the sample surface. This configuration allows for generation of a remote RF plasma with high concentrations of thermalized plasma generated radicals.[27, 55]

Depositions followed an ABAB…AB process sequence for TALD, or ABCABC…ABC process sequence for PEALD, where each letter represents a precursor exposure followed by an Ar purge. The overall cycle times were 138.5 s and 192 s for the TALD and PEALD, respectively. Each precursor step involved a 0.25 s pulse followed by a 30 s exposure prior to a 30 s Ar purge. For PEALD, H_2 was pulsed into the reactor and allowed to stabilize over 5 s to 100 mTorr prior to plasma ignition at 100 W for 10 s. Each plasma exposure was followed by a 30 s Ar purge. The total cycle time for TALD and PEALD were 139.5 s and 192 s, respectively. Depositions on Al_2O_3/Si were first performed for 40 cycles of either TALD or PEALD then for an additional 120 cycles. After each deposition, samples were transferred *in situ* for X-ray photoelectron spectroscopy (XPS).

4.3.3 In Situ Characterization

4.3.3.1 Ellipsometry

In situ multi-wavelength ellipsometry (MWE) was used for process monitoring during AlF_3 depositions. The MWE (Film Sense, FS-1) uses four light emitting diodes centered at 465 nm, 525 nm, 580 nm, and 635 nm. The ellipsometer was mounted at a fixed angle of ~45°. The ellipsometer determines the polarization state of the reflected beams by the Division-of-Amplitude-Polarimeter (DOAP) method where all four Stokes parameters are measured simultaneously.[56] Measurements were taken using the manufacturer supplied software (Film Sense, Desktop v1.15) at 1 s intervals. To enable accurate *in situ* measurements during growth, the initial surface (Al_2O_3/Native SiO_2/Si) was modeled using a pseudo substrate model. Use of a pseudo substrate model allows more accurate measurements as alignment and model inaccuracies are negated by averaging over an initial period.[57] As AlF_3 is transparent at the wavelengths, the layer was modeled using a Cauchy model with constants taken from Hennessey *et al*.[44] To account for the Al impurities in the PEALD AlF_3 film, the Bruggeman Effective Medium Approximation (EMA) was applied to estimate the film thickness and impurity concentration.[58, 59] The Al clusters were accounted for using a Drude model with parameters obtained from Palik.[60] Measurements are presented in terms of film thickness. Increases, and decreases, in film thickness are representative of changes of surface species and may not be completely representative of the film thickness. However, changes of surface species may also cause changes in signal that could be interpreted as changes in thickness. While changes during a single cycle may not represent actual thickness changes, considering the value at the

beginning and end of each ALD cycle will present a quantitative analysis of the thickness change during a cycle.

4.3.3.2 X-ray Photoelectron Spectroscopy

X-ray photoelectron spectroscopy (XPS) was employed to gain insight into surface film composition, chemical states, and defect configurations. The XPS instrument (VG Scientia, R3000) uses a monochromatic Al Kα source with a photon energy of 1482.35 eV. Data acquisition was performed using the manufacturer supplied software (VG Scientia, SES Software). The system pressure was below 7E-10 Torr during measurements. All core level scans were acquired with an energy resolution of 0.15 eV. Peak analysis was performed using an XPS software package (Casa Software LTD, CasaXPS). All photoelectron transitions were modeled with Gaussian-Lorentzian line shapes with Shirley backgrounds.[61] Film stoichiometry was determined using a standard method which has an uncertainty of 10 – 20%.[61-63]

4.4 Results

Thermal and plasma enhanced ALD (TALD and PEALD) AlF_3 films were compared on Si wafers passivated with ~10 nm of TALD Al_2O_3. Growth of the ALD AlF_3 was monitored by *in situ* ellipsometry. After deposition of the initial 40 cycles of AlF_3, films were analyzed by X-ray photoelectron spectroscopy (XPS). Determination of impurities, by XPS, allowed for the application of accurate optical models to the *in situ* ellipsometric data enabling calculation of film thickness and impurity concentration.

Finally, an additional 120 cycles for each process were performed to measure oxygen and carbon incorporation and surface stoichiometry.

4.4.1 X-ray Photoelectron Spectroscopy

The initial 10-minute UV-O_3 treated Al_2O_3 surfaces, FIG 4.1(a) and FIG 4.2(a), were found to be atomically clean. The O 1s spectra showed the presence of two peaks with the 1st peak centered at ~532.7 eV, with a FHWM of 1.7 – 1.8 eV, corresponding to Al-O chemical states. The second peak at 533.2 – 534.0 eV, with a FWHM of ~1.7 eV, was attributed to surface hydroxyl groups, denoted as Al-OH. The Al 2p region showed a singular peak at ~76 eV with a FWHM of ~1.5 consistent with Al-O chemical states for TALD Al_2O_3 grown using TMA and H_2O.[64] A full list of fitted peak parameters (peak center and FWHM) are listed in Table 4.1 for each process and step. It was noted that the surface charged during XPS measurements and the values for the Al-O core levels varied between 74.3 – 75.7 eV.[64-66]The energy separation between the Al-O core level, in the Al 2p and O 1s, was 456.6 eV suggesting fully oxidized O-Al-O bonds.[67, 68] Carbon was not detected on the initial surface or after any of the depositions.

After the initial 40 cycles of TALD AlF_3, FIG 4.1(b), the F 1s and Al 2p spectra showed evidence of Al-F core levels. The Al 2p region showed the addition of a high binding energy peak located 2.9 eV from the Al-O core level. This additional peak was identified as the Al-F core level and had a FWHM of 1.6 eV.[69] From the F 1s spectrum, two peaks were observed separated by 2.4 eV. The first peak, at 686.8 eV had a FWHM of 1.6 eV and accounted for 4 % of the total F 1s area. The second peak had a FWHM of 2.0 eV. Both peaks have been reported for crystalline AlF_3 and TALD AlF_3 using similar

precursors.[50, 69] The first and second peaks have been associated with fluorine dangling bonds and Al-F chemical states, respectively.[70]

The final TALD AlF_3 deposition, FIG 4.1(c), showed complete attenuation of the Al-O core levels in both the Al 2p and O 1s scans. In the Al 2p spectra, the Al-F core level had broadened by an additional 0.1 eV. Similar to the previous TALD AlF_3 deposition, the same two core levels were present in the F 1s spectrum though the peak to peak separation had increased by 0.5 eV. Relative to the previous deposition, the 1st peak had shifted to lower binding energies, by 0.7 eV, and only accounted for 3 % of the total F 1s area. The F 1s Al-F core level was noted to have broadened by 0.3 eV to 2.3 eV. Based on the integrated areas of all components of the F 1s and Al 2p core levels, in FIG 4.1(c), an F/Al ratio of 3.1 was obtained.

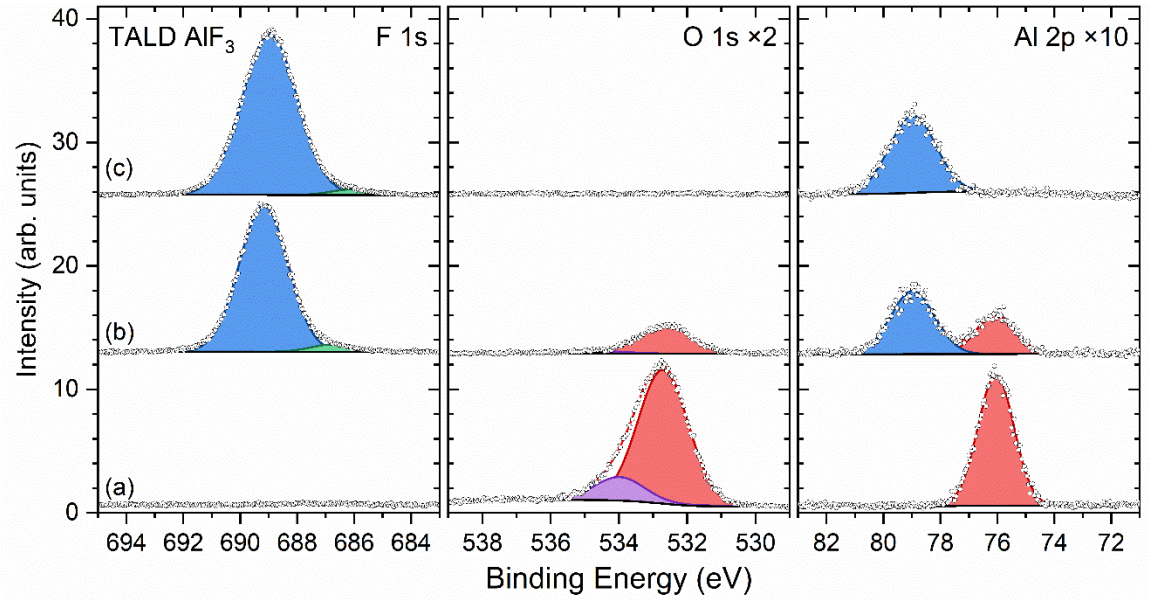

FIG 4.1 XPS spectra of the F 1s, O 1s, C 1s, and Al 2p core levels for TALD AlF_3. (a) shows the core levels of the initial UV-O_3 cleaned surface; (b) is after 40 TALD AlF_3 cycle

and (c) is after an additional 120 cycles. The components of each region are noted in Table 4.2 according to their binding energy.

XPS of the first 40 PEALD AlF_3 cycles, FIG 4.2(b), showed the presence of three peaks in the Al 2p region. The first peak, centered at 72.9 eV, had a FWHM of 1.2 eV and was assigned to an Al-Al chemical state.[63] The Al-Al peak area accounted for ~14 % of the PEALD AlF_3 layer. The 2nd peak, corresponding to Al-O chemical states, was essentially identical to the initial surface. Finally, the 3rd peak, identified as the Al-F chemical states, was located at 78.4 eV with a FWHM of 1.6 eV. Relative to the TALD AlF_3 film, the FWHM was 0.2 eV narrower with an energy separation, from the Al-O core level of 0.5 eV less. The only significant change in the O 1s region was the lack of a 2nd peak indicating removal of the hydroxyl groups. Similar to the TALD film, the PEALD film F 1s spectrum showed two peaks. The 1st peak located at 686.9 eV had a FWHM of 2.1 eV and has previously been attributed to fluorine dangling bonds.[50] The 2nd peak was identified as the Al-F chemical state, located at 688.7 eV, with a FHWM of 1.8 eV. In comparison to the TALD film, the peak-to-peak separation, between the two F 1s core levels was reduced by 0.5 eV. Additionally, the 1st peak comprised 9 % of the total area.

After the final PEALD AlF_3 deposition, FIG 4.2(c), Al-O chemical states were not observed in the O 1s or Al 2p regions. In the Al 2p, the 1st (Al-Al) and 3rd (Al-F) peak positions remained unchanged. The concentration of Al-Al chemical states remained at 14 %. Relative to the TALD film, the PEALD film Al 2p Al-F core level has a FHWM reduced by 0.3 eV. In the F 1s region, the FWHMs of both peaks remained. The energy separation between the 1st and 2nd F 1s peaks increased by 0.3 eV which was still 0.5 eV less than the TALD AlF_3 film. It was noted that the relative area of the 1st peak decreased comprising 6

% of the final PEALD AlF_3 layer which was 2 % more than the TALD film. Based on the total areas in the F 1s and Al 2p, FIG 4.2(c), the PEALD AlF_3 film F/Al ratio was found to be 2.8.

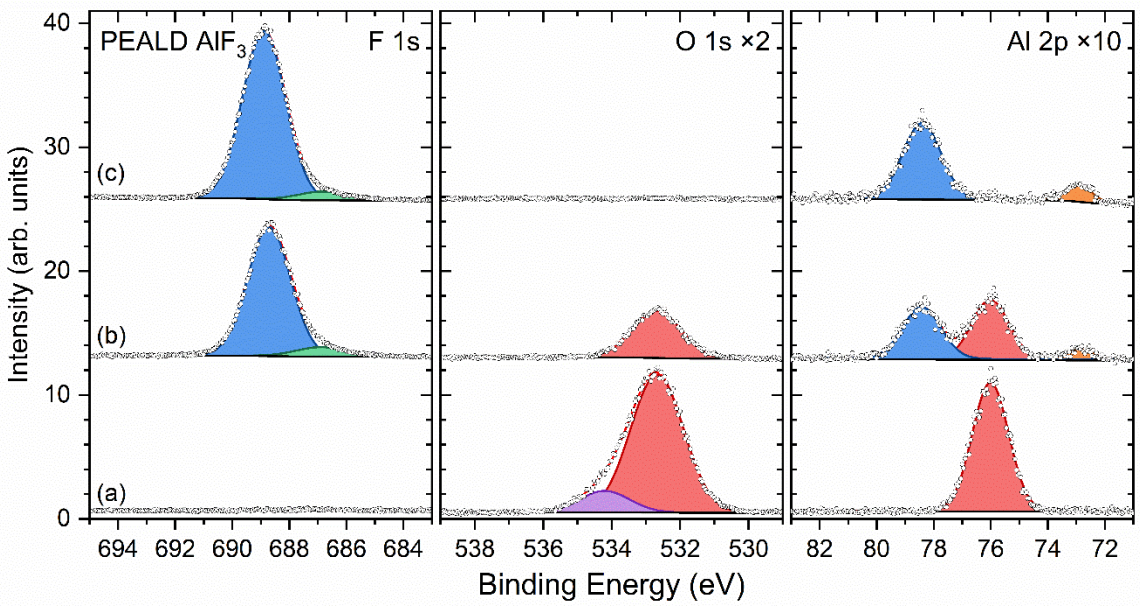

FIG 4.2. XPS spectra of the F 1s, O 1s, C 1s, and Al 2p core levels for PEALD AlF_3. (a) shows the core levels of the initial UV-O_3 cleaned surface; (b) is after 40 PEALD AlF_3 cycle and (c) is after an additional 120 cycles. The components of each region are noted in Table 4.2 according to their binding energy.

Table 4.2. Peak centers and FWHM (brackets) for all peak fitted core levels observed for the TALD and PEALD AlF_3 films on TALD Al_2O_3. Values were obtained using a Shirley background and Gaussian-Lorentzian line shapes. Constraints were not applied during the fit process. In the Al 2p region, a single peak was used for each core level as the 0.4 eV spin-orbit splitting could not be resolved. Peak centers were aligned to the Al_2O_3 substrate core levels. All values are in eV.

AlF_3 Thin Films		F 1s		O 1s		Al 2p		
		1st	2nd	1st	2nd	1st	2nd	3rd
TALD	(a)	-	-	532.7	534.0	-	76.1	-
	UV-O_3 Exposure	-	-	(1.7)	(1.7)	-	(1.5)	-
	(b)	686.8	689.2	532.6	534.6	-	76.1	79.0
	40 cycles	(1.7)	(2.0)	(1.8)	(1.9)	-	(1.6)	(1.8)
	(c)	686.1	689.0	-	-	-	-	79.0
	120 cycles	(1.6)	(2.3)	-	-	-	-	(1.9)
PEALD	(a)	-	-	532.7	534.2	-	76.0	-
	UV-O_3 Exposure	-	-	(1.8)	(1.7)	-	(1.5)	-
	(b)	686.9	688.7	532.7	-	72.9	76.0	78.4
	40 cycles	(2.1)	(1.8)	(1.7)	-	(1.2)	(1.5)	(1.6)
	(c)	686.8	688.9	-	-	72.9	-	78.4
	120 cycles	(2.1)	(1.8)	-	-	(1.0)	-	(1.6)

4.4.2 Ellipsometry

In situ ellipsometry of the TALD AlF_3, shown in FIG 4.3(a), was analyzed using a Cauchy model and a pseudo substrate model, for the AlF_3 layer and the substrate, respectively. The Cauchy parameters were taken from Hennessy et al. where AlF_3 films were grown using similar precursors.[44] FIG 4.3(a) shows the full 40 cycles while FIG 4.3(b) and FIG 4.3(c) show the 20^{th} – 21^{st} cycle with a breakdown of the cycle structure. On the first cycle, the initial exposure to TMA resulted in an apparent increase in thickness. The subsequent HF exposure produced an exceptionally large perceived increase in thickness. The apparent growth rate per cycle (GPC) remaining negative until the 8^{th} cycle. It is unlikely the apparent increase in thickness, from the first cycle, and subsequent decrease are indicative of the actual film thickness. The GPC approached a constant value after the 11^{th} cycle in which a GPC of 1.1 ± 0.1 Å was obtained. After completion of the 40 TALD AlF_3 cycles, a thickness of 3.67 ± 0.04 nm was indicated.

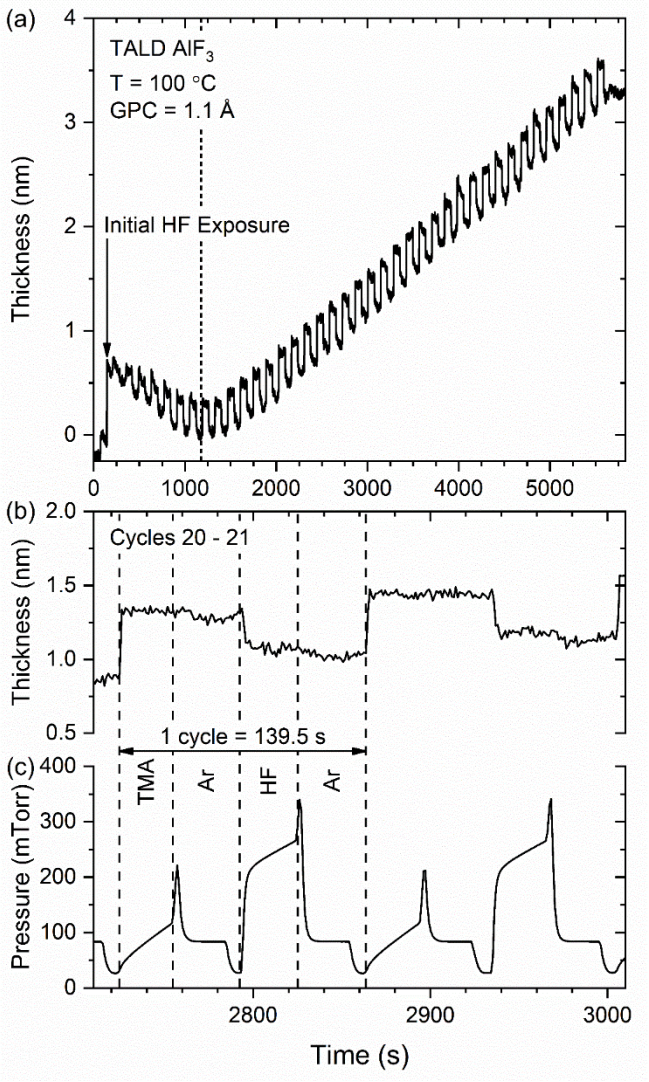

FIG 4.3. Film thickness from *in situ* ellipsometry and process pressure of the TALD AlF_3 growth. (a) shows the film thickness over the full process, 40 cycles, while (b) and (c) show the thickness and process pressure of the 20^{th} - 21^{st} cycles, respectively. The dashed line in (a) indicates the end of the inhibited growth period. In (b) and (c) is an expanded plot of the process indicating the cycle duration and location of precursor and purge steps for the 20^{th} cycle.

Analysis of the PEALD AlF_3 growth ellipsometry, FIG 4.3, was performed identically to the TALD AlF_3 ellipsometry. After the detection of Al-Al impurities by XPS

the optical model was adjusted to use a Drude model and the Bruggeman Effective Medium Approximation (EMA).[59, 60] Using this analysis, it was possible to determine the PEALD AlF_3 film thickness by accounting for the Al-rich clusters. The corrected thickness was 2.76 ± 0.07 nm. In FIG 4.3(a), the ellipsometry over the entire 40 cycle deposition is shown. Of note, the initial HF exposure resulted in a perceived increase in thickness similar to the TALD case, FIG 4.3(a). Upon ignition of the first H_2-plasma, a drastic drop in thickness, -0.75 ± 0.01 nm, was measured. Unlike the TALD case, the PEALD growth did not show a clear nucleation period. The growth rate was 0.7 ± 0.1 Å.

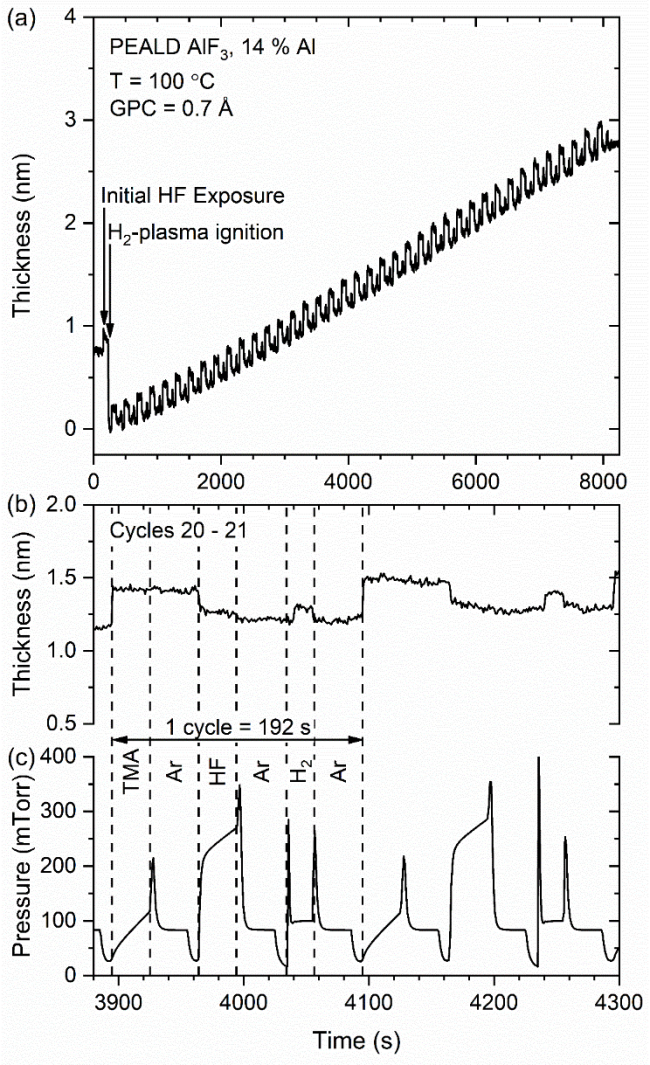

FIG 4.4. Film thickness, from *in situ* ellipsometry, and process pressure of the PEALD AlF_3 growth. The optical model accounts for Al impurities in the AlF_3 layer. (a) shows the corrected film thickness over the full process, 40 cycles, while (b) and (c) show the measured corrected thickness and process pressure of the 20th - 21st cycles, respectively. In (b) and (c) is an expanded plot of the process indicating the cycle duration and the location of precursor, purge, and plasma steps for the 20th cycle.

4.5 Discussion

In situ ellipsometry showed a distinct difference in the initial growth of the ALD AlF_3 films. For TALD, the growth was inhibited for a period lasting 8 cycles; after 11 cycles a constant growth rate was achieved. For PEALD AlF_3, the growth was initiated within the first PEALD cycle. Attempts to minimize the TALD AlF_3 nucleation period were made by starting with an HF exposure or H-terminating the surface with a H_2-plasma exposure. Neither attempt resulted in a decrease in the nucleation period. Additionally, the initial large jump in perceived thickness and the subsequent decrease were also observed. The growth rate of the TALD AlF_3 process was measured to be 1.1 Å, which is close to the 1.4 Å reported using the same precursors and temperature.[40] The PEALD AlF_3 GPC of 0.7 Å was 36 % less than the TALD AlF_3 GPC, at the same temperature. The reduction in growth rate could be related to the appearance of Al clusters in the PEALD film.

XPS analysis of the PEALD AlF_3 film indicated the presence of a third Al 2p chemical state at 72.9 eV. This low binding energy Al 2p state indicates Al-rich cluster impurities inside the PEALD film at ~14 % of the AlF_3 layer. It was observed that decreasing the purge times led to a decrease in Al cluster concentration to 5 % and an increase in growth rate. The observed decrease in Al cluster concentration could originate from residual HF due to the shorter purge times. The XPS also indicated that the Al 2p Al-F core level had a FHWM of 1.9 eV, for TALD, and 1.6 eV, for PEALD. The larger FWHM of the TALD layer could indicate less uniform short-range ordering compared to the PEALD layers.

The energy spacing, between the Al-O and Al-F Al 2p core levels, was 2.9 eV, for TALD, and 2.4 eV, for PEALD. Reported and reference values for the Al-O to Al-F core

level energy spacing is typically ~2 eV.[44, 63, 69] Since these peaks originate from adjoining layers, the differences in Al-F and Al-O energy spacing from reported values may represent a change in the band alignment of AlF_3 on Al_2O_3. The Al impurities in the AlF_3 are expected to act as a p-type dopant, which may contribute to the decrease in energy separation between the Al-O and Al-F core level peak positions.[70]

The cause of the Al clusters, in PEALD AlF_3, is unknown but suspected to be due to the application of an H_2-plasma, as the clusters were not present in TALD AlF_3 films. When TALD AlF_3 films were exposed to long (>30 minutes) H_2-plasmas, small amounts of Al clusters were detected. Variations in plasma power and pressure could also be employed to minimize the formation of Al clusters. Further analysis of the Al clusters formation is required to specifically determine the surface reactions leading to Al-Al cluster formation.

4.6 Summary and Conclusions

In this study, AlF_3 thin films were deposited by both thermal and remote plasma enhanced atomic layer deposition on amorphous Al_2O_3 using TMA, HF-P, and H_2-plasma. Growth was monitored by *in situ* multiwavelength ellipsometry while X-ray photoelectron spectroscopy was used for surface composition and impurity determination. Thermal, and plasma enhanced, ALD AlF_3 films were observed to have growth rates of 1.1 Å per cycle, and 0.7 Å per cycle, respectively, at 100°C. During deposition, it was observed that TALD growth was inhibited for 8 cycles while PEALD AlF_3 growth was immediate. The most significant observation is the presence of Al clusters in the PEALD layer at a concentration of ~14 %. Neither film showed a detectable amount of carbon originating from the

deposition process, indicating carbon contamination was not significant in either process. The comparison of these TALD and PEALD AlF_3 processes shows TALD has significant advantages for optical and electronic applications.

Acknowledgements

This research was supported through the National Aeronautics and Space Administration under Grant No. NNH14ZDA001N-SAT. We acknowledge the use of facilities within the Eyring Materials Center at Arizona State University supported in part by NNCI-ECCS-2025490. We acknowledge Jaime Quintero, from the ASU NanoFab at Arizona State University supported in part by NSF program NNCI-ECCS-1542160, for growing the Al_2O_3 films. Additionally, we thank Franz Koeck and Xingye Wang for their assistance in assembling the fluoride ALD reactor and to thank Kevin Hatch, Zhiyu Huang, and Yichen Yao for their helpful discussions.

Author Contributions

The authors confirm contribution to the paper as follows: study conception and design: D. C. Messina, B. S. Eller, P. A. Scowen, and R. J. Nemanich; data collection: D. C. Messina; Analysis and interpretation of results: D. C. Messina and R. J. Nemanich; draft manuscript preparation: D. C. Messina and R. J. Nemanich. All authors reviewed the results and approved the final version and manuscript.

References

[1] D. König, R. Scholz, D. R. T. Zahn and G. Ebest, Band diagram of the $AlF_3/SiO_2/Si$ system, Journal of Applied Physics **97**, 093707 (2005).

[2] J. L. Navarro, E. A. Albanesi, R. Vidal and J. Ferrón, A study on the structural, electronic and optical properties of the α-AlF_3 compound, Materials Research Bulletin **83**, 615-622 (2016).

[3] C.-C. Lee, M.-C. Liu, M. Kaneko, K. Nakahira and Y. Takano, Characterization of AlF_3 thin films at 193 nm by thermal evaporation, Appl. Opt. **44**, 7333-7338 (2005).

[4] M.-C. Liu, C.-C. Lee, B.-H. Liao, M. Kaneko, K. Nakahira and Y. Takano, Fluoride antireflection coatings deposited at 193 nm, Appl. Opt. **47**, C214-C218 (2008).

[5] T. Yoshida, K. Nishimoto, K. Sekine and K. Etoh, Fluoride antireflection coatings for deep ultraviolet optics deposited by ion-beam sputtering, Appl. Opt. **45**, 1375-1379 (2006).

[6] Z. Huang, D. C. Messina, B. Eller, F. A. Koeck, P. Scowen and R. J. Nemanich, Multilayer ultraviolet reflective coating based on atomic layer deposited aluminum oxide and fluoride Journal of Vacuum Science & Technology A **39**, 042402 (2021).

[7] J. Hennessy, K. Balasubramanian, C. Moore, A. Jewell, S. Nikzad, K. France and M. Quijada, Performance and prospects of far ultraviolet aluminum mirrors protected by atomic layer deposition, Journal of Astronomical Telescopes, Instruments, and Systems **2**, 041206 (2016).

[8] J. Del Hoyo and M. Quijada, *Enhanced aluminum reflecting and solar-blind filter coatings for the far-ultraviolet*. (SPIE, 2017).

[9] A. Egan, B. Fleming, J. Wiley, M. Quijada, J. Del Hoyo, J. Hennessy, B. Hicks, K. France, N. Kruczek and N. Erickson, *The development and characterization of advanced broadband mirror coatings for the far-UV*. (SPIE, 2017).

[10] Y. Wang, J. Qiu, Z. Yu, H. Ming, M. Li, S. Zhang and Y. Yang, AlF_3-modified $LiCoPO_4$ for an advanced cathode towards high energy lithium-ion battery, Ceramics International **44**, 1312-1320 (2018).

[11] G. R. Li, X. Feng, Y. Ding, S. H. Ye and X. P. Gao, AlF_3-coated $Li(Li_{0.17}Ni_{0.25}Mn_{0.58})O_2$ as cathode material for Li-ion batteries, Electrochimica Acta **78**, 308-315 (2012).

[12] J.-P. Jones, J. Hennessy, K. J. Billings, F. C. Krause, J. Pasalic and R. V. Bugga, Communication—Atomic Layer Deposition of Aluminum Fluoride for Lithium Metal Anodes, Journal of The Electrochemical Society **167**, 060502 (2020).

[13] Y. Chung, Y. Shin, Y. Liu, J. S. Park, C. L. Margez and T. A. Greszler, Synergetic effect of carbon and AlF_3 coatings on the lithium titanium oxide anode material for high power lithium-ion batteries, Journal of Electroanalytical Chemistry **837**, 240-245 (2019).

[14] C.-T. Chu, A. Mondal, N. V. Kosova and J.-Y. Lin, Improved high-temperature cyclability of AlF_3 modified spinel $LiNi_{0.5}Mn_{1.5}O_4$ cathode for lithium-ion batteries, Applied Surface Science **530**, 147169 (2020).

[15] Y. K. Sun, S. W. Cho, S. W. Lee, C. S. Yoon and K. Amine, AlF_3-Coating to Improve High Voltage Cycling Performance of $Li[Ni_{1/3}Co_{1/3}Mn_{1/3}]O_2$ Cathode Materials for Lithium Secondary Batteries, Journal of The Electrochemical Society **154**, A168 (2007).

[16] J. Zheng, M. Gu, J. Xiao, B. J. Polzin, P. Yan, X. Chen, C. Wang and J.-G. Zhang, Functioning Mechanism of AlF_3 Coating on the Li- and Mn-Rich Cathode Materials, Chemistry of Materials **26**, 6320-6327 (2014).

[17] D. König and G. Ebest, Novel external field source by localization of electrons for improvement of solar cells, Solar Energy Materials and Solar Cells **75**, 335-343 (2003).

[18] D. König and G. Ebest, The negatively charged insulator-semiconductor structure: concepts, technological considerations and applications, Solid-State Electronics **44**, 111-116 (2000).

[19] D. König, D. R. T. Zahn and G. Ebest, Field effect of fixed negative charges on oxidized silicon induced by AlF_3 layers with fluorine deficiency, Applied Surface Science **234**, 222-227 (2004).

[20] I. Thurzo, T. U. Kampen, D. R. T. Zahn and D. König, Electron capture kinetics at AlF_3/SiO_2 interfaces, Applied Surface Science **212-213**, 753-759 (2003).

[21] D. Konig, D. R. T. Zahn, R. Reich, K. Gottfried and G. Ebest, presented at the 3rd World Conference onPhotovoltaic Energy Conversion, 2003. Proceedings of, 2003 (unpublished).

[22] D. König, G. Ebest, R. Scholz, S. Gemming, I. Thurzo, T. U. Kampen and D. R. T. Zahn, Evidence for high negative charge densities in AlF_3 coatings on oxidized silicon: a promising source for large drift fields, Physica E: Low-dimensional Systems and Nanostructures **14**, 259-262 (2002).

[23] R. L. Puurunen, Surface chemistry of atomic layer deposition: A case study for the trimethylaluminum/water process, Journal of Applied Physics **97**, 121301 (2005).

[24] V. Miikkulainen, M. Leskelä, M. Ritala and R. L. Puurunen, Crystallinity of inorganic films grown by atomic layer deposition: Overview and general trends, Journal of Applied Physics **113**, 021301 (2013).

[25] N. E. Richey, C. de Paula and S. F. Bent, Understanding chemical and physical mechanisms in atomic layer deposition, The Journal of Chemical Physics **152**, 040902 (2020).

[26] H. Kim, Characteristics and applications of plasma enhanced-atomic layer deposition, Thin Solid Films **519**, 6639-6644 (2011).

[27] H. B. Profijt, S. E. Potts, M. C. M. van de Sanden and W. M. M. Kessels, Plasma-Assisted Atomic Layer Deposition: Basics, Opportunities , and Challenges, Journal of Vacuum Science & Technology A **29**, 050801 (2011).

[28] B. H. Kim, W. S. Jeon, S. H. Jung and B. T. Ahn, Interstitial Oxygen Incorporation into Silicon Substrate during Plasma Enhanced Atomic Layer Deposition of Al_2O_3, Electrochemical and Solid-State Letters **8**, G294 (2005).

[29] S.-W. Kim, S.-H. Kwon, S.-J. Jeong and S.-W. Kang, Improvement of Copper Diffusion Barrier Properties of Tantalum Nitride Films by Incorporating Ruthenium Using PEALD, Journal of The Electrochemical Society **155**, H885 (2008).

[30] T. O. Kääriäinen and D. C. Cameron, Plasma-Assisted Atomic Layer Deposition of Al_2O_3 at Room Temperature, Plasma Processes and Polymers **6**, S237-S241 (2009).

[31] A. Foroughi-Abari and K. C. Cadien, *In-Situ* Spectroscopic Ellipsometry Study of Plasma-Enhanced ALD of Al_2O_3 on Chromium Substrates, Journal of The Electrochemical Society **159**, D59-D64 (2011).

[32] H. Kim and I.-K. Oh, Review of plasma-enhanced atomic layer deposition: Technical enabler of nanoscale device fabrication, Japanese Journal of Applied Physics **53**, 03DA01 (2014).

[33] M. Mäntymäki, J. Hämäläinen, E. Puukilainen, F. Munnik, M. Ritala and M. Leskelä, Atomic Layer Deposition of LiF Thin Films from Lithd and TiF_4 Precursors, Chemical Vapor Deposition **19**, 111-116 (2013).

[34] T. Pilvi, E. Puukilainen, U. Kreissig, M. Leskelä and M. Ritala, Atomic Layer Deposition of MgF_2 Thin Films Using TaF_5 as a Novel Fluorine Source, Chemistry of Materials **20**, 5023-5028 (2008).

[35] T. Pilvi, M. Ritala, M. Leskelä, M. Bischoff, U. Kaiser and N. Kaiser, Atomic layer deposition process with TiF_4 as a precursor for depositing metal fluoride thin films, Appl. Opt. **47**, C271-C274 (2008).

[36] M. Mäntymäki, M. J. Heikkilä, E. Puukilainen, K. Mizohata, B. Marchand, J. Räisänen, M. Ritala and M. Leskelä, Atomic Layer Deposition of AlF_3 Thin Films Using Halide Precursors, Chemistry of Materials **27**, 604-611 (2015).

[37] T. Pilvi, K. Arstila, M. Leskelä and M. Ritala, Novel ALD Process for Depositing CaF_2 Thin Films, Chemistry of Materials **19**, 3387-3392 (2007).

[38] T. Pilvi, E. Puukilainen, F. Munnik, M. Leskelä and M. Ritala, ALD of YF_3 Thin Films from TiF_4 and $Y(thd)_3$ Precursors, Chemical Vapor Deposition **15**, 27-32 (2009).

[39] M. Putkonen, A. Szeghalmi, E. Pippel and M. Knez, Atomic layer deposition of metal fluorides through oxide chemistry, Journal of Materials Chemistry **21**, 14461-14465 (2011).

[40] Y. Lee, H. Sun, M. J. Young and S. M. George, Atomic Layer Deposition of Metal Fluorides Using HF–Pyridine as the Fluorine Precursor, Chemistry of Materials **28**, 2022-2032 (2016).

[41] Y. Lee, J. W. DuMont, A. S. Cavanagh and S. M. George, Atomic Layer Deposition of AlF_3 Using Trimethylaluminum and Hydrogen Fluoride, Journal of Physical Chemistry C **119**, 14185-14194 (2015).

[42] M. Ylilammi and T. Ranta-aho, Metal Fluoride Thin Films Prepared by Atomic Layer Deposition, Journal of The Electrochemical Society **141**, 1278-1284 (1994).

[43] J. Hennessy and S. Nikzad, Atomic Layer Deposition of Lithium Fluoride Optical Coatings for the Ultraviolet, Inorganics **6**, 46 (2018).

[44] J. Hennessy, A. D. Jewell, K. Balasubramanian and S. Nikzad, Ultraviolet optical properties of aluminum fluoride thin films deposited by atomic layer deposition, Journal of Vacuum Science & Technology A **34**, 01A120 (2015).

[45] J. Hennessy, A. D. Jewell, F. Greer, M. C. Lee and S. Nikzad, Atomic layer deposition of magnesium fluoride via bis(ethylcyclopentadienyl)magnesium and anhydrous hydrogen fluoride, Journal of Vacuum Science & Technology A **33**, 01A125 (2014).

[46] D. H. K. Jackson, M. R. Laskar, S. Fang, S. Xu, R. G. Ellis, X. Li, M. Dreibelbis, S. E. Babcock, M. K. Mahanthappa, D. Morgan, R. J. Hamers and T. F. Kuech, Optimizing AlF_3 atomic layer deposition using trimethylaluminum and TaF_5: Application to high voltage Li-ion battery cathodes, Journal of Vacuum Science & Technology A **34**, 031503 (2016).

[47] J. Hennessy, A. D. Jewell, J.-P. Jones, G. M. Crouch and S. Nikzad, Aluminum Precursor Interactions with Alkali Compounds in Thermal Atomic Layer Etching and Deposition Processes, ACS Applied Materials & Interfaces **13**, 4723-4730 (2021).

[48] M. F. J. Vos, H. C. M. Knoops, R. A. Synowicki, W. M. M. Kessels and A. J. M. Mackus, Atomic layer deposition of aluminum fluoride using $Al(CH_3)_3$ and SF_6 plasma, Applied Physics Letters **111**, 113105 (2017).

[49] M. F. J. Vos, H. C. M. Knoops, W. M. M. Kessels and A. J. M. Mackus, Reaction Mechanisms during Atomic Layer Deposition of AlF_3 Using $Al(CH_3)_3$ and SF_6 Plasma, The Journal of Physical Chemistry C (2021).

[50] A. Makarowicz, C. L. Bailey, N. Weiher, E. Kemnitz, S. L. M. Schroeder, S. Mukhopadhyay, A. Wander, B. G. Searle and N. M. Harrison, Electronic structure of Lewis acid sites on high surface area aluminium fluorides: a combined XPS and ab initio investigation, Physical Chemistry Chemical Physics **11**, 5664-5673 (2009).

[51] R. J. Carter, T. P. Schneider, J. S. Montgomery and R. J. Nemanich, In Situ Remote H-Plasma Cleaning of Patterned Si - SiO_2 Surfaces, Journal of The Electrochemical Society **141**, 3136-3140 (1994).

[52] J. S. Montgomery, T. P. Schneider, R. J. Carter, J. P. Barnak, Y. L. Chen, J. R. Hauser and R. J. Nemanich, Morphology of Si(100) surfaces exposed to a remote H plasma, Applied Physics Letters **67**, 2194-2196 (1995).

[53] S. W. King, R. F. Davis, R. J. Carter, T. P. Schneider and R. J. Nemanich, Hydrogen desorption kinetics for aqueous hydrogen fluoride and remote hydrogen plasma processed silicon (001) surfaces, Journal of Vacuum Science & Technology A **33**, 05E115 (2015).

[54] Y. Yang, T. Sun, J. Shammas, M. Kaur, M. Hao and R. J. Nemanich, Electron affinity of cubic boron nitride terminated with vanadium oxide, Journal of Applied Physics **118**, 165310 (2015).

[55] H. C. M. Knoops, T. Faraz, K. Arts and W. M. M. Kessels, Status and prospects of plasma-assisted atomic layer deposition, Journal of Vacuum Science & Technology A **37**, 030902 (2019).

[56] R. M. A. Azzam, Division-of-amplitude Photopolarimeter (DOAP) for the Simultaneous Measurement of All Four Stokes Parameters of Light, Optica Acta: International Journal of Optics **29**, 685-689 (1982).

[57] *FS-1 Manual v1.50*. (Film Sense, LLC, Lincoln, NE, 2017).

[58] J. N. Hilfiker, J. Sun and N. Hong, in *Spectroscopic Ellipsometry for Photovoltaics: Volume 1: Fundamental Principles and Solar Cell Characterization*, edited by H. Fujiwara and R. W. Collins (Springer International Publishing, Cham, 2018), pp. 59-88.

[59] D. A. G. Bruggeman, Berechnung verschiedener physikalischer Konstanten von heterogenen Substanzen. I. Dielektrizitätskonstanten und Leitfähigkeiten der Mischkörper aus isotropen Substanzen, Annalen der Physik **416**, 636-664 (1935).

[60] E. D. Palik, in *Handbook of Optical Constants of Solids* (Elsevier).

[61] F. A. Stevie and C. L. Donley, Introduction to x-ray photoelectron spectroscopy, Journal of Vacuum Science & Technology A **38**, 063204 (2020).

[62] J. H. Scofield, Hartree-Slater subshell photoionization cross-sections at 1254 and 1487 eV, Journal of Electron Spectroscopy and Related Phenomena **8**, 129-137 (1976).

[63] J. F. Moulder, W. F. Stickle, P. E. Sobol and K. D. Bomben, (Perkin-Elmer Corporation, Eden Prairie, Minnesota, USA 1979), pp. 25-26.

[64] J. Frascaroli, E. Cianci, S. Spiga, G. Seguini and M. Perego, Ozone-Based Sequential Infiltration Synthesis of Al_2O_3 Nanostructures in Symmetric Block Copolymer, ACS Applied Materials & Interfaces **8**, 33933-33942 (2016).

[65] A. Pirkle, S. McDonnell, B. Lee, J. Kim, L. Colombo and R. M. Wallace, The effect of graphite surface condition on the composition of Al_2O_3 by atomic layer deposition, Applied Physics Letters **97**, 082901 (2010).

[66] L. Cheng, X. Qin, A. T. Lucero, A. Azcatl, J. Huang, R. M. Wallace, K. Cho and J. Kim, Atomic Layer Deposition of a High-k Dielectric on MoS_2 Using Trimethylaluminum and Ozone, ACS Applied Materials & Interfaces **6**, 11834-11838 (2014).

[67] W. M. Mullins and B. L. Averbach, Bias-reference X-Ray photoelectron spectroscopy of sapphire and yttrium aluminum garnet crystals, Surface Science **206**, 29-40 (1988).

[68] B. Lee, S.-Y. Park, H.-C. Kim, K. Cho, E. M. Vogel, M. J. Kim, R. M. Wallace and J. Kim, Conformal Al_2O_3 dielectric layer deposited by atomic layer deposition for graphene-based nanoelectronics, Applied Physics Letters **92**, 203102 (2008).

[69] J. Hennessy, A. D. Jewell, K. Balasubramanian and S. Nikzad, Ultraviolet optical properties of aluminum fluoride thin films deposited by atomic layer deposition, Journal of Vacuum Science & Technology A **34** (2016).

[70] R. König, G. Scholz, K. Scheurell, D. Heidemann, I. Buchem, W. E. S. Unger and E. Kemnitz, Spectroscopic characterization of crystalline AlF3 phases, Journal of Fluorine Chemistry **131**, 91-97 (2010).

[71] N. W. Ashcroft and N. D. Mermin, in *Solid State Physics* (2021).

CHAPTER 5

ATOMIC LAYER ETCHING OF GALLIUM NITRIDE ENABLED BY WATER VAPOR AND O_2 – PLASMA OXIDATION

In collaboration with D. C. Messina, K. A. Hatch, S. Vishwakarma, D. Smith, Y. Zhao, and R. J. Nemanich in preparation for submission to the Journal of Vacuum Science and Technology A.

5.1 Abstract

Different atomic layer etching (ALE) methods are implemented for crystalline GaN based on oxidation, fluorination, and ligand exchange. For the first step, the GaN surfaces were oxidized using either water vapor or remote O_2-plasma exposures to produce a thin oxide layer. Removal of the surface oxide was addressed using alternating exposures of hydrogen fluoride (HF) and trimethylgallium (TMG) via fluorination and ligand exchange, respectively. A number of HF and TMG super cycles were implemented to remove the surface oxide. Each ALE process was monitored *in situ* using multiwavelength ellipsometry. X-ray photoelectron spectroscopy was employed for characterization of surface composition and impurity states. Additionally, the thermal and plasma enhanced ALE (TALE and PEALE) methods were performed on patterned wafers allowing the use of transmission electron microscopy (TEM). XPS indicated F and O impurities remained on etched surfaces for both ALE processes. Ellipsometry indicated a slight reduction in thickness. TEM indicated an etching rate that was much less than predicted.

5.2 Introduction

Gallium nitride (GaN) is an emerging semiconducting material with applications for power electronics owing to its wide band gap (~3.4 eV), high critical electric field (>3 MV/cm), electron mobility (~2000 $cm^2 V^{-1} s^{-1}$), and dielectric constant (~9).[1-3] These properties make GaN attractive for power conversion and fast switches potentially with smaller volumes in comparison to their silicon or silicon carbide counter parts.[4-7] As patterning is essential for device fabrication, GaN devices are typically produced using dry plasma etch processes.[8, 9] The inert nature of GaN makes wet chemical etching, either with acids or bases, ineffective.[10] In plasma dry etching of GaN, halogen based plasmas are most common due to the formation of volatile gallium halides.[8, 9, 11] However, the use of a plasma can induce various defects, which can degrade device performance by increasing leakage current or lowering breakdown voltage.[12, 13] Recently, multi-step etch processes and post etch treatments have been developed to mitigate plasma induced damage.[14, 15] Atomic layer etching (ALE) is one such method.

Atomic layer etching (ALE) is a self-limiting or pseudo self-limiting thin film removal technique with sub-nanometer precision.[16, 17] ALE achieves self-limiting material removal using sequential exposures of precursors, or reactants, separated by inert gas purges. A model ALE process would consist of a surface modification step and a removal step separated by purging steps. Self-limiting etching is achieved as there is a limited number of reactive surface sites for precursor adsorption. The self-limiting aspect does not have to occur during the second reactant exposures. Instead, the second reactant must be inert towards the unmodified surface. A thermal ALE process can be classified in a variety of ways based on the precursor used; the number of steps required or the reaction

mechanisms. To date, a number of different mechanisms have been identified for thermal ALE.[18] These mechanisms commonly revolve around surface conversion, oxidation, fluorination, and ligand exchange.

In ALE there is not a well-defined temperature window in which the etch rate is constant. The etch window, or process window, is chosen to optimize the reaction rates of each step as well as the byproduct desorption rate. Outside of this process window, etching may not occur and is same cases deposition may occur. Within the process window, the etch per cycle (EPC) can vary depending on the temperature dependence of the reaction and desorption rates of each precursor. The etch rates can be less than or greater than one atomic layer per cycle but are typically less than 1 nm.

Previously developed ALE processes for GaN have used thermal and plasma enhanced methods. Plasma enhanced ALE (PEALE) methods focus on the use of halide-containing plasmas (e.g. F, Cl, Br) to produce $GaCl_3$ which is then removed by bombardment.[14, 19-22] In some instances PEALE methods use alternating exposures of O_2 and BCl_3 plasma to produce a self-limiting etch.[23] A reported thermal ALE (TALE) process for GaN implements alternating exposures of XeF_2 and BCl_3 to enable self-limiting material removal.[14] XeF_2 has been known to fluorinate GaN with the proposed surface reaction $GaN_{(s)} + 3XeF_{2(g)} \rightarrow GaF_{(s)} + NF_{3(g)} + 3Xe_{(g)}$.[14, 24] Bermudez noted that XeF_2 exposures do not form stoichiometric GaF_3 but rather a "GaF_3-like" species as if GaF_x islands had formed.[24, 25] For the TALE GaN process, Johnson *et al* proposed that the GaF_x layer was removed via ligand exchange with the surface reactions $GaF_{3(s)} + BCl_{3(g)} \rightarrow GaCl_{3(g)} + NF_{3(g)} + BF_{3(g)}$ or $GaF_{3(s)} + BCl_{3(g)} \rightarrow GaCl_{3(g)} + NF_{3(g)} + 3BFCl_{2(g)}$.[14]

The resulting TALE etch rate was found to be 0.72 Å per cycle at a substrate temperature of 300 °C.

An alternative to direct halogenation of GaN is oxidation. The surface oxide could be removed using halogenation and ligand exchange which has been demonstrated for Al_2O_3 and Ga_2O_3.[26, 27] Oxidation of GaN has been studied extensively using thermal, plasma, photoelectochemical (PEC), excimer laser induced, and saturated water vapor oxidation to create oxide layers.[28] Typically, GaN oxidation studies have used temperatures exceeding 500 °C and long exposure times to produce thick oxide layers typically tens or hundreds of nanometers thick. High temperature annealing of GaN induces the desorption of nitrogen leading to nitrogen vacancies and enhanced oxide growth rates.[28, 29]

Low temperature oxidation (<500 °C) of GaN has been accomplished using remote O_2-plasma. In a remote plasma, there is a high concentration of free radicals which can enabled surface reactions.[30] Bae and Lucovsky found that when GaN was exposed to a remote O_2/He-plasma, the surface oxide thickness was dependent on the substrate temperature and the plasma exposure time.[31] The oxide thickness showed a power law dependence with the plasma exposure time. Moreover, Yamanoto *et al* showed a Ar/O_2 plasma exposure produced similar results where an oxide thickness of 3.5 nm was achieved.[32, 33] Regardless of the use of He or Ar, the surface oxide compositions were found to be near stoichiometric with ~6 at. % N incorporated.[31, 32] In both cases, remote plasma oxidation did not show morphological changes. Remote plasma oxidation thus provides a plasma enhanced method that could enable GaN ALE.

A thermal route to oxidizing GaN is through a water vapor exposure. Previous reports have indicated that monoclinic Ga_2O_3 could be grown on GaN (0001) using water vapor at high temperatures (700 – 900 °C).[34, 35] Recent reports indicate that water absorption onto a GaN (0001) surface by association and dissociation creates ~ 1 ML, or ~ 0.5 nm, of oxide.[36, 37] Recently, these results were confirmed using X-ray photoelectron spectroscopy.[38] The chemisorption of water vapor to form a thin surface oxide provides a purely thermal route to GaN ALE.

Recently, methods of Ga_2O_3 ALE have been developed revolving around fluorination and ligand exchange. Lee *et al* showed that Ga_2O_3 can be fluorinated using HF to produce a GaF_3 layer.[26] It was shown that the GaF_3 can be removed via ligand exchange using a variety of precursors including BCl_3, $AlCl(CH_3)_2$, $Al(CH_3)_3$, $TiCl_4$, and $Ga(N(CH_2)_3$.[26] Recently, Hatch *et al* showed that trimethylgallium (TMG) could also be used to remove the surface GaF_3.[27] It was found that when etching amorphous Ga_2O_3 using sequential exposures of HF and TMG. Use of TMG is preferable for etching GaN as most etch process leave behind residual metals. The implementation of a Ga_2O_3 ALE process enables the etching of GaN assuming an the GaN surface can be converted to an oxide.

In this work, two multi-step processes were implemented for the ALE of GaN (0001), schematically shown in FIG 5.1. The two processes differed by the oxidation method and the number of Ga_2O_3 etch cycles required to remove the converted oxide. The oxidation methods employed were a remote O_2-plasma exposure or a water vapor exposure to create a thin surface oxide layer. The removal of the surface oxide proceeded using the aforementioned Ga_2O_3 ALE process. The GaN ALE processes were monitored using *in*

situ ellipsometry and then studied by X-ray photoelectron spectroscopy (XPS). XPS allowed for determination of impurity states and surface composition. The GaN ALE processes were then repeated on a set of patterned surfaces suitable for transmission electron microscopy allowing directed observation of the surface condition after the ALE processes.

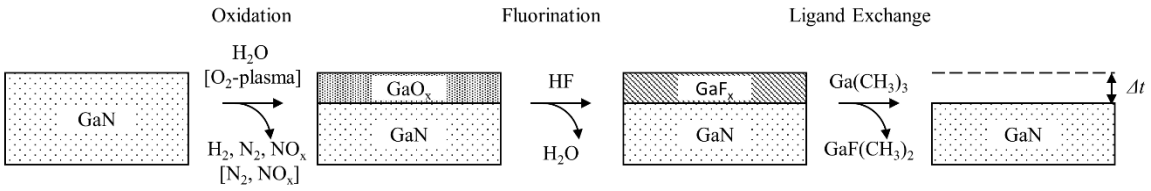

FIG 5.1. A schematic illustration of the GaN ALE processes. The GaN was oxidized either using a water vapor or remote O_2-plasma exposure to create a thin surface oxide. The surface oxide was removed using a Ga_2O_3 ALE process.

5.3 Experimental

Atomic layer etching (ALE) of GaN (0001) surfaces were performed on unintentionally doped (UID) GaN on sapphire. The GaN surfaces were cleaned *ex-situ* prior to insertion into an ultra-high vacuum (UHV) multi-chamber system. The UHV multi-chamber system includes a load-locked chamber, a transfer line, a fluoride ALE reactor, an X-ray photoelectron spectroscopy (XPS) system, and various other growth and characterization chambers.[39, 40] XPS was performed before and after etching of the unpatterned GaN wafer. The etched experiments were then repeated on GaN with Au/Ti patterning for transmission electron microscopy (TEM) measurements.

5.3.1 Sample Preparation

The thermal ALE (TALE) and plasma enhanced ALE (PEALE) processes were performed on 15 mm × 15 mm UID single-side polished GaN (0001) substrates (Kyma Technologies, GT.U.100.0050.B). Each sample consisted of 5.0 ± 0.5 μm UID GaN / ~170 nm AlN / Sapphire (0001). GaN surfaces were cleaned ex situ using a 10-minute UV O_3 exposure followed by a 10-minute HCl dip. Transmission electron microscopy samples were patterned with Ti/Au via photolithography.

5.3.2 Equipment

GaN surfaces were etched in a custom-built ALE reactor capable of generating remote radio frequency (RF) inductively coupled plasma (ICP). The ALE reactor utilized two pumping systems for high vacuum sample transfer and the second for processing. The high vacuum pumping (base pressure 2E-8 Torr) was achieved using a turbomolecular pump (Pfieffer, HiPace 80) backed by a dry roots pump (Pfieffer, ACP 15). During etching, a larger two-stage dry roots pump (Ebara, A70W) was used (base processing pressure 4E-5 Torr). A multi-filter trap (Mass-Vac, Multi-Trap) was placed on the A70W inlet to abate unreacted trimethylgallium. On the A70W outlet, an acid dry bed (CS Clean, NovaSafe) was implemented to neutralize unreacted hydrogen fluoride. To ensure longevity of the process pump, a N_2 (99.998%) dilution flow was used with a flow rate of 14.2 slm (standard liters per minute). The N_2 dilution flow was observed to back flow into the ALE reactor with a partial pressure of ~5E-5 Torr.

The GaN (0001) surfaces were oxidized using either water vapor (Sigma-Aldrich, HPLC grade) or a remote O_2-plasma from O_2 gas (Air Liquide, 99.9999%). Gallium oxide

ALE reactions were performed using trimethylgallium ($Ga(CH_3)_3$, TMG) (STREM, 97%) and hydrogen fluoride-pyridine ($(C_5H_5N)\cdot(HF)_x$, HF-P) (Alfa-Asear, 70 % w.t. HF). The HF-P was transferred into a stainless-steel cylinder under an inert N_2 (Matheson Tri-gas, 99.99%) atmosphere using a glove box. During HF-P transfer, the glove box had a dew point of >-40 °C corresponding to a O_2 concentration <128 ppm. Due to the high vapor pressure of TMG, a 100 μm orifice was used to limit the amount of vapor delivered to the reactor. Precursors were dosed into an Ar carrier gas (Matheson Tri-gas, 99.9999%). N_2 gas (Matheson Tri-gas, 99.9999%) was used as the purge gas. The Ar carrier gas was supplied at 5 sccm (standard centimeters per minute) for TMG while 15 sccm was used for H_2O and HF. Ar flow rates were chosen to prevent precursors from back flowing. O_2 and N_2 gas was supplied at 35 and 30 sccm, respectively. Flow rates were controlled using mass flow controllers (MKS, GE50A). Additionally, precursor delivery tubing and reactor walls were heated to 100 °C, to prevent precursor condensation. Substrates were radiatively heated, to 300 °C, using a nichrome heating element, C-type thermocouple, and a PID controller (Eurotherm, 2216e).

Reactor pressure was dynamically controlled using an exhaust throttling valve (MKS, 253B), a capacitance manometer (MKS, 627F), and a PID controller (MKS, 651C). Pressure was recorded using a custom LabVIEW program at 1 s intervals. Plasma excitations were achieved using a 13.56 MHz RF generator (MKS, Elite 300), a 50 Ω impedance matching network (MKS, MWH-05), and a 13-turn copper coil wound around a 32 mm diameter fused quartz tube. The quartz tube extended into the ALE reactor to ~25 cm above the sample surface. This configuration allows for generation of a remote RF plasma with high concentrations of thermalized plasma generated radicals.[30, 41]

Etch processes were structures in a $A^n(BC)^m$ format where A, B, and C denote a reactant steps while *m* and *n* denote the number of repetitions. Each reactant step including an inert gas purge. For the TALE process, each water vapor exposure was followed by five alternating HF and TMG step; the process structure was $A^1(BC)^5$. In the PEALE case, each O_2-plasma exposure required ten HF and TMG steps or $A^1(BC)^{10}$. TMG, HF, and H_2O were pulsed for 0.1 s, into an Ar carrier gas, followed by a 30 s exposure and 30 s N_2 purge. In a remote O_2-plasma step, O_2 was pulsed into the chamber where the pressure stabilized to 100 mTorr over 5 s. The plasma was ignited at 100 W for 10 s after which the chamber was purged with N_2 for 30 s. In previous experiments, the resulting surface oxide thickness was measured to be ~ 1.0 nm. The duration of each super cycle, in TALE and PEALE, was ~13 minutes and ~25 minutes, respectively.

X-ray photoelectron spectroscopy (XPS) was employed to gain insight into surface film composition and and defect configurations. The XPS instrument (VG Scientia, R3000) uses a monochromatic Al K_α source with a photon energy of 1486.7 eV. Data acquisition was performed using the manufacturer supplied software (VG Scientia, SES Software). The system pressure was below 7E-10 Torr during measurements. Survey and high-resolution narrow scans were taken. Scans had an energy resolutions 0.15 eV and a step size of 0.05 eV. Peak analysis was performed using an XPS software package (Casa Software LTD, CasaXPS). XPS intensities were normalized using the corresponding photoionization cross-sections.[42] Surface composition was determined using a standard method which has an accuracy between 10 – 20 %.[42-44]

In situ multi-wavelength ellipsometry (MWE) was used for process monitoring during processing. The MWE (Film Sense, FS-1) uses four light emitting diodes (LED)

centered at 465 nm, 525 nm, 580 nm, and 635 nm. The ellipsometer was mounted at a fixed angle of ~45°. The ellipsometer determines the polarization state of the reflected beams by the Division-of-Amplitude-Polarimeter (DOAP) method where all four Stokes parameters are measured simultaneously.[45] Measurements were taken using the manufacturer supplied software (Film Sense, Desktop v1.15) at 1s intervals. Ellipsometry is presented in terms of the ellipsometric parameter Δ for the blue LED as Δ is the most surface sensitive.[46, 47] Changes in Δ may not be completely representative of the film thickness. However, changes of surface species or plasma ignition may also cause changes in the signal interpreted as changes in Δ. For a heterogeneous structure, increases in Δ are associated with decreases in film thickness. Conversely, decreases in Δ represent an increase in film thickness. Due to the thickness of the GaN samples, the ellipsometer cannot resolve the sapphire substrate.

Samples suitable for cross-sectional observation by transmission electron microscopy (TEM) were prepared by focused ion beam (FIB) (Thermo Fisher Scientific, Helios 5 UX dual beam system) initially operated at 30 kV, with further thinning at 5 kV, and a final cleaning at 2 kV. High-resolution TEM images were recorded using a field emission analytical electron microscopy (JOEL, JEM 2010F) operated at 200 kV and with an aberration corrected TEM (Thermo Fisher Scientific, FEI Titan) operated at 300 kV.

5.4 Results

Two oxidation methods were implemented on GaN (0001) surfaces to enable atomic layer etching. The unpatterned surfaces were initially treated with a 10-minute UV-O_3 exposure then a 10-minute HCl dip prior to insertion into the UHV transfer line. X-ray

photoelectron spectra of the GaN surfaces after the following: (a) the initial ex-situ cleaned, (b) remote O_2-plasma clean, (c) 10 alternating HF and TMG exposures, (d) two super cycles of GaN PEALE, and (e) four super cycles of GaN TALE. *In situ* ellipsometry was measured during by an initial O_2-plasma exposure followed by 10 alternating exposures of HF and TMG and during the PEALE and TALE processes. Finally, transmission electron microscopy (TEM) of three samples are shown. TEM was performed on a control sample along with PEALE and TALE samples. The TALE process employed twice the number of super cycles of (d) as to obtain a projected similar etched removal thickness (2 nm). Finally, transmission electron microscopy (TEM) of three samples is shown. TEM was performed on a control sample along with PEALE and TALE samples.

5.4.1 X-ray Photoelectron Spectroscopy

The X-ray photoelectron spectroscopy taken after each step of the ALE processes is shown in FIG 5.2. After the *ex situ* clean the O 1s and C 1s spectra indicated the initial surface had a native oxide and a small amount of adventitious carbon. The GaN samples were then exposed to a remote O_2-plasma (100 mTorr at 100 W for 10 s) to clean and oxidize the surface. The resulting O_2-plasma processed surface showed (FIG 5.2(b)) carbon impurities near the detection limit. Broadening of the O 1s Ga-O peak was observed which was interpreted as indicating multiple oxide configurations. Relative to the other process steps, the O_2-plasma exposed surface showed a shift to lower binding energies indicating band bending which is consistent with previous reports.[31-33]

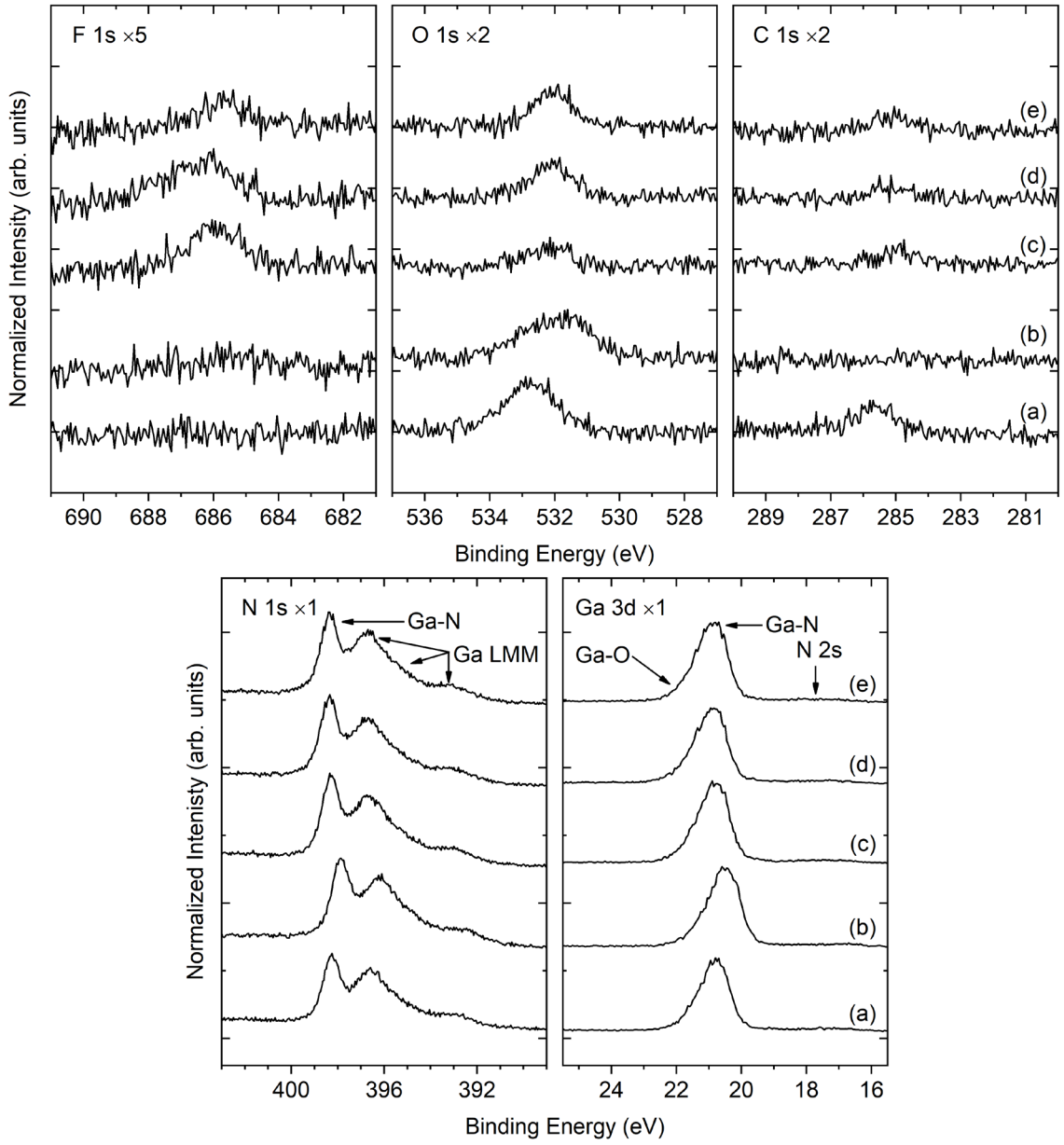

FIG 5.2. F 1s, O 1s, C 1s, N 1s, and Ga 3d core levels of the GaN (0001) surfaces at various process steps. In (a), the *ex situ* cleaned surface is shown, (b) a O_2-plasma exposure, (c) ten alternating exposures of HF and TMG, (d) two super cycles of GaN PEALE, and (e) four super cycles of GaN TALE.

After the O_2-plasma, samples were subjected to ten alternating HF and TMG steps to remove the converted oxide the XPS scans are shown in FIG 5.2(c). The XPS indicated

that a small amount of carbon remained on the surface, which is interpreted as unreacted methyl groups.[44] The carbon signal was too weak for more detailed analysis. The O 1s spectra, FIG 5.3(c), showed a decrease in O concentration. Additionally, fluorine was detected on the surface which is assumed to indicate the presence of GaF_x.[24] After the ten alternating HF and TMG steps, the aforementioned band bending was reverted to the original state.

The surface stoichiometry was calculated from the XPS for each process step shown in FIG 5.3. The *ex situ* cleaned surface indicating the N:Ga was roughly the same. After the O_2-plasma and removal of hydrocarbon impurities, the surface was more Ga-rich. Additionally, the oxygen concentration remained almost constant. After the application of ten HF-TMG cycles, the oxygen concentration decreased by ~ 74 % and ~0.3 at. % of fluorine was left on the surface. After each ALE process, slight changes in the oxygen and fluorine concentrations were observed. Interestingly, the N:Ga was relatively constant through each step excluding the initial *ex situ* clean. The C 1s peak intensities in FIG 5.3 were too close to the XPS detection limit for analysis.

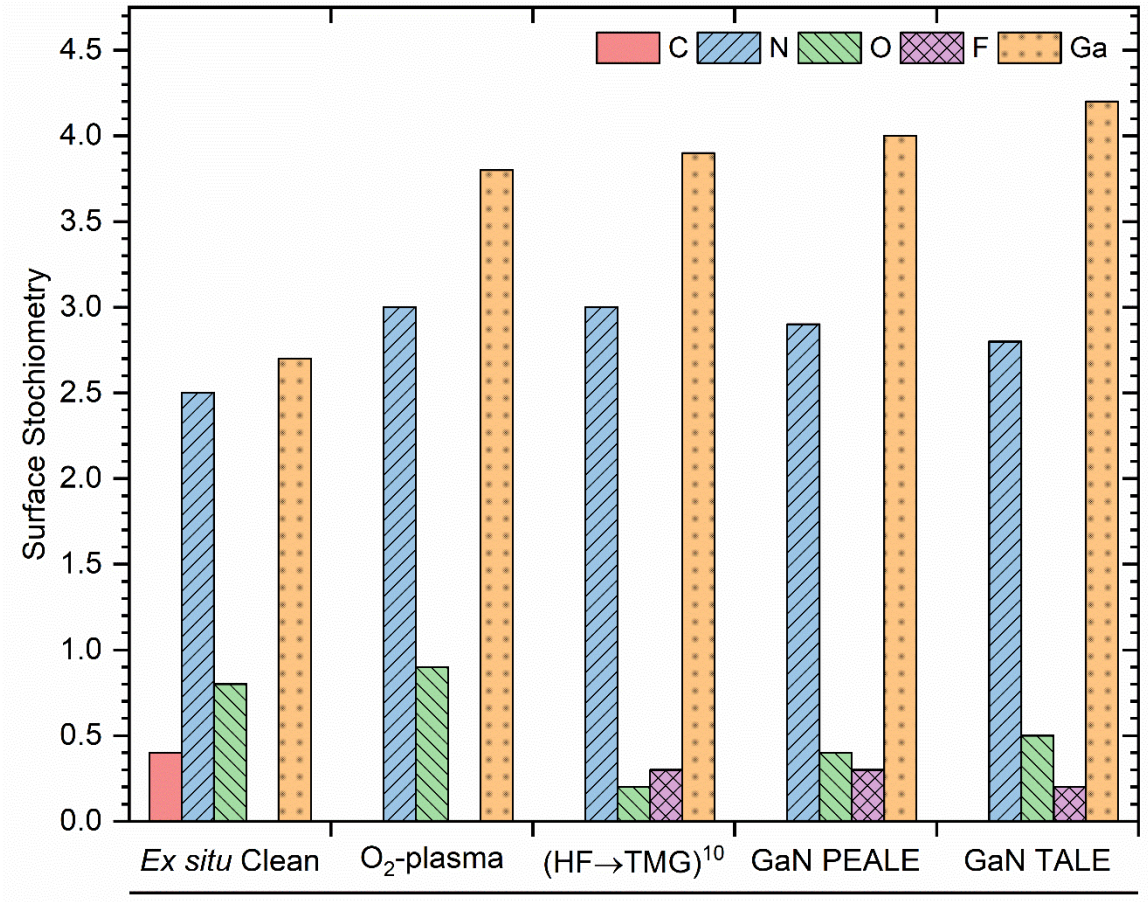

FIG 5.3. Surface stoichiometry for each process step.

GaN PEALE and TALE processes were performed on separate samples, and the XPS scans are shown in FIG 5.2(d) and FIG 5.2(e) respectively. Each etched sample was subjected to the same initial steps: *ex situ* clean, O_2-plasma, and 10 HF-TMG cycles. XPS of the PEALE and TALE samples were quite similar with minor differences in the F 1s, O 1s, and C 1s. Both processes show some residual carbon, oxygen, and fluorine surface impurities. For O, this corresponds to ~50 % of the O_2-plasma exposure surface but ~50 % more O than the surface after ten HF and TMG steps, FIG 5.3.

5.4.2 Ellipsometry

In situ ellipsometry scans during the PEALE and TALE GaN processes are shown in FIG 5.4. The ellipsometry results are presented in terms of the change in the ellipsometric parameter Δ with respect to the average of Δ over an initial period of 60 s prior to the process start, $\overline{\Delta}_0$. For each ALE process, a remote O_2-plasma exposure was applied, which was followed by ten alternating HF and TMG steps. Upon the ignition of each O_2-plasma, a large change in Δ was observed. The change in delta due to an O_2-plasma ignition lasted ~ 2 minutes during which an HF step occurred, FIG 5.4(b) – (c). The small .05 – 0.1 change in $\Delta - \overline{\Delta}_0$ indicates no significant accumulation of oxides or etch impurities for either ALE process.

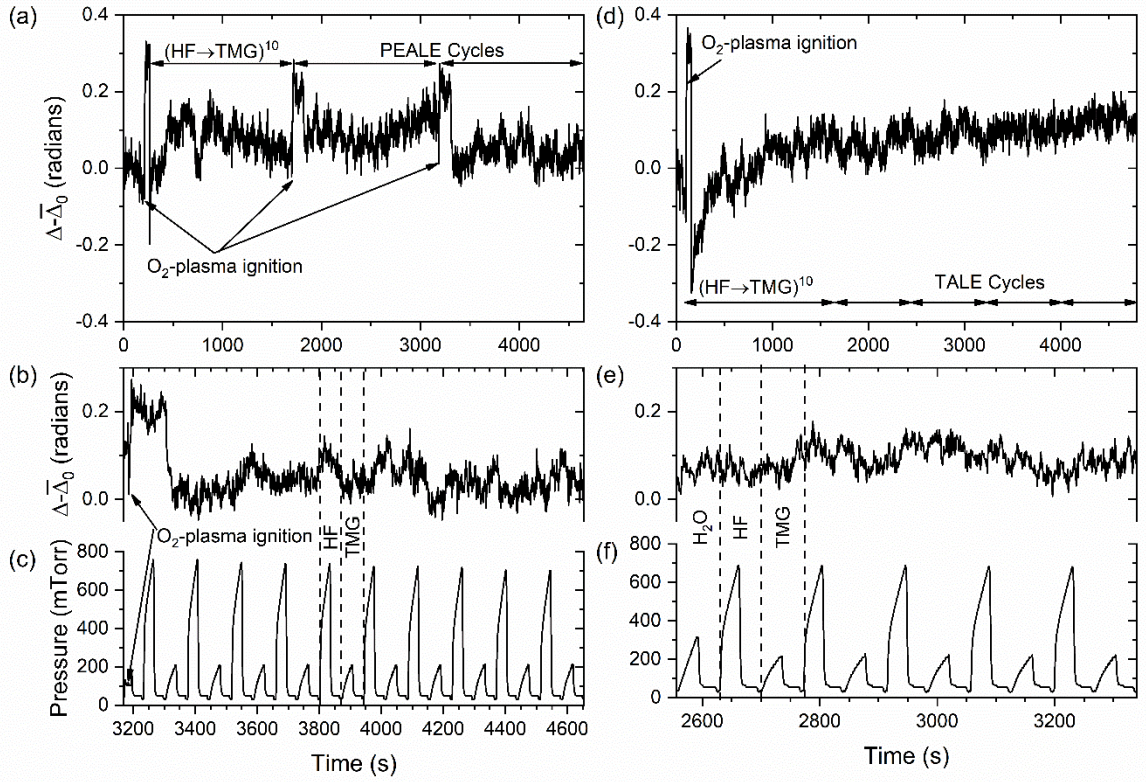

FIG 5.4. *In situ* ellipsometry scans during the GaN PEALE and TALE processes. In (a) – (c) and (d) – (f) the PEALE and TALE processes are shown, respectively. In (a) and (d) the full ALE processes are shown. The ellipsometry ($\Delta - \overline{\Delta}_0$) and the process pressure for the second PEALE cycle is shown in (b) and (c), respectively. In (e) and (f), the ellipsometry and process pressure are shown for the third TALE cycle.

5.4.3 Transmission Electron Microscopy

A set of three samples were prepared for transmission electron microscopy (TEM): a control sample and two GaN surfaces patterned with metal contacts. The patterned GaN surfaces were subjected to either 5 or 10 super cycles of the PEALE and TALE process, respectfully. The processes were designed such that a thickness of 5 nm would be removed for both processes. After the processes were completed, cross sectional TEM was

performed on each sample and results are shown in FIG 5.5. In FIG 5.5(a) – (b), the control sample is shown. In FIG 5.5(b), some surfaces fringes are observed indicating a degree of surface roughness. The PEALE sample is shown in FIG 5.5(c) – (d). FIG 5.5(c) shows the area under a metal contact with a PEALE process exposed area to the right. Evidently, the GaN removed during the ALE processes was less than anticipated and probably less than 2 nm. An area similar to FIG 5.5(c) is shown in FIG 5.5(e). Like the PEALE sample, the TALE sample does not show clear evidence of etching. Similar to the control sample, fringes are observed in FIG 5.5(d) indicating surface roughness but to a lesser extent than FIG 5.5(b). A minor difference between the two process is the TALE exposed area, FIG 5.5(f), shows fewer surface fringes indicating a lesser degree of surface roughness in these areas.

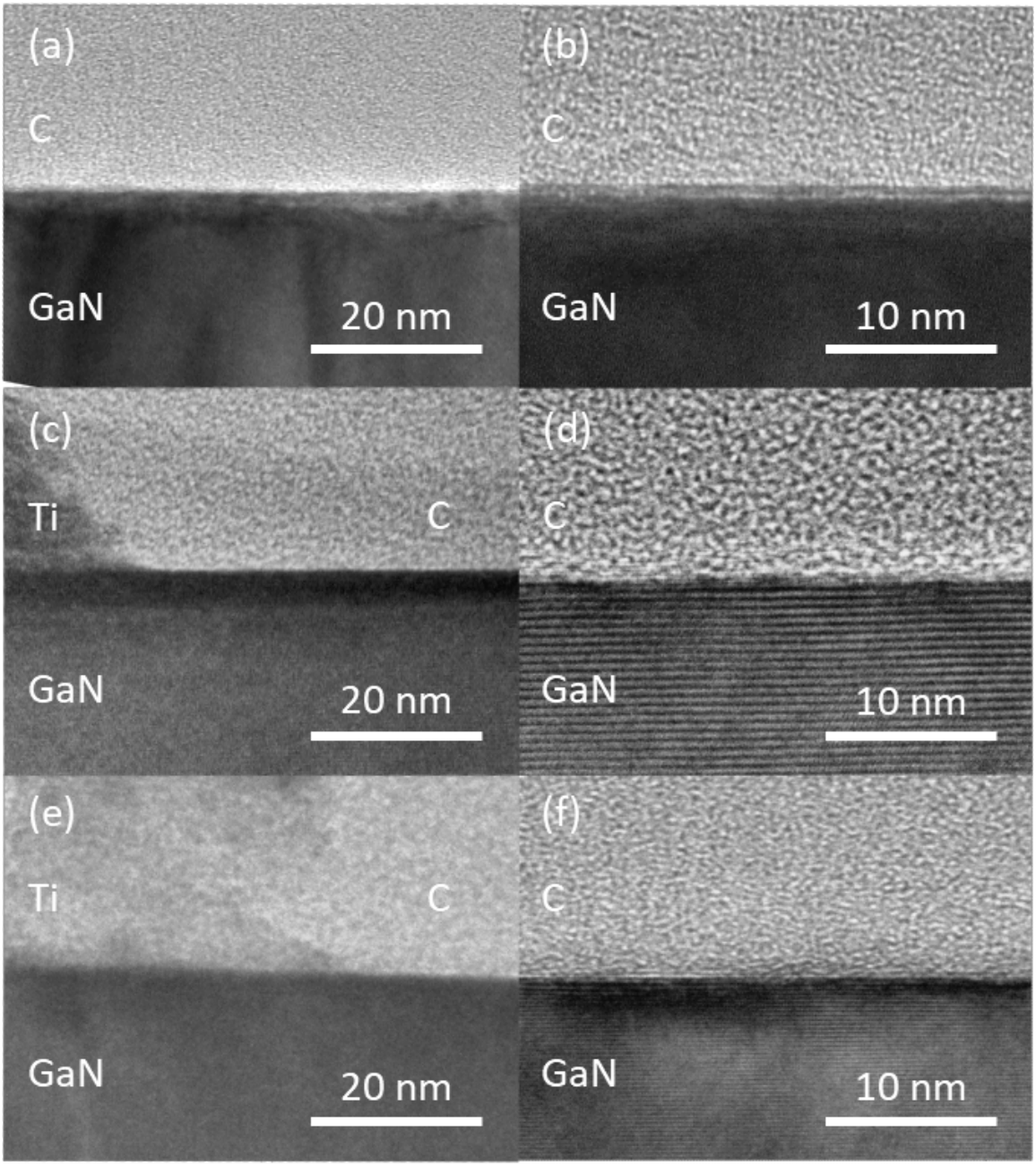

FIG 5.5. Transmission electron microscopy of the (a – b) control sample, (c – d) the plasma oxidized, and (e – f) thermally oxidized GaN samples. The control sample had no patterning. (c) and (d) show the edge of the metal contact (Ti) while (d) and (f) are far away from the contact.

5.5 Discussion

The ellipsometry showed a small positive increase in the ellipsometric parameter Δ for both PEALE and TALE process. However, the change in Δ of this scale (>0.1) could indicate etching a small degree. From previous reports, it was expected the water vapor and O_2-plasma exposures would create ~0.5 nm and ~1.0 nm of GaO_x, respectively. Over the 5 and 10 super cycles of PEALE and TALE, respectively, performed on patterned surfaces an etched thickness of ~5 nm was expected. TEM of both ALE processes could be interpreted as a maximum 1 – 2 nm reduction in thickness. Additionally, TEM indicated the processes surfaces were smoother.

XPS analysis indicated that the alternating HF and TMG step could reduce the surface oxide by ~74 %. The HF-TMG etch process left a near undetectable, by XPS, amount of carbon. Fluorine species were also present at ~3 at. %. The application of PEALE or TALE cycles resulted in a similar level of C, F, and O impurities on the GaN surfaces. TEM showed the overall surface quality may have improved with possibly 1 – 2 nm of GaN removed for processed samples.

These results show that either the converted oxide could not effectively be etched, or the amount of oxide created was far less than expected. As alternating exposures of HF and TMG is known to etch amorphous Ga_2O_3, it is expected the native oxide and converted oxides, from the water vapor or O_2-plasma exposures, would be etched.[27] Recently, Dycus *et al* indicated that the native oxide on GaN (0001) was arranged similar to bulk β-Ga_2O_3 with a thickness of ~ 2 nm.[48] This implies that the Ga_2O_3 ALE method may be ineffective for crystalline Ga_2O_3. Moreover, Murdzek *et al* showed that while alternating exposures of HF and trimethylaluminum were effective for etching amorphous Al_2O_3, crystalline Al_2O_3

was not etched past the first ~1.0 nm.[49] The ability to etch amorphous Al_2O_3 but not crystalline Al_2O_3 was attributed to the difference in density between the polymorphs.

Future studies could incorporate a high temperature (≥750 °C) NH_3 or H_2/N_2 anneal to remove the native oxide prior to the application of the TALE and PEALE method.[25] Alternatively, the inability to etch the surface Ga_2O_3 with the amorphous Ga_2O_3 ALE process motivates further research into ALE of β-Ga_2O_3. Additionally, modulation of the O_2-plasma composition to include Ar or He may be beneficial for producing an amorphous surface oxide.[31-33, 50] Removal of surface etch impurities could accomplished using either a remote H_2, or NH_3,-plasma.

5.6 Conclusions

Two atomic layer etching (ALE) methods for gallium nitride have been presented. These methods differed in the oxidation method; using either water vapor or remote O_2-plasma exposures. Both methods were studied by *in situ* ellipsometry, X-ray photoelectron spectroscopy (XPS), and *ex situ* transmission electron microscopy (TEM). Ellipsometry indicating a small change in Δ which could be interpreted as a small change in thickness. XPS showed the etch processes left a small amount of impurities (F, O, C) on the surface accounting for 8 – 10 at. % of the surface composition. TEM of etched patterned samples indicated a maximum of 1 – 2 nm of GaN may have been removed. Additionally, a slight reduction in surface roughness relative a control sample. TEM results indicate the two ALE processes may be ineffective for GaN which was attributed to the presence of the ordered surface oxide. Future experiments could include removal of the native oxide prior to ALE or methods of producing a disordered surface oxide.

Acknowledgements

Research was supported through the Advanced Research Projects Agency-Energy, as part of PNDIODES, under Grant No. DE-AR0000868 (research on thermal oxidation and analysis of TALE GaN) and by the U.S. Department of Energy (DOE), Office of Science, as part of ULTRA, an energy Frontier Research Center funded by Basic Energy Sciences (BES), under Award No. DE-SC0021230 (research on plasma oxidation and analyzed of PEALE GaN). We acknowledge the use of facilities within the John. M. Cowley Center for High Resolution Electron Microscopy and the NanoFab, at Arizona State University, supported in part by the NSF program NNCI-ECCS-1542160. We acknowledge Kari Slotten in patterning the GaN samples and Martha McCartney for their aid performing TEM. We thank Franz Koeck for assistance in assembling the fluoride ALE reactor and to Zhiyu Huang, Jesse Brown, Avani Patel, Xingye Wang, and Mei Hao for their helpful discussions.

Author Contributions

The authors confirm contribution to the paper as follows: study conception and design: D. C. Messina, K. A. Hatch, D. Smith, Y. Zhao, R. J. Nemanich; data collection: D. C. Messina (Ellipsometry and XPS) and S. Vishwakarma (TEM); Analysis and interpretation of results: D. C. Messina, S. Vishwakarma, D. Smith, and R. J. Nemanich; draft manuscript preparation: D. C. Messina and R. J. Nemanich.

References

[1] G. E. Town, presented at the 2015 IEEE 11th International Conference on Power Electronics and Drive Systems, 2015 (unpublished).

[2] B. J. Baliga, Gallium nitride devices for power electronic applications, Semiconductor Science and Technology **28**, 074011 (2013).

[3] Y. Zhang, A. Dadgar and T. Palacios, Gallium nitride vertical power devices on foreign substrates: a review and outlook, Journal of Physics D: Applied Physics **51**, 273001 (2018).

[4] S. Chowdhury, Gallium nitride based power switches for next generation of power conversion, physica status solidi (a) **212**, 1066-1074 (2015).

[5] J. Tian, C. Lai, G. Feng, D. Banerjee, W. Li and N. C. Kar, Review of recent progresses on gallium nitride transistor in power conversion application, International Journal of Sustainable Energy **39**, 88-100 (2020).

[6] M. Danilovic, Z. Chen, R. Wang, F. Luo, D. Boroyevich and P. Mattavelli, presented at the 2011 IEEE Energy Conversion Congress and Exposition, 2011 (unpublished).

[7] M. J. Scott, L. Fu, X. Zhang, J. Li, C. Yao, M. Sievers and J. Wang, Merits of gallium nitride based power conversion, Semiconductor Science and Technology **28**, 074013 (2013).

[8] S. J. Pearton, J. C. Zolper, R. J. Shul and F. Ren, GaN: Processing, defects, and devices, Journal of Applied Physics **86**, 1-78 (1999).

[9] R. J. Shul, G. B. McClellan, S. A. Casalnuovo, D. J. Rieger, S. J. Pearton, C. Constantine, C. Barratt, R. F. K. Jr., C. Tran and M. Schurman, Inductively coupled plasma etching of GaN, Applied Physics Letters **69**, 1119-1121 (1996).

[10] D. Zhuang and J. H. Edgar, Wet etching of GaN, AlN, and SiC: a review, Materials Science and Engineering: R: Reports **48**, 1-46 (2005).

[11] M. E. Lin, Z. F. Fan, Z. Ma, L. H. Allen and H. Morkoç, Reactive ion etching of GaN using BCl_3, Applied Physics Letters **64**, 887-888 (1994).

[12] S. Huang, Q. Jiang, K. Wei, G. Liu, J. Zhang, X. Wang, Y. Zheng, B. Sun, C. Zhao, H. Liu, Z. Jin, X. Liu, H. Wang, S. Liu, Y. Lu, C. Liu, S. Yang, Z. Tang, J. Zhang, Y. Hao and K. J. Chen, presented at the 2014 IEEE International Electron Devices Meeting, 2014 (unpublished).

[13] H. S. Lee, D. Y. Jung, Y. Park, J. Na, H. G. Jang, H. S. Lee, C. H. Jun, J. Park, S. O. Ryu, S. C. Ko and E. S. Nam, 0.34 V_T AlGaN/GaN-on-Si Large Schottky Barrier Diode With Recessed Dual Anode Metal, IEEE Electron Device Letters **36**, 1132-1134 (2015).

[14] N. R. Johnson, J. K. Hite, M. A. Mastro, C. R. EddyJr. and S. M. George, Thermal atomic layer etching of crystalline GaN using sequential exposures of XeF_2 and BCl_3, Applied Physics Letters **114**, 243103 (2019).

[15] P. Peri, K. Fu, H. Fu, Y. Zhao and D. J. Smith, Characterization of As-Grown and Regrown GaN-on-GaN Structures for Vertical p-n Power Devices, Journal of Electronic Materials **50**, 2637-2642 (2021).

[16] K. J. Kanarik, T. Lill, E. A. Hudson, S. Sriraman, S. Tan, J. Marks, V. Vahedi and R. A. Gottscho, Overview of atomic layer etching in the semiconductor industry, Journal of Vacuum Science & Technology A **33**, 020802 (2015).

[17] A. Fischer, A. Routzahn, S. M. George and T. Lill, Thermal atomic layer etching: A review, Journal of Vacuum Science & Technology A **39**, 030801 (2021).

[18] S. M. George, Mechanisms of Thermal Atomic Layer Etching, Accounts of Chemical Research **53**, 1151-1160 (2020).

[19] C. Kauppinen, S. A. Khan, J. Sundqvist, D. B. Suyatin, S. Suihkonen, E. I. Kauppinen and M. Sopanen, Atomic layer etching of gallium nitride (0001), Journal of Vacuum Science & Technology A **35**, 060603 (2017).

[20] C. Mannequin, C. Vallée, K. Akimoto, T. Chevolleau, C. Durand, C. Dussarrat, T. Teramoto, E. Gheeraert and H. Mariette, Comparative study of two atomic layer etching processes for GaN, Journal of Vacuum Science & Technology A **38**, 032602 (2020).

[21] Y. Zhang, S. Huang, K. Wei, S. Zhang, X. Wang, Y. Zheng, G. Liu, X. Chen, Y. Li and X. Liu, Millimeter-Wave AlGaN/GaN HEMTs With 43.6% Power-Added-Efficiency at 40 GHz Fabricated by Atomic Layer Etching Gate Recess, IEEE Electron Device Letters **41**, 701-704 (2020).

[22] D. Ohori, T. Sawada, K. Sugawara, M. Okada, K. Nakata, K. Inoue, D. Sato and S. Samukawa, Selective atomic layer reaction between GaN and SiN in HBr neutral beam etching, Journal of Vacuum Science & Technology A **39**, 042601 (2021).

[23] I.-H. Hwang, H.-Y. Cha and K.-S. Seo, Low-Damage and Self-Limiting (Al)GaN Etching Process through Atomic Layer Etching Using O_2 and BCl_3 Plasma, Coatings **11**, 268 (2021).

[24] V. M. Bermudez, Investigation of the initial chemisorption and reaction of fluorine (XeF_2) with the GaN(0001)-(1 × 1) surface, Applied Surface Science **119**, 147-159 (1997).

[25] V. M. Bermudez, The fundamental surface science of wurtzite gallium nitride, Surface Science Reports **72**, 147-315 (2017).

[26] Y. Lee, N. R. Johnson and S. M. George, Thermal Atomic Layer Etching of Gallium Oxide Using Sequential Exposures of HF and Various Metal Precursors, Chemistry of Materials **32**, 5937-5948 (2020).

[27] K. A. Hatch, D. C. Messina, X. Wang and R. J. Nemanich, Plasma Enhanced Atomic Layer Deposition and Atomic Layer Etching of Gallium Oxide Using Trimethylgallium, (Unpublished).

[28] H. S. Oon and K. Y. Cheong, Recent development of gallium oxide thin film on GaN, Materials Science in Semiconductor Processing **16**, 1217-1231 (2013).

[29] O. Ambacher, M. S. Brandt, R. Dimitrov, T. Metzger, M. Stutzmann, R. A. Fischer, A. Miehr, A. Bergmaier and G. Dollinger, Thermal stability and desorption of Group III nitrides prepared by metal organic chemical vapor deposition, Journal of Vacuum Science & Technology B: Microelectronics and Nanometer Structures Processing, Measurement, and Phenomena **14**, 3532-3542 (1996).

[30] H. B. Profijt, S. E. Potts, M. C. M. van de Sanden and W. M. M. Kessels, Plasma-Assisted Atomic Layer Deposition: Basics, Opportunities , and Challenges, Journal of Vacuum Science & Technology A **29**, 050801 (2011).

[31] C. Bae and G. Lucovsky, Low-temperature preparation of GaN-SiO_2 interfaces with low defect density. II. Remote plasma-assisted oxidation of GaN and nitrogen incorporation, Journal of Vacuum Science & Technology A **22**, 2411-2418 (2004).

[32] T. Yamamoto, N. Taoka, A. Ohta, N. X. Truyen, H. Yamada, T. Takahashi, M. Ikeda, K. Makihara, M. Shimizu and S. Miyazaki, Low-temperature formation of Ga-oxide/GaN interface with remote oxygen plasma and its interface properties, Japanese Journal of Applied Physics **57**, 06JE01 (2018).

[33] T. Yamamoto, N. Taoka, A. Ohta, N. X. Truyen, H. Yamada, T. Takahashi, M. Ikeda, K. Makihara, O. Nakatsuka, M. Shimizu and S. Miyazaki, Energy band structure and electrical properties of Ga-oxide/GaN interface formed by remote oxygen plasma, Japanese Journal of Applied Physics **57**, 06KA05 (2018).

[34] E. D. Readinger, S. D. Wolter, D. L. Waltemyer, J. M. Delucca, S. E. Mohney, B. I. Prenitzer, L. A. Giannuzzi and R. J. Molnar, Wet thermal oxidation of GaN, Journal of Electronic Materials **28**, 257-260 (1999).

[35] R. Korbutowicz, J. Prazmowska, Z. Wagrowski, A. Szyszka and M. Tlaczala, presented at the 2008 International Conference on Advanced Semiconductor Devices and Microsystems, 2008 (unpublished).

[36] H. Ye, G. Chen, H. Niu, Y. Zhu, L. Shao and Z. Qiao, Structures and Mechanisms of Water Adsorption on ZnO(0001) and GaN(0001) Surface, The Journal of Physical Chemistry C **117**, 15976-15983 (2013).

[37] M. Sato, Y. Imazeki, T. Takeda, M. Kobayashi, S. Yamamoto, I. Matsuda, J. Yoshinobu, Y. Nakano and M. Sugiyama, Atomistic-Level Description of GaN/Water Interface by a Combined Spectroscopic and First-Principles Computational Approach, The Journal of Physical Chemistry C **124**, 12466-12475 (2020).

[38] X. Zhang and S. Ptasinska, Electronic and chemical structure of the H_2O/GaN(0001) interface under ambient conditions, Scientific Reports **6**, 24848 (2016).

[39] S. W. King, R. F. Davis, R. J. Carter, T. P. Schneider and R. J. Nemanich, Hydrogen desorption kinetics for aqueous hydrogen fluoride and remote hydrogen plasma processed silicon (001) surfaces, Journal of Vacuum Science & Technology A **33**, 05E115 (2015).

[40] Y. Yang, T. Sun, J. Shammas, M. Kaur, M. Hao and R. J. Nemanich, Electron affinity of cubic boron nitride terminated with vanadium oxide, Journal of Applied Physics **118**, 165310 (2015).

[41] H. C. M. Knoops, T. Faraz, K. Arts and W. M. M. Kessels, Status and prospects of plasma-assisted atomic layer deposition, Journal of Vacuum Science & Technology A **37**, 030902 (2019).

[42] J. H. Scofield, Hartree-Slater subshell photoionization cross-sections at 1254 and 1487 eV, Journal of Electron Spectroscopy and Related Phenomena **8**, 129-137 (1976).

[43] F. A. Stevie and C. L. Donley, Introduction to x-ray photoelectron spectroscopy, Journal of Vacuum Science & Technology A **38**, 063204 (2020).

[44] J. F. Moulder, W. F. Stickle, P. E. Sobol and K. D. Bomben, (Perkin-Elmer Corporation, Eden Prairie, Minnesota, USA 1979), pp. 25-26.

[45] R. M. A. Azzam, Division-of-amplitude Photopolarimeter (DOAP) for the Simultaneous Measurement of All Four Stokes Parameters of Light, Optica Acta: International Journal of Optics **29**, 685-689 (1982).

[46] a. J B Theeten and D. E. Aspnes, Ellipsometry in Thin Film Analysis, Annual Review of Materials Science **11**, 97-122 (1981).

[47] A. Tikhonravov, M. Trubetskov, E. Masetti, A. Krasilnikova and I. Kochikov, *Sensitivity of the ellipsometric angles psi and delta to the surface inhomogeneity*. (SPIE, 1999).

[48] J. H. Dycus, K. J. Mirrielees, E. D. Grimley, R. Kirste, S. Mita, Z. Sitar, R. Collazo, D. L. Irving and J. M. LeBeau, Structure of Ultrathin Native Oxides on III–Nitride Surfaces, ACS Applied Materials & Interfaces **10**, 10607-10611 (2018).

[49] J. A. Murdzek, A. Rajashekhar, R. S. Makala, and S. M. George, Thermal atomic layer etching of amorphous and crystalline Al_2O_3 films, Journal of Vacuum Science & Technology A **39**, 042602 (2021)

[50] C. Bae and G. Lucovsky, Low-temperature preparation of GaN-SiO_2 interfaces with low defect density. I. Two-step remote plasma-assisted oxidation-deposition process, Journal of Vacuum Science & Technology A **22**, 2402-2410 (2004).

CHAPTER 6

SUMMARY AND FUTURE WORK

6.1 Summary and Current Work

In this study, methods for atomic layer deposition and etching of two wide band gap materials were presented. First, to enable the deposition and etching of wide band gap materials, two atomic layer deposition and etching reactors were designed and constructed, detailed in Chapter 3. In Chapter 4, a comparison of thermal and plasma enhanced atomic layer deposited aluminum fluoride (AlF_3) is presented. The results indicated that the plasma enhanced variant showed the incorporation of Al clusters which were later found to be detrimental to ultraviolet and electronic applications. In Chapter 5, two methods for atomic layer etching (ALE) of gallium nitride is presented. The two ALE methods implemented a three-step process consisting of oxidation, fluorination, and ligand exchange. The results indicated that the two methods were ineffective at removing GaN layers which was attributed to an ordered surface oxide similar to β-Ga_2O_3.[1]

Recently, the AlF_3 plasma enhanced atomic layer deposition (PEALD) process discussed in Chapter 4 was implemented to fabricate a middle ultraviolet (UV) reflective coating. The coating was fabricated using alternating layers of AlF_3 and Al_2O_3 which were deposited by atomic layer deposition.[2] This middle UV coating had a predicted ultimate reflectance of ~100 % at 225 nm. However, the incorporation of the Al-rich clusters in the AlF_3 layer increased absorption at lower wavelengths leading to a decrease in the predicted ultimate reflectance to 43 % and a shift of the center wavelength to ~235 nm. Consequently, the PEALD AlF_3 process showed degraded performance for middle UV coatings. The

thermal ALD AlF_3 process did not display Al-rich clusters and the layers may prove more effective for UV optical coatings.

Currently, efforts are focused on using thermal ALD AlF_3 as a gate dielectric on diamond devices. Due to the large band gap of AlF_3 (>10 eV),[3-5] AlF_3 layers may be able to confine carriers at diamond – AlF_3 interfaces.[4, 5] Prior to employment of AlF_3 for diamond devices, the band alignment of AlF_3 with diamond must be established. Initial research indicates that the use of PEALD AlF_3 layers results in pinning of the Fermi level due to the incorporation of Al-rich clusters. As such, TALD AlF_3 may offer superior properties for electronic applications.

A major challenge for TALD AlF_3 films is obtaining stochiometric layers as fluorine deficient films may induce Fermi level pinning. While the TALD AlF_3 presented in Chapter 4 had a stoichiometry of 3.1, the uncertainty was 10 – 20 %.[6] Additional experiments will be needed to reduce this uncertainty. As fluorine is preferentially sputtered, stoichiometry from Rutherford backscattering (RBS) or secondary ion mass spectroscopy (SIMS) may be obscured.[7-9] An alternative experiment would be the direct measurement of the effective attenuation length (EAL) of a substrate's electrons in AlF_3 and of the photoionization cross-section of AlF_3 Al 2p and F 1s core levels. Such an experiment would require energy electron loss spectroscopy (EELS) and XPS.[10, 11] Measurement of the EAL and photoionization cross-sections would remove the large uncertainty for calculation of stoichiometry by XPS.

The implementation of AlF_3 ALD and GaN ALE processes improve upon the current understanding of fluorine chemistry and surface interactions for the ALD and ALE of wide band gap materials.

6.2 Outline of Future Work

6.2.1 Atomic Layer Deposition of Gallium Fluoride

Gallium fluoride (GaF_3) has an ultrawide band gap >9.6 eV and dielectric constant between 6.6 and 10.8.[12] GaF_3 films have applications as III-V material surface passivation, [13] and as a dielectric on GaAs transistors.[14] Additionally, the large band gap and dielectric constant implies GaF_3 may have use in ultraviolet optics or as a gate dielectric for wide band gap semiconductors. The application of GaF_3 to ultraviolet and electronic applications would require the deposition of high purity, uniform and conformal, layers with a precise thickness. As such, atomic layer deposition could be an ideal process.

GaF_3 has previously been deposited by annealing gallium metal or GaAs in ammonium difluoride (NH_4F_2) or in F_2 at temperatures ≤500 °C.[12, 13, 15] For the deposition of high purity films, minimization of the possible contaminants is preferred. As gallium does not form a stable carbide, carbon incorporation is less likely.[16, 17] As such, organometallics containing gallium could be implemented (e.g. $Ga(C_2H_5)_3$, $Ga(CH_3)_3$, $Ga(C_4H_9)_3$, etc). A fluoride source for a thermal process could include HF, XeF_2, SF_4, NH_4F, or NH_4F_2. In the Nanoscience Lab's Oxide PEALP reactor, trimethylgallium ($Ga(CH_3)_3$, TMG) and hydrogen fluoride pyridine ($(C_5H_5)N{\cdot}HF_x$, HF-P) are present. Thus, the proposed thermal ALD process could consist of alternating exposures of TMG and HF. The half reactions are expected to be similar to thermal ALD AlF_3 and are shown in Eq. (6.1) and Eq. (6.2).[9]

$$GaF_3|HF + Ga(CH_3)_{3(g)} \rightarrow GaF_3|GaF(CH_3)_2 + CH_{4(g)} \quad (6.1)$$

$$GaF_3|GaF(CH_3)_2 + 3HF_{(g)} \rightarrow GaF_3|GaF_3|HF + 2CH_{4(g)} \quad (6.2)$$

Here, the vertical bar denotes the separation between the surface and surface species. Like AlF_3 and other metal fluoride, HF molecules are still expected to absorb onto the surface as GaF_3 is slightly acidic.[18, 19]

An alternative to the GaF_3 TALD would be to implement a remote H_2-plasma after each TMG exposure. In the analogous PEALD AlF_3 process, the H_2-plasma decomposed the dimethylaluminum surface adduct to aluminum carbide (Al_4C_3). Since gallium does not form a stable carbide, the carbon may desorb leaving the gallium atoms.[16, 17] While gallium tends to clump, the amount of gallium on the surface is expected to be determined by the previous adsorption of TMG. Thus, one gallium atom per surface site is expected assuming no steric hindrance. The chemical reactions of the plasma enhanced step shown in Eq. (6.3) with the subsequent HF step in Eq. (6.4).

$$GaF_3\big|GaF(CH_3)_2 + 4H^*_{(g)} \rightarrow GaF_3\big|GaFH_2 + 2CH_{4(g)} \tag{6.3}$$

$$GaF_3\big|GaFH_2 + 3HF_{(g)} \rightarrow GaF_3\big|GaF_3\big|HF + H_{2(g)} \tag{6.4}$$

Here, the "*" denotes the H radicals from the remote H_2-plasma. This method assumes that the surface hydride would remain on the surface rather than desorb. It is uncertain whether GaF_3 film growth is via this method would suffer the analogous impurity incorporation as the PEALD AlF_3 films discussed in Chapter 4 (i.e. Ga-rich clusters).

6.2.2 Plasma Enhanced Atomic Layer Etching of Gallium Oxide Polymorphs Grown by Plasma Enhanced Atomic Layer Deposition

Gallium oxide (Ga_2O_3) is an emerging material for high-power and high-temperature electronics and ultraviolet applications. The wide band gap (≥4.8 eV),[20-23] high dielectric constant (>8),[20, 22] high critical field (>8 MW/cm),[20, 24] and electron

mobility (≥300 cm^2/Vs)[20, 24, 25] enables applications of Ga_2O_3 to field effect transistors (FETs),[20, 26, 27] metal-oxide-semiconductor high-electron-mobility transistors (MOS-HEMTs),[25] thin film transistors,[28-33] and Schottky barrier diodes.[26, 34, 35] Due to the large band gap and refractive index of (~1.89 at 633 nm)[21-23], Ga_2O_3 is an attractive material for ultraviolet applications where it has been used for solar blind photodetectors,[36-39] phototransistors,[40, 41] and polarization detectors.[42] Use of Ga_2O_3 in electronic and ultraviolet applications requires the deposition and etching of high purity, uniform and conformal, layers with precise thickness control.

Atomic layer deposition (ALD) and atomic layer etching (ALE) are thin film processing techniques that meet these requirements. Both ALD and ALE are self-limiting chemical vapor techniques, which employ vapor transport to enable gas-solid interactions. Plasma enhanced ALD (PEALD) of Ga_2O_3 using alternating exposures of remote O_2-plasma and trimethylgallium (TMG) has been previously reported.[43-49] Recently, Wheeler *et al* showed that by tuning the plasma parameters (e.g. power, pressure, composition) one could achieve phase selectivity and deposit various polymorphs of Ga_2O_3. It was shown that the most stable phase (β) and metastable phases (α, ε, κ) could easily be deposited between 265 °C – 475 °C. It was noted that the metastable phases had slightly larger band gaps than β-Ga_2O_3.

Atomic layer etching techniques have not been developed for crystalline Ga_2O_3. At present, two methods exist for etching amorphous Ga_2O_3 grown by PEALD.[50, 51] Both techniques rely on sequential halogenation and ligand exchange reactions to remove material. Recent studies have shown that ALE of amorphous Ga_2O_3 using hydrogen fluoride (HF) and trimethylgallium was ineffective for etching the native β-Ga_2O_3 on GaN

(0001).[1, 52] Recently, a similar study was presented on the ALE of amorphous and crystalline Al_2O_3.[53] It was shown that using alternating exposures of HF and trimethylaluminum (TMA) for fluorination and ligand exchange resulted in the etching amorphous Al_2O_3 but not α-Al_2O_3 (sapphire).[53] Murdzek *et al* found that regardless of the thermal fluorination agents used for crystalline Al_2O_3, etching was not observed past the first 1 – 2 nm. The inability to etch crystalline Al_2O_3 was attributed to the difference in densities between the amorphous and crystalline phases. An alternative route to etching crystalline oxides could be the implementation of plasma halogenation agents such as SF_6, SF_4, NF_3, CF_3, BF_3, or BCl_3. A plasma enhanced ALE (PEALE) method would require a plasma halogenation step to create a volatile metal halide that could then be removed via ligand exchange in the next half reaction. An important step in developing the PEALE process would be to show the plasma halogenation step is self-limiting. Additional studies would be required to determine the impurity corporation (S, N, C and B) from the halogen plasmas and methods of reduction.

The NSL oxide plasma enhanced atomic layer processing (PEALP) reactor is configured for the PEALD of Ga_2O_3 thin films but does not currently support any of the aforementioned halides, though the system could be modified to accommodate them. SF_6 and NF_3 are two nontoxic gases which could be obtained in a lecture bottle and mounted directly onto the PEALP reactor. The use a halogen plasma would require replacement of the quartz tube and windows due to etching.[54-57] A suitable replace for the dielectric tube and windows may be sapphire or aluminum nitride.

References

[1] J. H. Dycus, K. J. Mirrielees, E. D. Grimley, R. Kirste, S. Mita, Z. Sitar, R. Collazo, D. L. Irving and J. M. LeBeau, Structure of Ultrathin Native Oxides on III–Nitride Surfaces, ACS Applied Materials & Interfaces **10**, 10607-10611 (2018).

[2] Z. Huang, D. C. Messina, B. Eller, F. A. Koeck, P. Scowen and R. J. Nemanich, Multilayer ultraviolet reflective coating based on atomic layer deposited aluminum oxide and fluoride Journal of Vacuum Science & Technology A **39**, 042402 (2021).

[3] D. König, G. Ebest, R. Scholz, S. Gemming, I. Thurzo, T. U. Kampen and D. R. T. Zahn, Evidence for high negative charge densities in AlF_3 coatings on oxidized silicon: a promising source for large drift fields, Physica E: Low-dimensional Systems and Nanostructures **14**, 259-262 (2002).

[4] D. König, R. Scholz, D. R. T. Zahn and G. Ebest, Band diagram of the $AlF_3/SiO_2/Si$ system, Journal of Applied Physics **97**, 093707 (2005).

[5] J. L. Navarro, E. A. Albanesi, R. Vidal and J. Ferrón, A study on the structural, electronic and optical properties of the α-AlF_3 compound, Materials Research Bulletin **83**, 615-622 (2016).

[6] D. C. Messina, B. S. Eller, P. Scowen and R. J. Nemanich, Comparison of aluminum fluoride thin films growth by thermal and plasma enhanced atomic layer deposition, (unpublished).

[7] K. Iwahori, M. Furuta, Y. Taki, T. Yamamura and A. Tanaka, Optical properties of fluoride thin films deposited by RF magnetron sputtering, Appl. Opt. **45**, 4598-4602 (2006).

[8] Y. Taki, Film structure and optical constants of magnetron-sputtered fluoride films for deep ultraviolet lithography, Vacuum **74**, 431-435 (2004).

[9] Y. Lee, J. W. DuMont, A. S. Cavanagh and S. M. George, Atomic Layer Deposition of AlF_3 Using Trimethylaluminum and Hydrogen Fluoride, Journal of Physical Chemistry C **119**, 14185-14194 (2015).

[10] C. T. Chantler and J. D. Bourke, Low-energy electron properties: Electron inelastic mean free path, energy loss function and the dielectric function. Recent

measurements, applications, and the plasmon-coupling theory, Ultramicroscopy **201**, 38-48 (2019).

[11] M. Gorgoi, F. Schäfers, S. Svensson and N. Mårtensson, Relative sub-shell photoionization cross-sections of nickel metal determined by hard X-ray high kinetic energy photoemission, Journal of Electron Spectroscopy and Related Phenomena **190**, 153-158 (2013).

[12] A. S. Barrière, G. Couturier, G. Gevers, H. Guégan, T. Seguelond, A. Thabti and D. Bertault, Preparation and characterization of gallium(III) fluoride thin films, Thin Solid Films **173**, 243-252 (1989).

[13] A. S. Barrière, B. Desbat, H. Guégan, L. Lozano, T. Séguelong, A. Tressaud and P. Alnot, Physico-chemical characterization of thin films obtained by fluorination of GaAs under 5 bar of fluorine, Thin Solid Films **170**, 259-271 (1989).

[14] H. Ricard, K. H. Kim, K. Aizawa and H. Ishiwara, Electrical Properties of Gallium Fluoride(GaF_3)/GaAs Interface with and without Sulfur Treatment, Japanese Journal of Applied Physics **29**, L2460-L2462 (1990).

[15] A. S. Barriére, G. Couturier, H. Guegan, T. Séguelong, A. Thabti, P. Alnot and J. Chazelas, Interface GaAs - gallium fluoride thin film grown by fluorination: Electrical behaviour of the obtained MIS fluorinated GaAs structures, Applied Surface Science **41-42**, 383-389 (1990).

[16] B. Hájek, V. Kohout and V. Flemr, Note on thermodynamic instability of M_4C_3-type carbides of gallium group metals, Monatshefte für Chemie - Chemical Monthly **117**, 1157-1164 (1986).

[17] V. B. Kumar, M. Monte, O. Mathon, S. Pascarelli, Z. e. Porat and A. Gedanken, The interaction between molten gallium and the hydrocarbon medium induced by ultrasonic energy—can gallium carbide be formed?, Journal of the American Ceramic Society **100**, 3305-3315 (2017).

[18] Y. Lee, H. Sun, M. J. Young and S. M. George, Atomic Layer Deposition of Metal Fluorides Using HF–Pyridine as the Fluorine Precursor, Chemistry of Materials **28**, 2022-2032 (2016).

[19] B. Neumüller, Organometal fluorides of aluminium, gallium, indium and thallium, Coordination Chemistry Reviews **158**, 69-101 (1997).

[20] M. Higashiwaki, K. Sasaki, A. Kuramata, T. Masui and S. Yamakoshi, Gallium oxide (Ga_2O_3) metal-semiconductor field-effect transistors on single-crystal β-Ga_2O_3 (010) substrates, Applied Physics Letters **100**, 013504 (2012).

[21] M. F. Al-Kuhaili, S. M. A. Durrani and E. E. Khawaja, Optical properties of gallium oxide films deposited by electron-beam evaporation, Applied Physics Letters **83**, 4533-4535 (2003).

[22] F. K. Shan, G. X. Liu, W. J. Lee, G. H. Lee, I. S. Kim and B. C. Shin, Structural, electrical, and optical properties of transparent gallium oxide thin films grown by plasma-enhanced atomic layer deposition, Journal of Applied Physics **98**, 023504 (2005).

[23] M. Rebien, W. Henrion, M. Hong, J. P. Mannaerts and M. Fleischer, Optical properties of gallium oxide thin films, Applied Physics Letters **81**, 250-252 (2002).

[24] M. Higashiwaki, K. Sasaki, A. Kuramata, T. Masui and S. Yamakoshi, Development of gallium oxide power devices, physica status solidi (a) **211**, 21-26 (2014).

[25] H.-Y. Shih, F.-C. Chu, A. Das, C.-Y. Lee, M.-J. Chen and R.-M. Lin, Atomic Layer Deposition of Gallium Oxide Films as Gate Dielectrics in AlGaN/GaN Metal–Oxide–Semiconductor High-Electron-Mobility Transistors, Nanoscale Research Letters **11**, 235 (2016).

[26] Z. Liu, P.-G. Li, Y.-S. Zhi, X.-L. Wang, X.-L. Chu and W.-H. Tang, Review of gallium oxide based field-effect transistors and Schottky barrier diodes, Chinese Physics B **28**, 017105 (2019).

[27] S. Krishnamoorthy, Z. Xia, S. Bajaj, M. Brenner and S. Rajan, Delta-doped β-gallium oxide field-effect transistor, Applied Physics Express **10**, 051102 (2017).

[28] K. D. Chabak, D. E. Walker, A. J. Green, A. Crespo, M. Lindquist, K. Leedy, S. Tetlak, R. Gilbert, N. A. Moser and G. Jessen, presented at the 2018 IEEE MTT-S International Microwave Workshop Series on Advanced Materials and Processes for RF and THz Applications (IMWS-AMP), 2018 (unpublished).

[29] B. Chatterjee, K. Zeng, C. D. Nordquist, U. Singisetti and S. Choi, Device-Level Thermal Management of Gallium Oxide Field-Effect Transistors, IEEE Transactions on Components, Packaging and Manufacturing Technology **9**, 2352-2365 (2019).

[30] J.-W. Yu, P.-C. Yeh, S.-L. Wang, Y.-R. Wu, M.-H. Mao, H.-H. Lin and L.-H. Peng, Short channel effects on gallium nitride/gallium oxide nanowire transistors, Applied Physics Letters **101**, 183501 (2012).

[31] L. Chen, W. Xu, W. Liu, S. Han, P. Cao, M. Fang, D. Zhu and Y. Lu, Polymer-Assisted Deposition of Gallium Oxide for Thin-Film Transistor Applications, ACS Applied Materials & Interfaces **11**, 29078-29085 (2019).

[32] J. Sheng, E. J. Park, B. Shong and J.-S. Park, Atomic Layer Deposition of an Indium Gallium Oxide Thin Film for Thin-Film Transistor Applications, ACS Applied Materials & Interfaces **9**, 23934-23940 (2017).

[33] R. E. Presley, D. Hong, H. Q. Chiang, C. M. Hung, R. L. Hoffman and J. F. Wager, Transparent ring oscillator based on indium gallium oxide thin-film transistors, Solid-State Electronics **50**, 500-503 (2006).

[34] A. M. Armstrong, M. H. Crawford, A. Jayawardena, A. Ahyi and S. Dhar, Role of self-trapped holes in the photoconductive gain of β-gallium oxide Schottky diodes, Journal of Applied Physics **119**, 103102 (2016).

[35] B. Chatterjee, A. Jayawardena, E. Heller, D. W. Snyder, S. Dhar and S. Choi, Thermal characterization of gallium oxide Schottky barrier diodes, Review of Scientific Instruments **89**, 114903 (2018).

[36] L. Li, E. Auer, M. Liao, X. Fang, T. Zhai, U. K. Gautam, A. Lugstein, Y. Koide, Y. Bando and D. Golberg, Deep-ultraviolet solar-blind photoconductivity of individual gallium oxide nanobelts, Nanoscale **3**, 1120-1126 (2011).

[37] S. H. Lee, S. B. Kim, Y.-J. Moon, S. M. Kim, H. J. Jung, M. S. Seo, K. M. Lee, S.-K. Kim and S. W. Lee, High-Responsivity Deep-Ultraviolet-Selective Photodetectors Using Ultrathin Gallium Oxide Films, ACS Photonics **4**, 2937-2943 (2017).

[38] X. Chen, F.-F. Ren, J. Ye and S. Gu, Gallium oxide-based solar-blind ultraviolet photodetectors, Semiconductor Science and Technology **35**, 023001 (2020).

[39] X. Chen, F. Ren, S. Gu and J. Ye, Review of gallium-oxide-based solar-blind ultraviolet photodetectors, Photon. Res. **7**, 381-415 (2019).

[40] T. Chang, S. Chang, C. J. Chiu, C. Wei, Y. Juan and W. Weng, Bandgap-Engineered in Indium–Gallium–Oxide Ultraviolet Phototransistors, IEEE Photonics Technology Letters **27**, 915-918 (2015).

[41] T. H. Chang, C. J. Chiu, S. J. Chang, T. Y. Tsai, T. H. Yang, Z. D. Huang and W. Y. Weng, Amorphous InGaZnO ultraviolet phototransistors with double-stack Ga_2O_3/SiO_2 dielectric, Applied Physics Letters **102**, 221104 (2013).

[42] Q. Chen, Y. Zhang, T. Zheng, Z. Liu, L. Wu, Z. Wang and J. Li, Polarization detection in deep-ultraviolet light with monoclinic gallium oxide nanobelts, Nanoscale Advances **2**, 2705-2712 (2020).

[43] T. G. Allen and A. Cuevas, Electronic passivation of silicon surfaces by thin films of atomic layer deposited gallium oxide, Applied Physics Letters **105**, 031601 (2014).

[44] H. Hao, X. Chen, Z. Li, Y. Shen, H. Wang, Y. Zhao, R. Huang, T. Liu, J. Liang, Y. An, Q. Peng and S. Ding, Remote plasma-enhanced atomic layer deposition of gallium oxide thin films with NH_3 plasma pretreatment, Journal of Semiconductors **40**, 012806 (2019).

[45] H. Kröncke, F. Maudet, S. Banerjee, J. Albert, S. Wiesner, V. Deshpande and C. Dubourdieu, Effect of O_2 plasma exposure time during atomic layer deposition of amorphous gallium oxide, Journal of Vacuum Science & Technology A **39**, 052408 (2021).

[46] R. O'Donoghue, J. Rechmann, M. Aghaee, D. Rogalla, H.-W. Becker, M. Creatore, A. D. Wieck and A. Devi, Low temperature growth of gallium oxide thin films via plasma enhanced atomic layer deposition, Dalton Transactions **46**, 16551-16561 (2017).

[47] T. G. Allen and A. Cuevas, Plasma enhanced atomic layer deposition of gallium oxide on crystalline silicon: demonstration of surface passivation and negative interfacial charge, physica status solidi (RRL) – Rapid Research Letters **9**, 220-224 (2015).

[48] A. Mahmoodinezhad, C. Janowitz, F. Naumann, P. Plate, H. Gargouri, K. Henkel, D. Schmeißer and J. I. Flege, Low-temperature growth of gallium oxide thin films by plasma-enhanced atomic layer deposition, Journal of Vacuum Science & Technology A **38**, 022404 (2020).

[49] V. D. Wheeler, N. Nepal, D. R. Boris, S. B. Qadri, L. O. Nyakiti, A. Lang, A. Koehler, G. Foster, S. G. Walton, C. R. Eddy and D. J. Meyer, Phase Control of Crystalline Ga_2O_3 Films by Plasma-Enhanced Atomic Layer Deposition, Chemistry of Materials **32**, 1140-1152 (2020).

[50] Y. Lee, N. R. Johnson and S. M. George, Thermal Atomic Layer Etching of Gallium Oxide Using Sequential Exposures of HF and Various Metal Precursors, Chemistry of Materials **32**, 5937-5948 (2020).

[51] K. A. Hatch, D. C. Messina, X. Wang and R. J. Nemanich, Plasma Enhanced Atomic Layer Deposition and Atomic Layer Etching of Gallium Oxide Using Trimethylgallium, (Unpublished).

[52] D. C. Messina, K. A. Hatch, X. Wang, D. Smith, Y. Zhao and R. J. Nemanich, Atomic layer etching of gallium nitride (0001) enabled by water vapor or remote O_2-plasma oxidation, (unpublished).

[53] J. A. Murdzek, A. Rajashekhar, R. S. Makala and S. M. George, Thermal atomic layer etching of amorphous and crystalline Al_2O_3 films, Journal of Vacuum Science & Technology A **39**, 042602 (2021).

[54] R. d'Agostino and D. L. Flamm, Plasma etching of Si and SiO_2 in SF_6–O_2 mixtures, Journal of Applied Physics **52**, 162-167 (1981).

[55] V. M. Donnelly, D. L. Flamm, W. C. Dautremont-Smith and D. J. Werder, Anisotropic etching of SiO_2 in low-frequency CF_4/O_2 and NF_3/Ar plasmas, Journal of Applied Physics **55**, 242-252 (1984).

[56] P. Machima and N. Hershkowitz, SiO_2 and Si_3N_4 etch mechanisms in NF_3/hydrocarbon plasma, Journal of Physics D: Applied Physics **39**, 673-684 (2006).

[57] M. Matsui and K. Kuwahara, Highly selective SiO_2 etching over Si_3N_4 using a cyclic process with BCl_3 and fluorocarbon gas chemistries, Japanese Journal of Applied Physics **57**, 06JB01 (2018).

REFERENCES

CHAPTER 1 – INTRODUCTION:

S. Fujita, Wide-bandgap semiconductor materials: For their full bloom, Japanese Journal of Applied Physics **54**, 030101 (2015).

J. Y. Tsao, S. Chowdhury, M. A. Hollis, D. Jena, N. M. Johnson, K. A. Jones, R. J. Kaplar, S. Rajan, C. G. Van de Walle, E. Bellotti, C. L. Chua, R. Collazo, M. E. Coltrin, J. A. Cooper, K. R. Evans, S. Graham, T. A. Grotjohn, E. R. Heller, M. Higashiwaki, M. S. Islam, P. W. Juodawlkis, M. A. Khan, A. D. Koehler, J. H. Leach, U. K. Mishra, R. J. Nemanich, R. C. N. Pilawa-Podgurski, J. B. Shealy, Z. Sitar, M. J. Tadjer, A. F. Witulski, M. Wraback and J. A. Simmons, Ultrawide-Bandgap Semiconductors: Research Opportunities and Challenges, Advanced Electronic Materials **4**, 1600501 (2018).

M. Higashiwaki, R. Kaplar, J. Pernot and H. Zhao, Ultrawide bandgap semiconductors, Applied Physics Letters **118**, 200401 (2021).

S. Guha and N. A. Bojarczuk, Ultraviolet and violet GaN light emitting diodes on silicon, Applied Physics Letters **72**, 415-417 (1998).

S. Han, S. Yang and K. Sheng, Fluorine-Implanted Termination for Vertical GaN Schottky Rectifier With High Blocking Voltage and Low Forward Voltage Drop, IEEE Electron Device Letters **40**, 1040-1043 (2019).

H. Umezawa, M. Nagase, Y. Kato and S.-i. Shikata, High temperature application of diamond power device, Diamond and Related Materials **24**, 201-205 (2012).

I. C. Kizilyalli, T. Prunty and O. Aktas, 4-kV and 2.8-mΩ -cm^{-2} Vertical GaN p-n Diodes With Low Leakage Currents, IEEE Electron Device Letters **36**, 1073-1075 (2015).

A. Alzahrani, A. Alruqi, B. Karki, M. Kalutarakoralalage, J. Jasinski and G. U. Sumanasekera, Direct fabrication and characterization of vertically stacked Graphene/h-BN/Graphene tunnel junctions, Nano Express (2021).

H. Fu, K. Fu, C. Yang, H. Liu, K. A. Hatch, P. Peri, D. Herath Mudiyanselage, B. Li, T.-H. Kim, S. R. Alugubelli, P.-Y. Su, D. C. Messina, X. Deng, C.-Y. Cheng, R. Vatan Meidanshahi, X. Huang, H. Chen, T.-H. Yang, J. Zhou, A. M. Armstrong,

A. A. Allerman, E. T. Yu, J. Han, S. M. Goodnick, D. J. Smith, R. J. Nemanich, F. A. Ponce and Y. Zhao, Selective area regrowth and doping for vertical gallium nitride power devices: Materials challenges and recent progress, Materials Today (2021).

Y. Zhang, Z. Liu, M. J. Tadjer, M. Sun, D. Piedra, C. Hatem, T. J. Anderson, L. E. Luna, A. Nath, A. D. Koehler, H. Okumura, J. Hu, X. Zhang, X. Gao, B. N. Feigelson, K. D. Hobart and T. Palacios, Vertical GaN Junction Barrier Schottky Rectifiers by Selective Ion Implantation, IEEE Electron Device Letters **38**, 1097-1100 (2017).

Y. Zhang, M. Sun, Z. Liu, D. Piedra, M. Pan, X. Gao, Y. Lin, A. Zubair, L. Yu and T. Palacios, presented at the 2016 IEEE International Electron Devices Meeting (IEDM), 2016 (unpublished).

F. A. Koeck, M. Benipal, H. Surdi and R. J. Nemanich, presented at the 2020 IEEE 21st International Conference on Vacuum Electronics (IVEC), 2020 (unpublished).

S. Zhao, S. Y. Woo, S. M. Sadaf, Y. Wu, A. Pofelski, D. A. Laleyan, R. T. Rashid, Y. Wang, G. A. Botton and Z. Mi, Molecular beam epitaxy growth of Al-rich AlGaN nanowires for deep ultraviolet optoelectronics, APL Materials **4**, 086115 (2016).

V. Jmerik, A. Toropov, V. Davydov and S. Ivanov, Monolayer-Thick GaN/AlN Multilayer Heterostructures for Deep-Ultraviolet Optoelectronics, physica status solidi (RRL) – Rapid Research Letters **15**, 2100242 (2021).

W. Sun, C.-K. Tan and N. Tansu, AlN/GaN Digital Alloy for Mid- and Deep-Ultraviolet Optoelectronics, Scientific Reports **7**, 11826 (2017).

J. Holmes, M. Dutta, F. A. Koeck, M. Benipal, J. Brown, B. Fox, R. Hathwar, H. Johnson, M. Malakoutian, M. Saremi, A. Zaniewski, R. Alarcon, S. Chowdhury, S. M. Goodnick and R. J. Nemanich, A 4.5 μm PIN diamond diode for detecting slow neutrons, Nuclear Instruments and Methods in Physics Research Section A: Accelerators, Spectrometers, Detectors and Associated Equipment **903**, 297-301 (2018).

J. M. Holmes, M. Dutta, F. A. Koeck, M. K. Benipal, R. Hathwar, J. Brown, B. Fox, H. Johnson, A. Zaniewski, R. Alarcon, S. Chowdhury, S. M. Goodnick and R.

J. Nemanich, Neutralizing the polarization effect of diamond diode detectors using periodic forward bias pulses, Diamond and Related Materials **94**, 162-165 (2019).

J. Holmes, J. Brown, F. A. Koeck, H. Johnson, M. K. Benipal, P. Kandlakunta, A. Zaniewski, R. Alarcon, R. Cao, S. M. Goodnick and R. J. Nemanich, Performance of 5-μm PIN diamond diodes as thermal neutron detectors, Nuclear Instruments and Methods in Physics Research Section A: Accelerators, Spectrometers, Detectors and Associated Equipment **961**, 163601 (2020).

R. Hall, 5G and GaN: Future innovations (Published, 2021)

N. Flaherty, (eenewseurope.com, 2021).

D. Zhuang and J. H. Edgar, Wet etching of GaN, AlN, and SiC: a review, Materials Science and Engineering: R: Reports **48**, 1-46 (2005).

S. J. Pearton, J. C. Zolper, R. J. Shul and F. Ren, GaN: Processing, defects, and devices, Journal of Applied Physics **86**, 1-78 (1999).

M. E. Lin, Z. F. Fan, Z. Ma, L. H. Allen and H. Morkoç, Reactive ion etching of GaN using BCl_3, Applied Physics Letters **64**, 887-888 (1994).

R. J. Shul, G. B. McClellan, S. A. Casalnuovo, D. J. Rieger, S. J. Pearton, C. Constantine, C. Barratt, R. F. K. Jr., C. Tran and M. Schurman, Inductively coupled plasma etching of GaN, Applied Physics Letters **69**, 1119-1121 (1996).

S. Huang, Q. Jiang, K. Wei, G. Liu, J. Zhang, X. Wang, Y. Zheng, B. Sun, C. Zhao, H. Liu, Z. Jin, X. Liu, H. Wang, S. Liu, Y. Lu, C. Liu, S. Yang, Z. Tang, J. Zhang, Y. Hao and K. J. Chen, presented at the 2014 IEEE International Electron Devices Meeting, 2014 (unpublished).

H. S. Lee, D. Y. Jung, Y. Park, J. Na, H. G. Jang, H. S. Lee, C. H. Jun, J. Park, S. O. Ryu, S. C. Ko and E. S. Nam, 0.34 V_T AlGaN/GaN-on-Si Large Schottky Barrier Diode With Recessed Dual Anode Metal, IEEE Electron Device Letters **36**, 1132-1134 (2015).

J. H. Choi, Y. Mao and J. P. Chang, Development of hafnium based high-k materials—A review, Materials Science and Engineering: R: Reports **72**, 97-136 (2011).

N. R. Johnson, J. K. Hite, M. A. Mastro, C. R. EddyJr. and S. M. George, Thermal atomic layer etching of crystalline GaN using sequential exposures of XeF_2 and BCl_3, Applied Physics Letters **114**, 243103 (2019).

P. Peri, K. Fu, H. Fu, Y. Zhao and D. J. Smith, Characterization of As-Grown and Regrown GaN-on-GaN Structures for Vertical p-n Power Devices, Journal of Electronic Materials **50**, 2637-2642 (2021).

M. R. Esmaeili-Rad, F. Li, A. Sazonov and A. Nathan, Stability of nanocrystalline silicon bottom-gate thin film transistors with silicon nitride gate dielectric, Journal of Applied Physics **102**, 064512 (2007).

S. Takagi, T. Maeda, N. Taoka, M. Nishizawa, Y. Morita, K. Ikeda, Y. Yamashita, M. Nishikawa, H. Kumagai, R. Nakane, S. Sugahara and N. Sugiyama, Gate dielectric formation and MIS interface characterization on Ge, Microelectronic Engineering **84**, 2314-2319 (2007).

C. G. Parker, G. Lucovsky and J. R. Hauser, Ultrathin oxide-nitride gate dielectric MOSFET's, IEEE Electron Device Letters **19**, 106-108 (1998).

S. K. Jang, J. Youn, Y. J. Song and S. Lee, Synthesis and Characterization of Hexagonal Boron Nitride as a Gate Dielectric, Scientific Reports **6**, 30449 (2016).

T. P. Ma, Making silicon nitride film a viable gate dielectric, IEEE Transactions on Electron Devices **45**, 680-690 (1998).

M. Coll, J. Fontcuberta, M. Althammer, M. Bibes, H. Boschker, A. Calleja, G. Cheng, M. Cuoco, R. Dittmann, B. Dkhil, I. El Baggari, M. Fanciulli, I. Fina, E. Fortunato, C. Frontera, S. Fujita, V. Garcia, S. T. B. Goennenwein, C. G. Granqvist, J. Grollier, R. Gross, A. Hagfeldt, G. Herranz, K. Hono, E. Houwman, M. Huijben, A. Kalaboukhov, D. J. Keeble, G. Koster, L. F. Kourkoutis, J. Levy, M. Lira-Cantu, J. L. MacManus-Driscoll, J. Mannhart, R. Martins, S. Menzel, T. Mikolajick, M. Napari, M. D. Nguyen, G. Niklasson, C. Paillard, S. Panigrahi, G. Rijnders, F. Sánchez, P. Sanchis, S. Sanna, D. G. Schlom, U. Schroeder, K. M. Shen, A. Siemon, M. Spreitzer, H. Sukegawa, R. Tamayo, J. van den Brink, N. Pryds and F.

M. Granozio, Towards Oxide Electronics: a Roadmap, Applied Surface Science **482**, 1-93 (2019).

C. T. Carver, J. J. Plombon, P. E. Romero, S. Suri, T. A. Tronic and R. B. Turkot, Atomic Layer Etching: An Industry Perspective, ECS Journal of Solid State Science and Technology **4**, N5005-N5009 (2015).

R. L. Puurunen, Surface chemistry of atomic layer deposition: A case study for the trimethylaluminum/water process, Journal of Applied Physics **97**, 121301 (2005).

V. Miikkulainen, M. Leskelä, M. Ritala and R. L. Puurunen, Crystallinity of inorganic films grown by atomic layer deposition: Overview and general trends, Journal of Applied Physics **113**, 021301 (2013).

N. E. Richey, C. de Paula and S. F. Bent, Understanding chemical and physical mechanisms in atomic layer deposition, The Journal of Chemical Physics **152**, 040902 (2020).

S. M. George, A. W. Ott and J. W. Klaus, Surface Chemistry for Atomic Layer Growth, The Journal of Physical Chemistry **100**, 13121-13131 (1996).

M. Mäntymäki, J. Hämäläinen, E. Puukilainen, F. Munnik, M. Ritala and M. Leskelä, Atomic Layer Deposition of LiF Thin Films from Lithd and TiF_4 Precursors, Chemical Vapor Deposition **19**, 111-116 (2013).

T. Pilvi, E. Puukilainen, U. Kreissig, M. Leskelä and M. Ritala, Atomic Layer Deposition of MgF_2 Thin Films Using TaF_5 as a Novel Fluorine Source, Chemistry of Materials **20**, 5023-5028 (2008).

T. Pilvi, M. Ritala, M. Leskelä, M. Bischoff, U. Kaiser and N. Kaiser, Atomic layer deposition process with TiF_4 as a precursor for depositing metal fluoride thin films, Appl. Opt. **47**, C271-C274 (2008).

M. Mäntymäki, M. J. Heikkilä, E. Puukilainen, K. Mizohata, B. Marchand, J. Räisänen, M. Ritala and M. Leskelä, Atomic Layer Deposition of AlF_3 Thin Films Using Halide Precursors, Chemistry of Materials **27**, 604-611 (2015).

T. Pilvi, K. Arstila, M. Leskelä and M. Ritala, Novel ALD Process for Depositing CaF_2 Thin Films, Chemistry of Materials **19**, 3387-3392 (2007).

T. Pilvi, E. Puukilainen, F. Munnik, M. Leskelä and M. Ritala, ALD of YF_3 Thin Films from TiF_4 and $Y(thd)_3$ Precursors, Chemical Vapor Deposition **15**, 27-32 (2009).

Y. Lee, H. Sun, M. J. Young and S. M. George, Atomic Layer Deposition of Metal Fluorides Using HF–Pyridine as the Fluorine Precursor, Chemistry of Materials **28**, 2022-2032 (2016).

Y. Lee, J. W. DuMont, A. S. Cavanagh and S. M. George, Atomic Layer Deposition of AlF_3 Using Trimethylaluminum and Hydrogen Fluoride, Journal of Physical Chemistry C **119**, 14185-14194 (2015).

M. Ylilammi and T. Ranta-aho, Metal Fluoride Thin Films Prepared by Atomic Layer Deposition, Journal of The Electrochemical Society **141**, 1278-1284 (1994).

J. Hennessy and S. Nikzad, Atomic Layer Deposition of Lithium Fluoride Optical Coatings for the Ultraviolet, Inorganics **6**, 46 (2018).

J.-P. Jones, J. Hennessy, K. J. Billings, F. C. Krause, J. Pasalic and R. V. Bugga, Communication—Atomic Layer Deposition of Aluminum Fluoride for Lithium Metal Anodes, Journal of The Electrochemical Society **167**, 060502 (2020).

J. Hennessy, A. D. Jewell, K. Balasubramanian and S. Nikzad, Ultraviolet optical properties of aluminum fluoride thin films deposited by atomic layer deposition, Journal of Vacuum Science & Technology A **34**, 01A120 (2015).

J. Hennessy, A. D. Jewell, F. Greer, M. C. Lee and S. Nikzad, Atomic layer deposition of magnesium fluoride via bis(ethylcyclopentadienyl)magnesium and anhydrous hydrogen fluoride, Journal of Vacuum Science & Technology A **33**, 01A125 (2014).

M. F. J. Vos, H. C. M. Knoops, R. A. Synowicki, W. M. M. Kessels and A. J. M. Mackus, Atomic layer deposition of aluminum fluoride using $Al(CH_3)_3$ and SF_6 plasma, Applied Physics Letters **111**, 113105 (2017).

M. F. J. Vos, H. C. M. Knoops, W. M. M. Kessels and A. J. M. Mackus, Reaction Mechanisms during Atomic Layer Deposition of AlF_3 Using $Al(CH_3)_3$ and SF_6 Plasma, The Journal of Physical Chemistry C (2021).

Z. Huang, D. C. Messina, B. Eller, F. A. Koeck, P. Scowen and R. J. Nemanich, Multilayer ultraviolet reflective coating based on atomic layer deposited aluminum oxide and fluoride Journal of Vacuum Science & Technology A **39**, 042402 (2021).

K. J. Kanarik, T. Lill, E. A. Hudson, S. Sriraman, S. Tan, J. Marks, V. Vahedi and R. A. Gottscho, Overview of atomic layer etching in the semiconductor industry, Journal of Vacuum Science & Technology A **33**, 020802 (2015).

A. Fischer, A. Routzahn, S. M. George and T. Lill, Thermal atomic layer etching: A review, Journal of Vacuum Science & Technology A **39**, 030801 (2021).

S. M. George, Mechanisms of Thermal Atomic Layer Etching, Accounts of Chemical Research **53**, 1151-1160 (2020).

W. Lu, Y. Lee, J. Murdzek, J. Gertsch, A. Vardi, L. Kong, S. M. George and J. A. d. Alamo, presented at the 2018 IEEE International Electron Devices Meeting (IEDM), 2018 (unpublished).

W. Lu, Y. Lee, J. C. Gertsch, J. A. Murdzek, A. S. Cavanagh, L. Kong, J. A. del Alamo and S. M. George, In Situ Thermal Atomic Layer Etching for Sub-5 nm InGaAs Multigate MOSFETs, Nano Letters **19**, 5159-5166 (2019).

M.-L. Chen, X. Sun, H. Liu, H. Wang, Q. Zhu, S. Wang, H. Du, B. Dong, J. Zhang, Y. Sun, S. Qiu, T. Alava, S. Liu, D.-M. Sun and Z. Han, A FinFET with one atomic layer channel, Nature Communications **11**, 1205 (2020).

F. K. Hsueh, C. Y. Lee, C. X. Xue, C. H. Shen, J. M. Shieh, B. Y. Chen, Y. C. Chiu, H. C. Chen, M. H. Kao, W. H. Huang, K. S. Li, C. T. Wu, K. L. Lin, K. M. Chen, G. W. Huang, M. F. Chang, C. Hu and W. K. Yeh, presented at the 2019 IEEE International Electron Devices Meeting (IEDM), 2019 (unpublished).

J. Hennessy, C. S. Moore, K. Balasubramanian, A. D. Jewell, K. France and S. Nikzad, Enhanced atomic layer etching of native aluminum oxide for ultraviolet optical applications, Journal of Vacuum Science & Technology A **35**, 041512 (2017).

C. Auth, C. Allen, A. Blattner, D. Bergstrom, M. Brazier, M. Bost, M. Buehler, V. Chikarmane, T. Ghani, T. Glassman, R. Grover, W. Han, D. Hanken, M. Hattendorf, P. Hentges, R. Heussner, J. Hicks, D. Ingerly, P. Jain, S. Jaloviar, R. James, D. Jones, J. Jopling, S. Joshi, C. Kenyon, H. Liu, R. McFadden, B. McIntyre, J. Neirynck, C. Parker, L. Pipes, I. Post, S. Pradhan, M. Prince, S. Ramey, T. Reynolds, J. Roesler, J. Sandford, J. Seiple, P. Smith, C. Thomas, D. Towner, T. Troeger, C. Weber, P. Yashar, K. Zawadzki and K. Mistry, presented at the 2012 Symposium on VLSI Technology (VLSIT), 2012 (unpublished).

N. Draeger, FinFETs Give Way to Gate-All-Around (Lam Research, Published, 2020)

CHAPTER 2 – EXPERIMENTAL TECHNIQUES:

A. Einstein, Concerning an Heuristic Point of View Toward the Emission and Transformation of Light, American Journal of Physics **33**, 5 (1965).

M. P. Seah and W. A. Dench, Quantitative electron spectroscopy of surfaces: A standard data base for electron inelastic mean free paths in solids, Surface and Interface Analysis **1**, 2-11 (1979).

A. G. Shard, Practical guides for x-ray photoelectron spectroscopy: Quantitative XPS, Journal of Vacuum Science & Technology A **38**, 041201 (2020).

J. F. Moulder, W. F. Stickle, P. E. Sobol and K. D. Bomben, (Perkin-Elmer Corporation, Eden Prairie, Minnesota, USA 1979), pp. 25-26.

J. H. Scofield, Hartree-Slater subshell photoionization cross-sections at 1254 and 1487 eV, Journal of Electron Spectroscopy and Related Phenomena **8**, 129-137 (1976).

C. J. Powell, Practical guide for inelastic mean free paths, effective attenuation lengths, mean escape depths, and information depths in x-ray photoelectron spectroscopy, Journal of Vacuum Science & Technology A **38**, 023209 (2020).

H. Shinotsuka, S. Tanuma, C. J. Powell and D. R. Penn, Calculations of electron inelastic mean free paths. X. Data for 41 elemental solids over the 50 eV to 200 keV range with the relativistic full Penn algorithm, Surface and Interface Analysis **47**, 871-888 (2015).

M. P. Seah, An accurate and simple universal curve for the energy-dependent electron inelastic mean free path, Surface and Interface Analysis **44**, 497-503 (2012).

A. Jablonski and J. Zemek, Overlayer thickness determination by XPS using the multiline approach, Surface and Interface Analysis **41**, 193-204 (2009).

A. Jablonski, Evaluation of procedures for overlayer thickness determination from XPS intensities, Surface Science **688**, 14-24 (2019).

A. Jablonski and C. J. Powell, Improved algorithm for calculating transport cross sections of electrons with energies from 50 eV to 30 keV, Physical Review B **76**, 085123 (2007).

A. Jablonski, Corrigendum: Photoelectron transport in the surface region of solids: universal analytical formalism for quantitative applications of electron spectroscopies (2015J. Phys. D: Appl. Phys.48075301), Journal of Physics D: Applied Physics **49**, 289501 (2016).

NIST Database for the Simulation of Electron Spectra For Surface Analysis (SESSA), (National Institute of Standards and Technology, Gaithersburg, MD, 2018); https://www.nist.gov/srd/nist-standard-reference-database-100

D. C. Messina, B. S. Eller, P. Scowen and R. J. Nemanich, Comparison of aluminum fluoride thin films growth by thermal and plasma enhanced atomic layer deposition, (unpublished).

J. Yang, B. S. Eller, M. Kaur and R. J. Nemanich, Characterization of plasma-enhanced atomic layer deposition of Al2O3 using dimethylaluminum isopropoxide, Journal of Vacuum Science & Technology A **32**, 021514 (2014).

FS-1 Manual v1.50. (Film Sense, LLC, Lincoln, NE, 2017).

R. M. A. Azzam, Division-of-amplitude Photopolarimeter (DOAP) for the Simultaneous Measurement of All Four Stokes Parameters of Light, Optica Acta: International Journal of Optics **29**, 685-689 (1982).

N. W. Ashcroft and N. D. Mermin, in *Solid State Physics*, edited by N. W. Ashcroft and N. D. Mermin (Cengage Learning, 2021).

O. Stenzel, in *Optical Coatings: Material Aspects in Theory and Practive*, edited by O. Stenzel (Springer, 2014), pp. 21.

D. A. G. Bruggeman, Berechnung verschiedener physikalischer Konstanten von heterogenen Substanzen. I. Dielektrizitätskonstanten und Leitfähigkeiten der Mischkörper aus isotropen Substanzen, Annalen der Physik **416**, 636-664 (1935).

R. L. Puurunen, Surface chemistry of atomic layer deposition: A case study for the trimethylaluminum/water process, Journal of Applied Physics **97**, 121301 (2005).

V. Miikkulainen, M. Leskelä, M. Ritala and R. L. Puurunen, Crystallinity of inorganic films grown by atomic layer deposition: Overview and general trends, Journal of Applied Physics **113**, 021301 (2013).

N. E. Richey, C. de Paula and S. F. Bent, Understanding chemical and physical mechanisms in atomic layer deposition, The Journal of Chemical Physics **152**, 040902 (2020).

H. Kim, Characteristics and applications of plasma enhanced-atomic layer deposition, Thin Solid Films **519**, 6639-6644 (2011).

H. B. Profijt, S. E. Potts, M. C. M. van de Sanden and W. M. M. Kessels, Plasma-Assisted Atomic Layer Deposition: Basics, Opportunities , and Challenges, Journal of Vacuum Science & Technology A **29**, 050801 (2011).

B. H. Kim, W. S. Jeon, S. H. Jung and B. T. Ahn, Interstitial Oxygen Incorporation into Silicon Substrate during Plasma Enhanced Atomic Layer Deposition of Al_2O_3, Electrochemical and Solid-State Letters **8**, G294 (2005).

S.-W. Kim, S.-H. Kwon, S.-J. Jeong and S.-W. Kang, Improvement of Copper Diffusion Barrier Properties of Tantalum Nitride Films by Incorporating Ruthenium Using PEALD, Journal of The Electrochemical Society **155**, H885 (2008).

T. O. Kääriäinen and D. C. Cameron, Plasma-Assisted Atomic Layer Deposition of Al_2O_3 at Room Temperature, Plasma Processes and Polymers **6**, S237-S241 (2009).

A. Foroughi-Abari and K. C. Cadien, *In-Situ* Spectroscopic Ellipsometry Study of Plasma-Enhanced ALD of Al_2O_3 on Chromium Substrates, Journal of The Electrochemical Society **159**, D59-D64 (2011).

H. Kim and I.-K. Oh, Review of plasma-enhanced atomic layer deposition: Technical enabler of nanoscale device fabrication, Japanese Journal of Applied Physics **53**, 03DA01 (2014).

M. A. Lieberman and A. J. Lichtenber, (John Wiley & Sons, New York, 2005).

K. J. Kanarik, T. Lill, E. A. Hudson, S. Sriraman, S. Tan, J. Marks, V. Vahedi and R. A. Gottscho, Overview of atomic layer etching in the semiconductor industry, Journal of Vacuum Science & Technology A **33**, 020802 (2015).

A. Fischer, A. Routzahn, S. M. George and T. Lill, Thermal atomic layer etching: A review, Journal of Vacuum Science & Technology A **39**, 030801 (2021).

S. M. George, Mechanisms of Thermal Atomic Layer Etching, Accounts of Chemical Research **53**, 1151-1160 (2020).

CHAPTER 3 – DEVELOPING ATOMIC LAYER PROCESSING REACTORS ENABLED BY FLUORINE CHEMISTRY:

G. Vass, G. Tarczay, G. Magyarfalvi, A. Bödi and L. Szepes, HeI Photoelectron Spectroscopy of Trialkylaluminum and Dialkylaluminum Hydride Compounds and Their Oligomers, Organometallics **21**, 2751-2757 (2002).

NIST Chemistry WebBook Standard Reference Database Number 69, (National Institute of Standards and Technology, 2021);

P. Jong-Chul and K. Bongkoo, Impedance model of helical resonator discharge, IEEE Transactions on Plasma Science **25**, 1398-1405 (1997).

MWH-5 Automatic Matching Impedance Network. (MKS, 2005).

MV Multi-Trap® High Capacity, High Efficiency Vacuum Inlet or Exhaust Trap. (Mass-Vac, North Billerica, MA, 2021).

Multi-Stage Dry Vacuum Pump. (Ebara Corporation).

Novasafe Dry Bed Abatement System. (CS Clean Systems, Danbury, CT, 2017).

Guide to Installation and Operation, Gas Detector SH-1003-WAD, SH-1007-WAD. (Bionics Instruments, Tokyo, Japan, 2009).

B. D. Piercy and M. D. Losego, Tree-based control software for multilevel sequencing in thin film deposition applications, Journal of Vacuum Science & Technology B **33**, 043201 (2015).

CHAPTER 4 – COMPARISON OF ALUMINUM FLUORIDE THIN FILMS GROWN BY THERMAL AND PLASMA ENHANCED ATOMIC LAYER DEPOSITION

D. König, R. Scholz, D. R. T. Zahn and G. Ebest, Band diagram of the $AlF_3/SiO_2/Si$ system, Journal of Applied Physics **97**, 093707 (2005).

J. L. Navarro, E. A. Albanesi, R. Vidal and J. Ferrón, A study on the structural, electronic and optical properties of the α-AlF_3 compound, Materials Research Bulletin **83**, 615-622 (2016).

C.-C. Lee, M.-C. Liu, M. Kaneko, K. Nakahira and Y. Takano, Characterization of AlF_3 thin films at 193 nm by thermal evaporation, Appl. Opt. **44**, 7333-7338 (2005).

M.-C. Liu, C.-C. Lee, B.-H. Liao, M. Kaneko, K. Nakahira and Y. Takano, Fluoride antireflection coatings deposited at 193 nm, Appl. Opt. **47**, C214-C218 (2008).

T. Yoshida, K. Nishimoto, K. Sekine and K. Etoh, Fluoride antireflection coatings for deep ultraviolet optics deposited by ion-beam sputtering, Appl. Opt. **45**, 1375-1379 (2006).

Z. Huang, D. C. Messina, B. Eller, F. A. Koeck, P. Scowen and R. J. Nemanich, Multilayer ultraviolet reflective coating based on atomic layer deposited aluminum oxide and fluoride Journal of Vacuum Science & Technology A **39**, 042402 (2021).

J. Hennessy, K. Balasubramanian, C. Moore, A. Jewell, S. Nikzad, K. France and M. Quijada, Performance and prospects of far ultraviolet aluminum mirrors protected by atomic layer deposition, Journal of Astronomical Telescopes, Instruments, and Systems **2**, 041206 (2016).

J. Del Hoyo and M. Quijada, *Enhanced aluminum reflecting and solar-blind filter coatings for the far-ultraviolet*. (SPIE, 2017).

A. Egan, B. Fleming, J. Wiley, M. Quijada, J. Del Hoyo, J. Hennessy, B. Hicks, K. France, N. Kruczek and N. Erickson, *The development and characterization of advanced broadband mirror coatings for the far-UV*. (SPIE, 2017).

Y. Wang, J. Qiu, Z. Yu, H. Ming, M. Li, S. Zhang and Y. Yang, AlF_3-modified $LiCoPO_4$ for an advanced cathode towards high energy lithium-ion battery, Ceramics International **44**, 1312-1320 (2018).

G. R. Li, X. Feng, Y. Ding, S. H. Ye and X. P. Gao, AlF_3-coated $Li(Li_{0.17}Ni_{0.25}Mn_{0.58})O_2$ as cathode material for Li-ion batteries, Electrochimica Acta **78**, 308-315 (2012).

J.-P. Jones, J. Hennessy, K. J. Billings, F. C. Krause, J. Pasalic and R. V. Bugga, Communication—Atomic Layer Deposition of Aluminum Fluoride for Lithium Metal Anodes, Journal of The Electrochemical Society **167**, 060502 (2020).

Y. Chung, Y. Shin, Y. Liu, J. S. Park, C. L. Margez and T. A. Greszler, Synergetic effect of carbon and AlF_3 coatings on the lithium titanium oxide anode material for high power lithium-ion batteries, Journal of Electroanalytical Chemistry **837**, 240-245 (2019).

C.-T. Chu, A. Mondal, N. V. Kosova and J.-Y. Lin, Improved high-temperature cyclability of AlF_3 modified spinel $LiNi_{0.5}Mn_{1.5}O_4$ cathode for lithium-ion batteries, Applied Surface Science **530**, 147169 (2020).

Y. K. Sun, S. W. Cho, S. W. Lee, C. S. Yoon and K. Amine, AlF_3-Coating to Improve High Voltage Cycling Performance of $Li[Ni_{1/3}Co_{1/3}Mn_{1/3}]O_2$ Cathode Materials for Lithium Secondary Batteries, Journal of The Electrochemical Society **154**, A168 (2007).

J. Zheng, M. Gu, J. Xiao, B. J. Polzin, P. Yan, X. Chen, C. Wang and J.-G. Zhang, Functioning Mechanism of AlF_3 Coating on the Li- and Mn-Rich Cathode Materials, Chemistry of Materials **26**, 6320-6327 (2014).

D. König and G. Ebest, Novel external field source by localization of electrons for improvement of solar cells, Solar Energy Materials and Solar Cells **75**, 335-343 (2003).

D. König and G. Ebest, The negatively charged insulator-semiconductor structure: concepts, technological considerations and applications, Solid-State Electronics **44**, 111-116 (2000).

D. König, D. R. T. Zahn and G. Ebest, Field effect of fixed negative charges on oxidized silicon induced by AlF_3 layers with fluorine deficiency, Applied Surface Science **234**, 222-227 (2004).

I. Thurzo, T. U. Kampen, D. R. T. Zahn and D. König, Electron capture kinetics at AlF_3/SiO_2 interfaces, Applied Surface Science **212-213**, 753-759 (2003).

D. Konig, D. R. T. Zahn, R. Reich, K. Gottfried and G. Ebest, presented at the 3rd World Conference onPhotovoltaic Energy Conversion, 2003. Proceedings of, 2003 (unpublished).

D. König, G. Ebest, R. Scholz, S. Gemming, I. Thurzo, T. U. Kampen and D. R. T. Zahn, Evidence for high negative charge densities in AlF_3 coatings on oxidized silicon: a promising source for large drift fields, Physica E: Low-dimensional Systems and Nanostructures **14**, 259-262 (2002).

R. L. Puurunen, Surface chemistry of atomic layer deposition: A case study for the trimethylaluminum/water process, Journal of Applied Physics **97**, 121301 (2005).

V. Miikkulainen, M. Leskelä, M. Ritala and R. L. Puurunen, Crystallinity of inorganic films grown by atomic layer deposition: Overview and general trends, Journal of Applied Physics **113**, 021301 (2013).

N. E. Richey, C. de Paula and S. F. Bent, Understanding chemical and physical mechanisms in atomic layer deposition, The Journal of Chemical Physics **152**, 040902 (2020).

H. Kim, Characteristics and applications of plasma enhanced-atomic layer deposition, Thin Solid Films **519**, 6639-6644 (2011).

H. B. Profijt, S. E. Potts, M. C. M. van de Sanden and W. M. M. Kessels, Plasma-Assisted Atomic Layer Deposition: Basics, Opportunities , and Challenges, Journal of Vacuum Science & Technology A **29**, 050801 (2011).

B. H. Kim, W. S. Jeon, S. H. Jung and B. T. Ahn, Interstitial Oxygen Incorporation into Silicon Substrate during Plasma Enhanced Atomic Layer Deposition of Al_2O_3, Electrochemical and Solid-State Letters **8**, G294 (2005).

S.-W. Kim, S.-H. Kwon, S.-J. Jeong and S.-W. Kang, Improvement of Copper Diffusion Barrier Properties of Tantalum Nitride Films by Incorporating Ruthenium Using PEALD, Journal of The Electrochemical Society **155**, H885 (2008).

T. O. Kääriäinen and D. C. Cameron, Plasma-Assisted Atomic Layer Deposition of Al_2O_3 at Room Temperature, Plasma Processes and Polymers **6**, S237-S241 (2009).

A. Foroughi-Abari and K. C. Cadien, *In-Situ* Spectroscopic Ellipsometry Study of Plasma-Enhanced ALD of Al_2O_3 on Chromium Substrates, Journal of The Electrochemical Society **159**, D59-D64 (2011).

H. Kim and I.-K. Oh, Review of plasma-enhanced atomic layer deposition: Technical enabler of nanoscale device fabrication, Japanese Journal of Applied Physics **53**, 03DA01 (2014).

M. Mäntymäki, J. Hämäläinen, E. Puukilainen, F. Munnik, M. Ritala and M. Leskelä, Atomic Layer Deposition of LiF Thin Films from Lithd and TiF_4 Precursors, Chemical Vapor Deposition **19**, 111-116 (2013).

T. Pilvi, E. Puukilainen, U. Kreissig, M. Leskelä and M. Ritala, Atomic Layer Deposition of MgF_2 Thin Films Using TaF_5 as a Novel Fluorine Source, Chemistry of Materials **20**, 5023-5028 (2008).

T. Pilvi, M. Ritala, M. Leskelä, M. Bischoff, U. Kaiser and N. Kaiser, Atomic layer deposition process with TiF_4 as a precursor for depositing metal fluoride thin films, Appl. Opt. **47**, C271-C274 (2008).

M. Mäntymäki, M. J. Heikkilä, E. Puukilainen, K. Mizohata, B. Marchand, J. Räisänen, M. Ritala and M. Leskelä, Atomic Layer Deposition of AlF_3 Thin Films Using Halide Precursors, Chemistry of Materials **27**, 604-611 (2015).

T. Pilvi, K. Arstila, M. Leskelä and M. Ritala, Novel ALD Process for Depositing CaF_2 Thin Films, Chemistry of Materials **19**, 3387-3392 (2007).

T. Pilvi, E. Puukilainen, F. Munnik, M. Leskelä and M. Ritala, ALD of YF_3 Thin Films from TiF_4 and $Y(thd)_3$ Precursors, Chemical Vapor Deposition **15**, 27-32 (2009).

M. Putkonen, A. Szeghalmi, E. Pippel and M. Knez, Atomic layer deposition of metal fluorides through oxide chemistry, Journal of Materials Chemistry **21**, 14461-14465 (2011).

Y. Lee, H. Sun, M. J. Young and S. M. George, Atomic Layer Deposition of Metal Fluorides Using HF–Pyridine as the Fluorine Precursor, Chemistry of Materials **28**, 2022-2032 (2016).

Y. Lee, J. W. DuMont, A. S. Cavanagh and S. M. George, Atomic Layer Deposition of AlF_3 Using Trimethylaluminum and Hydrogen Fluoride, Journal of Physical Chemistry C **119**, 14185-14194 (2015).

M. Ylilammi and T. Ranta-aho, Metal Fluoride Thin Films Prepared by Atomic Layer Deposition, Journal of The Electrochemical Society **141**, 1278-1284 (1994).

J. Hennessy and S. Nikzad, Atomic Layer Deposition of Lithium Fluoride Optical Coatings for the Ultraviolet, Inorganics **6**, 46 (2018).

J. Hennessy, A. D. Jewell, K. Balasubramanian and S. Nikzad, Ultraviolet optical properties of aluminum fluoride thin films deposited by atomic layer deposition, Journal of Vacuum Science & Technology A **34**, 01A120 (2015).

J. Hennessy, A. D. Jewell, F. Greer, M. C. Lee and S. Nikzad, Atomic layer deposition of magnesium fluoride via bis(ethylcyclopentadienyl)magnesium and anhydrous hydrogen fluoride, Journal of Vacuum Science & Technology A **33**, 01A125 (2014).

D. H. K. Jackson, M. R. Laskar, S. Fang, S. Xu, R. G. Ellis, X. Li, M. Dreibelbis, S. E. Babcock, M. K. Mahanthappa, D. Morgan, R. J. Hamers and T. F. Kuech, Optimizing AlF_3 atomic layer deposition using trimethylaluminum and TaF_5: Application to high voltage Li-ion battery cathodes, Journal of Vacuum Science & Technology A **34**, 031503 (2016).

J. Hennessy, A. D. Jewell, J.-P. Jones, G. M. Crouch and S. Nikzad, Aluminum Precursor Interactions with Alkali Compounds in Thermal Atomic Layer Etching and Deposition Processes, ACS Applied Materials & Interfaces **13**, 4723-4730 (2021).

M. F. J. Vos, H. C. M. Knoops, R. A. Synowicki, W. M. M. Kessels and A. J. M. Mackus, Atomic layer deposition of aluminum fluoride using $Al(CH_3)_3$ and SF_6 plasma, Applied Physics Letters **111**, 113105 (2017).

M. F. J. Vos, H. C. M. Knoops, W. M. M. Kessels and A. J. M. Mackus, Reaction Mechanisms during Atomic Layer Deposition of AlF_3 Using $Al(CH_3)_3$ and SF_6 Plasma, The Journal of Physical Chemistry C (2021).

A. Makarowicz, C. L. Bailey, N. Weiher, E. Kemnitz, S. L. M. Schroeder, S. Mukhopadhyay, A. Wander, B. G. Searle and N. M. Harrison, Electronic structure of Lewis acid sites on high surface area aluminium fluorides: a combined XPS and ab initio investigation, Physical Chemistry Chemical Physics **11**, 5664-5673 (2009).

R. J. Carter, T. P. Schneider, J. S. Montgomery and R. J. Nemanich, In Situ Remote H-Plasma Cleaning of Patterned Si - SiO_2 Surfaces, Journal of The Electrochemical Society **141**, 3136-3140 (1994).

J. S. Montgomery, T. P. Schneider, R. J. Carter, J. P. Barnak, Y. L. Chen, J. R. Hauser and R. J. Nemanich, Morphology of Si(100) surfaces exposed to a remote H plasma, Applied Physics Letters **67**, 2194-2196 (1995).

S. W. King, R. F. Davis, R. J. Carter, T. P. Schneider and R. J. Nemanich, Hydrogen desorption kinetics for aqueous hydrogen fluoride and remote hydrogen plasma processed silicon (001) surfaces, Journal of Vacuum Science & Technology A **33**, 05E115 (2015).

Y. Yang, T. Sun, J. Shammas, M. Kaur, M. Hao and R. J. Nemanich, Electron affinity of cubic boron nitride terminated with vanadium oxide, Journal of Applied Physics **118**, 165310 (2015).

H. C. M. Knoops, T. Faraz, K. Arts and W. M. M. Kessels, Status and prospects of plasma-assisted atomic layer deposition, Journal of Vacuum Science & Technology A **37**, 030902 (2019).

R. M. A. Azzam, Division-of-amplitude Photopolarimeter (DOAP) for the Simultaneous Measurement of All Four Stokes Parameters of Light, Optica Acta: International Journal of Optics **29**, 685-689 (1982).

FS-1 Manual v1.50. (Film Sense, LLC, Lincoln, NE, 2017).

J. N. Hilfiker, J. Sun and N. Hong, in *Spectroscopic Ellipsometry for Photovoltaics: Volume 1: Fundamental Principles and Solar Cell Characterization*, edited by H. Fujiwara and R. W. Collins (Springer International Publishing, Cham, 2018), pp. 59-88.

D. A. G. Bruggeman, Berechnung verschiedener physikalischer Konstanten von heterogenen Substanzen. I. Dielektrizitätskonstanten und Leitfähigkeiten der Mischkörper aus isotropen Substanzen, Annalen der Physik **416**, 636-664 (1935).

E. D. Palik, in *Handbook of Optical Constants of Solids* (Elsevier).

F. A. Stevie and C. L. Donley, Introduction to x-ray photoelectron spectroscopy, Journal of Vacuum Science & Technology A **38**, 063204 (2020).

J. H. Scofield, Hartree-Slater subshell photoionization cross-sections at 1254 and 1487 eV, Journal of Electron Spectroscopy and Related Phenomena **8**, 129-137 (1976).

J. F. Moulder, W. F. Stickle, P. E. Sobol and K. D. Bomben, (Perkin-Elmer Corporation, Eden Prairie, Minnesota, USA 1979), pp. 25-26.

J. Frascaroli, E. Cianci, S. Spiga, G. Seguini and M. Perego, Ozone-Based Sequential Infiltration Synthesis of Al_2O_3 Nanostructures in Symmetric Block Copolymer, ACS Applied Materials & Interfaces **8**, 33933-33942 (2016).

A. Pirkle, S. McDonnell, B. Lee, J. Kim, L. Colombo and R. M. Wallace, The effect of graphite surface condition on the composition of Al_2O_3 by atomic layer deposition, Applied Physics Letters **97**, 082901 (2010).

L. Cheng, X. Qin, A. T. Lucero, A. Azcatl, J. Huang, R. M. Wallace, K. Cho and J. Kim, Atomic Layer Deposition of a High-k Dielectric on MoS_2 Using Trimethylaluminum and Ozone, ACS Applied Materials & Interfaces **6**, 11834-11838 (2014).

W. M. Mullins and B. L. Averbach, Bias-reference X-Ray photoelectron spectroscopy of sapphire and yttrium aluminum garnet crystals, Surface Science **206**, 29-40 (1988).

B. Lee, S.-Y. Park, H.-C. Kim, K. Cho, E. M. Vogel, M. J. Kim, R. M. Wallace and J. Kim, Conformal Al_2O_3 dielectric layer deposited by atomic layer deposition for graphene-based nanoelectronics, Applied Physics Letters **92**, 203102 (2008).

J. Hennessy, A. D. Jewell, K. Balasubramanian and S. Nikzad, Ultraviolet optical properties of aluminum fluoride thin films deposited by atomic layer deposition, Journal of Vacuum Science & Technology A **34** (2016).

R. König, G. Scholz, K. Scheurell, D. Heidemann, I. Buchem, W. E. S. Unger and E. Kemnitz, Spectroscopic characterization of crystalline AlF3 phases, Journal of Fluorine Chemistry **131**, 91-97 (2010).

N. W. Ashcroft and N. D. Mermin, in *Solid State Physics* (2021).

G. E. Town, presented at the 2015 IEEE 11th International Conference on Power Electronics and Drive Systems, 2015 (unpublished).

B. J. Baliga, Gallium nitride devices for power electronic applications, Semiconductor Science and Technology **28**, 074011 (2013).

Y. Zhang, A. Dadgar and T. Palacios, Gallium nitride vertical power devices on foreign substrates: a review and outlook, Journal of Physics D: Applied Physics **51**, 273001 (2018).

S. Chowdhury, Gallium nitride based power switches for next generation of power conversion, physica status solidi (a) **212**, 1066-1074 (2015).

J. Tian, C. Lai, G. Feng, D. Banerjee, W. Li and N. C. Kar, Review of recent progresses on gallium nitride transistor in power conversion application, International Journal of Sustainable Energy **39**, 88-100 (2020).

M. Danilovic, Z. Chen, R. Wang, F. Luo, D. Boroyevich and P. Mattavelli, presented at the 2011 IEEE Energy Conversion Congress and Exposition, 2011 (unpublished).

M. J. Scott, L. Fu, X. Zhang, J. Li, C. Yao, M. Sievers and J. Wang, Merits of gallium nitride based power conversion, Semiconductor Science and Technology **28**, 074013 (2013).

S. J. Pearton, J. C. Zolper, R. J. Shul and F. Ren, GaN: Processing, defects, and devices, Journal of Applied Physics **86**, 1-78 (1999).

R. J. Shul, G. B. McClellan, S. A. Casalnuovo, D. J. Rieger, S. J. Pearton, C. Constantine, C. Barratt, R. F. K. Jr., C. Tran and M. Schurman, Inductively coupled plasma etching of GaN, Applied Physics Letters **69**, 1119-1121 (1996).

D. Zhuang and J. H. Edgar, Wet etching of GaN, AlN, and SiC: a review, Materials Science and Engineering: R: Reports **48**, 1-46 (2005).

M. E. Lin, Z. F. Fan, Z. Ma, L. H. Allen and H. Morkoç, Reactive ion etching of GaN using BCl_3, Applied Physics Letters **64**, 887-888 (1994).

S. Huang, Q. Jiang, K. Wei, G. Liu, J. Zhang, X. Wang, Y. Zheng, B. Sun, C. Zhao, H. Liu, Z. Jin, X. Liu, H. Wang, S. Liu, Y. Lu, C. Liu, S. Yang, Z. Tang, J. Zhang, Y. Hao and K. J. Chen, presented at the 2014 IEEE International Electron Devices Meeting, 2014 (unpublished).

H. S. Lee, D. Y. Jung, Y. Park, J. Na, H. G. Jang, H. S. Lee, C. H. Jun, J. Park, S. O. Ryu, S. C. Ko and E. S. Nam, 0.34 V_T AlGaN/GaN-on-Si Large Schottky Barrier Diode With Recessed Dual Anode Metal, IEEE Electron Device Letters **36**, 1132-1134 (2015).

N. R. Johnson, J. K. Hite, M. A. Mastro, C. R. EddyJr. and S. M. George, Thermal atomic layer etching of crystalline GaN using sequential exposures of XeF_2 and BCl_3, Applied Physics Letters **114**, 243103 (2019).

P. Peri, K. Fu, H. Fu, Y. Zhao and D. J. Smith, Characterization of As-Grown and Regrown GaN-on-GaN Structures for Vertical p-n Power Devices, Journal of Electronic Materials **50**, 2637-2642 (2021).

K. J. Kanarik, T. Lill, E. A. Hudson, S. Sriraman, S. Tan, J. Marks, V. Vahedi and R. A. Gottscho, Overview of atomic layer etching in the semiconductor industry, Journal of Vacuum Science & Technology A **33**, 020802 (2015).

A. Fischer, A. Routzahn, S. M. George and T. Lill, Thermal atomic layer etching: A review, Journal of Vacuum Science & Technology A **39**, 030801 (2021).

S. M. George, Mechanisms of Thermal Atomic Layer Etching, Accounts of Chemical Research **53**, 1151-1160 (2020).

C. Kauppinen, S. A. Khan, J. Sundqvist, D. B. Suyatin, S. Suihkonen, E. I. Kauppinen and M. Sopanen, Atomic layer etching of gallium nitride (0001), Journal of Vacuum Science & Technology A **35**, 060603 (2017).

C. Mannequin, C. Vallée, K. Akimoto, T. Chevolleau, C. Durand, C. Dussarrat, T. Teramoto, E. Gheeraert and H. Mariette, Comparative study of two atomic layer etching processes for GaN, Journal of Vacuum Science & Technology A **38**, 032602 (2020).

Y. Zhang, S. Huang, K. Wei, S. Zhang, X. Wang, Y. Zheng, G. Liu, X. Chen, Y. Li and X. Liu, Millimeter-Wave AlGaN/GaN HEMTs With 43.6% Power-Added-Efficiency at 40 GHz Fabricated by Atomic Layer Etching Gate Recess, IEEE Electron Device Letters **41**, 701-704 (2020).

D. Ohori, T. Sawada, K. Sugawara, M. Okada, K. Nakata, K. Inoue, D. Sato and S. Samukawa, Selective atomic layer reaction between GaN and SiN in HBr neutral beam etching, Journal of Vacuum Science & Technology A **39**, 042601 (2021).

I.-H. Hwang, H.-Y. Cha and K.-S. Seo, Low-Damage and Self-Limiting (Al)GaN Etching Process through Atomic Layer Etching Using O_2 and BCl_3 Plasma, Coatings **11**, 268 (2021).

V. M. Bermudez, Investigation of the initial chemisorption and reaction of fluorine (XeF_2) with the GaN(0001)-(1 × 1) surface, Applied Surface Science **119**, 147-159 (1997).

V. M. Bermudez, The fundamental surface science of wurtzite gallium nitride, Surface Science Reports **72**, 147-315 (2017).

Y. Lee, N. R. Johnson and S. M. George, Thermal Atomic Layer Etching of Gallium Oxide Using Sequential Exposures of HF and Various Metal Precursors, Chemistry of Materials **32**, 5937-5948 (2020).

K. A. Hatch, D. C. Messina, X. Wang and R. J. Nemanich, Plasma Enhanced Atomic Layer Deposition and Atomic Layer Etching of Gallium Oxide Using Trimethylgallium, (Unpublished).

H. S. Oon and K. Y. Cheong, Recent development of gallium oxide thin film on GaN, Materials Science in Semiconductor Processing **16**, 1217-1231 (2013).

O. Ambacher, M. S. Brandt, R. Dimitrov, T. Metzger, M. Stutzmann, R. A. Fischer, A. Miehr, A. Bergmaier and G. Dollinger, Thermal stability and desorption of Group III nitrides prepared by metal organic chemical vapor deposition, Journal of Vacuum Science & Technology B: Microelectronics and Nanometer Structures Processing, Measurement, and Phenomena **14**, 3532-3542 (1996).

H. B. Profijt, S. E. Potts, M. C. M. van de Sanden and W. M. M. Kessels, Plasma-Assisted Atomic Layer Deposition: Basics, Opportunities , and Challenges, Journal of Vacuum Science & Technology A **29**, 050801 (2011).

C. Bae and G. Lucovsky, Low-temperature preparation of GaN-SiO_2 interfaces with low defect density. II. Remote plasma-assisted oxidation of GaN and nitrogen incorporation, Journal of Vacuum Science & Technology A **22**, 2411-2418 (2004).

T. Yamamoto, N. Taoka, A. Ohta, N. X. Truyen, H. Yamada, T. Takahashi, M. Ikeda, K. Makihara, M. Shimizu and S. Miyazaki, Low-temperature formation of Ga-oxide/GaN interface with remote oxygen plasma and its interface properties, Japanese Journal of Applied Physics **57**, 06JE01 (2018).

T. Yamamoto, N. Taoka, A. Ohta, N. X. Truyen, H. Yamada, T. Takahashi, M. Ikeda, K. Makihara, O. Nakatsuka, M. Shimizu and S. Miyazaki, Energy band structure and electrical properties of Ga-oxide/GaN interface formed by remote oxygen plasma, Japanese Journal of Applied Physics **57**, 06KA05 (2018).

E. D. Readinger, S. D. Wolter, D. L. Waltemyer, J. M. Delucca, S. E. Mohney, B. I. Prenitzer, L. A. Giannuzzi and R. J. Molnar, Wet thermal oxidation of GaN, Journal of Electronic Materials **28**, 257-260 (1999).

R. Korbutowicz, J. Prazmowska, Z. Wagrowski, A. Szyszka and M. Tlaczala, presented at the 2008 International Conference on Advanced Semiconductor Devices and Microsystems, 2008 (unpublished).

H. Ye, G. Chen, H. Niu, Y. Zhu, L. Shao and Z. Qiao, Structures and Mechanisms of Water Adsorption on ZnO(0001) and GaN(0001) Surface, The Journal of Physical Chemistry C **117**, 15976-15983 (2013).

M. Sato, Y. Imazeki, T. Takeda, M. Kobayashi, S. Yamamoto, I. Matsuda, J. Yoshinobu, Y. Nakano and M. Sugiyama, Atomistic-Level Description of GaN/Water Interface by a Combined Spectroscopic and First-Principles Computational Approach, The Journal of Physical Chemistry C **124**, 12466-12475 (2020).

X. Zhang and S. Ptasinska, Electronic and chemical structure of the H_2O/GaN(0001) interface under ambient conditions, Scientific Reports **6**, 24848 (2016).

S. W. King, R. F. Davis, R. J. Carter, T. P. Schneider and R. J. Nemanich, Hydrogen desorption kinetics for aqueous hydrogen fluoride and remote hydrogen plasma processed silicon (001) surfaces, Journal of Vacuum Science & Technology A **33**, 05E115 (2015).

Y. Yang, T. Sun, J. Shammas, M. Kaur, M. Hao and R. J. Nemanich, Electron affinity of cubic boron nitride terminated with vanadium oxide, Journal of Applied Physics **118**, 165310 (2015).

H. C. M. Knoops, T. Faraz, K. Arts and W. M. M. Kessels, Status and prospects of plasma-assisted atomic layer deposition, Journal of Vacuum Science & Technology A **37**, 030902 (2019).

J. H. Scofield, Hartree-Slater subshell photoionization cross-sections at 1254 and 1487 eV, Journal of Electron Spectroscopy and Related Phenomena **8**, 129-137 (1976).

F. A. Stevie and C. L. Donley, Introduction to x-ray photoelectron spectroscopy, Journal of Vacuum Science & Technology A **38**, 063204 (2020).

J. F. Moulder, W. F. Stickle, P. E. Sobol and K. D. Bomben, (Perkin-Elmer Corporation, Eden Prairie, Minnesota, USA 1979), pp. 25-26.

R. M. A. Azzam, Division-of-amplitude Photopolarimeter (DOAP) for the Simultaneous Measurement of All Four Stokes Parameters of Light, Optica Acta: International Journal of Optics **29**, 685-689 (1982).

a. J B Theeten and D. E. Aspnes, Ellipsometry in Thin Film Analysis, Annual Review of Materials Science **11**, 97-122 (1981).

A. Tikhonravov, M. Trubetskov, E. Masetti, A. Krasilnikova and I. Kochikov, *Sensitivity of the ellipsometric angles psi and delta to the surface inhomogeneity*. (SPIE, 1999).

J. H. Dycus, K. J. Mirrielees, E. D. Grimley, R. Kirste, S. Mita, Z. Sitar, R. Collazo, D. L. Irving and J. M. LeBeau, Structure of Ultrathin Native Oxides on III–Nitride Surfaces, ACS Applied Materials & Interfaces **10**, 10607-10611 (2018).

J. A. Murdzek, A. Rajashekhar, R. S. Makala, and S. M. George, Thermal atomic layer etching of amorphous and crystalline Al_2O_3 films, Journal of Vacuum Science & Technology A **39**, 042602 (2021)

C. Bae and G. Lucovsky, Low-temperature preparation of GaN-SiO_2 interfaces with low defect density. I. Two-step remote plasma-assisted oxidation-deposition process, Journal of Vacuum Science & Technology A **22**, 2402-2410 (2004).

CHAPTER 6 – SUMMARY AND FUTURE WORK

J. H. Dycus, K. J. Mirrielees, E. D. Grimley, R. Kirste, S. Mita, Z. Sitar, R. Collazo, D. L. Irving and J. M. LeBeau, Structure of Ultrathin Native Oxides on III–Nitride Surfaces, ACS Applied Materials & Interfaces **10**, 10607-10611 (2018).

Z. Huang, D. C. Messina, B. Eller, F. A. Koeck, P. Scowen and R. J. Nemanich, Multilayer ultraviolet reflective coating based on atomic layer deposited aluminum oxide and fluoride Journal of Vacuum Science & Technology A **39**, 042402 (2021).

D. König, G. Ebest, R. Scholz, S. Gemming, I. Thurzo, T. U. Kampen and D. R. T. Zahn, Evidence for high negative charge densities in AlF_3 coatings on oxidized silicon: a promising source for large drift fields, Physica E: Low-dimensional Systems and Nanostructures **14**, 259-262 (2002).

D. König, R. Scholz, D. R. T. Zahn and G. Ebest, Band diagram of the $AlF_3/SiO_2/Si$ system, Journal of Applied Physics **97**, 093707 (2005).

J. L. Navarro, E. A. Albanesi, R. Vidal and J. Ferrón, A study on the structural, electronic and optical properties of the α-AlF_3 compound, Materials Research Bulletin **83**, 615-622 (2016).

D. C. Messina, B. S. Eller, P. Scowen and R. J. Nemanich, Comparison of aluminum fluoride thin films growth by thermal and plasma enhanced atomic layer deposition, (unpublished).

K. Iwahori, M. Furuta, Y. Taki, T. Yamamura and A. Tanaka, Optical properties of fluoride thin films deposited by RF magnetron sputtering, Appl. Opt. **45**, 4598-4602 (2006).

Y. Taki, Film structure and optical constants of magnetron-sputtered fluoride films for deep ultraviolet lithography, Vacuum **74**, 431-435 (2004).

Y. Lee, J. W. DuMont, A. S. Cavanagh and S. M. George, Atomic Layer Deposition of AlF_3 Using Trimethylaluminum and Hydrogen Fluoride, Journal of Physical Chemistry C **119**, 14185-14194 (2015).

C. T. Chantler and J. D. Bourke, Low-energy electron properties: Electron inelastic mean free path, energy loss function and the dielectric function. Recent measurements, applications, and the plasmon-coupling theory, Ultramicroscopy **201**, 38-48 (2019).

M. Gorgoi, F. Schäfers, S. Svensson and N. Mårtensson, Relative sub-shell photoionization cross-sections of nickel metal determined by hard X-ray high kinetic energy photoemission, Journal of Electron Spectroscopy and Related Phenomena **190**, 153-158 (2013).

A. S. Barrière, G. Couturier, G. Gevers, H. Guégan, T. Seguelond, A. Thabti and D. Bertault, Preparation and characterization of gallium(III) fluoride thin films, Thin Solid Films **173**, 243-252 (1989).

A. S. Barrière, B. Desbat, H. Guégan, L. Lozano, T. Séguelong, A. Tressaud and P. Alnot, Physico-chemical characterization of thin films obtained by fluorination of GaAs under 5 bar of fluorine, Thin Solid Films **170**, 259-271 (1989).

H. Ricard, K. H. Kim, K. Aizawa and H. Ishiwara, Electrical Properties of Gallium Fluoride(GaF_3)/GaAs Interface with and without Sulfur Treatment, Japanese Journal of Applied Physics **29**, L2460-L2462 (1990).

A. S. Barriére, G. Couturier, H. Guegan, T. Séguelong, A. Thabti, P. Alnot and J. Chazelas, Interface GaAs - gallium fluoride thin film grown by fluorination: Electrical behaviour of the obtained MIS fluorinated GaAs structures, Applied Surface Science **41-42**, 383-389 (1990).

B. Hájek, V. Kohout and V. Flemr, Note on thermodynamic instability of M_4C_3-type carbides of gallium group metals, Monatshefte für Chemie - Chemical Monthly **117**, 1157-1164 (1986).

V. B. Kumar, M. Monte, O. Mathon, S. Pascarelli, Z. e. Porat and A. Gedanken, The interaction between molten gallium and the hydrocarbon medium induced by ultrasonic energy—can gallium carbide be formed?, Journal of the American Ceramic Society **100**, 3305-3315 (2017).

Y. Lee, H. Sun, M. J. Young and S. M. George, Atomic Layer Deposition of Metal Fluorides Using HF–Pyridine as the Fluorine Precursor, Chemistry of Materials **28**, 2022-2032 (2016).

B. Neumüller, Organometal fluorides of aluminium, gallium, indium and thallium, Coordination Chemistry Reviews **158**, 69-101 (1997).

M. Higashiwaki, K. Sasaki, A. Kuramata, T. Masui and S. Yamakoshi, Gallium oxide (Ga_2O_3) metal-semiconductor field-effect transistors on single-crystal β-Ga_2O_3 (010) substrates, Applied Physics Letters **100**, 013504 (2012).

M. F. Al-Kuhaili, S. M. A. Durrani and E. E. Khawaja, Optical properties of gallium oxide films deposited by electron-beam evaporation, Applied Physics Letters **83**, 4533-4535 (2003).

F. K. Shan, G. X. Liu, W. J. Lee, G. H. Lee, I. S. Kim and B. C. Shin, Structural, electrical, and optical properties of transparent gallium oxide thin films grown by plasma-enhanced atomic layer deposition, Journal of Applied Physics **98**, 023504 (2005).

M. Rebien, W. Henrion, M. Hong, J. P. Mannaerts and M. Fleischer, Optical properties of gallium oxide thin films, Applied Physics Letters **81**, 250-252 (2002).

M. Higashiwaki, K. Sasaki, A. Kuramata, T. Masui and S. Yamakoshi, Development of gallium oxide power devices, physica status solidi (a) **211**, 21-26 (2014).

H.-Y. Shih, F.-C. Chu, A. Das, C.-Y. Lee, M.-J. Chen and R.-M. Lin, Atomic Layer Deposition of Gallium Oxide Films as Gate Dielectrics in AlGaN/GaN Metal–Oxide–Semiconductor High-Electron-Mobility Transistors, Nanoscale Research Letters **11**, 235 (2016).

Z. Liu, P.-G. Li, Y.-S. Zhi, X.-L. Wang, X.-L. Chu and W.-H. Tang, Review of gallium oxide based field-effect transistors and Schottky barrier diodes, Chinese Physics B **28**, 017105 (2019).

S. Krishnamoorthy, Z. Xia, S. Bajaj, M. Brenner and S. Rajan, Delta-doped β-gallium oxide field-effect transistor, Applied Physics Express **10**, 051102 (2017).

K. D. Chabak, D. E. Walker, A. J. Green, A. Crespo, M. Lindquist, K. Leedy, S. Tetlak, R. Gilbert, N. A. Moser and G. Jessen, presented at the 2018 IEEE MTT-S

International Microwave Workshop Series on Advanced Materials and Processes for RF and THz Applications (IMWS-AMP), 2018 (unpublished).

B. Chatterjee, K. Zeng, C. D. Nordquist, U. Singisetti and S. Choi, Device-Level Thermal Management of Gallium Oxide Field-Effect Transistors, IEEE Transactions on Components, Packaging and Manufacturing Technology **9**, 2352-2365 (2019).

J.-W. Yu, P.-C. Yeh, S.-L. Wang, Y.-R. Wu, M.-H. Mao, H.-H. Lin and L.-H. Peng, Short channel effects on gallium nitride/gallium oxide nanowire transistors, Applied Physics Letters **101**, 183501 (2012).

L. Chen, W. Xu, W. Liu, S. Han, P. Cao, M. Fang, D. Zhu and Y. Lu, Polymer-Assisted Deposition of Gallium Oxide for Thin-Film Transistor Applications, ACS Applied Materials & Interfaces **11**, 29078-29085 (2019).

J. Sheng, E. J. Park, B. Shong and J.-S. Park, Atomic Layer Deposition of an Indium Gallium Oxide Thin Film for Thin-Film Transistor Applications, ACS Applied Materials & Interfaces **9**, 23934-23940 (2017).

R. E. Presley, D. Hong, H. Q. Chiang, C. M. Hung, R. L. Hoffman and J. F. Wager, Transparent ring oscillator based on indium gallium oxide thin-film transistors, Solid-State Electronics **50**, 500-503 (2006).

A. M. Armstrong, M. H. Crawford, A. Jayawardena, A. Ahyi and S. Dhar, Role of self-trapped holes in the photoconductive gain of β-gallium oxide Schottky diodes, Journal of Applied Physics **119**, 103102 (2016).

B. Chatterjee, A. Jayawardena, E. Heller, D. W. Snyder, S. Dhar and S. Choi, Thermal characterization of gallium oxide Schottky barrier diodes, Review of Scientific Instruments **89**, 114903 (2018).

L. Li, E. Auer, M. Liao, X. Fang, T. Zhai, U. K. Gautam, A. Lugstein, Y. Koide, Y. Bando and D. Golberg, Deep-ultraviolet solar-blind photoconductivity of individual gallium oxide nanobelts, Nanoscale **3**, 1120-1126 (2011).

S. H. Lee, S. B. Kim, Y.-J. Moon, S. M. Kim, H. J. Jung, M. S. Seo, K. M. Lee, S.-K. Kim and S. W. Lee, High-Responsivity Deep-Ultraviolet-Selective Photodetectors Using Ultrathin Gallium Oxide Films, ACS Photonics **4**, 2937-2943 (2017).

X. Chen, F.-F. Ren, J. Ye and S. Gu, Gallium oxide-based solar-blind ultraviolet photodetectors, Semiconductor Science and Technology **35**, 023001 (2020).

X. Chen, F. Ren, S. Gu and J. Ye, Review of gallium-oxide-based solar-blind ultraviolet photodetectors, Photon. Res. **7**, 381-415 (2019).

T. Chang, S. Chang, C. J. Chiu, C. Wei, Y. Juan and W. Weng, Bandgap-Engineered in Indium–Gallium–Oxide Ultraviolet Phototransistors, IEEE Photonics Technology Letters **27**, 915-918 (2015).

T. H. Chang, C. J. Chiu, S. J. Chang, T. Y. Tsai, T. H. Yang, Z. D. Huang and W. Y. Weng, Amorphous InGaZnO ultraviolet phototransistors with double-stack Ga_2O_3/SiO_2 dielectric, Applied Physics Letters **102**, 221104 (2013).

Q. Chen, Y. Zhang, T. Zheng, Z. Liu, L. Wu, Z. Wang and J. Li, Polarization detection in deep-ultraviolet light with monoclinic gallium oxide nanobelts, Nanoscale Advances **2**, 2705-2712 (2020).

T. G. Allen and A. Cuevas, Electronic passivation of silicon surfaces by thin films of atomic layer deposited gallium oxide, Applied Physics Letters **105**, 031601 (2014).

H. Hao, X. Chen, Z. Li, Y. Shen, H. Wang, Y. Zhao, R. Huang, T. Liu, J. Liang, Y. An, Q. Peng and S. Ding, Remote plasma-enhanced atomic layer deposition of gallium oxide thin films with NH_3 plasma pretreatment, Journal of Semiconductors **40**, 012806 (2019).

H. Kröncke, F. Maudet, S. Banerjee, J. Albert, S. Wiesner, V. Deshpande and C. Dubourdieu, Effect of O_2 plasma exposure time during atomic layer deposition of amorphous gallium oxide, Journal of Vacuum Science & Technology A **39**, 052408 (2021).

R. O'Donoghue, J. Rechmann, M. Aghaee, D. Rogalla, H.-W. Becker, M. Creatore, A. D. Wieck and A. Devi, Low temperature growth of gallium oxide thin films via plasma enhanced atomic layer deposition, Dalton Transactions **46**, 16551-16561 (2017).

T. G. Allen and A. Cuevas, Plasma enhanced atomic layer deposition of gallium oxide on crystalline silicon: demonstration of surface passivation and negative interfacial charge, physica status solidi (RRL) – Rapid Research Letters **9**, 220-224 (2015).

A. Mahmoodinezhad, C. Janowitz, F. Naumann, P. Plate, H. Gargouri, K. Henkel, D. Schmeißer and J. I. Flege, Low-temperature growth of gallium oxide thin films by plasma-enhanced atomic layer deposition, Journal of Vacuum Science & Technology A **38**, 022404 (2020).

V. D. Wheeler, N. Nepal, D. R. Boris, S. B. Qadri, L. O. Nyakiti, A. Lang, A. Koehler, G. Foster, S. G. Walton, C. R. Eddy and D. J. Meyer, Phase Control of Crystalline Ga_2O_3 Films by Plasma-Enhanced Atomic Layer Deposition, Chemistry of Materials **32**, 1140-1152 (2020).

Gallium Oxide Using Sequential Exposures of HF and Various Metal Precursors, Chemistry of Materials **32**, 5937-5948 (2020).

K. A. Hatch, D. C. Messina, X. Wang and R. J. Nemanich, Plasma Enhanced Atomic Layer Deposition and Atomic Layer Etching of Gallium Oxide Using Trimethylgallium, (Unpublished).

D. C. Messina, K. A. Hatch, X. Wang, D. Smith, Y. Zhao and R. J. Nemanich, Atomic layer etching of gallium nitride (0001) enabled by water vapor or remote O_2-plasma oxidation, (unpublished).

J. A. Murdzek, A. Rajashekhar, R. S. Makala and S. M. George, Thermal atomic layer etching of amorphous and crystalline Al_2O_3 films, Journal of Vacuum Science & Technology A **39**, 042602 (2021).

R. d'Agostino and D. L. Flamm, Plasma etching of Si and SiO_2 in SF_6–O_2 mixtures, Journal of Applied Physics **52**, 162-167 (1981).

V. M. Donnelly, D. L. Flamm, W. C. Dautremont-Smith and D. J. Werder, Anisotropic etching of SiO_2 in low-frequency CF_4/O_2 and NF_3/Ar plasmas, Journal of Applied Physics **55**, 242-252 (1984).

P. Machima and N. Hershkowitz, SiO_2 and Si_3N_4 etch mechanisms in NF_3/hydrocarbon plasma, Journal of Physics D: Applied Physics **39**, 673-684 (2006).

M. Matsui and K. Kuwahara, Highly selective SiO_2 etching over Si_3N_4 using a cyclic process with BCl_3 and fluorocarbon gas chemistries, Japanese Journal of Applied Physics **57**, 06JB01 (2018).

APPENDIX A

COPYRIGHT PERMISSION

Copyright permission for the re-use/re-print of the following figures were obtained or requested from the publishers. The detailed permission agreement for each figure or table with the copyright statement in the text can be provide upon request. Please contact me at dcmessina@asu.edu if there is any copyright violation in this dissertation.

A. 1 Permission Agreement Obtained for the Following Figures:

Figure 1.1: Reprinted/adapted by permission of American Chemical Society, Surface Chemistry for Atomic Layer Growth by S. M. George, A. W. Ott, and J. W. Klaus. Copyright © 1996, American Chemical Society

Figure 1.2: Reprinted/adapted by permission of American Vacuum Society, Multilayer ultraviolet reflective coating based on atomic layer deposited aluminum oxide and fluoride by Zhiyu Huang, Daniel C. Messina, Brianna S. Eller, et al, Copyright © 2021, American Vacuum Society

Figure 2.3: Reprinted/adapted by permission of John Wiley and Sons, Quantitative electron spectroscopy of surfaces: A standard data base for electron inelastic mean free paths in solids by M. P. Seah, W. A. Dench. Copyright © 1979, Heyden & Son Ltd.

Figure 2.6 and Figure 2.7: Reprinted/adapted by permission of Elsevier, Evaluation of procedures for overlayer thickness determination from XPS intensities by A. Jablonski. Copyright © 2019, Elsevier B.V.

Figure 2.17: Reprinted/adapted by permission of American Vacuum Society, Plasma-Assisted Atomic Layer Deposition: Basics, Opportunities, and Challenges by H. B. Profijt, S. E. Potts, M. C. M. van de Sanden, et al. Copyright © 2011, American Vacuum Society.

Figure 2.18: Reprinted/adapted by permission of American Chemical Society, Mechanisms of Thermal Atomic Layer Etching by Steven M. George. Copyright © 2020, American Chemical Society.

Figure 2.19: Reprinted/adapted by permission of American Vacuum Society, Thermal atomic layer etching: A review by Andreas Fischer, Aaron Routzahn, Steven M. George, et al. Copyright © 2021, American Vacuum Society.

Figure 3.5: Reprinted/adapted by permission of IEEE Transactions on Plasma Science, IEEE, Impedance model of helical resonator discharge by Jong-Chul Park. Copyright © 1997, IEEE.

A. 2 Permission Agreement Requested for the Following Figures:

As of October 16, 2021, the copyright permission agreements for the following figures have been requested. The detailed agreement can be provided if issues. If any of the following figures violates the copyright permissions of the publishers, the figures will be permanently removed. Unless further modifications requests sent to ProQuest, there are no copyright issues for the following figures. Please contact me at dcmessina@asu.edu for any questions regarding the copyright issues.

Figure 2.11: Copyright © 2017, Film Sense LLC

Figure 3.6: Copyright © 1997, ENI.

Figure 3.8: Copyright © 1987, Mass-Vac Inc.

Figure 3.9: Copyright © 1995, Ebara Corporation.

Figure 3.10: Copyright © 2015, CS Clean Systems Inc.

Figure 3.11: Copyright © 2021, New Cosmos BIE B.V.

A. 3 No Permission Agreement Required for the Following Figures:

Figure 1.3: Copyright © CC BY-NC-ND 4.0

A. 4 No Permission Agreement Required for the Following Tables:

Table 1.1: Copyright © CC BY-NC 4.0